Università Ca' Foscari

Scuola Dottorale di Ateneo
Graduate School

Dottorato di ricerca in
Scienza e Gestione dei Cambiamenti Climatici
Ciclo XXIX
Anno di discussione 2017

Aerosol deposition, trace elements and black carbon, over the highest glacier of the Eastern European Alps (Mt. Ortles, 3905 m) during the last 3000 years: environmental and climatic impacts

Candidate
Michele Bertò

Tutor
Prof. Carlo Barbante

Coordinator
Prof. Carlo Barbante

Abstract

For the first time, an ice core from the highest summit of the Eastern European Alps (*Alto dell'Ortles glacier*, 3905 m a.s.l) has been analysed through the use of a brand new melting and de-contamination system. The melting system was prepared and tuned in order to achieve the utmost level of de-contamination, stability of the melting speed and fluxes, and to allow a simultaneous double high-resolution discrete sampling. The continuous flow analyses system (CFA) methodology was tested as well as the results repeatability.

The firn and ice were drilled in 2011, processed at the University Ca' Foscari of Venice and stored at $-20\,^{\circ}\mathrm{C}$. The ice core was melted on a heated aluminium melting head and the melt water from the innermost part was pumped into the CFA tubing system. Four individual channels were installed after the de-bubbling system. The first line was connected to a Single Particle Soot Photometer (SP2) for refractory black carbon (rBC) concentration and diameter; the second to an Inductive Coupled Plasma Mass Spectrometer (ICP-MS) for trace elements (TE); the third to a conductivity micro-cell and an on-line particle counter with 32 dimensional channels and subsequent sampling; the last line was entirely devoted to the water sampling in pre-cleaned vials for TE, ultra-TE (ICP-QMS and CRC-ICP-MS) and further analyses.

The preservation of climatic and environmental signals was found to be more reliable below about 20 m of depth, corresponding to an ice age of about 30 years before present. The occurrence of intense percolation episodes, especially in the last two decades, strongly affected the firn part of the core. Seasonality however, is preserved for the high-resolution conductivity, dust and rBC profiles, even if a significant smoothing of the signals was detected. Crustal related trace elements (such as Ba or Al), also preserved a more or less evident seasonality in the high-resolution profiles.

In order to better evaluate the results obtained from the deep ice cores, a comprehensive glacio-chemical and radiative analysis was performed on the snow samples collected on the Alto dell'Ortles glacier during late August of 2015, after the second warmest summer since at least the last 200 years. A significant increase in concentrations of crustal and anthropogenic trace elements, dust and black carbon was detected in the snow summer layer. Therefore, despite the fact that the seasonality was still almost preserved, it's likely that subsequent summers characterized by high temperatures, as it's thought they will be in the future, will greatly degrade the climatic and environmental signals preserved in the snow and ice layers. Particular attention was given to understanding the major air masses provenance and atmospheric structure behavior.

The actual dating suggest that the Alto dell'Ortles ice core#1 spanned the last 3000 years. Anthropogenic induced depositions were observed in the deep ice layers dated back to the Roman Empire period, when, in fact, Lead and Copper mines

were very active. Others athropogenic induced contaminations were observed during the 10th century, the onset of the *Renaissance* period in Europe, which was characterized by great economic growth and significant mining activities. After the *Black Death* plague of the 1300 AD, a reduction of heavy metals deposition was observed in the core. After this minimum, another increase was detected from the beginning of the 15th century. Particularly, the quasi-simultaneous increase in concentration of Lead, Antimony, Arsenic, Bismuth and Silver strongly suggests that the sources of these elements were the European Silver mines. These depositions significantly decreased during the middle of the 17th century, when the American ores replaced the European ones.

Notably, the highest heavy metal concentrations in the ice core were detected in the 20th century layers, specifically increasing from the 1920s. Almost all of the anthropogenic metals increased due to the industrial growth of the European region. A relevant increase was found during the two decades from 1920 to 1940, probably due to enhanced emissions caused by the WWII manufacturing activities. The second highest peak of heavy metal concentrations was recorded during the 60s and the 70s.

A comparison with the available natural and anthropogenic emission inventories showed that the pollutants sources for the Ortles region are similar to those of the Colle Gnifetti region, and that both demonstrated less influence from emissions from Eastern European countries.

This project generated the longest ever-recorded black carbon deposition reconstruction from an Alpine ice core. During all of the pre-industrial period, the black carbon concentrations were very low, and the observed variations correlate with Lead and Bismuth, suggesting common emission sources, such as coal combustion. A concentration increase was observed from the first years of the 20th century, reaching two maximums during the 40s and the 60s, similarly to what observed in the heavy metals profiles. The refractory black carbon variability from 1850 to 2000 was compared with the available reconstructed European emission time series. The measured concentration appears to be in agreement with the inventories, showing a relevant decrease in the first years of the 70s.

The seasonality of black carbon is preserved in the Ortles ice core, whereas the concentrations during the last three decades are probably affected by the melt water percolation. A particle-dimensional analysis revealed an increasing trend in the median diameter of black carbon particles, from the last millennium to the industrial era.

The conductivity and dust profiles present a marked seasonal signal, despite partly influenced by water percolation events of the last decades. Many volcanic horizons were suggested for the first time, therefore contributing in a decrease of the dating uncertainties.

Contents

List of Figures

List of Tables

Part I

Introduction, the Ortles Ice Core and Analysis Methodology

Chapter 1

Introduction

This thesis describes the results and the data interpretation of the *continuous flow analyses* of the Alto dell'Ortles glacier's ice core#1. The first *Part* provides a brief description of the Earth's climate system and of the relevant changes that have occurred since the middle of the last century. Consequently, an overview of the atmospheric aerosols, of their properties, and of their impacts on climate is described. The available climate reconstructions are briefly reviewed both for the European region and, more specifically, for the Alpine region in the last millenniums and centuries, respectively.

In the second chapter the Mt. Ortles ice core and its physical and chemical characterizations are described in detail. Particularly, the data from the Automatic Weather Station (AWS) are investigated and the dating curve, dating methodology and related uncertainties are described.

In the following chapters the *continuous flow analyses* system is presented as well as the instruments used (*Single Particles Soot Photometer*, *Inductive Coupled Plasma Mass Spectrometer*, *Abakus Particle Counter* and conductivity micro-cell) and the *method validation*.

The second *Part*, describes and interprets the obtained results in four chapters. Firstly, the glacio-chemical response of the Alto dell'Ortles glacier to the warm-record summer of 2015 is given by interpreting the data from a three-meter-deep snow pit; the AWS data and the meteorological factors influencing the aerosol concentrations are also reviewed. Trace elements, dust and black carbon fluxes (and radiative impact) are evaluated in order to interpret the deep ice core results in case of extreme events.

The *trace elements* concentration profiles and the relative enrichments factors covering the last 3000 years are presented and divided in terms of anthropogenic and natural sources.

Conductivity and *number of particles'* profiles are then described in order to evaluate changes in the overall aerosol deposition and the presence of volcanic horizons.

The longest *black carbon* record in an Alpine ice core is presented and interpreted. Variations of the BC particles diameters' modes are also thoroughly investigated.

1.1 Climate Change

The Earth's climate is changing, and it also has already changed. Since the second half of the 20th century many parameters describing the climatological aspects of the climate system varied significantly. The global atmospheric temperature, the oceans' temperature and acidity, the cryosphere's total ice volume amount and snow-covered areas are just a small subset of the involved physical and chemical evidences of the changing climate.

The scientific community is now convinced, based on direct observations and theoretical efforts, that the primary cause for these changes observed in the last three/four decades, is humanity and the emissions from its activities. Particularly, in the most comprehensive and scientific-based fifth assessment report redacted by the *Intergovernmental Panel for Climate Change* (IPCC) in 2013, it's remarked that it's *very likely* that human influence has caused the temperature's increase since the middle of the last century (IPCC 2013 - Technical Report; T. Stocker et al. 2013). Others paleoclimate records and model simulations suggest that the Industrial Revolution Greenhouse gas emissions began to influence the Earth's climate as early as the 1830s, inducing an equatorial ocean response mechanisms (Abram et al. 2016).

The long term direct measurements time series provide unequivocal proof of the climate change. An increase of the global average surface atmospheric temperature of 0.85 °C was observed in the period 1880 - 2012 (Hartmann et al. 2013). Moreover, the last three decades were sequentially warmer, with the highest average temperatures since the beginning of the instrumental records (IPCC 2013 - Technical Report; T. Stocker et al. 2013). 2014 used to be the warmest year ever recorded on a global scale but 2015 was even warmer (following the NOAA, NASA, JMA databases). However, each of the first six months of 2016 was the warmest ever recorded on a global average (NASA's Goddard Institute for Space Studies). A temperature increase of 1.3 °C, compared to the end of the 18th century average temperature, made the first six months of 2016 the warmest half-year period ever recorded.

Other parameters reflects the changes in climate and few of them are reported in Fig. 1.1, taken from the IPCC 2013 - Technical Report (T. Stocker et al. 2013). Particularly, ocean heat content, sea level rise and specific humidity underwent significant increases during the last century (Fig. 1.1).

The cryopshere interacts with the atmospheric temperature variations via multi-feedback mechanisms. From the middle of the 1980s a global decrease was observed in the Northern Hemisphere March-April snow-covered areas compared to the 1971-2000 (Brown and Robinson 2011). Moreover, the summer Arctic sea ice extent drastically decreased from the 1960s, -45% at present days (Vaughan et al. 2013).

Mountain glaciers are melting and shrinking worldwide, and particularly in the European Alpine area, which is considered to be the most vulnerable to climate change in the European region (COM 2009): an enhanced temperature increase of about 2 °C was measured in this region since the last century. The glaciers' melting water appears to be by far the strongest contributor to the sea level rise. All glaciers and ice caps (including those on the peripheries of the Greenland and Antarctica ice sheets), indeed contribute about the 60% of the *eustatic* sea level rise (not due

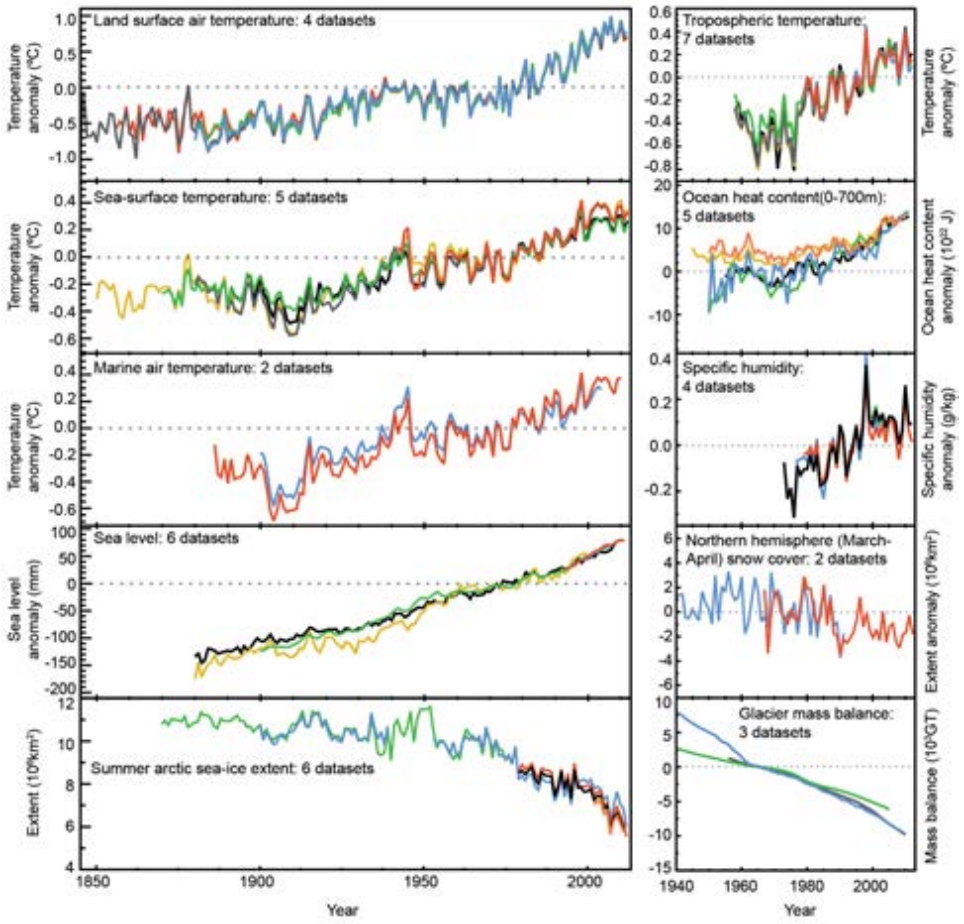

Figure 1.1: Multiple time series of measured climatic variables showing unequivocal trends in the changing climate. The periods considered are from 1850 to 2010 (graphs on the left) and from 1940 to 2010 (graphs on the right). The absolute values were normalized with the average value of a common period, resulting in values expressed as *anomalies*, except for the Arctic sea-ice extent and glaciers' mass balance (picture taken from the IPCC 2013 - Technical Report; T. Stocker et al. 2013). All the datasets used in this figure are list in the *Supplementary material* of Hartmann et al. 2013 (pages 19 and 20).

to water thermal expansion), whereas the Greenland's ice sheet about the 30% and the Antarctica's about the 10% (citemeier2007glaciers).

In the 1970s, Alpine glaciers had already lost about 35% of their maximum extent (reached in 1850), and more than 50% in 2000 (Zemp et al. 2006). A relevant decrease was observed in the generally low altitude glacier of the Eastern European Alps (Carturan, Filippi, et al. 2013). In the low-right graph of Fig. 1.1 the intensity of the mass balance decrease during the last century can be evaluated: the mass balance decrease is expressed as the *anomaly*. The three globally complete glaciers' mass balances are relative to the period 1961–1970; the datasets are from Arendt et al. 2012 (Randoph Glacier Inventory, dark grey), Leclercq et al. 2011 (green line) and Marzeion et al. 2012 (blue line).

1.2 Climate System, Natural Variability and Climate of the Past

An extremely complex network of feedback interactions between its various subsystems characterizes the climate system: the atmosphere, oceans, cryopshere, lithosphere and biosphere. Internal perturbations, such as large volcanic eruptions, may temporally alter the climatic state, and external perturbations also play a key role. Particularly, orbital parameters strongly influence the Earth's climate system, driving long-term climatic fluctuations by changing the total amount of received solar radiation, Earth's principal source of energy.

Ice core science fundamentally contributed to scientific understanding of the Earth's climate system and on the feedbacks mechanisms that are at its base. Reconstruction of the last eight glacial-interglacial cycles was performed in the framework of the EPICA ice core project (Augustin et al. 2004 and reference therein). *Natural variability* always played a dominant role in passing from glacial to interglacial periods. The natural oscillations of greenhouse gasses' concentrations in the atmosphere were found to be deeply connected with the Earth's temperature, as well as the atmospheric circulation patterns in transporting dust particles from different sources and with different intensities (Delmonte et al. 2002; Vallelonga, Gabrielli, et al. 2005; Lambert et al. 2008; Gabrielli, Wegner, et al. 2010).

The Holocene, the epoch we're living in, started about 11.7 Kyears BP, after the last glacial period. This warm period was characterized by a mite climate allowed the birth of the first civilizations and their expansion. From a climatic point of view, the human imprint started to become significant with the Industrial Revolution in the 19^{th} century. In this period greenhouse gasses emissions and the release of strongly light absorbing and reflecting particles in the atmosphere began influencing the Earth's radiative budget. This unprecedented increasing trend caused anthropogenic perturbations to become the dominant climate change factors, despite the huge role of natural factors that still influenced the Earth's climate.

1.3 Atmospheric Aerosols and their Impacts on Climate

Anthropogenic *global warming* is the result of the emission in the atmosphere of gasses and particles that affects the Earth's radiative budget. The emission rate has been greater compared to what the climate system could *afford* without resulting in significant changes in the short term. The *drivers* are the atmospheric factors contributing to the unbalancing, and the intensity with which each driver perturbs the radiative balance, contributing in warming or cooling the Earth, is called *radiative forcing* (RF, expressed in $W\,m^{-2}$): specifically, in the IPCC-2013 report, it is defined as the difference of the energy flux caused by each driver in 2011 and 1750 (T. Stocker et al. 2013).

Greenhouse gasses and aerosols are by far the strongest drivers of climate change. The total anthropogenic RF reported in the IPCC 2013 ranges from $1.13\,W\,m^{-2}$ to $3.33\,W\,m^{-2}$ (IPCC 2013-The Physical Science Basis; T. Stocker et al. 2013), leading to a net warming.

The total aerosol RF is estimated to be from $-0.77\,\mathrm{W\,m^{-2}}$ to $0.23\,\mathrm{W\,m^{-2}}$, with a negative average value; this means that the atmospheric aerosols' net effect is a cooling of the climate system. In the atmosphere the mineral dust, sulphates, nitrates and organic carbon aerosols contribute with negative RFs: they reflect the incoming solar radiation back and therefore decrease the total amount arriving to the Earth's surface. On the contrary, black carbon aerosols (BC) strongly absorb the solar radiation due to its particles' small diameter. Locally, BC particles decrease the solar radiation arriving to the surface, but globally the net effect is of warming, and the RF is about $0.6\,\mathrm{W\,m^{-2}}$ (IPCC 2013 - The Physical Science Basis; T. Stocker et al. 2013).

Many feedback mechanisms regulate the impact of the atmospheric aerosols. The most significant is certainly the aerosol-clouds interaction, which at the moment represents the highest source of uncertainty in the total anthropogenic RF estimation (T. Stocker et al. 2013). The best way to describe the aerosols' impact on the climate system is to use another parameter, called *effective* radiative forcing (ERF). ERF takes into account the *rapid adjustments* to perturbations. Particularly, for the anthropogenic aerosols the RF and the ERF may significantly differ because of their interaction with clouds and with the snow/ice surfaces. ERF may be subdivided again in order to describe the aerosol-radiation (ERF-ari) or the aerosol-clouds interaction (ERF-aci). Specifically, the ERF-ari requires a deep knowledge of the spectral absorption and scattering coefficients as a function of electromagnetic radiation wavelengths of each aerosol, the single scattering albedo and the phase function. These aerosols' particles properties depend on size, on the composition, and on the mixing state (IPCC 2013, Aerosol and Clouds; Boucher et al. 2013).

1.3.1 Definition and Classifications

An aerosol is a collection of solid or liquid particles suspended in a gas, and the particles and the liquid form a two-phase system (Hinds 2012). The aerosol particles can be subdivided in terms of their physical characteristics and sources of emission.

Dimensions The typical subdivision divides four aerosol particles' diameter (D_p) dimensional groups called *modes* (mode values of the aerosol particles log-normal distribution): the *nucleation* mode (D_p smaller than 10 nm), the *Aitken* mode (D_p between 10 nm and 0.1 µm), the *accumulation* mode (D_p between 0.1 µm and 2.5 µm) and *coarse* mode (D_p greater than 2.5 µm) (Fig. 1.2).

Sources A subdivision is made in terms of the aerosol source, natural or anthropogenic: in present-day atmosphere, the anthropogenic aerosol particles' components are mainly BC, sulphate, nitrate and ammonium. Natural emissions are still the strongest worldwide in terms of mass and accounts for sea salt, mineral dust and biogenic primal emission. Primary and secondary emission organic aerosols have both natural and anthropogenic emission sources (IPCC 2013, Aerosol and Clouds; Boucher et al. 2013).

Formation Mechanisms The formation mechanism is used to distinguish between two aerosol classes: *primary* and *secondary* aerosols. *Primary* particles if they have been emitted as they are in the atmosphere, or *secondary* if the primary

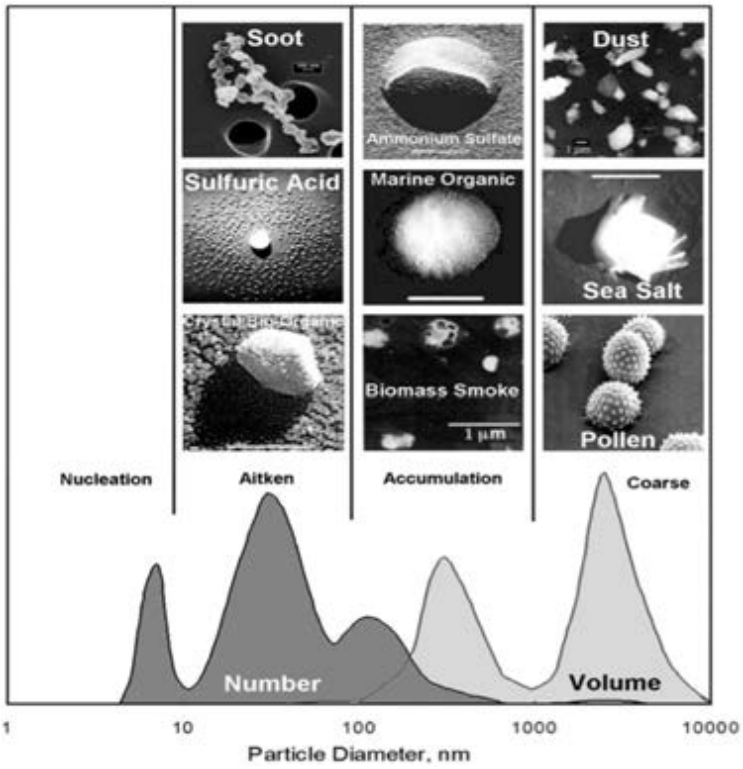

Figure 1.2: Number and volume of aerosols for the four dimensional modes (Dahl et al., 2005).

emitted aerosols underwent *coagulation* (formation of small size primary emitted aerosol agglomerates) and/or *condensation* (condensation on the primary emitted aerosol of low vapor pressure gaseous compounds) mechanisms. The gasses that are most commonly involved in the secondary aerosols production are suphfuric acid, ammonia or oxidized organic species. Nowadays, the sulphur cycle controls the secondary aerosol production, whereas in the preindustrial period marine biogenic emissions, such as gaseous dimethylsulfide (DMS), were the dominant factors. The oxides organics constitute the 20-50% of the fine particles' total mass, and not much is known about their atmospheric behaviours (Kanakidou et al. 2005).

Atmospheric Aerosols Composition In terms of composition the most abundant atmospheric aerosols are: inorganic species (sulphate, nitrate, ammonium, sea salt), organic species, BC (from the incomplete combustion of fossil and biomass fuels), mineral species (e.g. desert dust) and primary biological aerosol particles. Natural emitted primary aerosol account for about 80-90% of the total atmospheric aerosol load (Raynaud et al. 2003) and this is explained by strong aerosol emissions from the oceans and from the Earth's crust particles resuspension by wind. Instead, carbonaceous aerosol components, such as BC or organic matter, and industrial mineral dust are amongst the smaller components in terms of total mass, about less than 1%, 2% and 3% respectively, for the year 2000 (IPCC 2007; Solomon 2007).

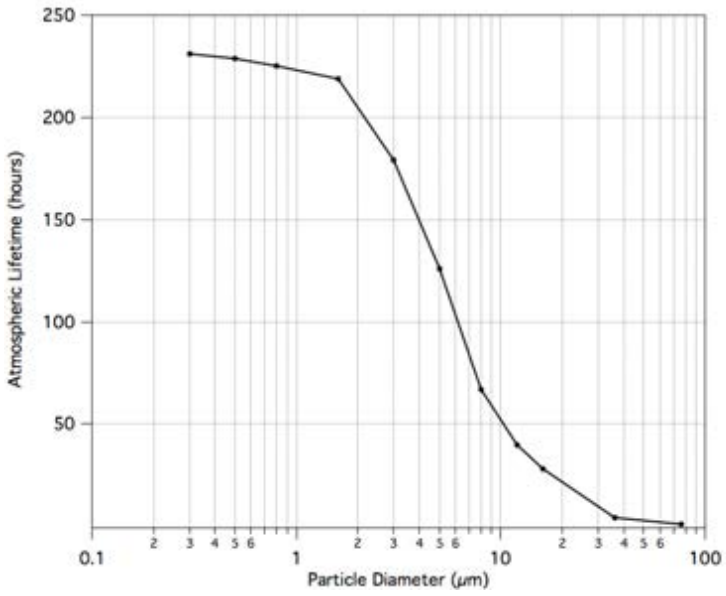

Figure 1.3: Atmospheric lifetime as a function of the aerosol's particles dimensions (adapted from Tegen and Fung 1994).

1.3.2 Transport Processes and Atmospheric Removals

Aerosols' particles can be transported over long distances from the source due to their small dimensions. However, the transport strongly depends on the particles' diameter, mass, shape and composition. The *residence time* in the atmosphere, also called *atmospheric lifetime*, is an averaged measure of the time a particle passes in the atmosphere before being scavenged from *wet* or *dry* deposition.

Starting from the concentration of an aerosol species at the emission source and the *residence time*, it is possible to compute the concentration at the sink, at a certain distance from the source and after a certain time from the emission. An exponential law describes the aerosol atmospheric transport behavior:

$$C_b = C_a \cdot f \cdot e^{-\frac{t}{T}}$$

C_b and C_a are the concentration at the sink and at the source, respectively. T is the specific *resident time* depending on the particles's characteristics, t is the time after the emissions to the deposition and f is a correction factor. The negative exponential makes that the longer the time from the source, the lower will be the concentration at the sink.

The atmospheric *residence time* is therefore a crucial parameter in describing the ability of the particles to be transported more or less far by atmospheric motions, especially during the pollutions effects after localized pollution episodes (e.g. Fukushima radioactive fallout; Terada et al. 2012).

Two main kinds of aerosols' depositions limit the atmospheric *residence time*: *wet* and *dry* depositions. *Dry* deposition, as well as *wet* deposition, are particles' size dependent. Therefore, the more time passes from the aerosols emission, the more size atmospheric filtering will act on the aerosols' total size distribution. The smaller particles usually are transported farther and in Fig. 1.3 the *atmospheric lifetime* is reported as a function of particles' dimensions.

Wet deposition

Wet deposition, as suggested by the name, is a removal mechanism that involves rain or snow events and it can happen inside or below clouds, during the droplets or ice nucleation or via rain collision, respectively. A simple wet deposition model was proposed in Junge 1963, in which the atmospheric chemical concentration in the water droplets (C_l) linearly depends from the aerosol concentration in the atmosphere (C_a), the water density (d) and the *scavenging factor* (E_s), whereas inversely from the cloud's liquid content (L).

$$C_l = C_a \cdot E_s \cdot \frac{d}{L}$$

Dry deposition

The two main *dry* deposition processes are: gravitational settling, due to the gravitational force (depending on the mass), and near surface turbulent atmospheric motions. However, different processes are involved in the *dry* deposition of particles with different diameters as described in Puxbaum and Limbeck 2008.

1. *Sedimentation* processes cause the biggest particles (greater than 10 µm) to deposit.
2. For particles between 1 µm and 10 µm *surface interception* is the predominant process.
3. For particles diameters between 0.1 µm and 1 µm the dominant processes are *turbulent* transport, *surface roughness* and *wind speed*.
4. The smallest particles *dry* deposition (smaller than 0.1 µm) is dominated by *Brownian motions* (in the laminar boundary layer between receptor surface and turbulent zone).

1.3.3 Trace Elements

Sources A variety of natural processes contribute to the large natural emission of trace elements in the atmosphere: surface winds, erosion, crustal minerals mobilizations, volcanic eruptions, but also ocean sea spray or natural biomass fires (forests or savannas). As reported in J. M. Pacyna 1998 the resuspended dust explains, on a global scale, more than 50% of the measured atmospheric content of Cr, Mn and V; more than 20% of Cu, Ni, Pb, Sb and Zn. Specifically, depending on the type and the strength, volcanic eruption can be the source of about 20% of Cd, Hg, As, Cr, Cu, Ni, Pb and Sb (J. M. Pacyna 1998). The ocean emissions also has an important contribution to the metals' natural emission, accounting for the 10% of the total emission. Heavy metals are also present in traces in the vegetation and are therefore released in case of natural fires (Cu, Zn and Pb) (Nriagu 1989).

Most of the anthropogenic induced metals emissions are caused by fossil fuel combustion. This kind of combustion is indeed the main source for atmospheric emissions of Be, Co, Hg, Mo, Ni, Sb, Se, Sn and V; combustion are also responsible for a large part of As, Cr, Cu, Mn and Zn (J. M. Pacyna 1998). The industrial metallurgical processes in general are the most relevant sources for As, Cd, Cu, Ni and

Source category	As	Cd	Cr	Cu	Hg	In
Stationary fossil fuel combustion	809	691	10 145	7 081	1 475	
Vehicular traffic						
Non-ferrous metal production	3 457	2 171	—	18 071	164	45
Iron and steel production	353	64	2 825	142	29	—
Cement production	268	17	1 335	—	133	—
Waste disposal	124	40	425	621	109	—
Other					325[a]	
Total	5 011	2 983	14 730	25 915	2 235	45
1983 emission[b]	18 820	7 570	30 480	35 370	3 560	25

Mn	Mo	Ni	Pb	Sb	Se	Sn	Tl	V	Zn
9 417	2 642	86 110	11 690 88 739	730	4 101	3 517	1 824	240 084	9 417
59	—	8 878	14 815	552	466	319	—	77	40 872
1 060	—	36	2 926	7	7	—	—	71	2 118
—	—	134	268	—	3	—	—	—	2 670
511	—	129	821	272	24	115	—	23	1 933
11 047	2 642	95 287	119 259	1 561	4 601	3 951	1 824	240 255	57 010
38 270	3 270	55 650	332 350	3 510	3 510	3 790	5 140	86 000	131 880

Figure 1.4: Worldwide trace elements emission for the most relevant anthropogenic sources for the mid 1990s period (in tonnes/year) (from J. M. Pacyna and E. G. Pacyna 2001).

Zn. The vehicular transport section is another important source of metals, especially for Pb when it was used as antiknock agent. Further, the road traffic exhaust emissions release Fe, Cu, Zn, Ni and Cd (J. M. Pacyna 1998). In Fig. 1.4 the heavy metals emissions during the mid 1990s are reported in term of the most relevant anthropogenic sources (J. M. Pacyna and E. G. Pacyna 2001).

Trend European heavy metal emissions have been decreasing for the last 40 years mainly due to policy regulations and technological innovations, and also because of a sectoral shift (E. G. Pacyna et al. 2007). The emission time series for As, Cd and Pb are reported in Fig. 1.5. In the European area the emissions of Cd and Hg decreased more than 75% during the period 1990-2013, while Pb of more than 90% (source: European Environmental Agency).

Size distribution Atmospheric trace elements containing particles follow a multimodal dimensional distribution. At least for the European background emissions, trace elements can be divided in three groups in terms of the corresponding aerosol particles dimensions. Cd, Sn, Pb, Zn, Ni and Se dimensional distributions maximums were found to be in the *accumulation* mode (0.5 μm); Cu, Co, Mn and Hg show spread dimensional distributions from *accumulation* to *coarse* modes; the dimensional distributions of Fe, Sr and Ba clearly peak in the *coarse* mode (A. Allen et al. 2001). Trace elements containing particles distributions for the England emission of March of 1999 are reported in Fig. 1.6.

In A. Allen et al. 2001 four different mechanisms were found to be involved in determining the observed dimensional distribution for the trace elements con-

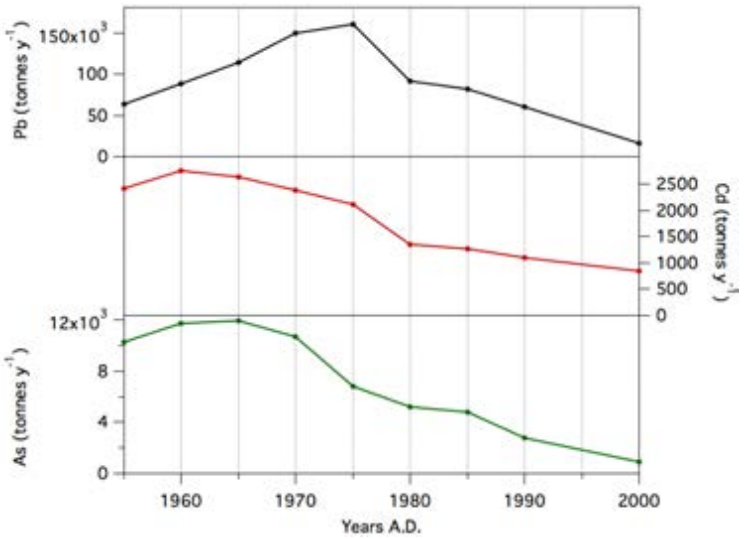

Figure 1.5: Worldwide As, Cd and Pb emission time series for the period 1955-2000 (adapted from E. G. Pacyna et al. 2007).

taining particles: a) the primary emissions of particles from combustion and/or industrial processes in the *accumulation* mode; b) the advection of air masses characterized by containing aged intermediate size aerosols and/or primary emissions of particles in this size range; c) resuspension of large particles and d) particles generated during frictionally processes, such as mechanical wear.

1.3.4 Black Carbon

Formation and Sources Black Carbon (BC) is a primary emitted carbonaceous particle that is mainly released in the atmosphere by fossil fuels combustion and biomass burning (T. C. Bond, Doherty, et al. 2013). The formation of black carbon particles during the combustion processes may be resumed in four steps, even if many of the actual processes are still partly unknown (Masiello 2004, Moosmüller et al. 2009, T. C. Bond, Doherty, et al. 2013, Weingartner et al. 1997): 1) thermal anaerobic degradation of the fuel (pyrolysis), 2) formation and consequent growth of *polycyclic aromatic hydrocarbons*, 3) condensation of gases to particles and 4) coagulation and surface growth resulting in water insoluble and hydrophobic *conglomerates of spherules*.

The most relevant properties of BC particles are the stability in the atmosphere and after the deposition, the direct absorption of solar radiation and the high *refractoriness*: BC vaporized at about 4000 K (Moteki and Kondo 2010).

From a global perspective BC sources during the preindustrial period were mainly natural and anthropogenic biomass combustion. Particularly, grassland fires were the main BC emitters up to the 1920s, followed by domestic sector emissions due to heating and cooking coal and biomass burning (Smith and T. C. Bond 2014). The industrial and transport (mainly *diesel* burning) sectors became strong BC sources from the 1970-80s, and with a lower intensity shipping and bio-fuel burning. In the year 2000 an estimation of 59% of the total global BC emissions were from the energy related sector, whereas biomass burning accounted for the 41% (T. C. Bond, Doherty, et al. 2013).

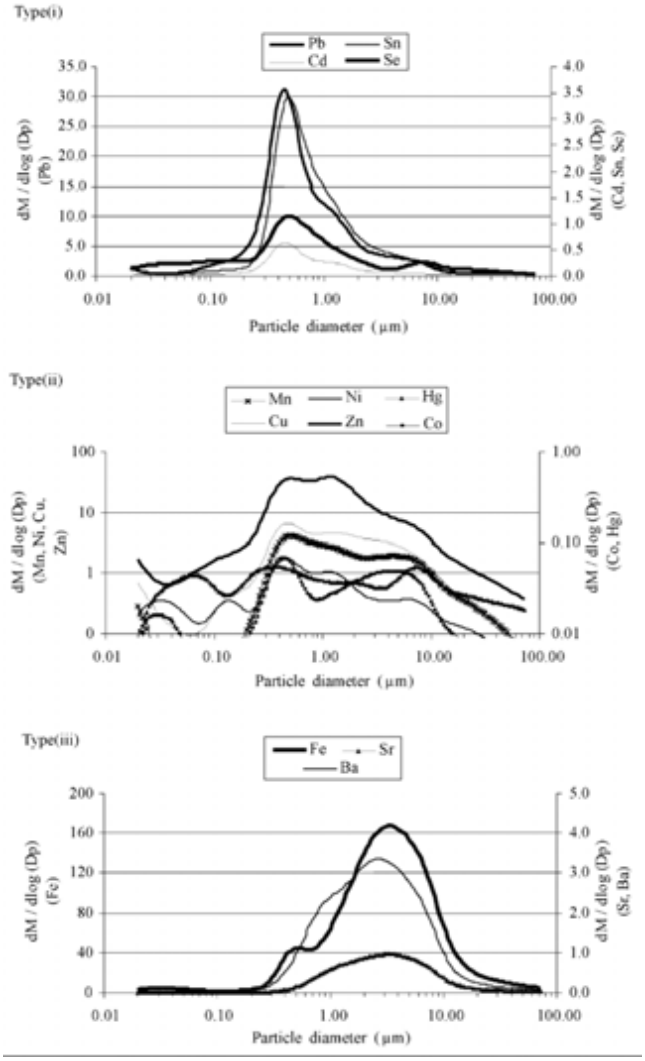

Figure 1.6: Trace elements' containing particles size distribution measured in central England in March 1999 (from A. Allen et al. 2001).

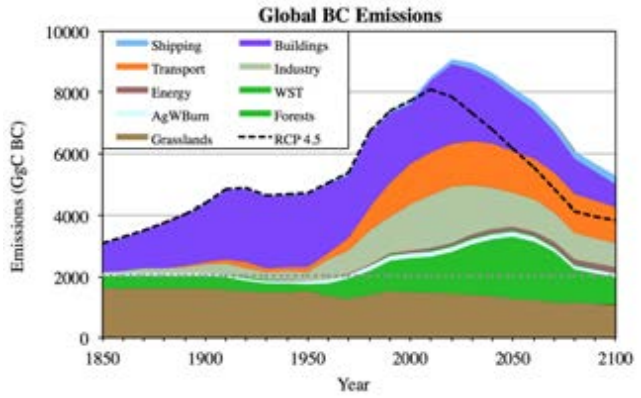

Figure 1.7: Historical and future BC emissions obtained with the global climate atmospheric model (GCAM) under the RCP4.5 climate policy scenario. The assumed preindustrial BC open burning emissions are shown with the grey dotted line. BC emission data from 1850 to 2000 are from T. C. Bond, Bhardwaj, et al. 2007; updated in Lamarque et al. 2010 (from Smith and T. C. Bond 2014).

The European region's BC emissions are characterized by a significant spatial variability. The European Monitoring and Evaluation Program (EMEP) includes 12 European rural background sites and two urban background sites and the one-year campaign results of 2002/2003 was described in Yttri et al. 2007. Significant differences in atmospheric BC concentrations were found, and particularly the lowest concentrations were found in the Northern European States with concentrations lower than 0.5 μg m^{-3}), whereas in the Continental Europe they were higher than 1 μg m^{-3} (Yttri et al. 2007).

A strong seasonality was also observed with highest atmospheric BC values during winter, when the residential heating emissions are maximum (Lukacs et al. 2007), and a summer minimum, when the most important sources are the anthropogenic and natural fires (Bovchaliuk et al. 2013).

At high altitude sites, in contrast, the highest BC concentrations are measured during summer. Particularly, in summer, the atmospheric BC concentrations are from two to ten times higher and this can be explained by considering the atmospheric structure: in winter the BC particles are concentrated close to the surface due to enhanced emissions and a low boundary layer depth, in contrast during summer upward transports are stronger and bring the pollutants at high altitude sites (Pio et al. 2007; Ripoll et al. 2014). This is of great importance in evaluating the BC data on the Alto dell'Ortles glacier (this work).

In the European region, BC emissions estimates from the ACCMIP (Emissions for Atmospheric Chemistry and Climate Model Inter-comparison Project; Lamarque et al. 2010) show that the Western Europe emissions in 2000 were of about 0.38 Tg $year^{-1}$, whereas Eastern Europe's emissions were of 0.13 Tg $year^{-1}$. 53% of the total BC emissions in Europe are from the vehicular transport sector (diesel engines), 20% from the domestic fuels burning, 20% from the industrial sector and the remaining from biomass burning and other smaller sources like, aviation, energy, waste, agricultural waste and ships (Lamarque et al. 2010); diesel engines as a source of BC is therefore the most relevant BC emission in the European region, as also reported in T. C. Bond, Doherty, et al. 2013 (the estimation was 70% of the total BC emissions).

A comprehensive description of the recent BC climatology and optical properties in the European region, in the frame of the ACTRIS monitoring project, can be found in Zanatta et al. 2016.

Historical Global Emissions and Future Projections The global historical and future emissions trend are reported in Fig. 1.7 (from Smith and T. C. Bond 2014). Starting from 1850, the aerosol emissions significantly increased globally and, at that time, BC emissions were already at the 20-40 percentile of the emissions during the year 2000 (Smith and T. C. Bond 2014) (Fig. 1.7). The main sources were biomass natural combustion (forests and grasslands), and domestic biomass combustion based heating and cooking (T. C. Bond, Bhardwaj, et al. 2007). The first emission peak was during the 1920s and then emissions stabilized until the 1960s. The greatest global BC emission increase started after the 1960s and it appears not to have achieved the projected peak yet in the "no policy" scenario (Smith and T. C. Bond 2014). The future emission peak is projected to be around the year 2020 in the RCP4.5 climate policy scenario (the future scenarios were obtained by the Global Change Assessment Model (GCAM), a detailed explanation is found in Smith and

T. C. Bond 2014).

Historical European Emissions Three main long-term historical European anthropogenic BC emissions reconstructions are available in literature, and all of them started in 1850. The reconstructions are based on *emission inventories*, which are derived from the evaluation of *emissions sources* and specific *emission factors* (this refers to BC emissions from a certain mass of a fuel burned in a specific process).

The historical reconstruction from T. C. Bond, Bhardwaj, et al. 2007 covers the period 1850-2000 and it is based on sectoral, fuel-specific reconstruction of fossil fuel consumption (with specific emissions factors) using many source data.

The Junker and Liousse 2008 reconstruction is from 1860 to 1997 and slightly differs both in methodology and in the final result from the other two. Particularly, the inventory was constructed on the basis of historical fuel production, use and trade data sets (The United Nations energy statistics database published by the United Nation's Statistical Division, 1997 and Etemad and Luciani 1991).

The third dataset covers the period 1850-2000, it's called *ACCMIP* (Emissions for Atmospheric Chemistry and Climate Model Intercomparison Project), and was created in order to be used during the *Coupled Model Inter-comparison Project Phase 5* (CMIP5) of the *World Climate Research Programme* (WCRP) (Granier et al. 2011), and it is the result of an harmonization of different reconstructions (Lamarque et al. 2010).

The reconstructions from T. C. Bond, Bhardwaj, et al. 2007 and Lamarque et al. 2010 are similar and in both of them the BC emissions started to increase in 1850, reaching a plateau in the 1910s. The emissions remained constant until the 1960s, after that they decreased significantly. The emissions in 2000 were still higher than those of the preindustrial period.

A quite different story was inferred in Junker and Liousse 2008: BC emissions increased with a higher trend from 1860 until 1910 and then decreased until the second half of the 1940s. Then the emissions tripled until 1960 and remained constant until 1990, after that they decreased abruptly until 2000.

These three datasets are compared with the black carbon concentrations measured in the Ortles ice core (this work) in Chapter 9.

1.3.5 The Impacts of Black Carbon on Climate

Atmospheric aerosols have a strong impact on climate, by interacting with the Earth's radiative energy budget and with the clouds formation and microphysics (see Section 1.3). Specifically, BC influences the Earth's climate by three main mechanisms: the atmospheric BC-radiation interaction, the *snow darkening* effect, and the BC-clouds interaction (not described in this work).

Atmospheric Black Carbon-Solar Radiation Interaction

BC particles suspended in the atmosphere directly absorb the incoming solar radiation in the visible part of the spectrum, and this characteristic made BC the second strongest atmospheric radiative forcing after CO_2 (T. C. Bond, Doherty, et al. 2013). On a very local scale, close to the emissions' sources, the presence of BC particles

in the atmosphere decreases the surface incoming radiation. However, on a global scale, the BC impact is characterized by a positive radiative forcing, therefore contributing to global warming (IPCC 2013; T. F. Stocker et al. 2013).

Particularly, BC radiative forcing, including the aerosols/radiation/clouds interactions and rapid adjustments, was estimated to be 1.1 $W\,m^{-2}$ (T. C. Bond, Doherty, et al. 2013). However, a 90% uncertainty affects this value and the ERF value ranges from 0.17 $W\,m^{-2}$ to 2.1 $W\,m^{-2}$ (Myhre et al. 2013). Most of the uncertainty derives from the aerosol-clouds interaction, but also the modelled atmospheric BC concentration altitudinal profile may accounts for 20 to 50% (Samset et al. 2013).

The most significant BC impact is solar radiation absorption, this effect is usually measured in terms of *absorption coefficient*. However, the latter also depends from the BC particles' physical characteristics, such as size, shape, concentrations and external coating or mixing state (T. C. Bond, Doherty, et al. 2013). Usually, the BC impact is expressed in terms of the *MAC* (mass absorption cross section), which is an intensive property obtained by normalizing the BC light absorption with its mass concentration. Higher MAC values mean higher light absorption with the same mass, and therefore a more positive ERF-ari. The latter was evaluated in two independent studies, T. C. Bond, Doherty, et al. 2013 and Myhre et al. 2013, obtaining the values 0.51 $W\,m^{-2}$ and 0.23 $W\,m^{-2}$, respectively.

The Impact of Black Carbon on Snow and Glaciers

In recent years, great attention has been given to the impact of BC particles on snow covered areas and glaciers. Theoretical and experimental results showed that the cryosphere is affected both by the BC-induced atmospheric warming and by direct and indirect BC radiative effects after deposition on snow surfaces.

BC-induced Atmospheric Warming Local atmospheric warming due to the advection of BC-induced warmer air from polluted regions may greatly enhance snow and ice melting, especially in Arctic regions or at mid-latitudes glaciers. Particularly, model results showed that in the Himalayan region, lower atmospheric warming induced by BC may be as significant as that caused by carbon dioxide, with a temperature increase of about 0.6 °C (Meehl et al. 2008; Ramanathan and Carmichael 2008).

BC on Snow and Ice Fresh snow surfaces reflect visible solar radiation very efficienciently, and particularly the albedo of fresh snow is amongst the highest found on Earth (higher than 0.9). The deposition of atmospheric impurities on snow surfaces can greatly reduce the surface albedo by direct absorption, and related heating, and by positive feedbacks enhancing snow aging and crystal size distribution.

Spectral models' results suggest that the presence of light absorbing impurities in fresh snow significantly increases the total amount of absorbed radiation (Wiscombe and S. G. Warren 1980; S. G. Warren and Wiscombe 1980; S. G. Warren 1982; S. Warren 1984). Particularly, the radiative absorption of impurities is enhanced by multiple scattering in the snow crystal structure, thus increasing the probability of radiation-BC interaction, and therefore, the fraction of reflected radiations decreases (i.e. the surface has a lower albedo). The effects on snow surfaces of BC

particles are not only due to the first order radiative absorption and consecutive heating, but also, most relevantly, by the positive feedbacks mechanisms induced by them.

1. BC particles warming causes an increase in snow temperature that hasten snow aging, and particularly the growth of snow crystals' effective radius, which causes strong darkening of the snow (M. G. Flanner and Zender 2006);

2. BC particles' radiative effect is enhanced in aged snow; the latter is characterized by larger effective radii (S. G. Warren and Wiscombe 1980);

3. A strong feedback, particularly important on temperate and mid-latitudes glaciers, derives from the surface melting and sublimation (especially during spring-summer) leaving on the surface all the particles larger than 5 μm and about 50% of hydrophobic BC particles (Clarke and Noone 1985; Conway et al. 1996), enhancing the melting (M. G. Flanner, Zender, et al. 2007).

In the literature the RF of the BC particles deposited on snow and ice was estimated on a global scale at $0.04\,W\,m^{-2}$ (IPCC 2013 - T. F. Stocker et al. 2013), at $0.035\,W\,m^{-2}$ (T. C. Bond, Doherty, et al. 2013) and at $0.035\,W\,m^{-2}$ (M. G. Flanner, Zender, et al. 2007). The absolute value appears to be quite low on a global scale, but on more local scales it can be one order of magnitude higher: $0.6\,W\,m^{-2}$ in the Arctic and $3\,W\,m^{-2}$ in the Himalayas (M. G. Flanner, Zender, et al. 2007).

Shortwave solar radiation is the main source of energy for glaciers or ice-sheets and therefore, even moderate changes in the albedo have significant influence on the glaciers' mass balance (Oerlemans et al. 2009). Moreover, an increase in the melting rate can be the result of repeated years with negative mass balance leading to the re-exposure of dust and BC particles, whose surface concentrations can increase by more than one order of magnitude (Sterle et al. 2013).

Many studies tackled the BC and impurities radiative effects on glaciers in a global perspective. The increased melting rate of the Himalayan glaciers was suggested to be caused by enhanced impurities deposition (B. Xu et al. 2009). It was found that BC and mineral dust depositions in the Colorado River Basin, in the western US region, influenced the river run-off timing by the enhanced warming rate (Painter, Deems, et al. 2010) and that the duration of snow cover was reduced by several weeks (Skiles et al. 2012).

In the European Alps, the impact of industrial BC was hinted to be the cause of the end of the Little Ice Age (LIA), by forcing the glaciers retreat at the end of the 19^{th} century despite still favourable meteorological conditions (Painter, M. G. Flanner, et al. 2013). However, recent findings showed that when BC deposition on the Colle Gnifetti glacier became significant, the Alpine glaciers already experienced about 70% of the 19^{th} century glaciers retreat (Sigl et al. 2016).

On the Mera Peak, Nepalese Himalaya, approximately 26% of total annual melting was found to be caused by BC and mineral dust deposition (Ginot, Dumont, et al. 2014); moreover, mineral dust components were found to dominate in the 40% snow albedo reduction (S. Kaspari et al. 2014).

Despite considerable uncertainties still remaining in evaluating the actual impacts of BC and mineral dust on snow, their importance was highlighted by many independent studies.

1.3.6 Aerosols and Human Health

Many epidemiological studies highlighted the particulate air pollution impacts on human health (Davidson et al. 2005; Brook 2008; Shah et al. 2013;Kim et al. 2015; Butt et al. 2016). In Shah et al. 2013 it was estimated that globally, each year, more than two millions deaths occurred because of lung and respiratory system diseases being directly linked to atmospheric pollution, 2.1 millions of those are attributable to PMs (Chuang et al. 2010). Particularly, exposure to particulate matter, was linked to adverse respiratory health effects, such as *asthma* attacks or *chronic bronchiti*, and cardiovascular morbidity and mortality.

Epidemiological results suggest that the smaller the particulates dimensions, the most dangerous their impact becomes on human health (Kim et al. 2015). The largest particles are generally stopped in the first parts of the respiratory apparatus, whereas the fine and ultra-fine components of the particulate matter (PM), such as the $PM_{2.5}$, penetrate in the *bronchioli* or even in the *alveoli*, from where are then released in the cardiovascular system (Kim et al. 2015). Moreover, the chemical composition of particulates (e.g. polycyclic aromatic hydrocarbons (PAH) or heavy metals) also influenced their health impact (Pope III and Dockery 2006).

Attention was given to the BC impacts on human health and several pathologies were found to be connected with it, such as heart arrhythmias and cardiovascular morbidity and mortality (Rich et al. 2005; Maynard et al. 2007). Moreover, $PM_{2.5}$ rich in BC were found to be more toxic than other compounds because of the presence of PAHs (Maynard et al. 2007; McCreanor et al. 2007). In 2011, the *International Agency for Research on Cancer* evaluate BC to be a possible human carcinogen (Evaluation of Carcinogenic Risks to Humans 2010). The World Health Organization concluded that BC particles, due to their small sizes, can act as carriers for many different toxic chemical compounds (e.g. PAHs; Janssen et al. 2011).

1.4 Climate Reconstructions of the European and Alpine regions

In the last few decades, the European continent has been object of many climatological studies. In particular, the high number of people living in this region and its central role in the global framework motivated, as a consequence, an intense research about its past-climatic variability and meteorological patterns.

In order to assess the importance of recent global and regional climate changes and variability, knowledge of previous climate conditions and of their underlying physical mechanisms is required, especially for the late Holocene period (P. D. Jones and Mann 2004). Moreover, an effort must be made in order to be able to create accurate future climate projections. The European Alps, like most of the European region, are exposed to many natural and anthropogenic hazards such as droughts and floods (Gobiet et al. 2014). Therefore, deep knowledge of the local climate behavior is required in order to control and prevented these future hazards.

1.4.1 The Northern Hemisphere Temperature Reconstruction

Many reconstructions of climatic parameters, such as temperature, precipitation and sea level pressure, have been produced at the hemispheric spatial scale and for

different time scales using suitable kinds of proxies (ice cores, tree rings, speleothems, etc.). The climatic conditions greatly influenced the pre-industrial societies. Particularly, the agricultural productivity and the health risks were amongst the principal factors in determining the societal evolutions and conflicts (Buntgen et al. 2011).

In Moberg et al. 2005 the Northern Hemisphere temperature reconstruction was obtained for the last 2000 years using various kinds of proxies and focusing on the natural climate variability during this period. The reconstruction was obtained by combining data from low-resolution proxies (such as lake sediments), which are usually good at describing the multi-centennial variability, with three rings data characterized by annual to decadal resolutions.

The first striking result of the reconstruction is that the temperature of the last three decades is the highest of the last 2000 years (Buntgen et al. 2011; Mann and P. D. Jones 2003; P. Jones, Briffa, et al. 1998). Two main climatic fluctuations can be detected in the reconstructions: a warmer period around 1000-1100 AD, called the *Medieval Warm Period*, characterized by temperatures similar to those of the period 1961-90, and a cold fluctuation around the 17th century, called the *Little Ice Age*, with a mean temperature anomaly of about 0.8 °C (Moberg et al. 2005). However, many other studies focused more on regional scale climatic reconstructions in order to achieve more accurate regional climatic situations. In fact, high-resolution regional climate reconstructions allow for the detection of important climatic features, for example, extremely hot summers or cold winters. The latters are generally overwhelmed by higher amplitude signals in large-scale reconstructions (Mann and P. D. Jones 2003).

1.4.2 The European Region Temperature Reconstruction

A European three-rings based high resolution climate reconstruction for the last 2500 years was performed by Buntgen et al. 2011. The climate oscillations were also connected with societal changes, as the growing and falling of the Roman Empire. The strong climate anomalies detected for the Northern Hemisphere as observed for the European region as well. Moreover, three cold periods characterized the European climate about 2300, 2000 and 400 years BP. These fluctuations were associated with the *celtic* expansion, the *Roman* conquest and the *migration period* in the European region, respectively (Buntgen et al. 2011).

The warming of the last three decades is unprecedented, as confirmed by the Buntgen et al. 2011 paleo-temperature reconstruction. During the Roman and the medieval periods the European climate was characterized by warm and wet summers, increasing the agricultural productivity. The reconstructed temperature were on average similar to the average of the period 1901-2000 AD, during the *Late Iron Age* (400-150 BC), the period 50-300 AD during the *Roman Empire* and from 700-1600 AD (except for the period 1280-1380 AD, associated to the *Black Death*). Occasionally, the summer temperature were 1 °C or more higher than the 1901-2001 average, particularly during the Roman Period. From 300 to 600 AD the reconstructed temperature was more than 1 °C below the average, and this climate variation contributed to the falling of the western Roman Empire.

Luterbacher et al. 2004 provided a reliable reconstruction of the last 500 yrs temperature variability and trends in the European region (25°W – 40°E, 35°N – 70°N). The data adopted are mainly homogenized and quality-checked instrument data

series and partly high temporal resolved proxy reconstructions (i.e. Greenland ice cores and Scandinavian and Siberian tree rings). Lower temperatures than those of the 20th century generally characterized European winters during the last 5 centuries. The coldest winters in the time series happened during the late 16th century and in the last decades of 17th and 19th centuries, whereas a strong warming period is shown during 1684-1738 and characterized by a warming trend of about 0.3 °C. This warming might be explained by the increased solar irradiance detected at the end of the 17th century that likely induced a shift towards a positive phase North Atlantic Oscillation (NAO) (Luterbacher et al. 2004). However, the solar irradiance recorded remained at high values until 1900 while, instead, the winter temperature and NAO index presented low values; the underlying mechanisms are still unknown. The anthropogenic role in increasing winter temperatures is detectable from about 1950 (Zwiers and X. Zhang 2003).

The reconstructed summer temperatures shows high values from 1750 to the second half of the 19th century (below the average value of the 19th century). This reconstruction shows that the summer of 2003 was the warmest in the last 500 years (until 2003).

1.4.3 The Alpine Region Temperature Reconstruction

A multi-proxy reconstruction for temperature and precipitations for the European Alpine region (4°E – 16°E, 43°N – 48°N) is reported in Casty et al. 2005 (Fig. 1.8).

It is clearly visible that low frequency fluctuations over the Alpine region are bigger in amplitude than those of the overall European region (Luterbacher et al. 2004). As for temperature, the strongest inter-annual variability is in the 15th century. A significant reduction during the second half of the 20th century is shown. Moreover, the winter fluctuations are generally larger than those in summer. The cooling that occurred due to the Tambora eruption in 1815 (Raible et al. 2016) is evident in the summer mean temperature anomaly.

Filtered data show that temperatures during the last 500 years were consistently lower then those of the 20th century, in according with European temperatures for this period (Luterbacher et al. 2004). Particularly the coldest periods in the annual mean Alpine temperature were the 1590s, 1690s, 1730s and 1890s (Fig. 1.8).

However, warm periods are observed in the periods 1780-1810, 1890-1945, and after the 1970s. The accumulation of positive temperature extremes during the last 10 years is also remarkable. In the Alpine area, 1994, 2000, 2002 and 2003 were the warmest within the last 500 years (until 2003). The warmest year in the reconstruction is 1540 (+1.4 °C with respect to the mean) while the coldest is 1740 (−2.5 °C) (Casty et al. 2005).

The coldest winter period was that at the end of the 17th century, consistent with what was observed for European temperatures (Luterbacher et al. 2004). A strong transition toward warmer winters from 1890 to 1915 is clearly visible, followed by a decrease until about 1960. 1829/1830 was the coldest Alpine winter on record with temperature anomalies in the order of −5 °C (winter mean temperature during the 20th is 0 °C) while the warmest was the winter of 1606/1607 one (+3.5 °C).

As for summer temperatures, their variability is lower than in winter. 2003 was the warmest summer (+4.4 °C) and in the 19th century the average was 16.1 °C.

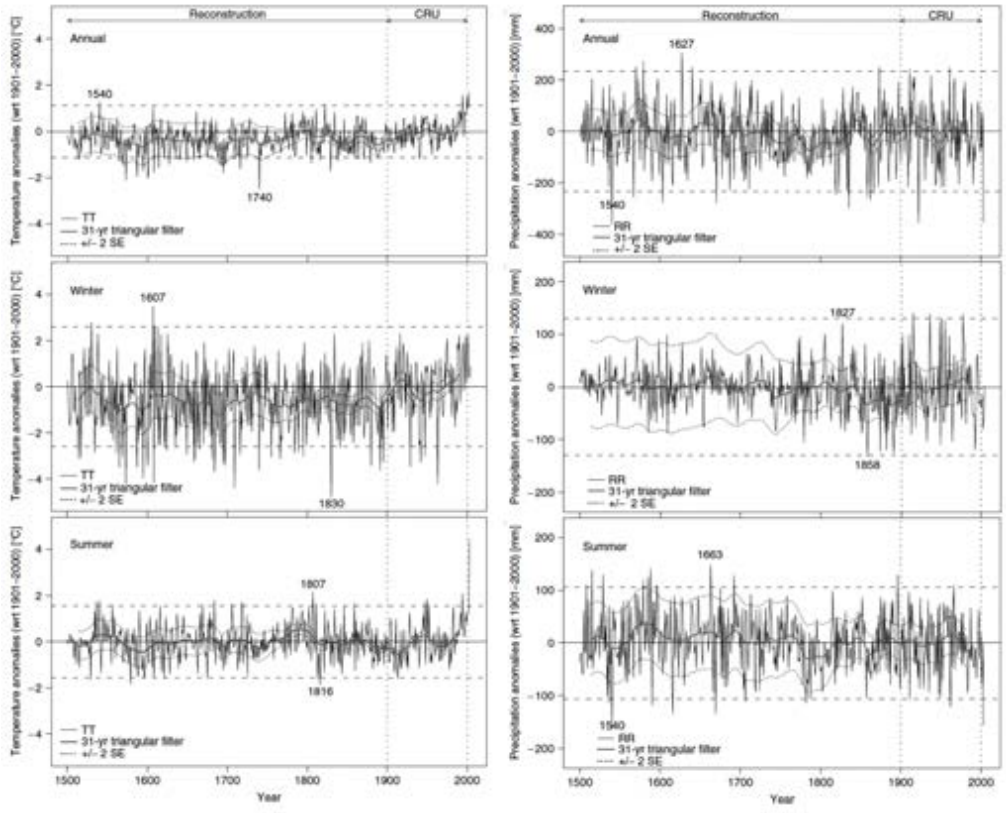

Figure 1.8: Annual mean Alpine temperature (left) and precipitation anomalies (right) from 1500 to 2003 computed with respect to the period (1901-2000). Values from 1500 to 1900 are reconstructions; values for T after 1900 are derived from the Mitchell et al. 2004 data-set. Black thick line: 31 triangular low pass filtered time series. Dotted line: +-2 standard error. Chart adapted from Casty et al. 2005.

The warmest Alpine summer was that of 1807 (+2.2 °C), while the coldest Alpine summer occurred in 1816 (–1.9 °C).

1.4.4 The Alpine Region Precipitation Reconstruction

Alpine reconstructed annual, winter and summer precipitations are shown in the right part of Fig. 1.8. The time series are characterized by a strong inter-annual variability, which increases for the winter mean precipitations during the end of the 19th century. The filtered reconstructed precipitations show a downward trend for both seasons, with superimposed decadal and inter-decadal fluctuations.

The correlation between reconstructed Alpine temperatures/precipitations and the North Atlantic Oscillation (NAO) index shows rarely significant values in the extended winter between 1659-2000 (Casty et al. 2005). The running correlation is not stable and rarely exceeds the 0.5 value. When a significant correlation exists, it is generally positive with temperature and negative with precipitations. The influence of the NAO is probably weak in the Alpine region where other large/small scale circulation patterns may have a dominant role (Casty et al. 2005). However, the downward trend of summer precipitations can be partially explained by the recent tendency towards larger value for the Azore high (Dunkeloh and Jacobeit

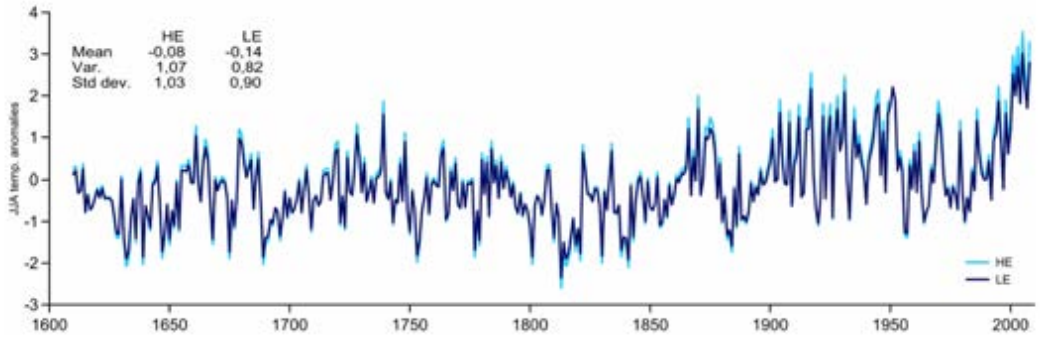

Figure 1.9: The summer (June-July-Agugust) three ring based temperature reconstruction (expressed as a temperature *anomaly* compared to the 1961-1990 period) in the Adamello-Presanella group for the period 1610-2008. The high/low elevation differences were scaled by using the HISTALP gridded dataset. Taken from Coppola et al. 2013.

2003).

1.4.5 Temperature Reconstruction in Central-Eastern Alps

Long temperature reconstruction time series for the Alpine Region are rare, particularly for the highly glaciated mountain areas and valleys. Coppola et al. 2013 described a dendrochronological annually resolved summer temperature reconstructions for the last four centuries (1610-2008 AD) in the Adamello-Presanella Group (Central-Eastern European Alps). The time series is showed in Fig. 1.9 and the recent years temperature increase, with the highest values in the last four centuries, is the first striking result. Relatively cold temperature were recorder from the beginning of the dataset, 1610 AD, to the end of the 19th century, with an average anomaly of about −0.5 °C. However, decadal to multi-decadal climatic fluctuation characterize the whole dataset and particularly, positive temperature anomalies are recorded in the second half of the 17th century, around the 1725 AD and the 1870 AD. Interestingly, the coldest period was in the 1812 and in the following 5-6 years, in correspondence of the *Tambora* eruption in the 1815 AD (Crowley 2000). The 1813–1821 AD period is indeed considered to be the coldest decade of the entire Little Ice Age, corresponding to the Dalton minimum in the solar activity (S. Wagner and Zorita 2005) and following an intense volcanic eruptions period, peaking in *the year without a summer* in 1816 AD (as a results of the Tambora eruption). The temperature started to increase at the beginning of the 20th century until the 1960s, with positive temperature anomalies (about 0.5 °C in the low pass filter 20-years smoothed curve).

1.4.6 Temperature Reconstruction on Alto dell'Ortles glacier

The first attempt in reconstructing an historical time series of the Alto dell'Ortles surface air temperature is described in Gabrielli, Carturan, et al. 2010. By using the humidity lapse rate the reconstruction was done using air-temperature data from Santis (about 120 km North-West; 2502 m), covering the 1864-2009 time period and the record from the *Careser-diga* station (about 15 km southwest; 2605 m),

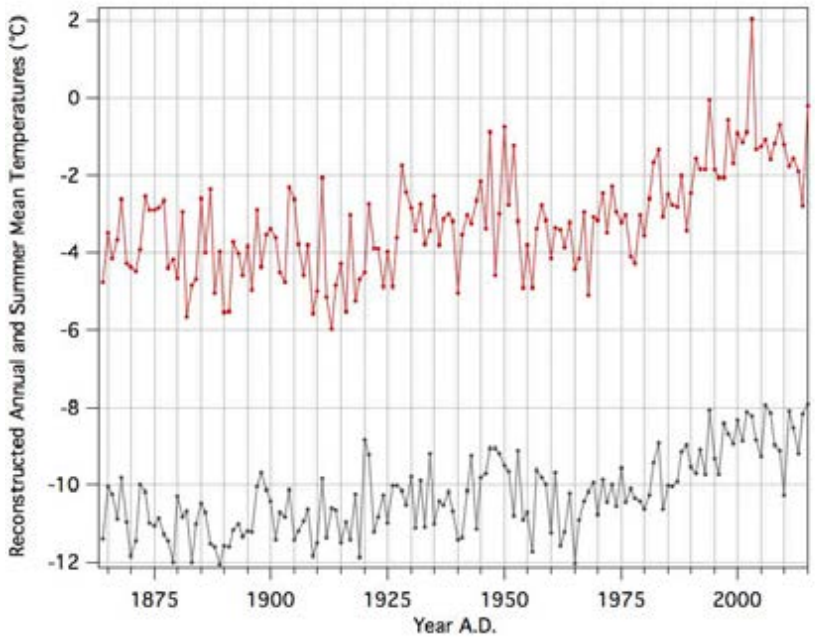

Figure 1.10: Annual (black line) and summer (red line) temperature reconstructions for the Alto dell'Ortles glacier (1864-2009) (adapted from Gabrielli, Carturan, et al. 2010).

from 1960 to 2009. An overall surface air temperature reconstruction on the Alto dell'Ortles glacier (at 3850 m) was obtained for the period 1864-2009 (Fig. 1.10).

The reconstructed summer temperature was stable on average during the period 1864-1924 with an average of about −4 °C, whereas an average increase of 1 °C was observed between 1925-1980. A significant increase in temperature of about +2 °C was observed from the 1980s for the summer mean (June-July-August) temperature. In the annual mean temperature reconstruction the increase was less pronounced, about 1 °C. Also the inter-annual variability was higher in the summer mean temperature compered to the annual mean values.

In the temperature time series some exceptional warm summer event can be spotted such as during the first years of the 1950s, the 1983-84 and 1993 summers and the summer of 2003. Particularly, during the 2003 heat wave the Alto dell'Ortles surface air temperature was about +2 °C on average; during this event the surface melting was likely unprecedented, at least during the reconstructed temperature period.

For the period 2005-2013 Carturan and De Blasi (personal communication) computed another temperature reconstruction by using the humidity lapse rate between the *Careser Diga* station and the *Ortles AWS*.

The first continuous in-situ atmospheric and radiative measurement started in 2010 when the first automatic weather station (AWS) was placed on the Alto dell'Ortles glacier. At the end of the 2011 ablation season a higher performance AWS was installed at 3830 m, at 2 m from the surface of the glacier. The new AWS' sensors measured temperature, pressure, precipitation, the AWS elevation, wind direction and intensity, the incoming and the snow-reflected solar radiation, the outgoing infrared radiation and the height of snow (by measuring the distance between the sensor and the snow surface).

Table 1.1: The Ortles temperature reconstructions datasets.

	Period	Source	Correction
Ortles reconstructed I	1864-2009	Santis (1864-1958) Careser diga (1959-2009)	Lapse rate between Careser and Cima Beltovo (−7.2 celsius/1000 m) Linear regression between Santis and Careser (T C. = $1.1082 * S. + 0.9098$)
Ortles reconstructed II	2005-2013	Careser diga	Lapse rate between Careser and Ortles AWS (−7.1 °C/1000 m)
Ortles AWS	2011-2015	Ortles AWS	None

In Table 1.1 a list of the temperature time series for the Alto dell'Ortles glacier, the corresponding covered period and the applied corrections are reported (adapted from Dreossi 2016).

1.5 The influence of NAO and AMO

1.5.1 The NAO

The NAO is a large-scale atmospheric pattern related to the North Atlantic area (Hurrell 1995). Its positive phase is associated with an anomalous high pressure near the Azores area and to a low pressure in Iceland, and vice versa for the negative phase. This pressure pattern affects the intensity and the main position of the westerlies flowing from the North Atlantic to the European region.

Usually during summer the Azores high is located in the Mediterranean basin, thus pushing the storm track pattern northward and resulting in dry and warm conditions in the southern part of Europe. During winter, instead, the high moves toward the Atlantic Ocean, and thus allowing low pressure systems to enter the Mediterranean area. An NAO index (called NAOI) can be defined by using the normalized sea level pressure difference between Iceland and Gibraltar (P. Jones, Jonsson, et al. 1997). With regard to the Alpine region, many studies have been performed in order to assess the relation between climatic parameters and the NAO. However, contrasting results have been found. Particularly, Quadrelli et al. 2001 found a significant correlation between winter precipitations and the NAO for the period 1971-1992: the NAO explains most of the precipitation variance (via the North-South displacement of the Atlantic storm track pattern). The NAO positive phase seems to cause the occurrence of drier periods over the whole Alpine region (Quadrelli et al. 2001). Schmidli et al. 2002 determined only a weak and generally unstable correlation for the period: 1901-1990, while more robust (but weak) correlation coefficients were found in the southern area.

In Brunetti et al. 2006 he correlation from 1800 to 2003 between the NAOI index and the N-S dipole index (based on precipitation differences) calculated for the greater Alpine region was found to have variations during different time intervals; however it is always positive and shows values higher then 0.5 only from 1985 (the correlation time series ends in 1990).

Schöner et al. 2009 analyzed the meteorological data and the snow depth from

the network of the Sonnblick region (Hohe Tauern, Austrian Alps) from 1928 AD. A significant positive correlation was found between the winter temperature and the NAOI winter air-temperature; however, for winter precipitation Schöner et al. 2009 didn't found any particular correlation.

In López-Moreno et al. 2011 a statistical significant positive correlation was found between the winter NAO index and the maximum, minimum and mean temperatures, whereas a negative correlation with the precipitations for the Alpine region and in the period (1950-2005). However, the correlation map was not uniform, thus resulting in areas with a non-significant correlation or even positive (especially in the Eastern part).

Bartolini et al. 2009 carried out an interesting study by investigating the gridded monthly precipitation time series CRU TS 1.2 (Mitchell et al. 2004) for the long period 1900-2000 obtaining that the Alps are characterized by the highest coefficient of variation in precipitations among the European region. Moreover, they established that no significant correlation exists between winter precipitations and the NAO in this region.

1.5.2 The AMO index

Another important source of variability for the European climate is the Atlantic Multi-decadal Oscillation (AMO). This oscillation is related to variations in the Northern Atlantic sea surface temperatures. An associated index (AMOI) allows describing its phase. It is defined as the de-trended anomalies in the sea surface temperature. Sea surface temperature (SST) variations are generally associated with changes in the thermohaline circulation (THC) (Delworth and Mann 2000; Knight et al. 2005). (R. Zhang et al. 2007 found that a part of the Northern Hemisphere multi-decadal variability in mean temperature can be explained by the North Atlantic SST variability. Recently, (Sutton and Dong 2012) identified the AMO as one of the major sources for the European climate variability especially during spring, summer and fall; the European climate shift during the 1990s that resulted in an increase in frequency of hot and dry summers in the southern part of Europe was explained by the increase in the North Atlantic SST.

The Alpine region is also influenced by the AMO and here the influence on the cryosphere is considered. Zampieri et al. 2013 analysed the behaviour of the spring snow in the Alps, which is not only interesting from a scientific point of view but it is also of crucial importance for the length of the snowy season and therefore for the tourism sector Elsasser and Messerli 2001. They used some observational regional datasets (e.g. HISTALP) and a snowfall reconstruction dataset: a monthly temperature and precipitation dataset for the *Greater Alpine region* (2°E – 20°E, 46°N – 49°N). Consequently, they found a statistically significant shift for most regions in spring snowfall duration from about 1995, when less snowy springs were observed. Using longer time series, since 1860, two fluctuations in the spring AMO index are visible (two periods of cold/negative index and three with warm/positive one) and a significant correlation is observed. Particularly they found a negative correlation between spring snowfall and the AMO: moderate/intense precipitations are observed during positive/negative AMO phases. Moreover a more robust correlation is found in the western part of the Alps where a variation in snowy precipitation during the AMO phase transitions is in the order of 20 % to 30 % (Zampieri et al.

2013).

In Huss et al. 2010 the 11-year mean mass balances anomalies for 30 Swiss Alps glaciers are compared to the AMO index derived by Enfield et al. 2001. A clear negative correlation between the mass balance and the AMO index is visible, suggesting atmospheric variations in this area during different AMO phases. The correlation is of the order of -0.7 with a significance of 95 %. Moreover the instrumental air temperature time series for the Alps (Auer et al. 2007) shows a clear correlation with the AMO index, suggesting that the physical process in explaining glaciers melting is connected to temperature variations.

Chapter 2

The Ortles Ice Core

2.1 The Alpine Ice Cores

The ice cores, drilled from the European Alpine glaciers are a unique source of information about the past climatic conditions and atmospheric composition, in terms of trace gasses and aerosols. A great advantage of these ice cores is the significant availability of precise instrumental record, in many cases going back to the beginning of the 20^{th} century, or earlier (Schotterer, Fröhlich, et al. 1997). Moreover, the emission sources of anthropogenic and natural pollutants are usually well known (Döscher et al. 1995, Maupetit et al. 1995). A detailed analysis of transport processes and deposition rates can be obtained; the direct comparison between the emission records and the concentration in the ice allow the reconstruction of the formers in the past, when instrumental dataset were absent.

Atmospheric seasonal variations are preserved in the ice cores and they can be visualized by the oscillations in the water isotopic content, mineral dust, black carbon, major ions concentrations and so on. These variations for the water isotopes are due to temperature and precipitation seasonality, whereas the aerosol variability depends on the atmospheric structure and transport processes or fluctuations in the intensity of emissions.

The annual accumulation rates on high altitude glaciers are usually between half a meter and several meters. However, the time resolution of climatic and environmental record preserved in the ice is usually larger then the sub-annual or monthly resolution when calibrated with instrumental data (Schwikowski M., 2006; `http://www.pages-igbp.org`).

A few glaciers in the Alpine region are suitable for drilling ice cores mainly because of two reasons: the complex bedrock topography leading to internal ice flows and foldings (Schwikowski, Brütsch, et al. 1999) and the atmospheric temperatures that has to be low enough, about $-10\,^{\circ}\mathrm{C}$ in the annual mean, as not to have strong surface melting and percolation affecting the climatic information; this is generally satisfied for glaciers above 4000 m (Orombelli and Barbante 2004).

In Table 2.1 the list of all the ice cores drilled in the European Alps is reported. Only a few ice cores have been drilled in the Eastern Alps due to the mean altitude of the glaciers, which is lower compared to the Western Alps, and therefore the melting, percolation and refreezing cycles are more frequent. Only the last three in Table 2.1 were drilled from the Eastern glaciers.

The dating of the Alpine ice cores can be difficult because of the strong thin-

Table 2.1: List of all the ice cores drilled from Alpine glaciers and the corresponding references.

Location		# of ice cores	date	References
Bernese Alps	Ewigschneefeld	1	2010	Paul Scherrer Institute (Switzerland)
	Fiescherhorn	2	1989, 2002	Schotterer, Fröhlich, et al. 1997, Schotterer, Stichler, et al. 2001, Schwikowski, Brütsch, et al. 1999 and Jenk 2006
	Jungfraujoch	3	1972, 1974	
	Plain Morte	3	1972	Rufli et al. 1976
Mt. Rosa Massif	Colle Gnifetti	several	from 1976 to 2005	Oeschger et al. 1977, Schotterer and Good 1978,Schotterer, Oeschger, et al. 1985,Lüthi and Funk 2001, Jenk 2006
	Colle del Lys	several	from 1996 to 2012	Maggi et al. 2000, DISAT-UNIMIB
	Grenzglescher	1	1994	Eichler, Schwikowski, Gäggeler, et al. 2000
Mt. Blanc Massif	Col de Brenva		1986	Ronseaux and Delmas 1988
	Col du Dome	several	from 1973 to 2016	Jouzel, Legrand, et al. 1984, Angelisi and Gaudichet 1991, Vincent et al. 2007, Preunkert et al. 2000, *Ice memory* project
	Dome du Guter	1	1998	Van de Velde, C. Boutron, et al. 1998
	Mt Bianco summit	1	1973	Jouzel, Merlivat, et al. 1977
Bernina Massif	Piz Zupo	2	2002	Palmer et al. 2003
Otzal Alps	Vernagtferner	5	1979, 1983	Oerter and Rauert 1982, Oerter, Baker, et al. 1985
Silvretta		1	2011	Paul Scherrer Institute (Switzerland)
Mt. Ortles	Alto dell'Ortles	4	2011	Gabrielli, Carturan, et al. 2010, Gabrielli, Barbante, Carturan, et al. 2012, Gabrielli, Barbante, Bertagna, et al. 2016

ning of the ice layer at depth. The overall weight of the ice causes a deformation of the basal ice that in turn causes horizontal stretching and corresponding thinning. The time ranges covered by the Alpine ice cores are usually in the order of centuries (Preunkert et al. 2000). New dating techniques based on filtering the ice and extracting the carbonaceous component of deposited aerosol for ^{14}C analyses revealed the presence of much older ice in the Colle Gnifetti and Alto dell'Ortles glaciers, more than 10 kyrs and 7 kyrs respectively (Jenk et al. 2009 and Uglietti, Zapf, et al. 2016).

2.2 The Alto dell'Ortles Glacier

The Alto dell'Ortles glacier is the highest glacier of the Ortles-Cevedale group (Trentino-Alto Adige region, Italy) and covers the northwestern part of Mt. Ortles, the highest summit (3905 m) (Fig.2.1). This mountain group is characterized by the presence of 3.5% of the whole Alpine glaciated areas, about 76.8 km^2, and it is the largest glacierised mountain group of the Italian Alps (Carturan, Filippi, et al. 2013). Since the end of the Little Ice Age (LIA) the glaciers of the Ortles-Cevedale group underwent a significant area reduction. Particularly, during the period 1987-2009 the overall glaciers surface decreased by about 23 %; however, under the current climatic conditions, a retreat of 50 % of the total surface is needed to reach the equilibrium (Carturan, Filippi, et al. 2013). Many glaciers of the Ortles-Cevedale group will completely disappear within a few decades as is the case with the Careser glacier (World Glacier Inventory code I4L00102519; WGMS, 1989), which has an average altitude of about 3000 m (Carturan, Baroni, et al. 2013).

The Alto dell'Ortles glacier starts close to the summit (3905 m) and flows for about 300 meters with a slope of about 9° (about 10 % of the whole surface). A small col is present in between the summit and the Vorgipfel (3845 m). Below the col the bedrock and the glacier surface get steeper and two tongues flow down to about 3018 m (Fig.2.1).

The glaciers surface in 2011 was about 1.12 km^2, whereas in 2013 about 1.07 km^2 (Gabrielli, Barbante, Bertagna, et al. 2016). Despite the last decade's surface decrease, the Ortles glacier is still characterized by a positive mass balance in the upper part. The average snow accumulation was of about 1200 mm w.e.yr^{-1} over the period 2003-2009 and the ablation of about 400 mm w.e.yr^{-1}. The recent (2011-2013) annual mean accumulation at the drilling site is of about 800 mm w.e.yr^{-1} (Gabrielli, Barbante, Bertagna, et al. 2016), whereas at the Automatic Weather Station (AWS) it was estimated to be about 1070 mm w.e.yr^{-1} (for the period 2004-2009, Festi et al. 2015).

The geological profile of the Mt. Ortles area was described in Desio et al. 1967: the massif is made by sedimentary rocks such as stratified dolomites with interblended laminated and slab-shaped black limestone.

The Alto dell'Ortles area is placed at the boundary between the central and southern European climate regions; the seasonality and the amount of precipitation in this geographical area are quite different from those in the Western Alps (B. A. Davis et al. 2003). Two different precipitation regimes are described by Brunetti et al. 2006 in the Northwestern Italian Alps and in the Northeastern ones. Particularly, the Ortles region is in the so-called *inner dry Alpine zone* (Frei

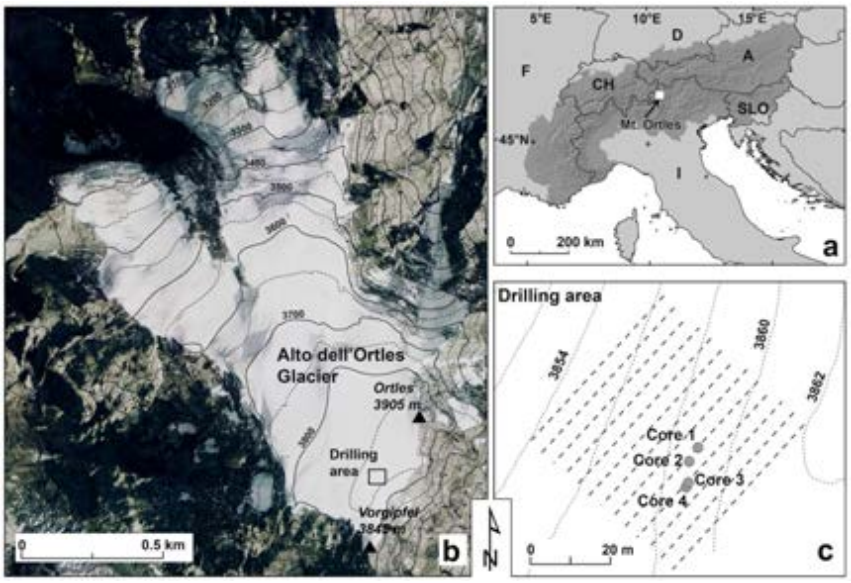

Figure 2.1: (a) Geographical local of Mt. Ortles, b) map ot the Alto dell'Ortles glacier and c) the drilling sites precise position (taken from Gabrielli, Barbante, Bertagna, et al. 2016).

and Schär 1998) receiving a mean annual precipitation amount of 750 mm yr^{-1}-850 mm yr^{-1} (on the other side of the Alps the Mt. Blanc area is characterized by an annual precipitation of 1100 mm yr^{-1}-1300 mm yr^{-1}). The highest precipitation amount is released on the southern and northern slopes of the Alps explaining the Alpine inner precipitation shadow. Moreover, no significant trend in precipitations is observed in this area (Schmidli et al. 2002).

The first extensive survey on the Alto dell'Ortles glaciers was completed in 2009, within the framework of the *Ortles project* (www.ortles.org). A 10 m shallow core was dug and processed at the Department of Environmental Science, Informatics and Statistics of the University of Venice. The presence of ice lenses in the shallow core immediately revealed the presence of melting and refreezing cycles in the summer season. The bedrock was found to be at a depth of about 75 m and the firn ice transition was below 24 m of depth (Gabrielli, Carturan, et al. 2010).

Since 2009 a snow pit was dug every year on the Ortles glacier at the AWS position and the samples for isotopic measurement were taken. After 2011 a snow pit was also dug every year at the drilling site in order to evaluate differences in the snow accumulation between the two locations. The drilling site is characterized on average by a 20% less of accumulation. Two surveys were performed in both 2012 and 2013, one at the beginning of the ablation period (June) and one at the end (late August). The author took part in four surveys (August 2013, June 2014, August 2015 and August 2016) and was personally involved in the snow pit analyses and sampling.

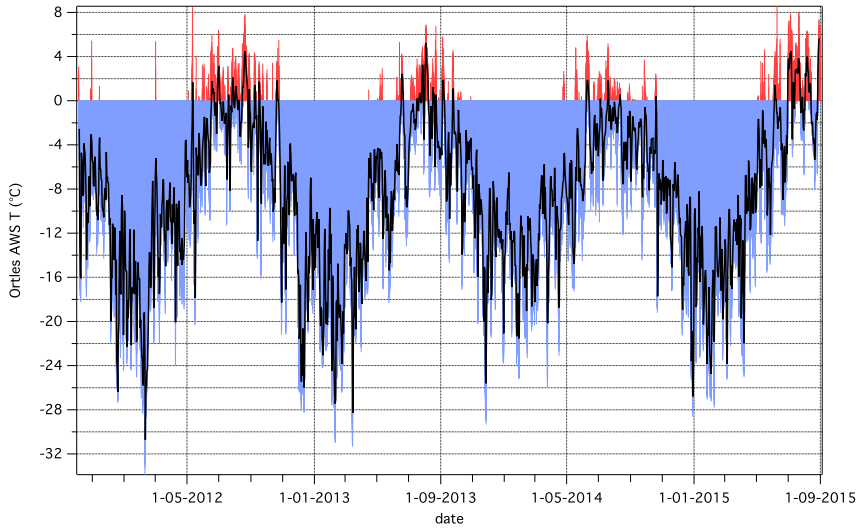

Figure 2.2: Surface air temperature time series measured with AWS at the Alto dell'Ortles glacier. Periods with temperatures lower/higher than zero are coloured in blu/red.

2.3 The 2011-2015 AWS Data

2.3.1 The Measured Surface Air Temperature

The Alto dell'Ortles surface air temperature was measured with hourly resolution by using a ventilated *Vaisala* sensor placed on the AWS (Carturan and De Blasi, personal communication). The period of observation is from October 2011 to August 2015. The whole dataset is reported in Fig.2.2.

The hourly-resolved dataset is showed by using red and blue colours in order to highlight the above zero and below zero temperatures, respectively. The thick black line represents the daily averaged temperature. This is the first time that the whole record is showed.

The highest hourly recorded temperature was 8.56 °C and it was recorded on the 9th of June 2015 at 12 AM; this value is higher than that previously reported in Dreossi 2016. The lowest value was recorder at 2 AM on the 10th of February 2012, −33.88 °C.

Until the end of the summer 2014 an average temperature above zero was observed only for one month in the entire record. The only month with an average temperature above zero was August 2012 with 0.23 °C (Dreossi 2016). In the complete dataset two more months have an average temperature above zero and both were in the summer of 2015. August 2015 was characterized by an average temperature of +0.19 °C and July 2015 by an average of +1.5 °C. The summer of 2015 was one of the warmest in the entire record, dating back to 1864. More details are given in Chapter 6, where the results of the analyses on the samples of the Ortles Snow Pit of 2015 will be described.

2.3.2 Wind Direction and Intensity

The wind direction and intensity hourly datasets, covering the period from 7-10-2011 to 29-6-2015, are shown in the chart of Fig.2.3

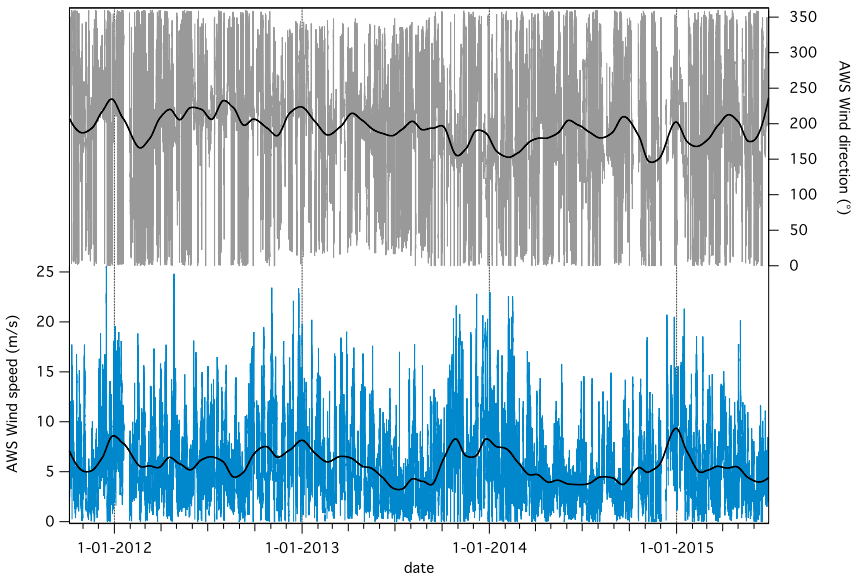

Figure 2.3: Alto dell'Ortles AWS data for wind direction and intensity.

The wind on Alto dell'Ortles glaciers is characterized by strong inter and intra-annual variability and, as observed by Dreossi 2016, it is responsible for the winter surface snow depletion. The wind speed ranges from some $\mathrm{m\,s^{-1}}$ to more than $20\,\mathrm{m\,s^{-1}}$ ($72\,\mathrm{km\,h^{-1}}$) and a significant seasonality is observed: the highest speed values are usually recorded during the winter periods (as reported in Fig.2.3, blue line). The strong winter winds blow with an average speed of about $8\,\mathrm{m\,s^{-1}}$–$9\,\mathrm{m\,s^{-1}}$, whereas usually lower values are measured in summer, $4\,\mathrm{m\,s^{-1}}$–$5\,\mathrm{m\,s^{-1}}$. The wind direction time series seems not to have any particular seasonality and a strong variability is observed (Fig.2.3). However, a more accurate analysis reveals that over all the dataset the relative frequency is higher for winds coming from South-West (Fig.2.4).

The wind direction relative frequency was calculated over 36 bins of 10° each. The times that the wind direction fell within in each bin was divided by the total number of measurements and multiplied by 100. A slight increase in the relative frequency is observed around 200° with a significant frequency peak for the 210°–220° bin. This results is quite in agreement with the results of the National Oceanic & Atmospheric Agency (NOAA) HYSPLIT model runs for the period 2007-2009 (Gabrieli, Carturan, et al. 2011).

Interesting information can be obtained by visualizing the wind-rose chart, where the wind frequencies are plotted as a function of the wind direction and the areas of the coloured rectangles represent the wind speed frequencies in that particular direction. The wind-rose chart for the Ortles AWS entire dataset shows the highest directional frequency in the South-West direction (Fig.2.5). The strongest winds (from $6\,\mathrm{ms^{-1}}$ to $25.61\,\mathrm{ms^{-1}}$) usually blow from South-West and the most frequent direction is from the South-West.

The wind direction in the mountainous areas can often be strongly influenced by orographic features, especially in the presence of high summits and closed valleys. The data interpretation in terms of sources and provenances of the air masses and pollutants from local measurements can thus be made with a high uncertainty level.

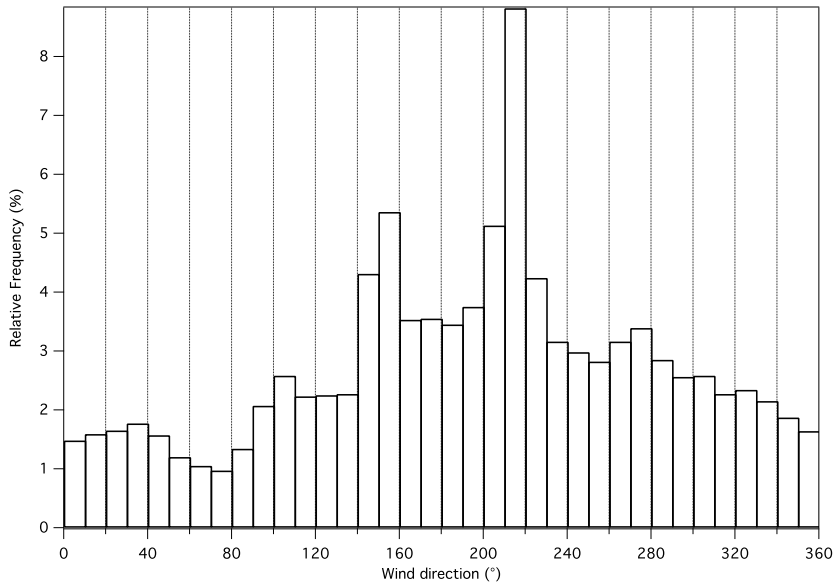

Figure 2.4: Relative frequency histogram for the Alto dell'Ortles wind direction.

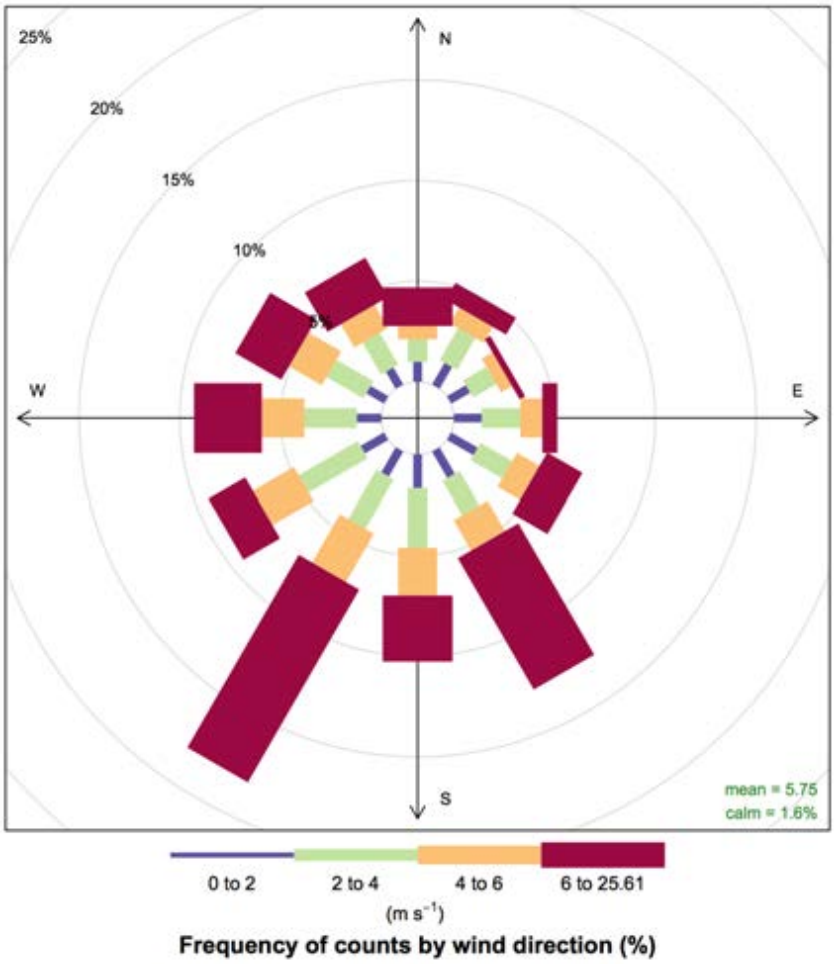

Figure 2.5: Wind-rose chart for the wind directions and speeds measured with the AWS.

2.3.3 Surface Snow Albedo and Radiative Data

A solar radiation measurement system was installed on the AWS during the period 7-10-2011 to 29-6-2015. Unfortunately, a malfunction in the instrument between 02-12-2011 and 19-06-2012 caused an interruption in data acquisition. Both the incoming solar radiation (short-wave radiation, ISW) and the outgoing (OSW) were measured with a frequency of 4 times per hour. This type of measurements on high altitude glaciers is necessary in order to know the radiative balance and to estimate the glacier mass balance (Mölg et al. 2009). The ISW and OSW time series can be used to compute the snow *albedo* (α). The albedo is a non-dimensional quantity, which describes the ability of a surface to reflect the incident radiation (in this work the albedo is only referred to the solar radiation). A value of 1 corresponds to a totally reflecting surface, whereas the value 0 describes a totally absorbing surface. Snow is one of the most reflecting natural surfaces on Earth (Hadley and Kirchstetter 2012). The amount of absorbed radiation (described by the the inverse of the albedo) describes how much a surface is heated by the ISR. Therefore, lower albedo values correspond to significant radiation absorption and heating of the surface, and vice versa.

The albedo can be simply computed from the OSW and ISW data with the equation: $\alpha = OSW/ISW$. The albedo values higher than 0.9, which was chosen as a reference value for the maximum albedo of fresh snow, were substituted with 0.9; this is due to the fact that probably the corresponding ISW value was an artifact because of the at least partial snow/ice deposition/formation over the ISW sensor. In the presence of albedo values higher than 0.9, this value was use for recalculating the ISW value through the inverse of the previous equation).

The albedo values of glacier snow can vary greatly over time; this is mainly due to two factors: snow aging/melting and dust/BC deposition on the surface (M. G. Flanner and Zender 2006; Hadley and Kirchstetter 2012).

The Ortles glacier surface albedo was computed by the author, for the first time, from the OSW and ISW time series for the whole AWS period (Fig.2.6).

The ISM and OSW time series clearly describes the annual solar radiation cycles and the cloud shadowing effect. The highest values are observed during the summer season (ISW of about 350 $\mathrm{W\,m^{-2}}$ and OSW of 220 $\mathrm{W\,m^{-2}}$) and the corresponding minimums in winter.

The albedo shows significant variability during the dataset at different time scales. A decreasing trend is observed during the summer periods and the snow aging, with dust deposition and concentration are the most likely causes. The lowest albedo value was recorded during the summer of 2013, starting from the end of April and culminating during June (on-going research). During the summer period the albedo ranges from 0.6 to 0.7, whereas during winter values greater than 0.8 are observed. The low albedo values during summer are due to aerosol deposition and snow aging; in summer the atmosphere is usually characterized by a strong instability and the boundary layer altitude reaches the highest altitudes during the year and therefore, the occurrence of air masses coming from the neighboring valleys causes an increase in dust deposition.

The highest average values are observed during spring, reflecting the fact that the most frequent snow depositions on Mt. Ortles are commonly observed during this periods.

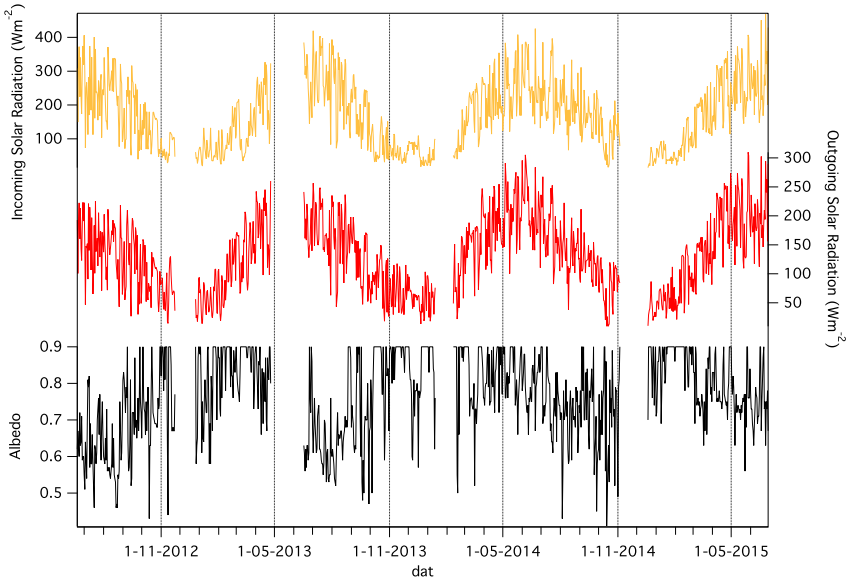

Figure 2.6: The incoming solar radiation, the outgoing solar radiation measured by the solar sensor on the AWS and the computed albedo.

2.4 The Ortles Ice Cores

During September and October 2011 four deep ice cores were drilled on the Alto dell'Ortles glacier by mean of a lightweight electromechanical drill (Zagorodnov et al. 2000). The final depth of the four cores were: 73.53 m (core #1), 74.88 m (core #2), 74.83 m (core #3) and 61 m (core #4; the drilling stopped because of a technical problem). The drilling of core #1 stopped at about 50 cm from the bedrock whereas core #2 and core #3 drilling reached the bedrock (the driller cutters were damaged in this process).

The ice cores show a good lamination but the presence of melting and refreezing cycles derived ice lenses were observed down to down to 60 m of depth. The largest fraction of Core #1 and the entire core #4 were stored at -20 °C at the University of Venice whereas the entire core #2 and the largest fraction of core #3 where brought to the Byrd Polar and Climate Research Center of Columbus (BPCRC, Ohio, USA).

During the drilling the presence of liquid water unequivocally demonstrated the presence of temperate firn and the occurrence of summer melting events. A thermistor chain was placed in the borehole #2 and the temperature measurement revealed the transitioning phase of the Alto dell'Ortles glacier from a cold to a temperate state. The upper part of temperate firn had a near or slightly above zero temperature down to about 30 m of depth. Below the firn-ice transition well preserved cold ice is still present and this was confirmed by low zero temperatures: −0.4 °C at 35 m, −1.8 °C at 55 m and −2.8 °C at 75 m closed to the bedrock (Gabrielli, Barbante, Carturan, et al. 2012). The cold ice preserved below 30 m is a unique remnant of the colder climate recorded before the 1980s.

2.4.1 The Ortles Core #1 Cutting and Samples Preparation

The Ortles core #1 was measured, cut at about 70 cm of length, and sealed in LDPE bags immediately after drilling. The core was then transported at the Ca' Foscari

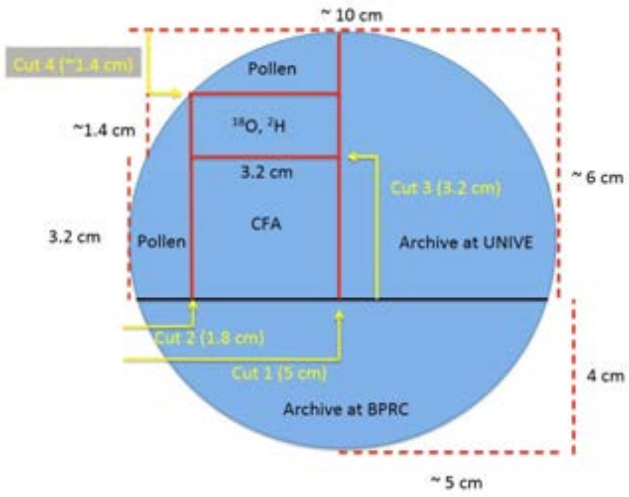

Figure 2.7: The Ortles core #1 cutting scheme.

University of Venice and stored in the CNR-IDPA cold room at the Department of Environmental Sciences, Informatics and Statistics. The bags were opened and the cores were processed at −20 °C. The length of each core was measured again and a log file was created. A visual inspection was carried out by placing each section on a neon lamp, thus allowing the operators to search for ice lenses, dust layers and to check the bubbles shape in the entire core. Just a few small particles were observed in the whole core except a 1 cm pebble at a depth of 72.5 m.

The ice core sections were cut in order to have the ice samples for the various analyses characterized by different ice volumes. The cutting scheme of the Ortles core #1 is shown in Fig.2.7.

The samples for the water stable isotopes analysis, for the CFA and for the pollens analysis were prepared and sealed in LDPE bags, as well as the remaining parts (stored at the University of Venice and at the Bird Polar and Climate Research Institute of Columbus, BPCRC, Ohio, USA).

The pollen samples were prepared from the external part of the core and sent to the Institute of Botany, University of Innsbruck, Innsbruck, Austria. The isotope sections were obtained from the inner part of the core where no fractionation could have happened during and after the drilling. The spatial resolution for the isotopes samples was from 9 cm in the first part of the core decreasing down to 2 cm. This sampling scheme was followed in order to be able to detect the seasonal oscillations. The innermost part of the cores was cut for the CFA (this study), resulting in a 32 mm × 32 mm section parallelepiped with the original section length. The central part of the core was chosen because it is the less contaminated for trace elements. The driller cutters generally contaminate the external surfaces of the core and therefore the surface ice samples are not suitable for trace elements analyses. Sections 35 to 55 were also cut in order to have samples to be analyzed for tritium. The tritium concentration peak in the ice is generally used as a time marker for the 1963 maximum in atmospheric nuclear tests.

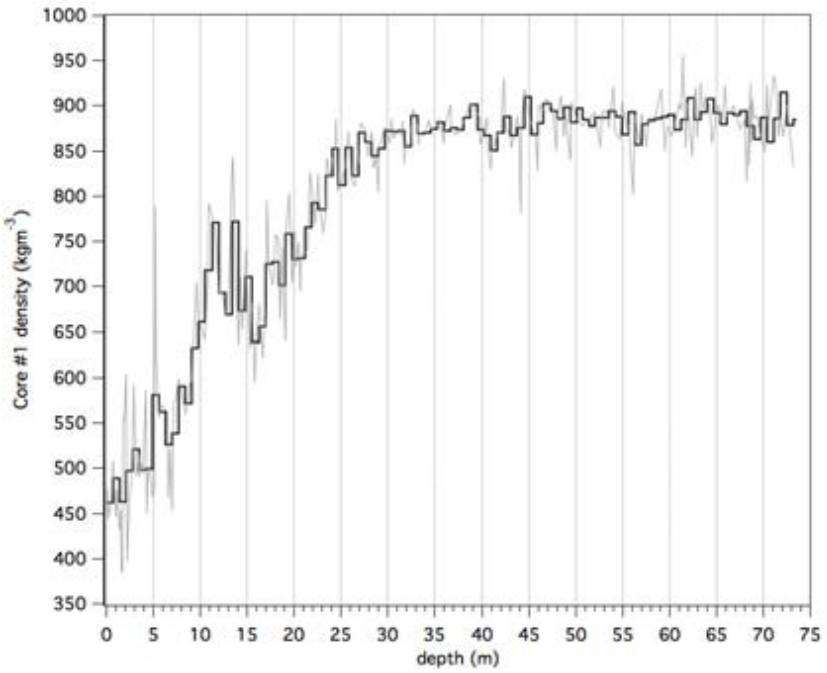

Figure 2.8: The Ortles core #1 density profile. Grey line: high resolution density, Black line: 70 cm averaged density.

2.4.2 The Ice Cores' Density

The author measured the density for the whole length of the Ortles core #1. All the sections cut for the continuous flow analysis were weighted and measured in the cold room (−20 °C). In order to decrease the uncertainty of the results at least three measurements were performed for the length and the width of each section, and the average value was used for the density computation. The cores were often already divided in two or more parts and therefore the density of each piece of ice was necessary. The density profile is shown in Fig.2.8, where the light grey line is the density computed per each ice piece and the black thick line is the density value of each 70 cm ice section.

In the first 30 m of the core the density increases starting from 450 kg m^{-3} to 500 kg m^{-3} and a logarithmic density increase is observed. A strong density increase is observed at a depth of 5 m, corresponding to presence of a thick ice lens of about 13 cm (Fig.2.9).

Another visible density increase can be observed between 10 and 15 m, with an average value of about 700 kg m^{-3} (15 % higher then the expected value). Ice lenses up to 30 cm width were measured in this depth range.

The core density increases until about 30 m of depth, where it reaches a plateau with densities data between 850 and 900 kg m^{-3}. The transition from firn to ice is continuous and this is an important result. The presence of hiatus (missing part of an ice core due to melting) would have been observed throughout the presence of a discontinuity, which is not the case. In many temperate glaciers, indeed, the transition between old ice and the more recent firn is sharp, because the firn melts and percolates before becoming ice.

The firn becomes more and more transparent going deeper because the external pressure caused the snow crystals to become compacted and the trapped air

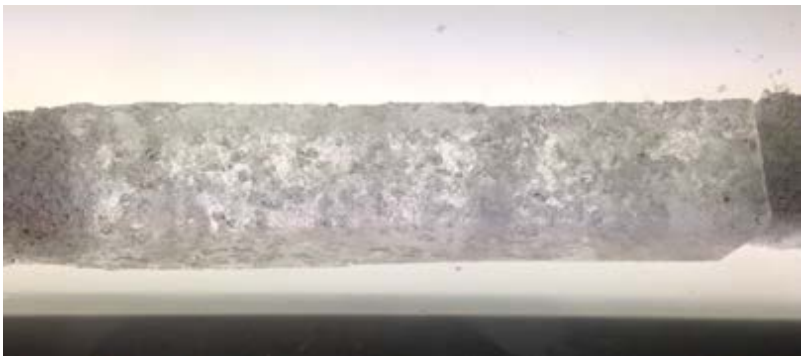

Figure 2.9: The thick ice lens at 5 m of depth. The firn is visible at the beginning and at the end of the lens.

bubbles to become smaller and smaller. In Fig.2.10 four pictures show the transition in the Ortles ice core from the firn to the cold ice (the pictures were taken by the author). The sections are placed over a lamp and their transparency increases at higher depths because the bubbles are fewer and smaller and the ice structure is more compacted.

The density profiles for the cores #1, #2 and #3 are reported in Gabrielli, Barbante, Bertagna, et al. 2016. The profiles are very similar except for the first 10 meters of core #2, where the density is higher then in core #1 and #3; probably this is due to a higher number of ice lenses.

2.4.3 Borehole Logging Profile

After drilling of core #1, #2 and #3 the entire boreholes images were taken by mean of a 360-degree continuous-imaging scanner (Optical Televiewer, Advanced Logic Technology, Luxemburg). The scanner consists of a LED light source, a mirror system and a CCD camera. The light reflectance of the firn and of the ice surfaces is proportional to the concentration and size of air bubbles, but it is also influenced by the presence of concentrated dust layers. However, in the Ortles ice cores the Saharan dust layers that are typically found in other Alpine ice cores (such as in the Colle Gnifetti cores), and used as temporal markers, were not directly observed. The image scan of the Ortles cores are therefore only a description of the ice layers and of the presence of ice lenses (where the bubbles concentration is almost zero).

The presence of ice lenses was recorded over the entire cores' lengths therefore showing that melting and refreezing cycles were always happening during the summer seasons over the Alto dell'Ortles glacier. The ice lenses were characterized by a tilting from 0° to 20°, possibly reflecting the bedrock slope (Gabrielli, Barbante, Bertagna, et al. 2016). By adding the ice lenses thicknesses it was possible to compute the percentage of the length made up of ice lenses. In the firn the ice lenses constitute the 20 % of length, 15 % between 30 and 55 m and only 5 % in the lower part of the core #1 between 55 and 65 m (Gabrielli, Barbante, Carturan, et al. 2012); below this depth it is no longer possible to distinguish the ice lenses.

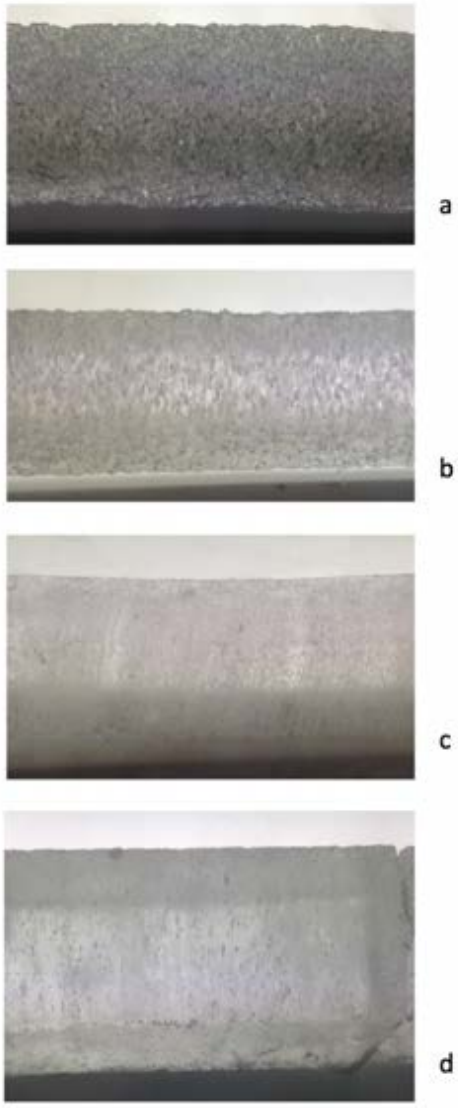

Figure 2.10: Real pictures of the Ortles ice core #1 sections, transitioning from firn to ice. The depths of the sections are about: a) 10 m, b) 30 m, c) 50 m, d) 70 m.

2.4.4 Using the Borehole Logging Technique to Reconstruct the Alpine Glaciers Density Profiles

The borehole logging technique is quite common for studying the internal structure of soils, rocks, ice sheets and glaciers.

Particularly, in Hawley and Morris 2006 a new optical technique in described (Borehole optical stratigraphy, BOS) and tested at the Summit Camp, on the Greenland Ice Sheet. They made a comparison between the BOS results and the density measured with the well-established neutron scattering density probe (NP) technique. The main result was that a significant positive correlation was found between the two logs in the first half of the 30 m borehole; then the correlation decreased becoming anti-correlation in the lowest 10 m. The author explains the results by the different physical mechanisms that control the snow compacting. In the first 15 m ($0.3\,\mathrm{g\,cm^{-3}}$–$0.55\,\mathrm{g\,cm^{-3}}$) the grain-boundary sliding (Alley 1987) is the dominant compaction mechanism, whereas deeper the densification takes

place by pressure sintering (0.5 g cm^{-3} to 0.8 g cm^{-3}). The first mechanism results in an increase of light scattering surfaces per cm^{-3} (surfaces between the ice/snow-air interfaces, characterized by different refractive indexes); the second causes a reduction of the reflected light because a reduction of the air spaces in between the crystals (pore close-off) an the formation of more rounded crystals decrease the scattering surface density. The relation between the ice crystal shapes and the reflected light is not explained.

In Hawley, Brandt, et al. 2008 a core optical stratigraphy (COS), an NP density profile and a gravimetric measured profile of 11 shallow core from Kongsvegen (Svalbard) are compared. The optical technique allowed a very fine firn internal structure description and evaluation of the radar back-scattering surfaces, but doesn't provide density quantification.

The LED light source is replaced with a laser in Bramall et al. 2005 in a new device for borehole optical measurement. The South Pole ice was studied and it was observed that the air bubbles scattering signals dominated at shallow depth (until 1300 m) showing a seasonal trend. In the deepest part, where the air bubbles become air clathrate crystals (Price et al. 2000), the dust scattering signals are clearly visible (detecting up to 1 cm dust layers). Moreover, a hot water drill was used, improving the optical signal by avoiding the ice-air surface refraction index criticalities.

The borehole optical scanner used in the Alto dell'Ortles glacier works by recording the light reflected (scattered) by the borehole surface ice; the optical signal results in a detailed image of the borehole where many different layers can be observed in the ice. The optical signal was then extrapolated from the borehole picture and divided in the three colors signal components (Red, Green and Blu; RGB). In Fig.2.11 the borehole image, the red signal and the density of the Ortles core #1 are shown.

Knowing the Alpine glacier internal structure is of primary importance within the frame of monitoring the glacier's behaviour under current climate conditions. However, a drilling campaign is usually very expensive and time consuming. Therefore, the chance to reconstruct the internal structure, the density profile and giving a depth to the firn-ice transition starting from the optical signal has been investigated by the author in this work.

The red component of the signal reflects the density variations of the core and, especially in the first 20 m, a good correlation can be observed between the signal and the 3 cm resolved gravimetric measured density profile (Fig.2.12).

The density profiles show that the firn-ice transition in the Ortles core is smooth, and this can be also appreciated by observing the red signal profile (Fig. 2.13, at a depth of about 25 m). The intensity of the red signal increases when the surface reflectance increases; indeed during the firn-ice transition a smooth decrease in the signal is observed. As reported in Hawley and Morris 2006 the decrease in reflectance of the borehole can be due to a transition between two different snow compacting mechanisms: the grain boundary sliding in the firn part and the pressure sintering in the ice. In the transition part of the core both mechanisms are acting and, as expected, a gradual decrease is observed in the red signal.

In order to explore the relation between the core density and the optical signal the two profiles where re-sample at 1 m and compared. The high frequency fluctuation of the signal, reveFuglaling the presence of ice lenses in the firn, where

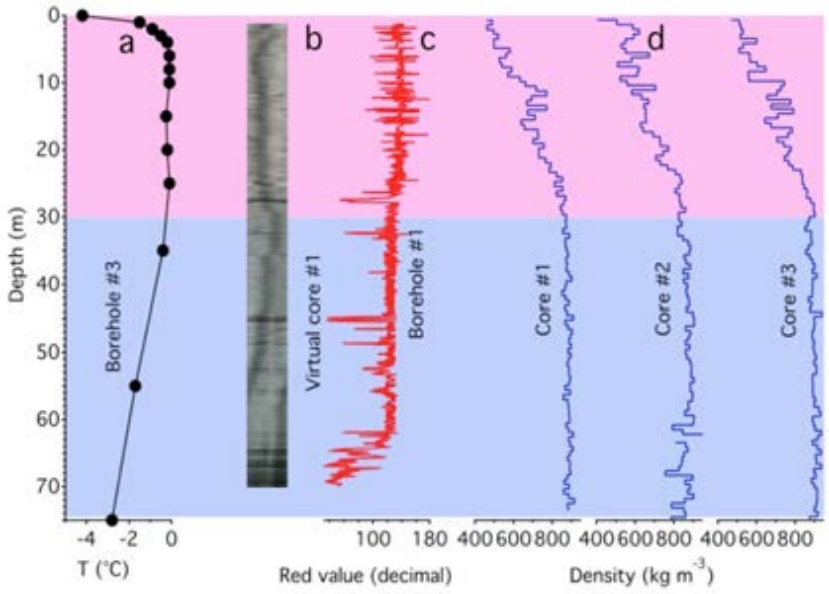

Figure 2.11: Physical properties of the Ortles cores: a) the borehole #3 temperature profile after 43 days from the drilling (Gabrielli, Barbante, Carturan, et al. 2012). b) Virtual image of core #1 reconstructed from the borehole optical scanning. c) Red component of the RGB digital signal of the borehole (high values means high reflection). d) Density of the Ortles core #1, #2 and #3. The chart is taken fromGabrielli, Barbante, Bertagna, et al. 2016.

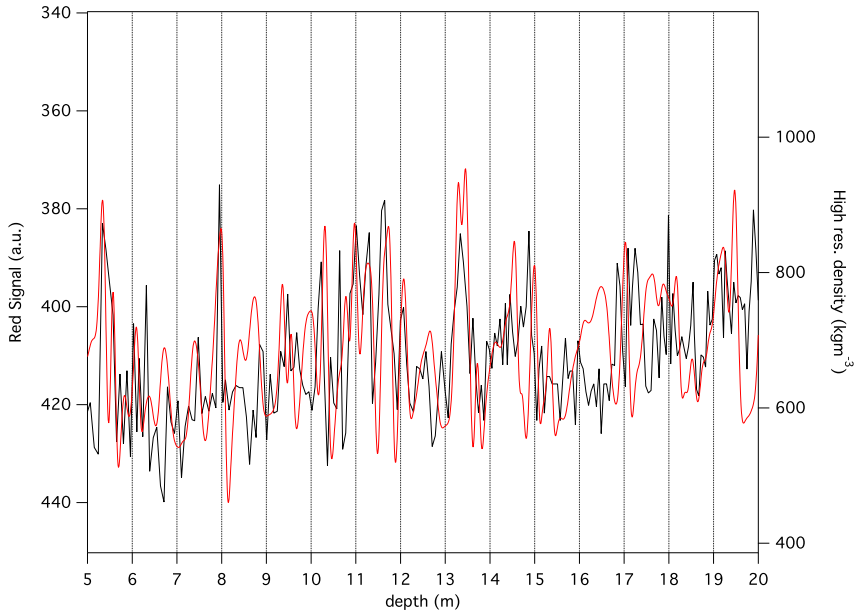

Figure 2.12: Comparison between the red signal-1cm (3 points moving averaged; red line) and the 3.5 cm density profile (3 points moving averaged; black line).

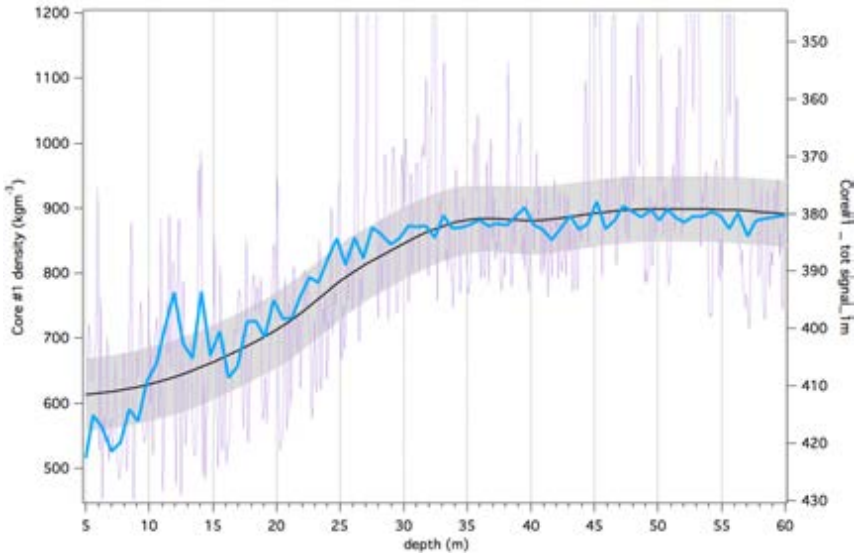

Figure 2.13: The 70 cm measured density (blu line), the 1 m re-sampled red signal (black line) with the 1.5 % variation range (grey thick line) and the 1 cm high resolution red signal (violet line).

filtered by the re-sampling. The first important observation is the linear relation that exists between the measured density (blu line) and the 1 m re-sampled red signal intensity (black line on a reversed scale) in Fig.2.13. The linearity makes the optical signal a simple potential way to reconstruct the glacier density profile.

Moreover, the grey solid line represent the 1.5 % variation of the 1 m re-sampled optical signal and it can be observed that the measured density is always in between this range (at those resolutions). By considering the 70 cm density profile a good agreement can still be observed with the high-resolution signal (violet line) in the first 20 m.

In order to test the feasibility of the optical signal in reconstruct the ice core density a linear regression between the 1 m re-sampled measured density ρ (for the core# 2, the only available at that time) and the 1 m re-sampled red signal values (rs) was performed. The linear fit was very accurate with an R^2 of 0.97. The obtained linear equation was: $\rho = -9rs + 4268$. However, the absolute values of this equation are strongly dependent from the camera used during the borehole logging and the optical signal selected, in this case the red one (the linear relation is still valid using the blue or the green component). In order to try to indirectly reconstruct the density profile of a glacier from the borehole logging optical signal by using a fixed equation and coefficients a method should be established (always selecting the same portion of the optical signal) and other glaciers should be investigated for checking the reproducibility.

Another possible and simpler way to create a reconstructed density profile consists in calibrating the optical signal with the known near surface density and with a reference density value for the ice in the deep part of the borehole. The firn density, indeed, can be easily measured by digging a snow pit and taking the average value of the snow density to calibrate the corresponding part of the optical signal; however, only a reference value can be used for the deep ice of the core which is usually close to 900 kg m^{-3} (in the Ortles ice core #1 the variations from the average value in the measured density are never above the 5%). By using these two value it

easy to calibrate the optical signal obtaining the core density within an estimated uncertainty of less than 5-10%.

This results of these brief review and this case study show that the optical borehole logging technique has many interesting application in the glaciological and ice core sciences. First of all the optical signal can be obtained by simply making a hot water borehole in a glacier (without the costs and the resources of a common drilling procedure). Secondly, the highly resolved glaciological and physical properties can be inferred from the detailed optical signal: the position of the firn ice transition, the presence of ice lenses, of layers of dust and potentially, the grain size variations. Thirdly, the linear relation between the optical signal and the snow/ice density makes this technique ideally suitable for reconstructing the whole density profile of a glacier or an ice sheet, by simply calibrating the signal with the surface firn measured density and a reference value for the deep ice.

2.4.5 The Ice Lenses

The Alpine glaciers ice cores usually present a rather peculiar aspect: the presence of thick ice lenses. During the summer periods when the temperature of the snow is above zero the surface of the glacier melts and the resulting liquid water percolates in the lower snow layers. If the temperature below the surface is at the freezing point the percolating water can immediately refreeze or, as it is the case for the warmest summers, it can go down below the snow of the previous year or until it reaches an impermeable surface (another ice lens for instance). The refreezing strata are usually characterized by lower air bubbles concentration because during the melting the air trapped in between the snow crystals is released. On the highest Alpine glaciers the melting water from the surface usually percolates only for some centimetres (Shumskii and Kraus 1958), whereas in temperate or polythermal glaciers, the melting water can penetrate even for meters during extreme warm summers.

On the Alto dell'Ortles glacier melting, percolating and refreezing cycles happen every summer especially under the current climate condition (summer average mean temperatures increased by 2 °C). It is very likely that during the summer of 2003, and less in 2015, the water from the surface percolated for many meters. The preserving of the cold ice below 30 m of depth despite the extreme percolation events can be likely explained by assuming a lateral drainage before the firn-ice transition (Gabrielli, Barbante, Carturan, et al. 2012).

Number, depth and thickness of all the naked-eye visible ice lenses were recorded during the Ortles core #1 processing in the cold room of the University of Venice (mainly by G. Dreossi, A. Spolaor, the author of this study and J. Garbieli). The sections of the core were placed on a neon lamp and the internal structures were then clearly visible. In the firn portion the ice lenses showed a sharp discontinuity (Fig.2.9), whereas in the cold ice only the air bubbles concentration decreasing allowed the detection of the lenses. The Figure 2.14 represent the ice lenses over the whole Ortles core #1. Each line represent an ice lens and the color is related to the thickness of the single lens (as described in the color legend). Considering the extreme summer events and the temperature increase trend of the last decades an increase in the ice lenses frequency and thickness is expected.

Ice lenses are distributed over the entire core's length and range from 0.5 cm to

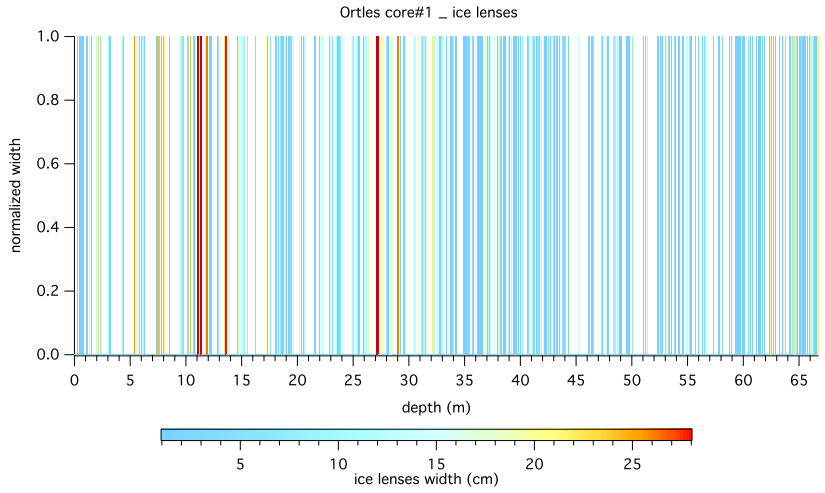

Figure 2.14: Ice lenses observed in the Ortles ice core #1. Each line represents an ice lens and the color corresponds to the lens thickness.

28 cm. The color visualization in Fig.2.14 makes clearly visible the presence of two very thick lenses between 10 and 15 m of depth (up to 28 cm) and between 27 and 30 m, very closed to the firn ice transition and this is probably the last impermeable surface before the cold ice. The lenses between 10 and 15 m caused a significant density increase (Fig.2.8). As expected, the largest lenses are found in the upper part of the core. In the first 30 m the ice lenses are the 22.5 % in length, whereas from 30 m to 60 m about 12 %.

The ice lenses frequency per section are reported in (Dreossi 2016); no clear trends are detectable but only a small increase both of frequency and in the total ice lenses thickness per bag from 30 m to 40 m of depth.

The thickness frequency density for the whole dataset is reported in Fig.2.15.The ice lenses thickness distribution is clearly centred over small thicknesses (about 0.5-1 cm) and decreases fast as the thickness increases. Over the whole lenses dataset more than 40 % are lenses with thickness of about 0.5 cm (the minimum resolution), 25 % of about 1 cm, 5 %–10 % until 4 cm and the thickers less than 5%.

2.5 The Ortles Chronology

2.5.1 Ice Cores Dating Techniques

To obtain an accurate and precise dating is one of the most important and difficult parts in ice core science. Many different techniques and methodologies are used nowadays to give a reliable chronology to an ice core.

The *annual layer counting* is commonly used and it consists in searching for seasonal oscillations of some variable in the ice. Many parameters/species found in the ice cores show a strong seasonality because of their production sources behaviour and/or the atmospheric transport processes that changes during the year (altitude of the atmospheric boundary layer). The analyses of the concentration of the seasonally varying parameters allow detection of the annual oscillations if the sampling frequency is high enough. The most used parameters/species for the

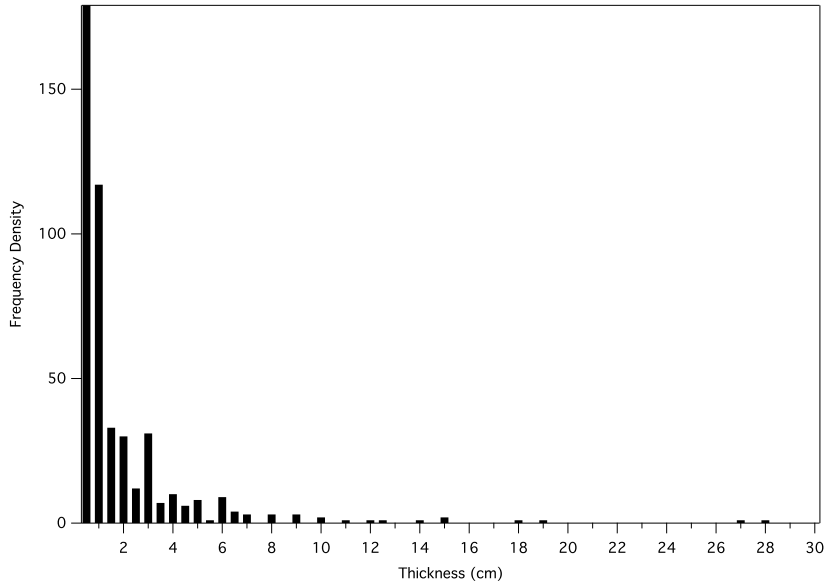

Figure 2.15: The Ortles ice lenses frequency density for the range 0.5 cm to 28 cm of thickness.

annual layer counting are the water stable isotopes (^{18}O, ^{2}H and deuterium excess), some ionic species as the ammonium (NH_4^+), the ice total conductivity (resulting from the sum of the conductivity of all the ionic compounds) and the dust content. This technique, however, can be adopted only where the annual snow accumulation is enough, whereas in very low accumulation zone (Antarctica) it is not feasible. Moreover, in the low latitude glaciers the post-depositional effects can make more difficult to recognize the seasonal oscillations.

The searching for time *markers* is another fundamental part of the ice cores dating. Some precise dated historical events are usually found in the ice layers, as it is the case for the nuclear explosion products (^{3}H, ^{137}Cs and beta emitting isotopes), for particularly strong Saharan dust events, or volcanic eruptions (tephra layer or sulphates and trace elements enriched layers).

The decay time and the concentration of some unstable isotopes can also be used to have dating points. Particularly, the activity of lead isotope ^{210}Pb can be used to date the core back to 100 years and it is characterized by a half-life time of about 22.20 years. For ice with ages from 200 to more than 10000 yrs the dating can be known by analysing the ^{14}C carbon radioactive isotope activity in the organic matter trapped in the ice (Uglietti, Zapf, et al. 2016); the ^{14}C has a half-time of 5.73 kyrs.

2.5.2 The Age of the Mt. Ortles Ice Cores

The complete dating of the Ortles ice cores was published in 2016 (on *The Cryosphere* and the author of this thesis is one of its co-authors. Particularly, the density of the core #1, the optical signal analyses and the preliminary co-variations of cores #1, #2 and #3 were where the author contributed the most. The paper is titled *Age of Mt. Ortles ice cores, the Tyrolean Iceman and glaciation of the highest summit of South Tyrol since the Northern Hemisphere Climatic Optimum.* The dating techniques and results are briefly described here.

The Alto dell'Ortles glacier is located only 37 km far from the ice field of Tisenjoch (3210 m), where in 1991 the mummy of the 5.2 kyrs Tyrolean Iceman emerged. The mummy was extremely well preserved thus suggesting its continuous embedding in the ice. This finding gave rise to the idea of the chance of having very old ice in the Eastern European Alpine glaciers.

The Ortles ice core dating was obtained by ^{210}Pb, ^{3}H, beta activity and ^{14}C determinations. The complete dating curve was then obtained by an empirical model (COPRA) and the result was a *chronologically ordered ice stratigraphy* with an age of 7 kyrs for the ice layers closed to the bedrock (Gabrielli, Barbante, Bertagna, et al. 2016).

The result of the dating seems to agree with the climatic conditions of the Northern Hemispere Climatic Optimum, the warmest period of the entire Holocene (Vollweiler et al. 2006). It is possible that the *Alto dell'Ortles* glacier completely disappeared during this period. The Neoglaciation started between 5.3 and 3.3 kyr BP when climate conditions became favourable to glacier expansion (Magny and Haas 2004). The glaciers faced great variations during this period and the three greatest LIA expansions happened during the 14th, 17th and 19th century (Holzhauser et al. 2005). After the last expansion of the 19th century started an ongoing period of extreme glacier melting (Zemp et al. 2006).

Beta Activity and Tritium

The dating of the Ortles ice cores were performed in different Institutes and Universities in order to obtained independent results. The Beta activity measurements were performed at the BPCRC and at the LGGE of Grenoble (France), the tritium content determination at the University of Bern (Switzerland) and at the University of Venice (Italy) using common techniques (for the detailed descriptions and methods references see the paper in the appendix). All the results agree by showing a strong peak in beta activity and tritium concentration at a depth of 44 m, indicating the well know 1963 radioactive horizon. The matching of the two peaks also shows that the melting and percolation did not affected the climatic and chemical signals below the 1980 ice (Gabrielli, Barbante, Bertagna, et al. 2016). The Chernobyl radioactive horizon was not observed at the depth corresponding to 1986 (dated with ^{210}Pb) but an intense signal was measured at a depth of 28 m (dated at 1979) and close to the firn ice transition. It is very likely that this peak is a result of the melting and percolation of water through the firn; the radio nuclei were brought from the upper layers and trapped in the refreeze water.

^{210}Pb

The activity of ^{210}Pb was measured down to 58.67m in core #2 using well-established methods. The linear regression of the logarithmic beta activity was used to find the age-depth relation. The ^{210}Pb-based chronology is consistent with the beta and tritium activity peak. The lowest sample was dated back to 82 ± 7 years before 2011 (1930).

^{14}C

The ^{14}C activity measurement of the water insoluble organic carbon fraction (WIOC) of the aerosol in the ice was conducted by filtering the melted samples, following the new method described in Uglietti, Zapf, et al. 2016. All the analyses were performed at the University of Bern (Lara Laboratory). The ^{14}C final dating points are five but all the samples were subdivided in three sub-sections and analysed separately. The table with the results both for ^{210}Pb and for ^{14}C and the corresponding uncertainties is reported in Gabrielli, Barbante, Bertagna, et al. 2016.

A larch leaf was found at 73.2 m depth in core #1 and the conventional ^{14}C dating analyses were performed. The result was in agreement with the other dating points with an age of 2612 ± 101 years BP.

All the dating points are chronologically consistent and they maintain the consistency even when a common depth scale is given for the cores.

Depth Scale Alignment and the COPRA Model

The common depth scale for cores #1, #2 and #3 was found by finding common variations in the stable isotopes records and matching the three datasets. The correlation between core #1 and #3 datasets after the matching was $r = 0.72$ and for core #2 and #3 it was $r = 0.67$. The drilling points of #1 and #3 were very closed and the two stratigraphies are very similar in fact; the major differences lie near the firn-ice transition part.

The depth-age curve was found by using a Monte Carlo based empirical fitting model (Breitenbach et al. 2012). The age model COPRA uses 2000 Monte Carlo simulation in order to find the best fit for the dating points and it returns the associated uncertainty values. The model does not require any glaciological model but it is purely empirical, only basing on the reliability and the precision of the dating points. The resulting uncertainties derived from the uncertainties of each dating point and the density of dating horizons.

The Dating Curve

The dating points used in the COPRA age model and the corresponding uncertainties are reported in Table 2.2.

The stratigraphy of the Mt. Ortles ice cores seems to be continuous despite the large uncertainties associated to the first ^{14}C dating points. At the moment the presence of a physical hiatus between 58 m and 68 m cannot be ruled out (Gabrielli, Barbante, Bertagna, et al. 2016); at least one more dating horizon between these two depths is necessary in order to drastically decrease the dating uncertainties. The core #1 ended at about 1 m from the bedrock and the deepest ice of this core, according to the dating curve, is dated back about 3 kyr BP.

The continuous dating curve as obtained with the COPRA model is reported in Fig.2.16.

Table 2.2: Data used in the age-depth modelling (adapted from Gabrielli, Barbante, Bertagna, et al. 2016). * The depth are referred to the depth of the Ortles core #2.

Time reference	Top depth (m)*	Bottom depth (m)*	Mid depth (m)*	Age (yr B2011)	Age (yr AD, BC)	σ age (yrs)
Surface constrain	0	0	0	0	2011.8	0
^{210}Pb	0	2.75	6.09	1.4	2010.4	0.1
^{210}Pb	13.85	16.64	10.39	16.7	1995.1	1.5
^{210}Pb	25.05	27.88	26.47	32.3	1979.5	2.8
^{210}Pb	30.68	33.52	32.1	41	1970.8	3.6
Tritium peak	40.58	41.27	40.92	48	1963	1
Beta emission peak	43.33	44.04	43.69	53	1958	1
^{210}Pb	44.74	47.48	46.11	63.7	1948.1	5.6
^{210}Pb	50.27	53.07	51.67	72.7	1939.1	6.4
^{210}Pb	55.88	58.67	57.28	82	1929.8	7.2
^{14}C in WIOC	67.9	68.61	68.26	652	1360	103
^{14}C in WIOC	71.15	71.6	71.38	1671	341	297
^{14}C in larch leaf	73.19	73.19	73.19	2674	−662	101
^{14}C in WIOC	73.84	74.11	73.98	4341	−2329	619
^{14}C in WIOC	74.11	74.31	74.21	5370	−3358	633
^{14}C in WIOC	74.31	74.53	74.42	6889	−4877	425

2.6 State of the Art of Mt. Ortles Ice Cores Analyses

2.6.1 Stable Isotopes Records

Many analyses were already performed on cores #1, #2 and #3. Particularly, the stable isotopes profiles for the cores are completed and they were used to find a common depth scale (Gabrielli, Barbante, Bertagna, et al. 2016). The stable isotopes record for core #1 was obtained at the University of Venice (Dreossi 2016) and it is reported in Fig.2.17.

The records show that Ortles ice core #1 is divided in three distinct regions: the upper firn part, the cold ice preserved under the firn-ice transition and the lowest part of the core characterized by a strong thinning of the ice layers (the record variability decreases due to the samples resolution and diffusion).

The record description reported in Dreossi 2016 is briefly summarized here. In the first 20 m it is possible to observe large oscillation but then, down to about 32 m they become less clear. From 32 m to 50 m the seasonality seems to be preserved (covering the period 1970-1940). At these depths the lowest δ^{18}O values are recorded. Below 50 m the thinning of the layers is noticeable and the seasonality signal is still visible (at some depth it appears smoothed). At 57 m depth the amplest seasonal variation is observed in only 5 cm of ice. From 60 m to 67 m depth the thinning remains constant and a positive trend is observed towards the deepest part. From 67 m to 74 m the amplitude of the oscillation further decreases and a positive trend is observed toward the end of the core; despite the positive trend the mean values remains lower than those observed in the first 10m of the core (Dreossi 2016).

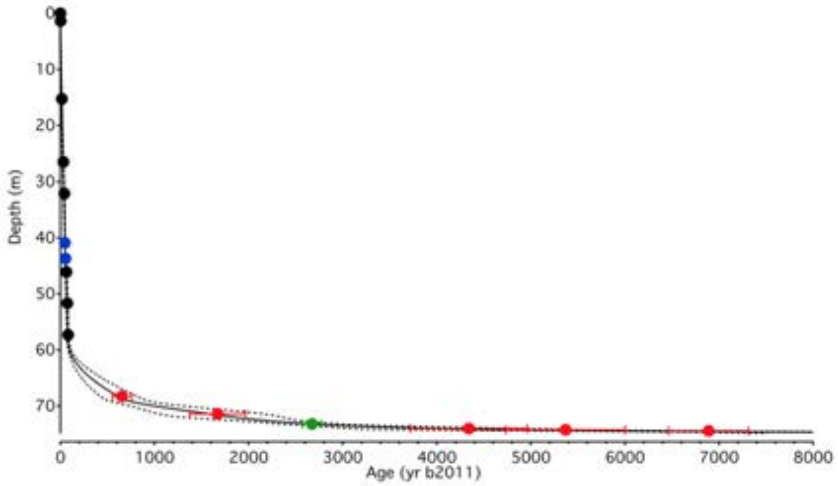

Figure 2.16: The Ortles ice cores dating curve obtained with 2000 Monte Carlo realizations fitting the empirical dating points (continuous black line; 25 % and 97.5 % quantile of uncertainty showed by the dotted line). The error associated to the empirical value is 1σ. Black dots: surface constrained and ^{210}Pb dating points. Blue dots: tritium 1963 and 1958 beta peaks. Red dots: ^{14}C WIOC dating points. Green dot: ^{14}C on the larch leaf. (adapted from Gabrielli, Barbante, Bertagna, et al. 2016).

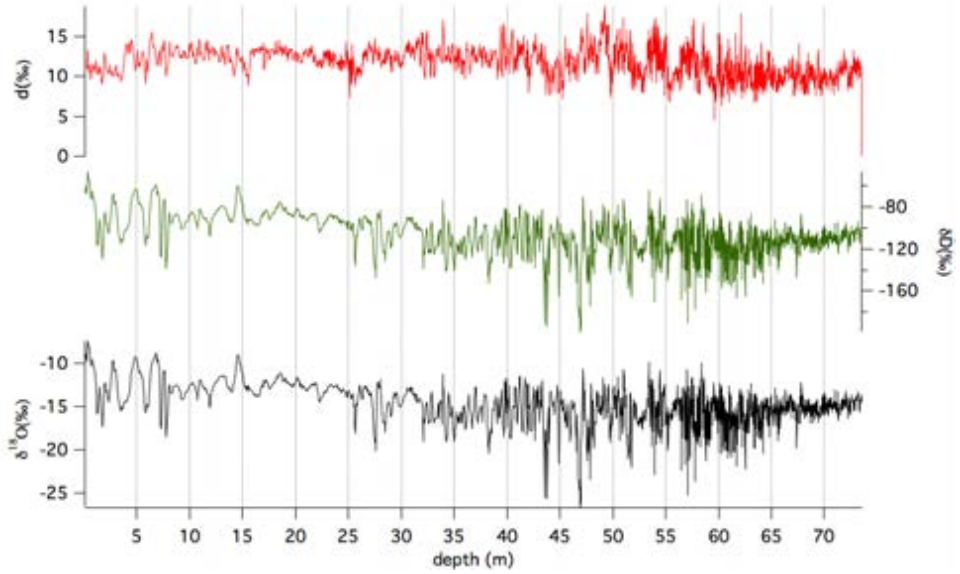

Figure 2.17: Core #1 δ^{18}O (black), δD (green) and d (red) Ortles core #1 profiles vs. depth (adapted from Dreossi 2016).

Chapter 3

Instruments and Theory

3.1 The Single Particle Soot Photometer (SP2)

The rBC measurements of this work were all performed by using a *single particles soot photometer* (SP2, Droplet Measurement Technologies, Boulder, Colorado). A detailed description of the instrument can be found in Stephens et al. 2003 and J. Schwarz, Gao, Fahey, et al. 2006.

The SP2 analytical technique is based on the laser induced incandescence of the rBC particles. rBC is the fraction of the carbonaceous particulate matter that vaporizes at temperatures of about 4000 K (J. Schwarz, Spackman, et al. 2010) and can be measured with this technique (Moteki and Kondo 2010). The mass of each rBC particle is retrieved indirectly by measuring the incandescence signal that is emitted before the particle vaporization.

rBC particles absorb the laser radiation at a specific wavelength (1064 nm) and being characterized by a very high refractoriness reach the vaporization point at elevated temperatures (about 4000 K). This phenomenon can be explained by using the Mie Theory (Mie 1908), based on the Maxwell's equations.

The main components of an SP2 are a laser system, a measurement chamber, four detectors and a rotary pump to control the fluxes. The radiation source needed for the rBC particles heating is a continuous intra-cavity Nd-YAG laser with a wavelength of 1064 nm (Fig. 3.1, photo taken during a complete cleaning session)

The aerosol sample flows in the system and finally reaches the measurement chamber. Around the chamber four different detectors record the incandescence radiations emitted from the vaporizing particles. The scheme of the SP2 measurement chamber and the detectors specifics are reported in Fig. 3.2.

The two photomultipliers detectors (in the upper part of Fig. 3.2) are used to measure the incandescence signal emitted from the rBC particles. The optical filters select the wavelength range: narrowband (630–800 nm) or broadband (350–800 nm). The other detectors are avalanche photodiodes and measure the purely scattering signals and the position of the particle in the chamber at the wavelength of the laser (1064 nm).

The photomultipliers detectors detect the intensity of the incandescence signal emitted by every rBC particle (coated or un-coated). The particles' mass is proportional to the incandescence signal and this relation can be found through a calibration with *fullerene* soot (Gysel et al. 2011).

The mass equivalent diameter is computed by assuming the rBC particles to

Figure 3.1: The SP2 Nd-YAG crystal, its support and power supply connections.

have spherical shape and a particle density of 1.8 g cm^{-3} (Moteki and Kondo 2010).

All the SP2 data obtained in this work were processed with the toolkit developed by M. Gysel (Paul Scherrer Institute PSI, Switzerland).

3.1.1 The APEX-Q Introduction System

The SP2 was coupled with an APEX-Q desolvation system, according to Lim et al., 2016. The APEX-Q jet nebulizer has the highest *particle size-independent aerosolization capability*, therefore preserving the rBC size distribution of the samples (**acp2016lim**).

A mass flow controller was used in order to have a compressed air flow of 1 L min^{-1} in the concentric glass nebulizer, where the sample was nebulized due to the pressure difference at the end of the capillary.

The APEX-Q system is formed by a series of heating (120 °C) and cooling (2 °C) glass chambers where the nebulized water becomes water vapor and then condenses on the cooling surfaces before being removed. After the water removal only the aerosol component of the sample is injected in the SP2.

3.2 The Inductive Coupled Plasma Mass Spectrometer (ICP-QMS)

The inductive coupled plasma mass spectrometry is a well-established technique used for the analysis of trace and ultra trace elements. This analytical technique offers the highest performance in terms of sensitivity, accuracy and precision. A detailed description of its principles and its components can be found in H. E. Taylor 2001.

The liquid sample is vaporized, atomized, ionized and then the ions are separated in terms of their mass to charge ratio. Finally the detector quantifies the elemental concentrations in term of counts. Through a calibration it is then possible to compute the real concentrations of each element.

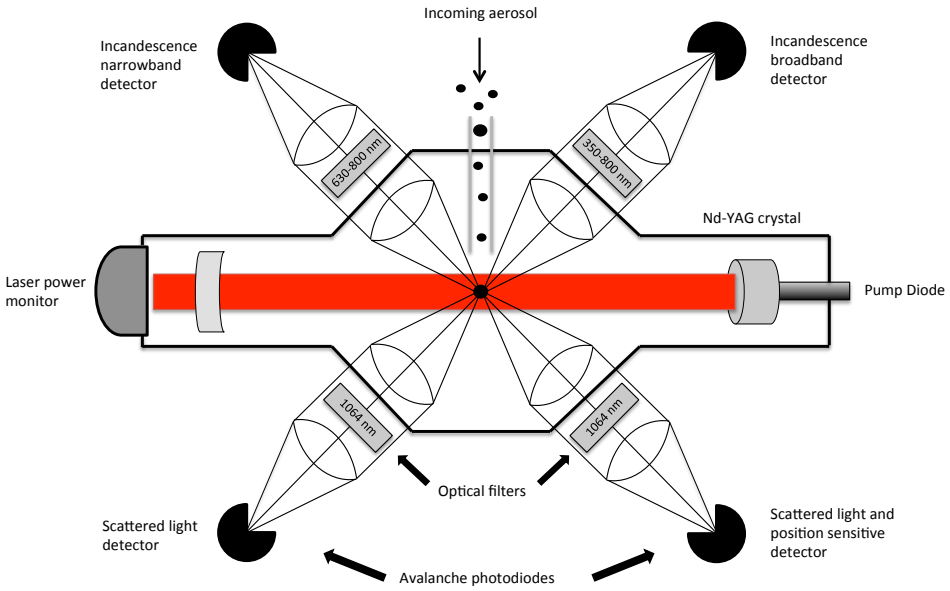

Figure 3.2: The SP2 measurement chamber configuration.

3.2.1 The ICP-QMS Components

The ICP-QMS is mainly composed by an introduction system, a radio frequency (RF) generator as plasma source, an interface region, the ion beam focusing region (with electrostatic lenses), a mass spectrometer and finally the detector.

The Introduction System

The introduction system is composed of two parts: a nebulizer unit and a spray chamber (Fig. 3.3).

The nebulizer is needed to nebulize the liquid sample thus producing an aerosol

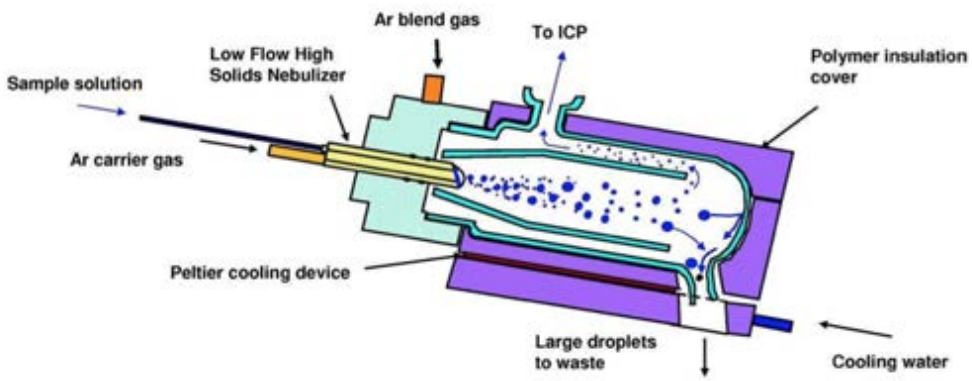

Figure 3.3: The double pass spray chamber configuration.

flux, whereas the spray chamber ensures the introduction in the ICP-MS of aerosol with a uniform size distribution, the smallest as possible. The introduction system has a very important role during the analytical sessions. The plasma ionization efficiency significantly decreases in the presence of large liquid droplets.

Two main types of nebulizer can be used: pneumatic or ultrasonic. In this work, a pneumatic concentric nebulizer was chosen due to its suitability in working with low particulate content samples. Particularly, in the concentric nebulizer a high speed Ar flux flows parallel to the capillary. The pressure difference at the end of the capillary makes the liquid to break in small droplets. The largest droplets collide on spray chamber walls and flow out of it through the drain system. After the spray chamber the aerosol size distribution has a Gaussian shape, centred at about 5 μm H. E. Taylor 2001. The spray chamber used for this work was externally cooled (2 °C) in order to decrease the amount of water in the outflowing aerosol flux. The scheme of a typical double pass spray chamber is shown in Fig. 3.3.

The Plasma Source and the Interface Region

The dimension filtered aerosol sample flows out of the spray chamber and arrives in the plasma region. The Ar carrier gas carries the samples in the torch, which is commonly made by three quartz concentric tubes. Around the torch there is the load coil connected with the RF electrical generator. The Ar gas for the plasma (auxiliary gas) is injected in the torch with a flow of 0.8 to 1.5 L min^{-1}. The plasma is then ignited by applying the RF power (27.12 MHz) to the load coil, thus generating a strong oscillating electromagnetic field, and producing a high voltage spark in the torch where the Ar auxiliary is flowing. The spark has enough energy to strip electrons from the Ar atoms, thus producing free electrons and Ar^+ ions. The free electrons are then retained and accelerated in the electromagnetic field thus ionizing other Ar atoms via collision-induced ionizations, inducing a reaction chain until a dynamic equilibrium is reached. The Ar plasma with a temperature of about 7000 K is then sustained by the continuous RF power supply through the inductive coupling process.

Ar was used according to its atomic characteristics: Ar is a chemically inert gas thus avoiding the formation of chemical compounds during the sample carrying; the Ar atoms have a high first ionization potential thus being enough to ionize all the periodic table elements (but not with the same efficiency).

The Ar gas carrier flux has to be enough to vaporize the liquid sample in the spray chamber and to bring it towards and inside the plasma through the central tube of the torch; the carrier flux is therefore a crucial parameter to be set up.

The interface region, the mass analyser and the ICP-MS detector operate under vacuum conditions. Usually a rotary pump is used at the interface region whereas a turbo-molecular pump produces the high vacuum level required for the mass analyser and the detector. The presence of atmospheric gasses would cause the scattering of the incoming ions and a high background noise level in the measurement.

The interface region is where the ionized sampled atoms flow from the plasma region, at atmospheric pressure, to the innermost part of the ICP (Fig. 3.4).

The ionized sample flows towards a blunt Ni cone (*sampler*) with a small orifice of 1 mm diameter (Fig. 3.4). Only the central part of the plasma, which has the

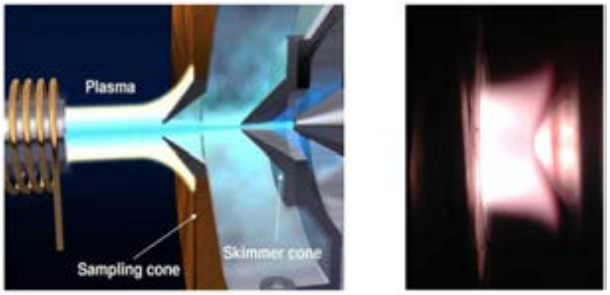

Figure 3.4: The interface region schematic and a real picture of the Ar plasma directed on the sampler cone.

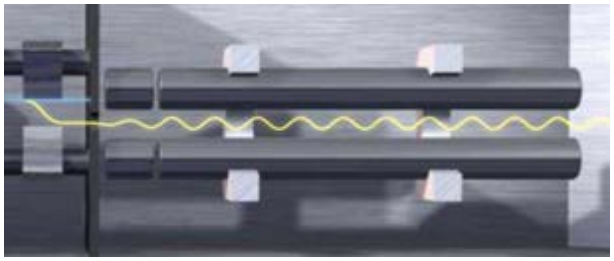

Figure 3.5: Quadrupole mass analyzer (from www.agilent.com)

highest sample ions concentration, passes through the hole whereas the remaining part is lost and evacuated by the aspiration system. The vacuum level at the interface region is of about 270 Pa. The Ni cone is surrounded by a Cu plate, which is cooled by an external fluid chiller.

The second cone is called a *skimmer*, and has a smaller orifice of 0.4 mm and more inclined surfaces (Fig. 3.4). The skimmer filters the incoming ions by selecting again the central part of the plasma, richest in sample ions.

The Ions Focusing Lenses, the Mass Analyser and the Detector

The sample ions that pass through the skimmer cone are focused and filtered by the ions focusing lenses. The lenses are a set of charged metallic plates placed between the skimmer and the mass analyser. Within this step the beam is filtered by photons, neutral species and from the matrix residuals. The ions focusing lenses have to transfer the maximum amount of sample ions to the mass analyser but at the same time have to filter and focus the beam in order to have a low background noise level.

In this work two different mass analyser were used: a quadrupole mass analyser (QMS) and a collision reactor cell (CRC). For the continuous flow analyses only the QMS was used whereas in the discrete analyses both systems were used.

The quadrupole analyser consists of two hyperbolic cross section rods (Fig. 3.5). By applying to the rods an AC high frequency opposite phase voltage and an opposite sign DC voltage a dynamic hyperbolic electric field is generated between them. The ions can follow a stable trajectory and arrive at the detector or may collide on the rods. By changing the voltages a mass analysis can be obtained, based on the charge to mass ratio of each particle. The voltage variations can be very fast thus permitting a complete mass scanning in a very short time (usually, a few seconds).

The ions with the selected mass to charge ratio finally arrive at the detector.

The ICP-MS detector is an electron multiplier, which is a device that generates a detectable electrical signal from a single ion collision. The positive ion is deflected toward a negatively charged dynode and the collision generate free electrons, which are in turn accelerated toward another charged dynode and an avalanche reaction is started. The electrons are finally collected on a conductor and the signal is recorded and elaborated.

3.2.2 The ICP-QMS Configuration

An Agilent 7500 ICP-QMS was used during the continuous ice core measurement. A water-cooled Scott-type spray chamber was coupled with a PFA nebulizer. Before every analytical session a tuning was performed by using a tuning solution with $^{7}\mathrm{Li}$, $^{89}\mathrm{Ir}$ and $^{203}\mathrm{Tl}$. The list of measured elements is showed in the calibration paragraph. For the selected elements we analyzed the most abundant isotope, except for $^{57}\mathrm{Fe}$ (because $^{56}\mathrm{Fe}$ is strongly influenced by the ArO interference).

3.3 The Abakus® Particle Counter

A Particle Counter Abakus® (Markus Klotz GmbH) was used during the analysis of the Ortles ice core for continuously measure the number and the size of the particles in the melted water. The liquid flow passes through a glass chamber and an LDS 23/23 laser beam. The detector detects each particle in a predefined size range with 32 channels. The laser detector is able to count up to 150.000 particles per minute and requires a minimum flow of about $3\,\mathrm{ml\,min^{-1}}$. The Abakus was connected to a computer via an RS 232 C port. The amount of particles in the fluid for the 32 channels was recorded by a LabView® based software (*ICE*; see paragraph 3.7) with a time resolution of 3 seconds.

The selected dimensional range and each dimensional class was chosen in order to detect the highest number of particles, according to the size distribution in the sample, and at the same time to check for the presence of larger particles (80 µm) (Table 3.1).

3.4 The Conductivity Micro-Cell

The total water conductivity was continuously analysed during the Ortles core continuous flow analysis. The cell was placed after the Abakus and connected with polyethylene tubes. The system doesn't have a controlled temperature but the temperature of the lab has always been stable as well as the cold temperature of the melted water.

3.5 The Coulter Counter®

During the dust concentration analyses with a Coulter Counter the samples are usually mixed with an electrolytic solution. The sample is then placed in the Coulter Counter where a tube with two electrodes is inserted in the solution. An electrical current flows between the two electrodes creating a *sensing area*. The sample

solution and the suspended particles are made to pass between the electrodes and during the passages they modify the impedance causing a variation of the current and an electric pulse. The pulse is proportional to the volume of the particles. Knowing the total pulses number it is possible to know the dust concentration of the sample.

The dust content in the snow samples taken in August of 2015 from a snow-pit at the drilling site of the Ortles glacier were analysed in the class-100 clean room laboratory of the LGGE laboratory (Grenoble, France). The insoluble dust particles total mass and size distribution was determined by a Coulter Counter© Multisizer III. The dimensional range was from 1.0 to 300 μm divided in 300 channels of 1 μm. By assuming a density of 2.5 gcm^{-3} (Delmonte et al. 2002) it was possible to compute the total mass from the volume size distribution.

3.6 Ion Chromatography

The ion chromatography is an analytical technique that is an affinity based chromatographic ionic separation.

The snow samples collected on the Ortles glacier were analysed with a Dionex© ICS3000 dual pump Ion Cromatography system (Thermo Scientific) at the LGGE laboratory of Grenoble (France). Cations (Li^+, Na^+, $NH_4{}^+$, K^+, Mg^{2+}, Mn^{2+}, Ca^{2+}, Sr^{2+}) were analyzed on CG16+CS16 (2 mm) columns and anions (F^-, Cl^-, $NO_2{}^-$, Br^-, $NO_3{}^-$, $(CH_2)_2C_2O_4{}^{2-}$, $SO_4{}^{2-}$, $C_2O_4{}^{2-}$) on AG11+AS11 (2 mm) columns, with suppressed conductivity detection.

3.7 The ICE Software

A LabView based software was developed in 2013 to monitor the CFA system. The ICE software interface shows the data coming from the draw-wire detector, from the Abakus system and from the conductimeter micro-cell. Six graphs are shown and are updated every second: the height of the melting core, the melting speed, the ice core electrical conductivity, the measured flux, the total number of particles and a 3D graph with the number of particles in the 32 dimensional channels as a function of time.

Once the operator starts the acquisition, the software begins to write a matrix on a .csv file. The particle contents for the 32 channels of the Abakus are written, followed by the conductivity, the core height, the measured flux and two columns for the alarms signal, (the operator can set up an alarm for the flux and one for the melting speed that ring when the highest/lowest values, fixed by the operator, are exceeded).

The software was updated in order to follow the needs of the operator during the set-up and the methods validation of the CFA system.

3.8 The MATLAB Codes

The whole continuous flow analyses system produced a very high number of data. Three main matrices are generated by the various instruments: the matrix from

the ICE software (37 columns with one row per second of analysis), the ICP-MS software (24 columns with a row of data every 2.5 seconds of analyses, and the calibration files), the files from the SP2 (directly analysed with the toolkit of M. Gysel (Paul Scherrer Institute PSI, Switzerland; http://aerosolsoftware.web.psi.ch/) and the matrix with the flow measurements in the SP2 line (see Section 4.4.1). Therefore, every 70 cm section melting resulted in about 55000 data for ICE software, 15000 for the ICP-MS, 1500 for the SP2 flux. For all the 105 sections of the Ortles ice core more then 7.500.000 data in all were obtained.

In order to handle the data the author created ad-hoc MATLAB scripts. The scripts allowed to check the data quality after each analytical section and to compute all the required time series.

The MATLAB script for elaborating the ICE software matrix computes the total particle time series and cleans it with a filter, produces the graphs for the melting speed, the melting core height and the conductivity (the correlation between the dust and the conductivity profile is also computed) and the 3D graph for the particle dimensional channels for the whole section by averaging the data for each channel for an operator-decided number of sub-sections. A final matrix is then created and saved.

The MATLAB script for reading the ICP-MS files begins with reading and cleaning the matrix. Then a control on the analytical method used is performed. If required, the normalization with internal standards is performed as well as the automatic blank subtraction. By reading the slopes values from a prepared external matrix a complete calibration is performed and the calibration results are shown on the screen. The correlation between the various elements can be easily obtained as well as the smoothed profiles. The concentration matrix is then saved.

The MATLAB script for the SP2 required the previous analyses with the SP2 IGOR based toolkit. The operator decides the beginning and the end of the sample profiles and the corresponding values are computed by the toolkit. A matrix with the preliminary rBC values, the number density and the mean diameter profiles is created with IGOR and saved as a txt file. The MATLAB code reads the matrix and converts the rBC data in concentration by using the flux values recorded by the flow meter. A final matrix is then created and saved.

The author created three more MATLAB codes to compute the complete ice core profiles starting from the profiles of the single sections. In the first part the code reads all the sections matrixes and computes the depth for all the sections by reading the external depth log of the core; finally it saves a matrix for every complete section. At the end the complete profiles are created and visualized. A graph with an element profile and vertical lines corresponding to the beginning and the end of each section allows the operator to check the presence of contaminations or analytical problems at the sections interfaces.

The last code generates a unique file with all the measured profiles in order to search for correlations and similarities.

Table 3.1: The Abakus 32 dimensional channels.

Channel	Particule size (μm)
1	0.8
2	0.9
3	1
4	1.1
5	1.2
6	1.3
7	1.4
8	1.6
9	1.8
10	2
11	2.2
12	2.4
13	2.6
14	2.9
15	3.2
16	3.5
17	3.9
18	4.3
19	4.8
20	5.3
21	5.8
22	6.4
23	7.1
24	7.8
25	8.6
26	9.5
27	10.5
28	11.6
29	12.8
30	14.1
31	15.5
32	80

Chapter 4

The Melting System

4.1 Ice Cores Sections Decontamination and Continuous Analysis

Within the framework of accurate ice core and firn analysis, the thorough decontamination of the core is imperative. Trace elements and ions measurment methods usually prescribe a core decontamination procedure. In fact, the external surface of the ice core encounters many potential sources of contamination during the drilling phase, the bagging and handling, and final storage in cold rooms (C. F. Boutron 1990). In order to remove as much contamination as possible, the external layers are precisely removed by chiselling the surface of the core, usually with pre-cleaned stainless steel blades. Chiselling however, is a procedure with many disadvantages; one of them is that it is time-consuming (especially with very old and fragile ice). Moreover, the blade surface could eventually contaminate the innermost part of the core, and bringing impurities from the external part of the core to the internal one. Another disadvantage of conventional chiseling is the quite low ice samples resolution that can be achieved.

In the last two decades a new technique known as the *ice core continuous melting* has been adopted, resulting in much faster analyses, in a higher decontamination efficiency, and in an unprecedented spatial resolution. The melting system consists of a heated melting head, where the ice is placed. During the melting phase, the water from the external part of the core is continuously separated from the water of the inner part, thus achieving a high level of decontamination. The melting head is structured in such a way as to divide the two water fluxes by having a hole in the middle and others close to the external borders, from where a pumping system pumps the two fluxes. The melting speed depends on the temperature of the melting head, which must be as constant as possible in order to have a linear resolution. It is then possible to couple the melting system with a continuous flow analysis (CFA) system or to a semi-continuous one, or to a discrete auto sampler, or even all of those in concert.

Sigg et al. 1994 and then Röthlisberger et al. 2000, coupled the first melting system device to a tubing system and continuously analysed the concentration in the ice of nitrates, calcium and other analytes. T. M. Huber et al. 2001 performed the first continuous determination of dust particles and in 2001 the first measure of ions by coupling an ion chromatograph to the melting system. M. Leuenberger

Figure 4.1: The Aluminium melting head used in this work.

and C. Huber 2002 measured oxygen stable isotopes ratios in the melted water with an on-line system and in 2003 were also able to determine the hydrogen isotopes ratios with an on-line continuous-flow isotopes ratio mass spectrometry (C. Huber and M. Leuenberger 2003). C. Huber and M. Leuenberger 2005 developed a new technique for the determination in the air extracted from ice cores of nitrogen, oxygen, and argon isotopes ratio.

McConnell, Lamorey, et al. 2002 continuously determined the trace elements concentration in ice cores for the first time. The melted water from the innermost part of the ice core was pumped in a CFA system and measured with an on-line inductive coupled plasma mass spectrometer (ICP-MS). The set of elements analyzed increased in Knüsel et al. 2003, who coupled the CFA system with a sector field mass spectrometry (ICP-SFMS). E. C. Osterberg et al. 2006 coupled a CFA system both with an automated fraction collector and an ICP-MS. A very high-resolution sampling with a high decontamination level was performed. McConnell, Edwards, et al. 2007 measured the black carbon (BC) concentration in an ice core for the first time, coupling the melting system and the CFA system with a water desolvation system and single particle soot photometer (SP2) for atmospheric BC measurement. In order to work directly in field campaigns Kaufmann et al. 2008 redesigned a CFA system to improve its "efficiency and flexibility, signal quality, compactness, and ease of use". Moreover, this system allows for the continuous extraction of air from the melted water flux for gas content analyses. Federer et al. 2008 developed a new method for the continuous on line measurement of total organic carbon (TOC). In Severi et al. 2015 the melting system is coupled with an ion-chromatography working with a very fast method (Cl^-, $NO_3{}^-$, and $SO_4{}^{2-}$ separated by only 1 minute).

4.2 The Aluminum Melting Head

The melting head structure and material are of primary importance in a melting system. The structure must be designed in a way that avoids mixing between the melted water from the external part of the core and that of the inner part while the CFA system is pumping the water. At the same time the whole surface has to be at constant temperature. The material has to be a good thermal conductor, hard enough so that it won't release micro-particles and to have a very smooth surface. Moreover, the chance of having releases and procedural contamination has to be carefully tested.

A new Aluminium melting head was designed and manufactured (Fig. 4.1). The surfaces of the melting head were anodized in order to create a thicker oxide layer.

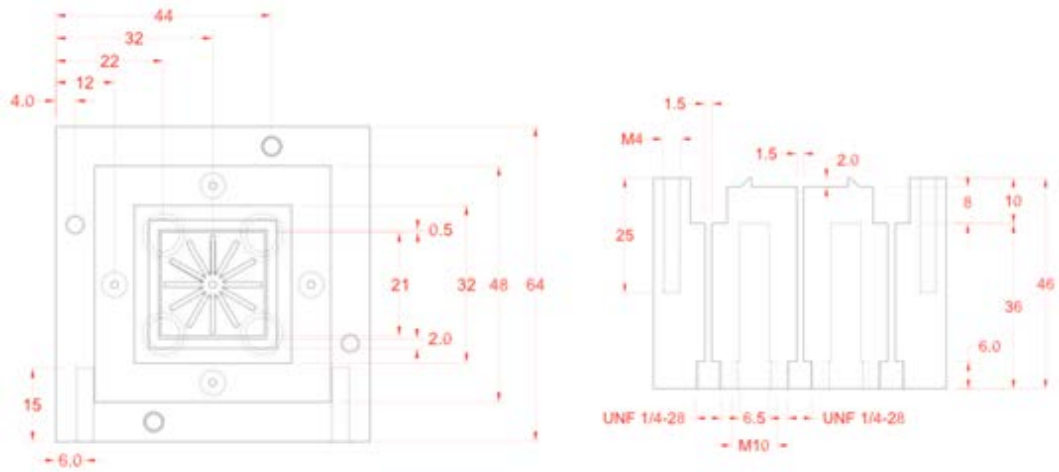

Figure 4.2: Design and dimensions of the melting head.

Figure 4.3: Frontal view of the controller. The *freezer*, *melthead* and *case* temperature sensor displays. On the left: the heating cartridges current display.

The anodizing of the surfaces greatly improves the resistance to wear and corrosion and also to galling due to friction. Aluminium has a high thermal conductivity and its surface is chemically stable, therefore preventing any possible procedural contamination of the sample during the melting phase.

The melting head is placed in a freezer at −20 °C and heated at 25 °C (Delchiaro 2014) by four heating cartridges with a total power of 500 W. The cartridges are inserted in four holes near the center in order to uniformly heat the surface where the core is placed.

The central part has a square shape of $32 \times 32\,\text{mm}^2$ (Fig. 4.2). The core surface dimensions are $32 \times 32\,\text{mm}^2$ and therefore it is completely in touch with the central part of the melt head in order to have a uniform heating.

The water from the innermost part of the core is pumped from the central 1.5 mm hole, which is in the middle of a $21 \times 21\,\text{mm}^2$ surface. In order to avoid mixing with the external water a 2 mm thick and wide layer surrounds the central surface (Fig. 4.2). In this configuration the water from the external 5.5 mm layer of the core flows out in the 8 mm lower area (Fig. 4.1 and Fig. 4.2), where it is pumped from 4 holes of 1.5 mm.

A digital thermostat (PID NTC-PTC) is used to maintain a constant temperature on the surface during the melting (Fig. 4.3, *Melthead*) and it is placed in a self-made temperature console (Fig. 4.3).

The thermostat works with a PID, a control loop feedback mechanism, which automatically maintains the temperature constant. An initial calibration is required: first of all it is possible to fix the selected temperature, and then an automatic calibration is performed during the ice melting. In this way the thermostat

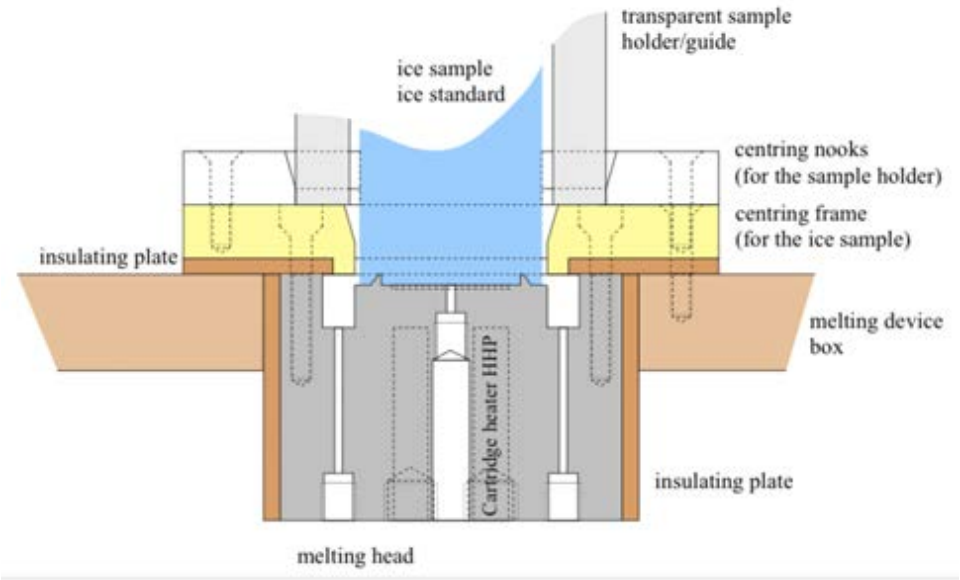

Figure 4.4: Vertical section of the melting head and its position in the box (picture by J. Gabrieli)

Figure 4.5: Connection between the draw-wire sensor cable and the weight in the holder.

is able to maintain the set temperature by increasing the current amplitude in the cartridges at specific time intervals (Fig. 4.3; white display on the left). The temperature console also includes the displays for checking the temperature of the freezer (*FREEZER*) and of the melting device box, where the melting head is placed (*CASE*) (Fig. 4.4). Some heating cables are placed in the internal surface of the box in order to ensure a temperature above 0 °C (about 8 °C).

4.3 The melting rate controller

A draw-wire sensor measured the core's melting rate. The main body of the sensor is placed in the melting device box. A small hole allows the connection of the wire to the pin of the weight placed in the holder above the core (Fig. 4.5).

The sensor signal is read by the ICE software resulting in a height value every second with high precision. The signal was calibrated as a function of the real height of the core when placed over the melting head in order to have the real

height value. An example of the height measurement during a melting phase is reported in Fig. 4.8.

4.4 Peristaltic pump and CFA

PTFE tubes were directly connected to the lowest part of the melting head. The melted water from the 5 holes was pumped by a 12 channels peristaltic pump (ISMATECH, type ISM942).

With a melting head temperature of 25 °C the measured ice melting rate was of (3.2 ± 0.3) cm min^{-1}. The typical ice density is about 0.9 kg/m^3 and with a 3.2 cm min^{-1} melting rate the theoretical water flux from the central channel, with a surface 4.41 cm^2, is 12.7 ml min^{-1}. In order to be sure that the melted water from the external part is not pumped into the central hole it is better to pump less water from it compared to the total available flux. Also in this way, a part of the water from the innermost part overflows the central surface of the melting head. In Delchiaro 2014 a flux of 11.66 ml min^{-1} was pumped with a peristaltic power of 49 % and with a melting speed of 3.2 cm min^{-1} (many tests showed in Delchiaro 2014, were performed together with the author of this work). For this work the fluxes were slightly changed in order to increase the stability of the system and the ability to remove the contaminated water. The pumping speed was maintained at 49 % but the flux from the central part of the melting head was decreased to 9.32 ml min^{-1}, about 27 % less than the total theoretical flux.

Tygon® tubes were used with the peristaltic pump and a set of different internal diameters (I.D.) was chosen. The dimensions of the tubes were chosen as a function of the peristaltic power (in this work 49 %), according to the values reported in Gabrieli 2008. The 9.32 ml min^{-1} flux from the central part of the melting head was obtained by using a tube with I.D.=2.06 mm.

The melted water from the external part of the ice core, as well as the overflow from the central part of the melting head, was pumped by 4 tubes of I.D.=2.54 mm. By using larger tubes it was possible to avoid the lower surface of the melting head to be full of water.

A de-bubbling system was used to remove the air bubbles from the flux from the innermost part of the core. The presence of air bubbles is a critical part for continuous flow systems. If one or more air bubbles reaches the instruments, wrong signals and artifacts are measured, and in the worst scenario, the flux may stop. In this work we used a *triangle* de-bubbler (Fig. 4.6).

The water flux arrives from the hole in the left corner and the bubbles move toward the top due to the buoyancy force. The flux that is pumped out from the hole on the right is less than the incoming one and therefore a part of the flux is lost, together with the bubbles, flowing out from the upper hole. In the configuration used in this work the out-flowing flux was of 8.03 ml min^{-1} (tube with I.D.=1.85 mm), with a sample loss of 1.29 ml min^{-1}, corresponding to about 14 % of the incoming flux.

After the de-bubbling system, the flux arrives at a Teflon® manifold where it is divided in 4 fluxes, one for each *section* of the CFA system. The total scheme of the CFA used in this work is reported in Fig. 4.7.

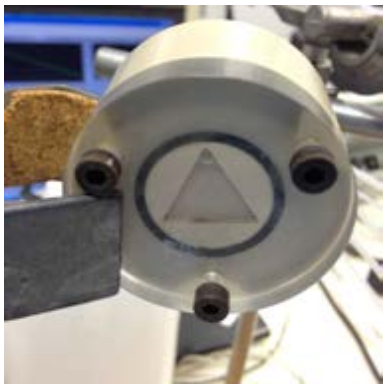

Figure 4.6: The *triangle* debubbler system used in this work.

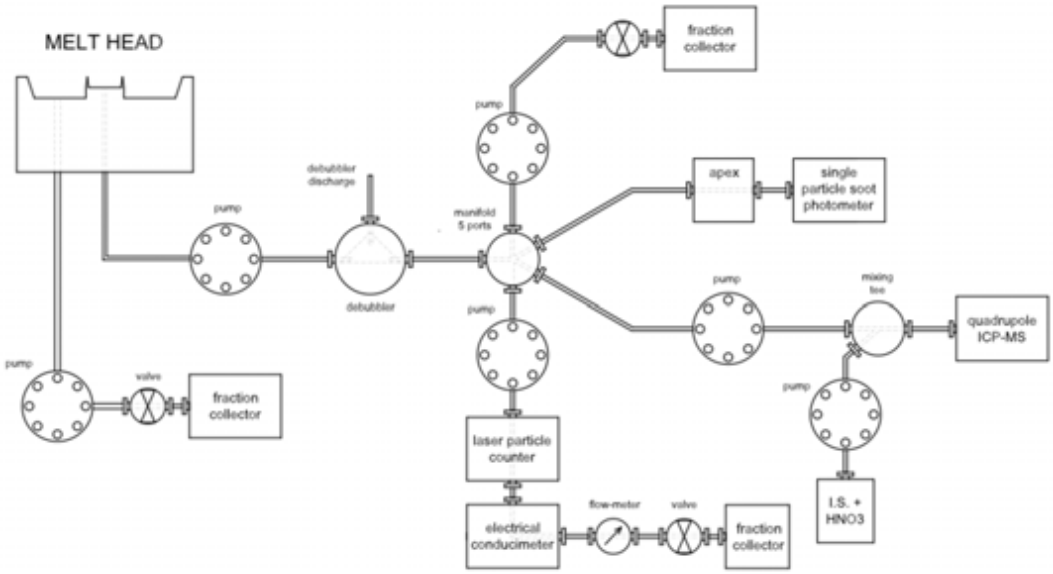

Figure 4.7: The melting and CFA system scheme (credit to J. Gabrieli).

4.4.1 On-line Continuous Analysis with the SP2

One of the 4 out-flow channels from the manifold was dedicated to rBC concentration analysis, with an SP2 (Fig. 4.7). The flux was controlled by an external peristaltic pump (also used for the ICP-QMS channel) set up with a rotation rate 0.06 rpm. By using a tube with I.D.=0.76 mm the flux was 0.2 ml min^{-1}. In order to be able to quantify the rBC content in the samples it is necessary to precisely know the incoming sample flux. For this reason a flow meter (SENSIRION©, SLI-2000) was placed after a Teflon 3 ways connection and the nebulizer unit (not showed in Fig. 4.7). The flux was recorded by the SENSIRION software on an external computer.

The MAINHARD glass nebulizer unit was connected to a compressed air supplier (4 bar) with an incoming air flux of 0.9 L min^{-1}. The compressed air flux allows the nebulizer to take a sample flux of about 60–70 µL min^{-1} from the Teflon connection, and the excess flow is lost in the connection. The out-flowing nebulized sample was injected in the APEX-Q desolvation system in order to remove the water from the sample before the injection in the SP2.

4.4.2 On-line Continuous Analysis with the ICP-QMS

The flux coming from one line was used for continuous ICP-QMS measurement of trace elements. An external peristaltic pump (the same as for SP2 line) and a tube with 0.76 mm of I.D. control the flux: 0.2 ml min^{-1}. The water was pumped to a 3 way Teflon® connection placed in a plastic box. The sample flux was mixed with a solution of 60 % ultra pure nitric acid and an internal standard. In this work the internal standards were Pt and Rh at 25 ng g^{-1}. The bottle and the peristaltic tubes used during the acidification process were previously cleaned with nitric acid solutions.

After the acidification, the samples take about 60 seconds before arriving to the torch and the plasma of the ICP-MS. It is worth remembering that the CFA systems usually underestimate the concentration of crustal elements because the acidification time isn't enough to completely dissolve the particles in the solution Knüsel et al. 2003. However, the acidification of the sample still is an important factor in order to have a high ionization level in the plasma.

4.4.3 Continuous Particles Content, Conductivity and Flux Measurement

The third line after the manifold was characterized by a flux of 2.84 ml min^{-1} (tube of 1.02 mm of I.D.). The melted water flew through 3 instruments before being sampled in pre-clean vials: a flow meter, a particle counter and a total conductimeter.

The melted water particles content was continuously measured with an Abakus® system (see paragrap 3.3). The signal was read by the ICE software (see paragraph 3.7) resulting in a datum every three seconds. 32 dimensional channels were used ranging from (0.8 µm to 80 µm; see Table 3.1).

A conductivity micro volume cell continuously measured the total water conductivity. This instrument is characterized by a very fast response. The conductivity signal was read by the ICE software (see paragraph 3.7) and has a temporal resolution of one datum per second.

The CFA fluxes were manually checked every day before the analytical session. Moreover, during the analyses, the on-line flow meter was crucial in checking the stability of the whole system. A problem in one line, indeed, usually caused a variation in the whole system, and this could be controlled with the flux signal. The sample flux in this line was pretty stable during the analyses (Fig. 4.8).

This line ended at the automatic auto-sampler where samples were collected in pre-cleaned vials (see the Sub-Section 4.4.4). The water from these samples passed through the flow meter, the ABAKUS system and conductimeter and could therefore be contaminated. However, many analyses can be made using these samples, for instance of levoglucosan (a chemical compound used as a proxy for biomass burning; Zennaro et al. 2014).

4.4.4 Discrete Sampling

A line was used solely for the discrete sampling, in order to exclude any possible contamination source. The flux was about of 4.4 ml min^{-1} without the use of the peristaltic pump. The sample was stored in pre cleaned low-density polyethylene

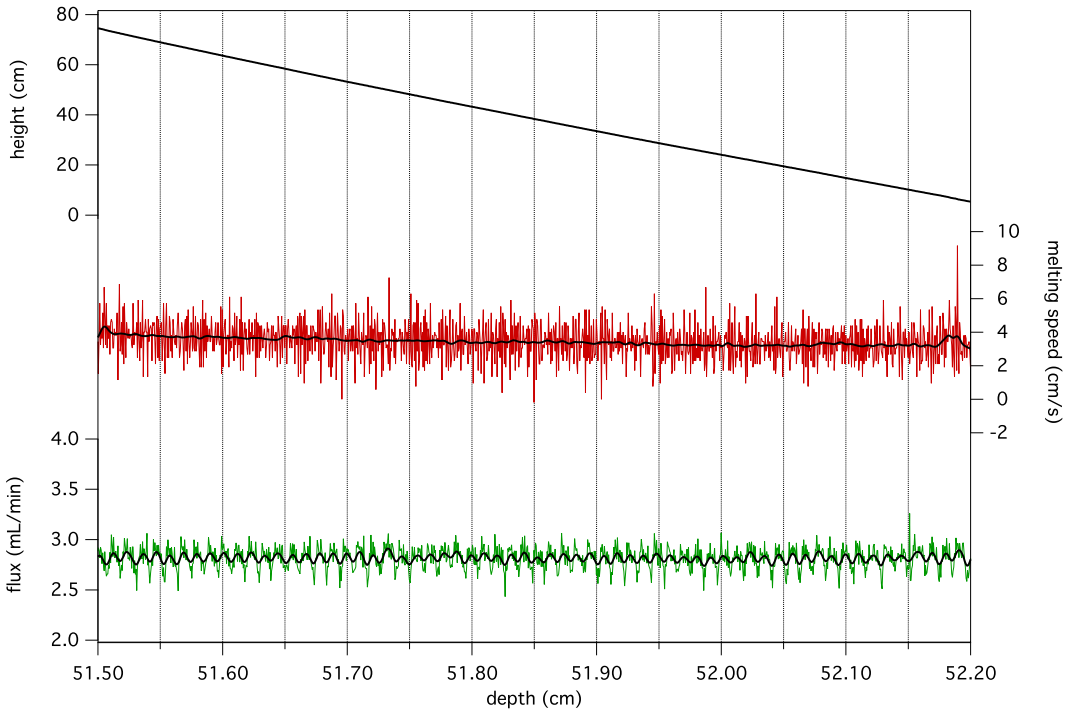

Figure 4.8: An example of the stability of the melting system during the analyses of the sections 73.

(LDPE) vials for further analyses. A part of the discrete samples was later used for ICP-QMS and CRC-ICP-MS discrete analyses. All the vials were previously cleaned by using ultrapure water and sonicated 3 times for 15 minutes each; the water was changed at the end of every sonication cycle.

In this work the LAMBDA OMNICOLL microprocessor-controlled programmable fraction collector-sampler was used. This auto-sampler is quite simple and could easily be used in field campaigns. By making white lines on two black plastic layers the operator can decide the positions of the various steps; the optical sensor detects these lines and defines a *motion* grid. The time between the steps can be set up; in this work a delay of one minute for each sample was selected. In this way a resolution ranging from 6 cm in the firn (it melted faster) and about 3 cm in the core was obtained.

The arrivals of the samples from the direct sampling line and from the flux-ABAKUS-conductimeter line were synchronized. Therefore, the two samples correspond to the same part of the core.

The sampling start is still not automated, thus, the operator should manually start the auto-sampler. This can be easily done by knowing the dead volumes and the corresponding delays of the CFA.

4.5 Ice Core Preparation and Melting Procedure

The Ortles core #1 arrived at the Department Environmental Sciences, Informatics and Statistic of the University of Venice in 2011 and was stored in the cold room at −20 °C. In 2013 the processing phase was started. The core was originally divided into 70 cm long sections, with a diameter of 10 cm and closed in polyethy-

lene plastic film bags. As described above, the part of the core preserved for the CFA analyses was a parallelepiped with section of $3.2 \times 3.2\,cm^2$.

The core preparation procedure followed in this work consisted in cleaning each core section before the CFA analyses. Each surface of the core was scraped with pre-cleaned stainless steel knives to remove the most contaminated ice layers; the knives were cleaned before every section's with a solution of 1 % nitric acid. The top and bottom core surfaces were scraped again with additional cleaned knives; those parts would be directly in contact with the internal part of the melting head. The cleaned section was consequently inserted in the polyethylene holder (Fig. 4.9) closed at its top (the holders where cleaned with ultra pure water after every analyses and carefully dried in the clean room).

A 7 cm long ice parallelepiped made with ultra pure water was placed before the section. If the melting phase consisted only in the melting of one section, a second 7 cm piece of blank core was placed at the end of the holder. Whereas, if more than one section were melted one after the other, the second blank core piece was placed at the end of the last analysed section. The use of blank cores has three main reasons: the first was to give the melting head the time to stabilize its temperature before the real sample; the second was to easily detect the beginning of the sample in the resulting profiles; and the third was to control the blank values before and after the analyses, in order to check instrumental drifts. The part of the core section closer to the glacier surface (TOP) was placed near the open part of the holder, thus being the first to melt. Then the holder was closed with a pre cleaned Teflon® *stopper* (Fig. 4.9) and closed in a polyethylene plastic film bag. The core/cores was/were then brought to the CFA laboratory and placed in the freezer.

A 250 g stainless steel and polyethylene weight was placed on the top of the core in the holder and connected by a pin to the melting rate device (Fig. 4.5). The weight applied to the core was crucial for stabilizing the melting speed.

A new system of valves was placed near the peristaltic pump (by the author) and all of the CFA system was constantly filled with ultra pure water in order to remove contaminants in the tubes and in the debubbling system. This procedure was repeated until the various instruments detected satisfactory blank levels. Moreover, the melting head was rinsed with ultrapure water and then connected with the whole CFA system. Usually, the melting head, the CFA system and the tubes were clean after ten to twenty minutes. A 70 cm blank core was melted and analysed every morning in order to verify the stability and proper cleaning of the system.

Once the whole system was cleaned, the holder was placed on the brand new polyethylene support (proposed and studied by the author) and fixed in the upper part with a polyethylene support. When everything was ready and the instruments were already acquiring data the stopper was removed and the core was gently placed on the melting head. During the melting of the very first part of the blank core the tube from the melting head to the valve was filled and at the same time ultrapure water from a bottle was injected in the CFA system. Then, after the tube was completely filled, the two valves were turned in such a way as to stop the injection of the ultrapure water and let the melted water flow in the system, and most importantly, without any air bubbles.

The auto-sampler was then turned on after the first conductivity signal, according to the CFA timings. If more than one section were melted consecutively the

Figure 4.9: The holder in the freezer filled with a core section placed on the melting head.

second/third holder was placed on the new polyethylene support before the ending of the previous section. The core was then gently placed on the remaining part of the melting section.

Fig. 4.9 shows the holder with the weight on it and the stopper closed. A polyethylene support is placed on the surface of the melting device box: this is a brand new device built up for this work. It allows for the melting of more than one core consecutively, thus saving both analysis and data processing time.

Chapter 5

Method Validation

5.1 Continuous SP2 Analysis

5.1.1 The SP2 Calibration

rBC particles absorb the laser radiation and get heated up to 4000 K before vaporizing, because of their high refractoriness. Once heated the rBC particles become incandescent and emit infrared (IR) radiation following the Plank's black body emission curve.

Two different calibrations are needed to determine the rBC concentration and the scattering signal. The scattering calibration was performed for this work but the scattering signal is not useful for snow and ice samples.

A complete description of the theory at the base of the SP2 functioning is described in Stephens et al. 2003 and in Moteki and Kondo 2007, Moteki and Kondo 2010. The main result is that, when heated by the laser absorption, the intensity of an rBC particle incandescence signal is linearly proportional to the volume of the rBC particle core.

The calibration is needed in order to parametrize the relation between the height of the incandescence peak signal, PkHtInc, (which is proportional to the measured laser induced incandescence signal) and the rBC particle mass. The calibration is performed by measuring the incandescence signal while injecting in the SP2 rBC particles with different mobility diameters. The effective density of the reference calibration material has to be known in order to compute the particle mass from the mobility diameter (volume). A monodisperse *fullerene* soot (Alpha Aesar; #FS12S011) was used for incandescence calibration (Baumgardner et al. 2012; Gysel et al. 2011; Laborde et al. 2012; Moteki, Kondo, et al. 2012). A differential mobility analyzer (DMA) was used to select the fullerene soot particles diameters before entering in the SP2. The corresponding masses were computed by knowing the density of the fullerene soot (Gysel et al. 2011). An example of a linear calibration curve for the incandescence signal obtained with the fullerene soot is shown in Fig. 5.1.

The calibration covered a mass equivalent diameter range from 60 to 620nm, covering the 80–90% of the rBC particles in snow and ice samples (Lim, Fain, Zanatta, et al. 2014). The SP2 is a single particle soot photometer and therefore it detects every single rBC particle in a certain dimensional range and with a mass above 0.3–1fg.

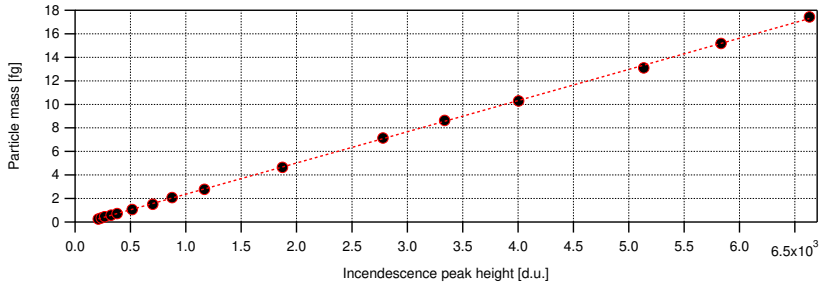

Figure 5.1: An example of a calibration curve performed using diameter selected fullerene soot.

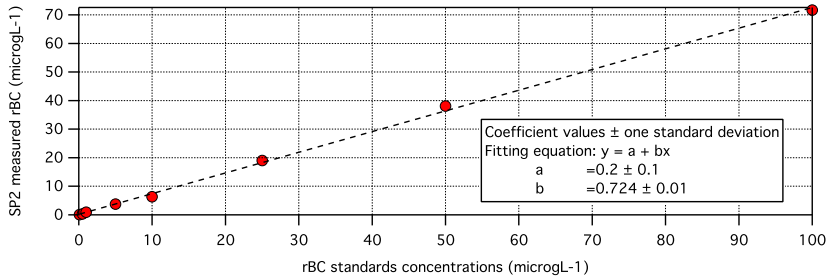

Figure 5.2: An example of the APEX-Q calibration curve.

The SP2 calibration is performed before the analysis period and it isn't supposed to change (unless the instrument is not physically displaced or damaged).

5.1.2 The APEX-Q Calibration

The SP2 analyses on snow and ice samples require a de-solvation system. In this work the APEX-Q system was used according to Lim, Fain, Zanatta, et al. 2014. The linearity of the nebulization efficiency as a function of the rBC concentration was checked before each analytical session. The reference calibration material was the Aquadag® (AQ, Acheson Inc., USA), *an aqueous colloidal dispersion of ultra fine graphite powder* (Lim, Fain, Zanatta, et al. 2014). A stock solution was prepared in a pre-cleaned polypropylene 50 ml vial with an rBC concentration of 10 000 ng g^{-1} (in this work the elemental carbon effective content in the AQ measured by Lim, Fain, Zanatta, et al. 2014 was used).

The stock solution was sonicated for 15 minutes and diluted to prepare the rBC standards at the following concentrations: 0.1, 0.5, 1, 5, 10, 25, 50 and 100 ng g^{-1}. In order to measure the incandescence signal also the SP2 was calibrated with an AQ disperse solution following the same procedure as with the fullerene soot. The aerosolification efficiency of the APEX-Q was constant and linear during the analyses period (Fig. 5.2).

5.1.3 Detection Limit

The APEX-Q can accumulate dust and rBC particles on the heating and cooling glass surfaces. Therefore, a complete cleaning of the system is necessary after any intense utilization. A 2 % solution of supra pure nitric acid was nebulized in the

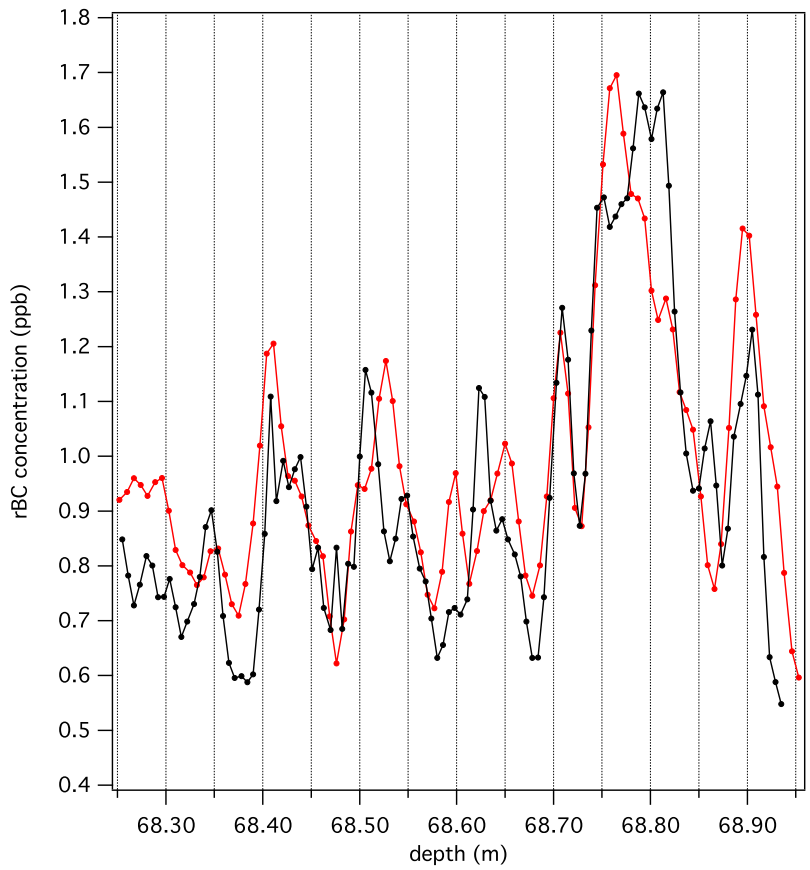

Figure 5.3: Comparison between the continuous rBC measurement of two parallel ice core sections.

APEX-Q for at least 30 minutes and after that a 30 minutes rinse with ultrapure water was performed.

The SP2-APEX-Q detection limit was calculated by averaging the rBC signal of ultrapure water. The measured detection limit was 0.01 ng g^{-1} (with a corresponding limit of quantification of 0.03 ng g^{-1}), the same results as in Lim et al., 2016.

5.1.4 Reproducibility

The reproducibility of the continuous SP2 analyses was verified by melting two parallel Ortles core sections (98 and 98B) with a length of about 70 cm. The two measurements were done in two different analytical sessions. The two measurements were in a very good agreement (Fig. 5.3) as well as for the mass equivalent diameter measurements (not shown).

5.2 Continuous ICP Analyses

5.2.1 The ICP Calibration

The ICP-QMS calibrations were performed using a time resolved analysis method. The standards solutions flowed into the same T connection used for the ice core analysis and therefore, the same mixing ratio between standards and nitric acid/IS

Table 5.1: The ICP-QMS continuous calibration scheme.

Time (min)	Solutions
15	Ultra pure water
10.00	2 % nitric acid washing solution
10.00	blank standard
5.00	IMS-101 standard 1
5.00	IMS-101 standard 2
5.00	IMS-101 standard 3
5.00	IMS-101 standard 4
5.00	IMS-101 standard 5
5.00	CRUSTAL standard 1
5.00	CRUSTAL standard 2
5.00	CRUSTAL standard 3
10.00	blank standard
5.00	CRM
10.00	2 % nitric acid washing solution
15	Ultra pure water

solution was obtained. A polyethylene plastic box kept the standards and the reference solution vials in a clean environment and allowed the simple transition from calibration to analysis mode. The standards solutions were injected from the calibration box into the CFA system before the mixing tee (Fig. 4.7); in this way the CFA contamination from the standards solutions was limited. The standards were similar to those used in Gabrieli 2008, but a concentration standard solution and a certified reference material (CRM; $TM - RAIN_04$; Environment Canada) were added. The procedural scheme of the ICP-QMS calibration is reported in Table 5.1.

The standards solutions were prepared in a clean environment in order to avoid the standards contamination. In this work five standards solutions were prepared using the IMS-101 multi elemental standard solution. A concentrated mother solution was prepared for crustal elements (Na, Mg, Al, K, Ca, Ti, Fe, Ba) by using single element standards and a solution of 2 % nitric acid and ultrapure water (this solution was used as the blank standard). The analytical ranges are shown in Table 5.2.

The resulting file of the calibration were analysed by a Matlab® code. The average values were computed for all the standards. The blank standard average value was subtracted from all the other signals. The calibration slopes were computed by a linear regression method (Table 5.2).

All the calibration curves were linear, as shown by the R^2 values (Table 5.2). Only the Ni calibrations were not accurate, probably due to an instrumental problem; the Ni profiles were therefore rejected. Cu blank values were too high during some runs and the corresponding measurements were rejected.

5.2.2 Procedural Blanks

The procedural blank was checked before every analytical session. Ultrapure water from the calibration box was continuously analysed by the ICP-QMS bypassing the

Table 5.2: ICP-QMS continuous calibration results: Element, analytical range, slope (*cps* means *counts per second*) and the regression coefficient.

Element	Analytical range (ng g^{-1})	Concentrations (ng g^{-1})	Slope (ng g^{-1} cps^{-1})	R^2
Li	0.005–10	0.005, 0.025, 0.1, 1, 10	3526	0.999
Na	1–100	5, 10, 50, 100, 250	8698	0.986
Mg	1–100	5, 10, 50, 100, 250	4928	0.984
Al	1–100	1, 10, 25, 50, 100	7028	0.991
K	1–100	1, 10, 25, 50, 100	34 309	0.985
Ca	1–100	5, 10, 50, 100, 250	121	0.987
Ti	1–100	1, 10, 25, 50, 100	638	0.986
V	0.005–10	0.005, 0.025, 0.1, 1, 10	7249	0.994
Mn	0.005–10	0.005, 0.025, 0.1, 1, 10	7972	0.999
Fe	1–100	1, 10, 25, 50, 100	192	0.986
Co	0.005–10	0.005, 0.025, 0.1, 1, 10	6281	0.974
Cu	0.005–10	0.005, 0.025, 0.1, 1, 10	3120	0.979
Zn	0.005–10	0.005, 0.025, 0.1, 1, 10	1131	0.998
Rb	0.005–10	0.005, 0.025, 0.1, 1, 10	6469	0.999
Sr	0.005–10	0.005, 0.025, 0.1, 1, 10	8806	0.998
Ag	0.005–10	0.005, 0.025, 0.1, 1, 10	3532	0.999
Cd	0.005–10	0.005, 0.025, 0.1, 1, 10	748	1.000
I	0.005–1	0.001, 0.025, 0.05, 0.1, 1	1253	0.999
Ba	0.005–10	0.005, 0.025, 0.1, 1, 10	1116	0.999
Tl	0.005–10	0.005, 0.025, 0.1, 1, 10	5269	1.000
Pb	0.005–10	0.005, 0.025, 0.1, 1, 10	4039	0.999
Bi	0.005–10	0.005, 0.025, 0.1, 1, 10	6466	0.999
U	0.005–10	0.005, 0.025, 0.1, 1, 10	7977	1.000

melting head. Then ultrapure water was continuously poured on the melting head and pumped in the CFA system. The procedure was repeated until the same blank level was obtained with both the procedures.

Blank cores were melted following the ice core melting procedure and again the melted water was continuously analysed. None of these tests revealed contamination levels higher than the DL of the ICP-QMS. The contamination values were lower than the Ortles core average concentrations (Table 7.1). The only possible source of contamination could have been from the first surface of the blank core before the real sample. After the cleaning of the melting head and before the placing of the core it may happen that some dust particles can be deposited on the melting head. However, the first part of the melted water from the blank core was always flushed out of the system before the opening of the CFA valve.

5.2.3 Detection Limit

The continuous ICP-QMS detection limits (DL) were computed as three times the standard deviation of the blank.

The DL values for the continuous flow measurements are reported in Table 5.3. The DL values were higher than the procedural blanks.

Table 5.3: Instrumental *detection limit* during the CFA analyses.

Element	DL ($ng\,g^{-1}$)
Li	0.04
Na	1
Mg	0.2
Al	0.2
K	1
Ca	16
Ti	0.09
V	0.01
Mn	0.03
Fe	5
Co	0.01
Cu	0.06
Zn	0.1
Rb	0.02
Sr	0.004
Ag	0.01
Cd	0.05
I	0.05
Ba	0.03
Tl	0.006
Pb	0.01
Bi	0.005
U	0.004

The decontamination efficiency test was not performed in this work but in Gabrieli 2008 with a very similar experimental set up. The cores were always closed in clean plastic polyethylene bags and they were exposed to air only under a laminar flow bench during the cutting phase. Contaminations were not observed in the melted water from the innermost part of the core exposed to unfiltered air in the freezer (test not recorded).

5.2.4 Accuracy and Precision

The accuracy and precision of the ICP-QMS system connected with the calibration box was checked during every calibration. The reference material used in this work was certified reference rainwater, CRM TM-RAIN04 (National Water Research Institute of Environment Canada). The concentration of 23 elements was given within a specified confidence interval (Table 5.4).

The recovery of the system ranges from 80 (for Na) to 117 (for Bi) (Table 5.4). Usually the recovery values were constant in the different calibrations within a 10 % interval. The recovery values for K showed significant variations from the reported value and the cause is still not clear.

Table 5.4: Comparison between the TM-RAIN04 certified element concentration and the results obtained with the ICP-QMS.

Element	TM-RAIN04 (ng g^{-1})	This work (ng g^{-1})	Recovery (%)
Li	0.51 ± 0.14	0.50 ± 0.06	98
Na	90 (NC)	72 ± 5	80
Mg	170 (NC)	178 ± 18	105
Al	2.03 ± 0.76	2.10 ± 0.15	103
K	40 (NC)	7 ± 2	18
Ca	660 (NC)	636 ± 39	96
Ti	0.52 ± 0.15	0.42 ± 0.14	81
V	0.68 ± 0.09	0.74 ± 0.05	109
Mn	6.7 ± 6.7	7.0 ± 0.4	104
Fe	24.6 ± 4.1	21.8 ± 7.4	89
Co	0.25 ± 0.06	0.27 ± 0.02	108
Cu	7.04 ± 0.82	7.56 ± 0.38	107
Zn	8.40 ± 2.38	7.97 ± 0.49	95
Rb	0.03 (NC)	0.03 ± 0.01	100
Sr	1.82 ± 0.28	1.87 ± 0.08	103
Ag	ND	0.02 ± 0.02	ND
Cd	0.52 ± 0.06	0.56 ± 0.09	108
I	ND	0.22 ± 0.01	ND
Ba	0.87 ± 0.12	0.98 ± 0.09	113
Tl	0.38 ± 0.07	0.41 ± 0.03	108
Pb	0.35 ± 0.07	0.35 ± 0.03	100
Bi	0.6 (NC)	0.68 ± 0.05	117
U	0.29 ± 0.03	0.29 ± 0.02	100

5.2.5 Reproducibility

Two parallel Ortles core ice sections were continuously analysed (sections 93–94) in order to check the reproducibility of the CFA system results. The two analyses were performed with a temporal difference of more than one month. The concentration profiles of Pb, Sr and Na of the two sections are shown in Fig. 5.4. All the elements generally show a good reproducibility, therefore confirming the reproducibility of the whole CFA system.

5.3 Discrete ICP-QMS and CRC-ICP-MS Analysis

5.3.1 Calibration

The calibration of the ICP-QMS was performed by using the same standards used for the continuous analyses but adding the standards solutions for Sb, Te, Bi, and Hg (Table 5.5). The Sb, Te and Bi standard solutions were prepared by using a multi-elemental standard solution (1000 ng g^{-1}). The Hg standard was a single element standard (10 000 ng g^{-1}).

During the calibration and the analyses the Xe concentration was monitored

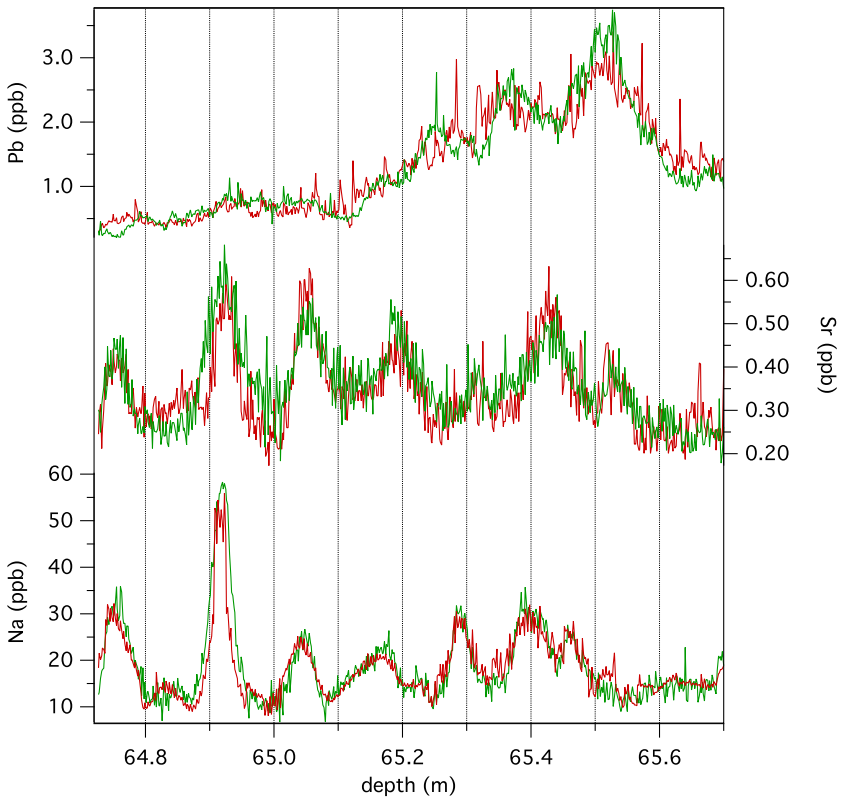

Figure 5.4: Pb, Sr and Na profiles for two parallel Ortles core sections (green and red lines).

in order to control the plasma stability and to verify contaminations from the gas line. During all the analytical sessions the Xe concentration was stable.

The list of the analyzed elements, the analytical range, the slope (computed by a linear regression) and the root mean squared is showed in Fig. 5.5.

5.3.2 Detection limit

The detection limit was computed as three times the standard deviation of a long series of blank solutions with a 2 % ultrapure nitric acid.

The measurement made by the Q2 ICP-QMS in discrete mode resulted in lower DL values for all the elements. This is probably due to a higher cleaning level and to a higher stability of the system. The DL for the selected elements is reported in Table 5.6.

5.3.3 Accuracy and Precision

The accuracy and precision of the ICP-QMS in the discrete analysis method was checked by using a certified reference material: CRM-TM-RAIN04 (National Water Research Institute of Environment Canada). The recovery ranged from 84 of Na to 143 of Al and all the elements were in agreement with the CRM values (Table 5.7).

Table 5.5: Discrete ICP-QMS measured elements and DLs.

Element	Analytical range (ng g^{-1})	Concentrations (ng g^{-1})	Slope (ng g^{-1} cps^{-1})	R^2
Li	0.005–10	0.005, 0.025, 0.1, 1, 10	42 022	0.999
Na	1–100	5, 10, 50, 100, 250	25 723	0.997
Mg	1–100	5, 10, 50, 100, 250	15 109	0.996
Al	1–100	1, 10, 25, 50, 100	18 421	0.953
K	1–100	1, 10, 25, 50, 100	17 091	0.999
Ca	1–100	5, 10, 50, 100, 250	59	0.999
Ti	1–100	1, 10, 25, 50, 100	2184	0.999
V	0.005–10	0.005, 0.025, 0.1, 1, 10	25 509	0.999
Cr	0.005–10	0.005, 0.025, 0.1, 1, 10	22 136	0.998
Mn	0.005–10	0.005, 0.025, 0.1, 1, 10	38 862	0.999
Fe	1–100	1, 10, 25, 50, 100	941	0.999
Co	0.005–10	0.005, 0.025, 0.1, 1, 10	35 207	0.999
Cu	0.005–10	0.005, 0.025, 0.1, 1, 10	24 278	0.999
Zn	0.005–10	0.005, 0.025, 0.1, 1, 10	5152	0.998
As	0.005–10	0.005, 0.025, 0.1, 1, 10	3869	0.998
Se	0.005–10	0.005, 0.025, 0.1, 1, 10	569	0.990
Sr	0.005–10	0.005, 0.025, 0.1, 1, 10	42 321	0.999
Ag	0.005–10	0.005, 0.025, 0.1, 1, 10	29 793	0.999
Cd	0.005–10	0.005, 0.025, 0.1, 1, 10	4709	0.999
Sb	0.005–5	0.001, 0.01, 0.1	14 734	0.997
Te	0.005–5	0.001, 0.01, 0.1	805	0.997
I	0.005–1	0.001, 0.025, 0.05, 0.1, 1	16 737	0.995
Cs	0.005–10	0.005, 0.025, 0.1, 1, 10	52 551	0.999
Ba	0.005–10	0.005, 0.025, 0.1, 1, 10	6672	0.999
Hg	0.001–0.015	0.0005, 0.001, 0.015	7296	0.998
Tl	0.005–10	0.005, 0.025, 0.1, 1, 10	60 575	1.000
Pb	0.005–10	0.005, 0.025, 0.1, 1, 10	45 553	0.999
Bi	0.005–10	0.001, 0.01, 0.1	6466	0.999
U	0.005–10	0.005, 0.025, 0.1, 1, 10	105 712	0.999

5.3.4 Continuous Particle Content and Conductivity Measurement

Both the ABAKUS system and conductivity micro-cell do not require calibration. A correction factor should be applied to the ABAKUS system in order to have more realistic data. A comparison between samples measured both with a Coulter Counter and ABAKUS could give the calibration factor. However, only a more precise number of particles value would be obtained, but the conversion from number of particles to mass would still not be possible.

The DL for the ABAKUS and for the conductimeter was lower than the Ortles minimum values. The measured values during the cleaning of the CFA system by using ultrapure water were from 0 to 5 for the number of particles and 0.02 µS for the conductimeter. Their time response in the CFA system was very short (short variations in Fig. 5.5).

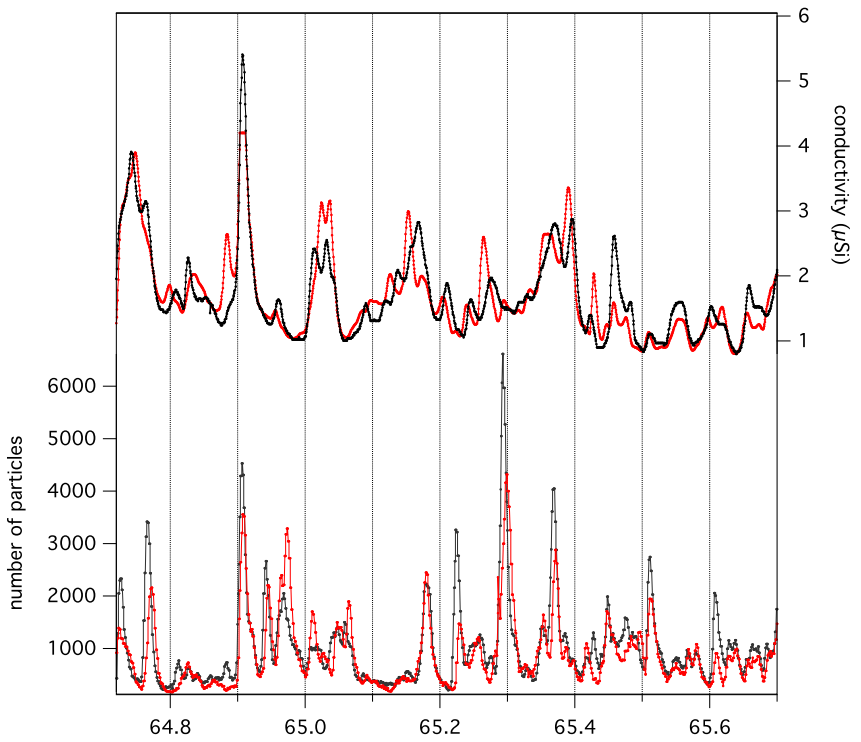

Figure 5.5: Reproducibility of the continuous particle content and conductivity measurement. Results from the melting of two parallel core sections.

5.3.5 Repeatability

The repeatability was controlled by melting two parallel Ortles ice core sections (93–94 and 93B-94B) in two different analytical sessions. Both the particles number and the conductivity measurements were in excellent agreement in the two profiles (Fig. 5.5).

5.3.6 Discrete IC and dust content measurements

The samples from the Ortles snow pit 2015 were analysed for ions and total dust at the LGGE of Grenoble (France).

The detection limit of ion chromatography was below 1 ppb. The accuracy of the system was checked by using six standard calibrations and the relative standard deviation was less than 2 % for all measured compounds.

The analytical precision was controlled by measuring the standard deviation of multiple analyses of the same standard. The standard deviation was less then 2 %.

The Coulter Counter method that was followed has already been described and validated in Delmonte et al. 2002.

Table 5.6: ICP-QMS and CRC-ICP-MS *detection limit* for the discrete analyses' analytical sessions.

Element	DL ($ng\,g^{-1}$)
Li	0.001
Na	3
Mg	0.01
Al	0.017
K	4
Ca	1
Ti	0.006
V	0.001
^{52}Cr	0.007
^{53}Cr	0.009
Mn	0.001
Fe	1.5
Co	0.001
Cu	0.006
Zn	0.006
As	0.03
Se	0.01
Sr	0.001
Ag	0.001
Cd	0.001
Sb	0.001
Te	0.01
I	0.002
Cs	0.001
Ba	0.002
Hg	0.0005
Tl	0.001
Pb	0.001
Bi	0.001
U	0.001

Table 5.7: ICP-QMS analyses of CRM-TM-RAIN04. Comparison between certified and measured data and the instrumental recovery.

Element	TM-RAIN04 (ng g^{-1})	This work (ng g^{-1})	Recovery (%)
Li	0.51 ± 0.14	0.53 ± 0.01	102
Na	90 (NC)	76 ± 2	84
Mg	170 (NC)	183 ± 55	108
Al	2.03 ± 0.76	2.9 ± 0.8	143
K	40 (NC)	34 ± 1	85
Ca	660 (NC)	671 ± 20	102
Ti	0.52 ± 0.15	0.54 ± 0.02	104
V	0.68 ± 0.09	0.72 ± 0.01	106
Cr	0.88 ± 0.18	0.93 ± 0.02	106
Mn	6.7 ± 6.7	7.0 ± 0.2	104
Fe	24.6 ± 4.1	28.22 ± 0.08	115
Co	0.25 ± 0.06	0.267 ± 0.006	107
Cu	7.04 ± 0.82	7.45 ± 0.15	106
Zn	8.40 ± 2.38	8.23 ± 0.39	98
As	1.14 ± 0.18	1.14 ± 0.02	100
Se	0.84 ± 0.27	1.12 ± 0.03	133
Sr	1.82 ± 0.28	1.92 ± 0.04	105
Ag	ND	0.007 ± 0.001	ND
Cd	0.52 ± 0.06	0.63 ± 0.01	121
Sb	0.35 ± 0.08	0.4 ± 01.2	114
Te	ND	<DL	ND
I	ND	0.18 ± 0.05	ND
Cs	ND	<DL	ND
Ba	0.87 ± 0.12	0.91 ± 0.02	105
Hg	ND	0.006 ± 0.003	106
Tl	0.38 ± 0.07	0.43 ± 0.01	113
Pb	0.35 ± 0.07	0.373 ± 0.007	107
Bi	0.6 (NC)	0.64 ± 0.02	107
U	0.29 ± 0.03	0.313 ± 0.006	108

Part II

Results and Discussion

Chapter 6

The Alto dell'Ortles Glacio-Chemical and Radiative Response to the Warm Summer of 2015

6.1 Introduction

During the last three decades the surface air temperature of the Alpine region has grown by 2 °C (Auer et al. 2007), this increase is greater than the global average of 0.85 °C (Hartmann et al. 2013 in T. F. Stocker et al. 2013). The Alpine region has been included in the EU White Paper on Adaptation (COM 2009) as the most affected and vulnerable to climate change in Europe. This temperature increase has led to a widespread and intense glaciers shrinking of the alpine glaciers, especially in the Eastern part of the Alps (Carturan, Filippi, et al. 2013, Carturan, Baroni, et al. 2013).

An Automatic Weather Station (AWS) was installed close to the top of the Alto dell'Ortles glacier (3905 m, South Tyrol, Autonomous Province of Bolzano, Italy) for the period 2011-2015 and obtained a continuous record of temperatures with hourly resolution. The summer of 2015 was amongst the warmest of the last 150 years by considering the reconstructed temperature dataset for this location (Gabrielli, Carturan, et al. 2010). Particularly, during the month of July temperatures well above zero characterized 23 of 31 days. During this period a strong surface melt and accumulation of dust was observed.

The emissions pollutants in the atmosphere from natural and anthropogenic sources influence the climate system and the cryosphere. The evaluation of emissions intensity is of great interest, both from an air quality point of view, and from the impacts of the aerosols on the glacier's snow radiative properties (Oerlemans et al. 2009, Ginot, Dumont, et al. 2014). The wet and dry aerosol deposition on the surface snow causes a reduction of the Albedo, and therefore increases the radiative absorption at different wavelengths (S. Warren 1984). The amount of deposited aerosol and dust particles influences snow absorption of solar radiation and increases the melting rate, thus affecting the glacier's mass balance (B. Xu et al. 2009, Gabbi et al. 2015 and reference therein).

Europe was one of the highest black carbon emitters in 1950, but a great reduc-

tion in coal combustions and improvement in technology caused a strong reduction of about 95% of emissions in 2000; the reduction was mainly due to a sectoral shift (-82%), an improvement of emissions for the industry (-12%) and from the power sector (-24%) (T. C. Bond, Bhardwaj, et al. 2007).

The trace element analyses of glacier snow can be used to reconstruct the anthropogenic emission in the surrounding area and the natural background level (Barbante, Gabrieli, et al. 2011, Hong, K. Lee, et al. 2009, Uglietti, Gabrielli, Cooke, et al. 2015, Gabrielli and Vallelonga 2015). Particularly, the Alpine glaciers locations are usually close to cities and valleys characterized by a high number of inhabitants and industrial production activities. As reported in Schwikowski, Barbante, et al. 2004 the efficacy of the European policies can be directly checked by knowing the concentrations of pollutants in the glaciers during the last centuries and after their implementation; the Lead concentration in Colle Gnifetti ice core greatly decreased after the European policy forbidding its use in gasoline as an anti-knock agent (Schwikowski, Barbante, et al. 2004, Gabrieli and Barbante 2014).

For the first time, Van de Velde, C. Boutron, et al. 1998 analysed the trace elements concentration in an Alpine ice core from the Western European Alps; particularly, an ice core of 140 m in length was drilled from the Dome du Gouter (4304 m, Mt. Blanc Massif). The seasonal concentration of Pb, Zn, Cu, Cd, Bi, Mn and Al was determined only for the period 1960-68; the whole ice core was then analyzed for the concentration of Co, Cr, Mo, Sb (Van de Velde, Ferrari, et al. 1999) and Au, Ag, Pt, Pd and Rh (Van de Velde, Barbante, et al. 2000) covering the period from 1780-1990. The U concentration profile was analyzed in the same core and discussed in Barbante, Van De Velde, et al. 2001. An ice core drilled in 1982 on Colle Gnifetti (4450 m, Monte Rosa), covering the period 1650-1994, was analyzed for the concentration of Cr, Cd, Zn, Co, Ni, Mo, Rh, Pd, Ag, Cd, Sb, Bi, Pt, Au, U (Barbante, Schwikowski, et al. 2004). The same ice core was analyzed for the concentration of Pb (Schwikowski, Barbante, et al. 2004). Two more 80 m deep ice cores were drilled at Colle Gnifetti in 2003, covering the last 10.000 years, and were analyzed by mean of a continuous flow analyses system for more then 23 trace elements (Gabrieli 2008).

Few analyses related to the trace elements content in seasonal snow were published for the European Alpine region. Gabrielli, Cozzi, et al. 2008 performed a statistical description for trace elements concentration in winter snow from the Eastern Alps with altitude ranges from 1000 m to 3000 m. Veysseyre et al. 2001 analyzed heavy metals in fresh snow samples from the area around Chamonix (France), close to Mt. Blanc. On the Mt. Ortles superficial snow dust, total organic carbon (TOC), trace elements and major ions concentration were analyzed in a 4.5 m snow pit, covering the 2007 and 2009 years (Gabrieli, Carturan, et al. 2011).

Only a few ice cores in the Alpine region were analyzed for carbon soot components. Particularly, the elemental carbon (EC) concentration from an ice core drilled at the Colle Gnifetti, revealed a large increase during the mid 19th century until 1980 (Thevenon et al. 2009). A sharp increase was observed in the EC after the World War II in a Col du Dome ice core (Legrand, Preunkert, Schock, et al. 2007). Snow pit samples from the Col du Dome glacier were analyzed for refractory black carbon (rBC) during a methodology comparison (Lim, Fain, Zanatta, et al. 2014). At the best of our knowledge this is the first study of (rBC) fluxes on a high altitude glacier of the Eastern European Alps.

Ionic compounds were studied in several ice cores and surface snow samples from the Alpine region. The first long reconstruction was done by analyzing ice core from the western Alps, at Col du Dome (Preunkert et al. 2000). In 2004 ionic compounds were studied in two ice cores from the Monte Rosa massif, from the Grenzgletscher (Eichler, Schwikowski, Furger, et al. 2004), and from Fieschrnhorngletscher in the Bernese Alps (Eichler, Schwikowski, Furger, et al. 2004). Later, ionic compounds were analyzed in ice cores from the Colle Gnifetti (Monte Rosa massif) in 2006 and 2009 (Bolius 2006; Sigl 2009). In 1998 the surface snow of the Careser glacier, the Stubai glacier and the Sonnblick were analyzed for ionic compounds concentrations (Novo and Rossi 1998; Kuhn et al. 1998, Puxbaum and Tscherwenka 1998).

In this study, 78 samples from a 234 cm snow pit dug at the end of August of 2015 on the Alto dell'Ortles glaciers were analyzed for rBC, dust content, $\delta^{18}O$, δD, deuterium excess, a large set of trace elements, rare Earth elements and ionic compounds. The effects of the extraordinary warm summer of 2015 and of the intense snow melting and percolation will be studied in order to verify the presence of a preserved seasonality in climate and environmental signals. The radiative effect of the rBC and of the dust content will be computed and the elemental concentrations will be compared with the previous results for the Alto dell'Ortles glacier; the Po Valley as principal aerosol source will be checked again (Gabrieli, Carturan, et al. 2011). The intense aerosol deposition and concentration during July and August of 2015 would be useful in order to evaluate the results from the deep ice cores drilled in 2011.

6.2 Methods

6.2.1 Study Area

The snow samples were taken on the Alto del'Ortles glacier (46°30′32″N, 10°32′41″E), on the 31st of August 2015. The sampling glacier and its geological profile are described in details in the Chapter 2.2 of this study.

6.2.2 Sampling Method

The samples were collected by following the clean sampling procedure described in Planchon et al. 2003. A slab of LDPE was used to remove at least 5 cm of snow after digging, that were potentially contaminated by the shovels, before sampling the snow wall. The slab and the LDPE bottles used for sampling were pre-cleaned with a diluted solution of ultra-pure HNO_3^- (Ultrapure grade, Romil, Cambridge, UK). A final rinse with ultra-pure water (Purelab Ultra Analytic, Elga Lab Wa- ter, High Wycombe, UK) was performed after cleaning with the acid. During sampling the operator wore a complete clean-suite for cleaning samplings and polyethylene gloves.

The 3 cm samples were obtained by inserting the LDPE vials perpendicularly in the snow wall, removing them and closing them immediately after. The vials were numbered, stored in two plastic bags and preserved frozen. The samples were then brought to the cold room (−20 °C) at the University of Venice. The melted samples water was from 15 ml to 40 ml depending of the density of the snow. A parallel

sampling was done for for stable water isotopes and pollen analyses (ongoing research).

The stratigraphy of the snow pit was performed and the snow physical parameters (snow stratigraphy, density, hardness, temperature and the grain size/shape) were recorded. The grains shape and dimensions were decided following the *International Association of Cryospheric Science classification* (Fierz et al. 2009).

6.2.3 Samples Preparation and Analyses

The samples were melted in the vials at room temperature in the class 100 clean room of the LGGE laboratory (Grenoble). The samples for the trace elements analyses were sub-sampled in pre-clean LDPE vials and immediately refrozen. The analyses of total dust content, rBC concentration and ionic compounds were done immediately after the samples melting at the LGGE.

The snow samples collected on the Ortles glacier were analysed with a Dionex© ICS3000 dual pump Ion Cromatography system (Thermo Scientific) at the LGGE laboratory of Grenoble (France). Cations (Li^+, Na^+, NH_4^+, K^+, Mg^{2+}, Mn^{2+}, Ca^{2+}, Sr^{2+}) were analyzed on CG16+CS16 (2 mm) columns and anions (inorganics: F^-, Cl^-, NO_2^-, Br^-, NO_3^-, SO_4^{2-} and organics: formate (HCO_2^-), acetate ($CH_3CO_2^-$), glyoxylate ($HCOCO_2^-$), propionate ($CH_3CH_2CO_2^-$), lactate ($CH_3CHOCO_2^-$), oxalate ($C_2O_4^{2-}$), succinate ($(CH_2)_2C_2O_4^{2-}$), glutarate ($(CH_2)_3C_2O_4^{2-}$) and pyruvate ($CH_3COCOOH$)) on AG11+AS11 (2 mm) columns, with suppressed conductivity detection.

The insoluble dust particles total mass and size distribution was determined by a Coulter Counter© Multisizer III. The dimensional range was from 1.0 µm to 300 µm divided in 300 channels of 1 µm. By assuming a density of 2.5 gcm^{-3} (Delmonte et al. 2002) it was possible to compute the total mass from the volume size distribution. rBC concentration analyses were performed by using a Single Particle Soot Photometer (SP2, Droplet Measurement Techniques, Boulder, Colorado). SP2 uses a Nd-YaG laser to heat the aerosol particles arriving in the laser beam intra-cavity. Only the rBC particles reach temperatures of about 4000 K, due to their high refractoriness, and emit an incandescence signal before vaporizing; the signal seems to be independent from the particles' morphology and from the external particles' coating material (Stephens et al. 2003, Moteki and Kondo 2007, Moteki and Kondo 2010, E. S. Cross et al. 2010, J. Schwarz, Gao, Fahey, et al. 2006). The incandescence signal is proportional to the rBC particle mass; a fullerene soot calibration (Gysel et al. 2011) allows to compute the mass of each individual rBC particle from the incandescence signal. In order to remove the solvent from the samples before the SP2 an APEX-Q (EPOND, Switzerland) with a glass nebulizer unit was used (Lim, Fain, Zanatta, et al. 2014). Before every analytical session the APEX-Q nebulization efficiency was measured with Aquadag standards (Gysel et al. 2011) with concentration from 0.1 ng g^{-1} to 100 ng g^{-1}. The mean efficiency during the measurement was about 0.5. However, we didn't multiply the rBC measurement results and therefore the dataset could be underestimate. The samples were kept frozen until the analyses and therefore no correction has to be applied (Lim, Fain, Zanatta, et al. 2014).

Water stable isotopes ($\delta^{18}O$, δD) were determined by a Picarro liquid analyzer L1102-i CRDS coupled with a HTC PAL autosampler (Leap Technologies).

Trace elements (Li, Na, Mg, Al, K, Ca, Ti, V, Cr, Mn, Fe, Co, Cu, Zn, Se, Rb, Sr, Ag, Cd, Sn, Sb, I, Cs, Hg, Ba, Tl, Pb, Bi and U) and rare Earth elements (Y, La, Ce, Pr, Nd, Sm, Eu, Gd, Tb, Dy, Ho, Er, Tm, Yb, Lu, Th) concentration were measured by a Inductively Coupled Plasma Mass Spectrometer (Agilent Instrument 7500 series ICP-MS). The samples were acidified at 2% using ultra-pure Nitric acid and analyzed after less than 5 hours. The methods is described in Chapter 5 of this work.

6.3 Results and Discussion

6.3.1 The Record Warm Summer of 2015

The Summer of 2015 was the warmest ever recorded on a global scale as reported on the NOAA, NASA and JMA databases. In the Mt. Ortles region, however, the summer of 2015 was the second warmest, after the summer of 2003, since 1864 (reconstructed temperature in Gabrielli, Carturan, et al. 2010). In 2011 an Automatic Weather Station (AWS) was installed on the Alto dell'Ortles glacier, about 50 meters West of the drilling site. A four years long time series of temperature was obtained with a ventilated *Vaisala* sensor (Carturan and De Blasi, personal communication), with hourly resolution. The summer of 2015 is the warmest of the whole dataset and two of the three monthly temperatures above zero are in July and August of 2015 (August was characterized by an average temperature of +0.19 °C and July by an average of +1.5 °C).

Moreover, another important parameter favoring the surface snow melting is the number of days with temperatures higher than zero. In the upper part of Fig. 6.1 the number of days with temperature above 0 °C are reported for June, July and August and the summer (JJA) average from 2012 to 2015 (the available dataset). It is clearly visible that in the Summer of 2015 the highest number of days with T>0 °C was recorded as well as the remarkable results for July of 2015: 23 days with daily temperature above zero (16 days with hourly temperature always above 1 °C). The monthly average temperatures for July and August of 2015 were above zero and despite a quite cold June the summer (JJA) average value in 2015 was about 0 °C: during July and August the average temperature was of 0.85 °C.

The Summer temperature data suggest that intense melting and water percolation characterized the Alto dell'Ortles glacier in this period. Melting, percolation and refreezing cycles are the biggest issue while working on Alpine glaciers. The relocation of chemical species, such us the ionic compounds or the soluble aerosol components, usually takes place when the melted water percolates in the snow layers. Several works studied the effects of percolation on the chemical species in the snow, by focusing on their relocation. The ionic compounds seems to be the most affected (Vega et al. 2016) followed by the water soluble component of mineral dust and aersols, the water stable isotopes and finally the insoluble dust components (Eichler, Schwikowski, and Gäggeler 2001, Pohjola et al. 2002). During the summer period of 2015 about 1.5 meters of snow melted (L. Carturan personal communication) on the Alto dell'Ortles glacier. It was therefore expected to find completely smoothed chemical and climatic signals below the summer layer of 2015. Moreover, it was also expected that the high number of days without snow precipitation, with high temperatures and intense melting led to the formation of a dust-enriched layer.

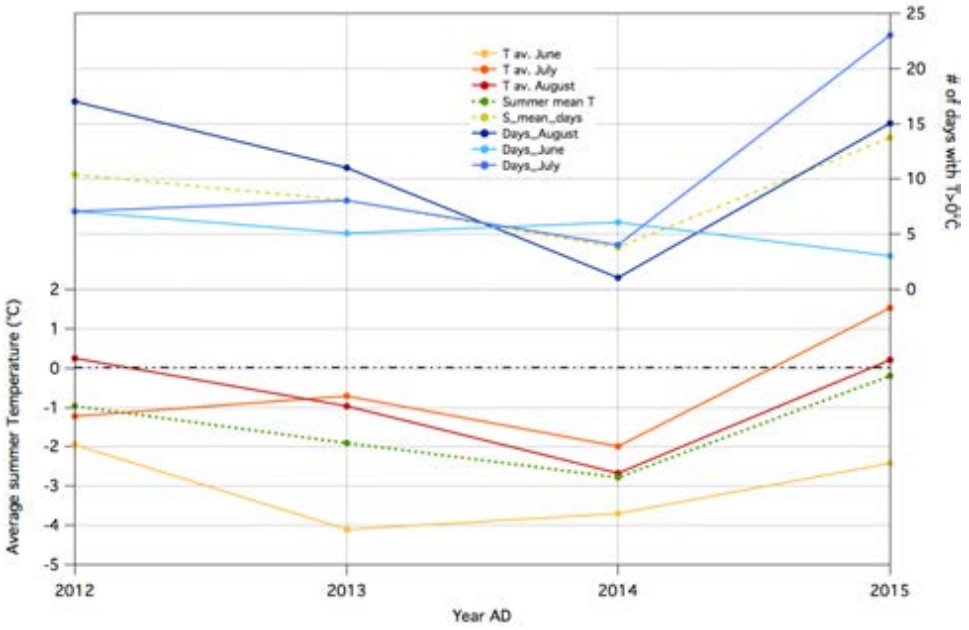

Figure 6.1: Summer of 2015: number of days with daily average temperature above 0 °C and the summer (JJA) average (upper graph). Monthly temperatures for June, July and August and the summer (JJA) average temperature (lower graph).

The data statistics are reported in Table 6.1.

6.3.2 Stratigraphic Profile

In 2015 a complete description on the snow pit stratigraphy was done by R. Pinggera and the results is shown in Fig. 6.2. The temperature profiles revealed that almost all the snow pit had a temperature equal to 0 °C, except for the first 25 cm–30 cm of fresh snow (cooled by wind), therefore confirming the significant water percolation during the summer of 2015.

Almost the entire snow pit was characterized by melt forms grains and the snow was visibly wet. The first 30 cm–35 cm from the top was fresh snow that fell 3 to 4 days before the campaign. The snow was made by melt forms indicating that a partial melting was already happening even if the density was low as well as the hardness index; the water stable isotopes show the lowest values in this first layer.

At a depth of about 35 cm a dusty layer was observed above a 3 cm–4 cm thick ice lens. This discontinuity layer was the transition between the fresh snow and the layer of summer of 2015. In this layer the highest concentration of trace elements and species was measured (see Section 6.4). The water stable isotopes (Section 7.3) achieve here less negative values (–10 ‰) and then remain constant, whereas the NH_4^- has a maximum and then decreased with some secondary peaks (Sections 6.4.1 and 7.3) .

From 45 cm to 110 cm, alternations of melt forms grains and small ice lenses was observed, the density increased from 440 kg m^{-3} (in the first 50 cm including the fresh snow) to 480 kg /m^3 and the hardness index from 250 N to 600 N.

At a depth of 90 cm to 100 cm, a melt-freeze crust was observed with the presence of melt-freeze polycrystals and the hardness index increased to about 800 N. In this layer an increased in the concentration of the ionic compound is observed,

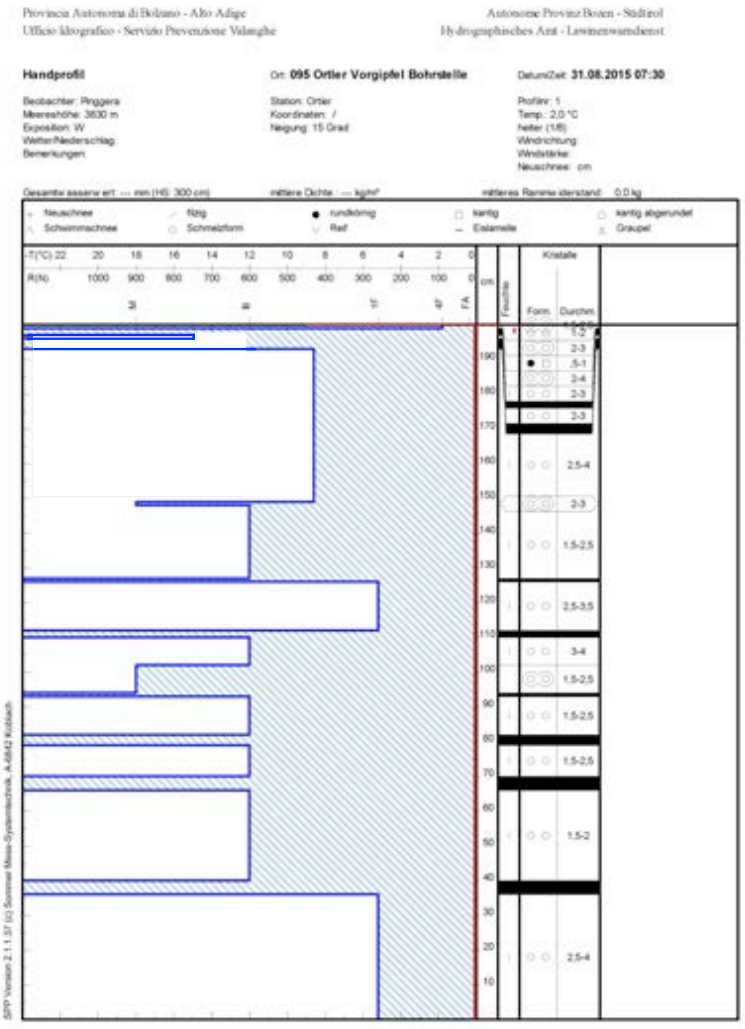

Figure 6.2: Stratigraphic profile of the Alto dell'Ortles snow pit dug in 2015: hardenss index, shape classification and dimensions.

especially of NH_4^-, NO_3^-, Cl^- and MSA (which has the maximum concentration at this level) (Section 6.4.1). Trace elements show a small increase at a depth of 110 cm, below the lens (Section 6.4).

From 110 cm to 160 cm, the water isotopes again show low values as well as the ionic compounds and the trace elements concentrations. At 150 cm, a thin melt-freeze crust is observed together with a small increase in the ionic concentration. The 50 cm resolution density smoothly increased down to the base of the snow pit where a value of about 550 kg m^{-3} was measured. The water stable isotopes started to increase again towards lower negative values from 180 cm. The ionic compound concentration increases in correspondence of two thick ice lenses before 200 cm. 10 cm lower a dusty layer was recorded in terms of dust, rBC content (Section 6.4.2) and some trace elements concentration.

The transition between the summer of 2014 layer and the autumn of 2014 snow was not clearly visible but was then found at these depths. A clear separation is observed between 190 cm and 210 cm: the ionic compounds showed a maximum

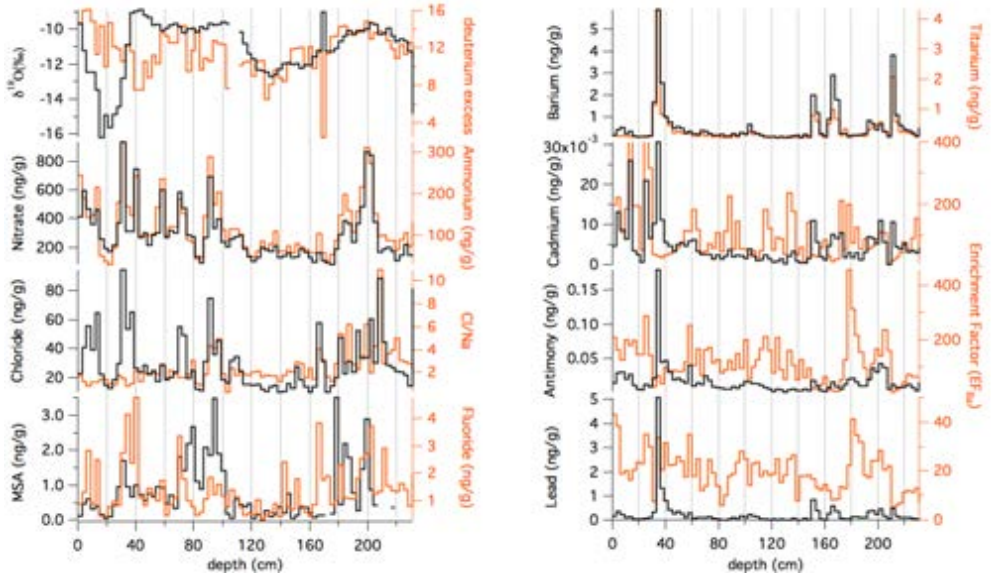

Figure 6.3: The Alto dell'Ortles 2015 snow pit profile of $\delta^{18}O$, d and some major ions (left) and of selected trace elements and relative enrichment factor (right).

in between 190 cm and 200 cm as well as the halogens (Br^- and I), Hg and others; whereas the dust and rBC peak was observed below, together with the concentration peak of the crustal elements and the rare Earth elements. It is likely that post-depositional processes as the melting and refreezing cycle, strongly affected this layers. The ice lenses were probably the results of percolating water from above that re-froze on the ice lenses formed on the summer 2014 layer (on-going research). The presence of ice lenses may stop the percolating water and at the same time modify the concentration distribution via a wet-dry migration of both particulates and chemical species in the snow.

6.3.3 Seasonality

In Fig. 7.32, on the left, the profiles of some selected ionic compound, of the $\delta^{18}O$ and the deuterium excess (d) are reported, whereas on the right, the profiles of some trace element and the corresponding enrichment factors (the charts are similar to those reported in Gabrieli, Carturan, et al. 2011 for an easily comparison). Cadmium, Antimony and Lead enrichment factors were computed using Barium as a crustal reference element, using the upper crust concentrations values as reported in Wedepohl 1995.

The halogens profiles (Bromine and Iodine), Cesium, Tin, Mercury, Thorium, rBC and the total mass of the insoluble dust component are reported in Fig. 6.4. Those elements and rBC were measured for the first time on the Alto dell'Ortles glacier in this work, and as far as we know, also in the snow from the Eastern part of the Alps.

The $\delta^{18}O$ profile is characterized by a visible seasonal pattern even if smoothed likely from the strong water percolation. The highest values are close to −8 ‰ whereas the lowest, recorded in the first 35 cm of fresh snow (fallen 4-5 days before the sampling), is of −16 ‰. Despite the fact that seasonal oscillation is still

visible, the highest and the lowest values are smaller (in absolute value) than those previously reported Gabrieli, Carturan, et al. 2011.

The ionic compounds NH_4^+, NO_3^- and SO_4^{2-} (which have mainly anthropogenic origin) profiles are still clearly seasonal even if the percolation has redistributed them at least in the first upper half on the snow pit. A concentrated layer is found between 90 cm and 100 cm were the stratigraphic profile reports a hard layer with melted and refreeze like snow ice grains. On average NO_3^- and NH_4^+ have a summer to winter ratio of about 3 and 4 respectively. It is likely that the water percolating through the layers partly stopped at this depth, causing the enrichment for almost all the measured ions. Ca^{2+}, Mg^{2+} and K^+ profiles (not shown) are characterized by a very concentrated (about 1.8 times the values reported by Gabrieli, Carturan, et al. 2011) layer during the summer of 2015 but instead the layer corresponding to the summer of 2014 seems to be much less concentrated.

The marine elements Cl^- and Na^+ show a seasonal pattern and they are well correlated ($R^2 = 0.81$) with each other. The ratio Cl^-/Na^+ is variable in the profile and the value is on average very closed to that reported for the sea salt value (1.8) and that reported in Gabrieli, Carturan, et al. 2011. At the 90 cm–100 cm and 160 cm–230 cm depth intervals the value increase to about 4, and this can be a proof of the melt post-depositional effect because Cl^- was found to be more resistant to the percolation compared to Na^+ (Eichler, Schwikowski, and Gäggeler 2001). MSA and Fluoride profiles show smoothed seasonal signals and particularly, the MSA concentration peak is not found in correspondence of the NH_4^+ summer peak, but on the 90 cm–100 cm layer and therefore the post depositional processes greatly affected this acid.

Barium and Titanium profiles show a well-preserved and clear seasonality and correlates with a correlation coefficient of 0.89. The summer 2014 surface is thought to be at a depth of 210 cm where most of the crustal elements profiles peak (also the total mass of the insoluble dust component peaks at this depth, Fig. 6.4). However, two peaks were also found at 150 cm and 165 cm for many chemical species, elements and dust probably due to two Saharan dust events (on-going research). Cadmium, Antimony and Lead show high concentration only in the summer layer of 2015 but then their value are low. The EF, however, is higher than 10 for almost all the depth suggesting an anthropogenic origin. The highest EF values are observed in a depth between 170 cm and 210 cm, in correspondence to the thick ice lenses and the transition between the summer layer of 2014 and the winter 2014/2015.

In Fig. 6.4 the profiles of two halogen elements are shown. Both Bromine and Iodine have usually marine origin but their atmospheric chemistry behaviour and deposition is quite complex (Gilfedder et al. 2008). However, seasonality is observed for both of them, even if their concentration maximums are in the ice lenses layer before the dusty surface of the summer 2014. The summer to winter ratio is about 4 for Bromine and for Iodine.

Cesium, Tin, Mercury and Thorium was measured for the first time and their profile are showed in Fig. 6.4. The Mercury values are below the detection limit (0.6 pg g^{-1}) for almost all the samples except for the summer layers, where values of about 1.4 pg g^{-1}–1.7 pg g^{-1} were measured.

rBC and total dust mass profiles show the most evident seasonality in the Alto dell'Ortles snow. Particularly, the summer layers of 2015 and 2014 are clearly vis-

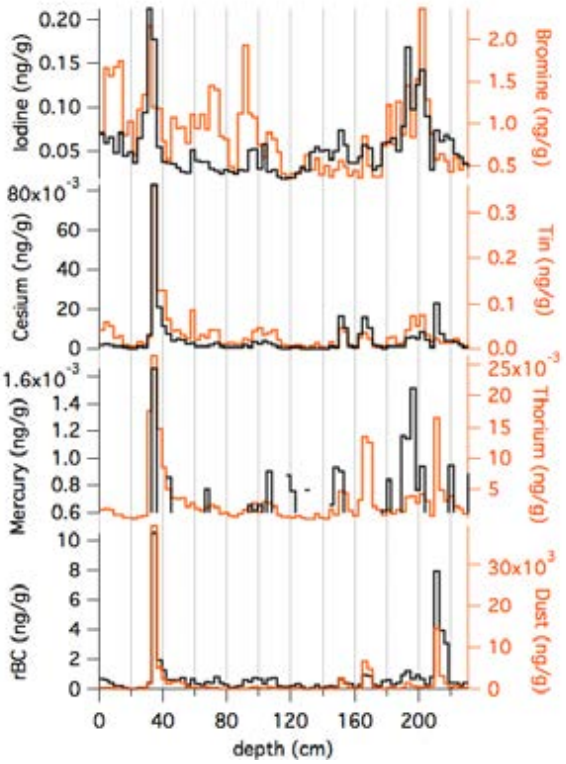

Figure 6.4: The Alto dell'Ortles 2015 snow pit profile of Bromine, Iodine, Cesium, Tin, Mercury, Thorium, rBC and the dust total mass.

ible. The insoluble dust particles are characterized by the biggest diameters compared to the other chemical species (up to 300 µm in this measurements) and they are therefore stacked in the snow/firn matrix. rBC concentration show the highest value in the summer 2015 layer, about 10.5 ng g^{-1} and 8 ng g^{-1} for the summer of 2014. The summer to winter ratio is about 30; however, it's important to remember that the surface melting could have caused a post-depositional concentration of the rBC and the dust content. The large dust concentration likely affected the snow reflectivity especially during summer of 2015 (see Paragraph 6.4.2).

6.4 Trace and Rare Earth Elements

Trace Elements In all of the snow pit profile and snow samples the concentration of the trace species and elements are characterized by a very large range of concentrations ranging from some pg g^{-1} (or lower the detection limit, DL), such as for Sb, I or Se, to 3641 ng g^{-1} for the maximum of Ca (Table 6.1). However, the mean average concentrations are always very low, except for the two summer layers of 2014 and 2015. In the summer layer of 2015 all the measured trace and rare Earth elements have the maximum values. Ca, Mg, Al, K and Fe are by far the most abundant elements, with mean concentrations in the order of 100 ng g^{-1} for Ca and Mg and of 20 ng g^{-1} for Al, K and Fe (these elements are usually the most abundant in the average terrestrial crust). The maximum to minimum ratio mainly reflects the ratio between the concentrations of the summer layer of 2015 and the winter of 2014. The ratios are bigger than 12, for I, and arrive up to 3628, for Cs; U, Co and

^{57}Fe increased about 1000 times. By comparing the max/min ratio reported for the snow pit of 2009 the maximum value was of 356 for Mn (Gabrieli, Carturan, et al. 2011). In the rightmost column the max to min concentration ratios for the 2009 snow pit are reported (Gabrieli, Carturan, et al. 2011). Except for Li and Co, the elements with a medium atomic mass increased in the same order of magnitude, whereas the heavy elements (Ag, Cd, Sb, Ba, Pb, Bi and U) in 2015 increased to more than double.

As previously reported the summer of 2015 was characterized by extremely high temperatures at Mt. Ortles and by long periods of sunny days and without any kind of precipitation. Both the high deposition rate and the surface concentration of dust due to melting contributed to the formation of the dust enriched layer.

Rare Earth Elements During the winter periods the rare Earth elements concentrations are extremely low and often below the instrumental detection limit, whereas during the summers they show a significant increase, and the seasonality is well preserved despite the strong melting. The median value of the max to min ratio is about 1500, suggesting that almost all the deposition is during summer.

In Table 6.2 the concentrations of the snow pit of 2015 are compared to those of the snow pit of 2009 (Gabrieli, Carturan, et al. 2011) and to the Colle Gnifetti firn (Mt. Rosa) concentration for the period 1980-1993 (Gabrieli 2008).

Comparison The average concentrations recorded in the snow pits on the Alto dell'Ortles are comparable for the selected elements (except for Al and Fe that were 8 and 4 times more in 2015). The differences in the average values are clearly affected by the enriched summer layer of 2015. The average values were lower compared to the Colle Gnifetti firn concentrations for the period 1980-1993 (except for Cr, Co, Al, Fe).

The elemental concentrations depend on the snow accumulation and therefore a more realistic comparison between the two Ortles datasets and the Colle Gnifetti firn can be obtained computing the *fluxes*. The average yearly snow accumulation on the Alto dell'Ortles glaciers was about 800 mm of water equivalent (w.e.) in the period 2011-2013 (Gabrielli, Barbante, Bertagna, et al. 2016). However, by the stratigraphic profile obtain on the Ortles snow pit of 2015 an accumulation of about 1000 mmw.e. was inferred. In the right part of the Table 6.2 the fluxes of the datasets are compared and the fluxes of 2015 are significantly higher. A smaller crustal dust deposition was inferred comparing the snow pit 2009 and the Colle Gnifetti core (Gabrieli, Carturan, et al. 2011). However, the results of this work seems to show that for Al, Fe and Mn the fluxes were higher on the Ortles glacier during the warm year 2015 than on the Colle Gnifetti in the period 1980-1993. In order to limit the importance of the layer of summer of 2015 the median could be used instead of the average; in this case the values would have been much closer to those of the snow pit of 2009.

The common way to establish the crustal (rock or soil dust) and non-crustal origin of an element is to compute its crustal enrichment factor (EFC). The EF is a dimensionless number that is obtained by the ratio of the concentration of an element with that of a reference element, usually one of the main component of the rock and soil of the neighbouring areas, and normalizing it with the ratio of the concentrations of the same elements but using reference values. The most common

Table 6.1: Concentration values and statistics of the trace elements, rare Earth elements, ionic compounds, dust content and rBC, measured in the snow pit on the Alto dell'Ortles of 2015. All the concentrations are expressed in ng g^{-1}.

	Mean	SD	Median	Max	Min	Max/min	Max/min (1)
Li	0.023	0.047	0.008	0.36	0.001	381	15
Na	16	16	10	71	4.3	17	
Mg	100	327	34	2867	9.5	301	
Al	28	63	11	502	1.9	266	321
K	15	21	9.5	169	2.6	66	
Ca	148	413	71	3641	21	175	
Ti	0.29	0.56	0.11	4.3	0.04	107	105
V	0.071	0.12	0.043	0.92	0.012	77	105
Cr	0.075	0.083	0.055	0.61	0.015	42	28
Mn	1.3	2.0	0.53	13	0.1	138	356
^{56}Fe	22	48	12	416	1.4	303	257
^{57}Fe	21	68	5.9	584	0.7	839	
Co	0.019	0.039	0.006	0.28	<DL	880	80
Cu	0.35	0.47	0.23	4.0	0.1	39	41
Zn	0.87	0.98	0.58	6.6	0.18	37	20
Se	0.054	0.029	0.056	0.13	0.008	17	
Rb	0.048	0.090	0.021	0.71	0.005	141	117
Sr	0.31	0.58	0.16	4.6	0.049	94	755
Ag	0.0011	0.003	0.0006	0.026	<DL	323	76
Cd	0.0048	0.005	0.003	0.03	<DL	404	23
Sn	0.031	0.045	0.02	0.36	0.002	219	
Sb	0.016	0.021	0.011	0.18	0.001	138	98
I	0.053	0.035	0.045	0.21	0.018	12	
Cs	0.0042	0.01	0.001	0.083	<DL	3628	
Hg	0.0005	0.0003	0.0004	0.0017	<DL	71	
Tl	0.0018	0.005	0.0008	0.044	<DL	347	13
Ba	0.54	0.9	0.22	5.9	0.05	119	278
Pb	0.25	0.59	0.12	5.1	0.023	218	68
Bi	0.004	0.0098	0.002	0.082	<DL	897	45
U	0.0057	0.024	0.002	0.21	0.001	986	61
Y	0.031	0.081	0.008	0.63	0.0010	1276	
La	0.042	0.12	0.009	0.89	0.0006	1522	
Ce	0.090	0.24	0.02	1.8	0.0012	1496	
Pr]	0.012	0.031	0.002	0.24	<DL	1145	
Nd	0.047	0.13	0.01	0.95	0.0007	1449	
Sm	0.010	0.026	0.002	0.20	<DL	1286	
Eu	0.002	0.006	<DL	0.042	<DL	1606	
Gd	0.009	0.025	0.002	0.18	<DL	2249	
Tb	0.001	0.003	<DL	0.025	<DL	1270	
Dy	0.007	0.017	0.001	0.13	<DL	3145	
Ho	0.001	0.003	<DL	0.024	<DL	18694	
Er	0.003	0.008	0.001	0.063	<DL	2336	
Tm	<DL	0.001	<DL	0.008	<DL	34562	
Yb	0.002	0.006	0.0006	0.05	<DL	850	
Lu	<DL	0.001	<DL	0.007	<DL	3399	
Th	0.003	0.004	0.002	0.027	<DL	113	
F^-	1.4	0.94	1.1	4.7	0.3	16	
Cl^-	30	19	24	94	9.9	9.5	58
NO_2^-	9.1	5.2	7.5	38	2.5	15	
Br^-	0.87	0.45	0.8	2.4	0.34	7	
NO_3^-	286	185	233	934	80	12	38
SO_4^{2-}	91	74	66	586	23	25	120
Na^+	11	10	7	57	2.13	27	
NH_4^+	120	67	100	324	29	11	390
MSA	0.8	0.82	0.47	3.5	<DL	352	
Acetate	50	79	5.7	273	0.52	528	
Propionate	3.3	5.8	0.51	19	<DL	465	
Formate	15	43	0.77	191	0.3	628	
Pyruvate	0.62	0.52	0.47	1.7	<DL	43	
Succinate	6	8.8	0.23	23	<DL	254	
Oxalate	4	4.3	2.8	17	0.15	110	
Dust total mass	1346	4748	257	39022	11	3439	
rBC	0.85	1.7	0.42	10	0.037	286	

Table 6.2: Mean concentration values for few selected trace elements and major ions measured on the Mt. Ortles snow pit of 2015 (this work), 2009 (Gabrieli, Carturan, et al. 2011) and the values of the Colle Gnifetti firn (Monte Rosa) for the period 1980-1993 (Gabrieli 2008).

	Concentrations ($pg\,g^{-1}$)				Fluxes ($\mu g\,m^{-2}yr^{-1}$)		
	Mt. Ortles			Colle Gnifetti firn	Mt. Ortles		Colle Gnifetti firn
	2007–2009(1)	2014-2015	2015/2009	1980–1993(2)	2007–2009(1)	2014-2015	1980–1993(2)
Cr	45	75	1.7	54	36	75	24
Cu	155	350	2.3	214	122	350	96
Zn	955	870	0.9	3410	755	870	1535
Co	13	19	1.5	38	10	19	17
Cd	6.6	4.8	0.7	38	5.2	4.8	17
Sb	16	16	1.0		13	16	
Bi	2.1	4	1.9	3.6	1.7	4	1.6
U	2	5.7	2.9	13.6	1.6	5.7	6.1
Pb	108	250	2.3	1655	85	250	745
Ba	380	540	1.4	1680	300	540	755
V	140	71	0.5	223	111	71	100
Mn	823	1300	1.6	2140	650	1300	960
Fe	5340	21337	4.0	16800	4220	21337	7560
Al	3440	28937	8.4	24320	2715	28937	10950

way is to use the upper continental crust concentration values (Wedepohl 1995) or the measured concentration of the elements composing the rocks around the study area. In this study we chose the Barium as the reference crustal element and the resulting EFC formula was (for Cadmium):

$$\mathrm{EFC(Pb)}=([\mathrm{Cd}]/[\mathrm{Ba}])_{\mathrm{snow}}/([\mathrm{Cd}]/[\mathrm{Ba}])_{\mathrm{crustal}}$$

In order to compare the results of this study with those of the 2009 snow pit (Gabrieli, Carturan, et al. 2011), the reference values of the upper crust were used as well. Typically, an element is considered to have non-crustal origin when the EFC is higher than 10; this because the airborne particles can have different sources area and their chemical composition can differ from the upper crust composition reference values. In this study almost all the trace elements show an EFC lower than 10. Some elements have EFC values between 10 and 100, as for Cu, Zn, Ag, Pb, Sn and Bi and only Cd, As, Sb and Se have an average EFC higher than 100. The results suggest that the formers have mainly anthropogenic but also crustal origin, whereas it is likely that the latters have a predominant non-crustal deposition. The results are similar to those obtained by Gabrieli, Carturan, et al. 2011.

6.4.1 Ionic Compounds

The Ionic compound has a strong influence in the Alto dell'Ortles snow having a concentration higher compared with the trace elements, excluding the crustal ones, from two to three orders of magnitude (this study and Gabrieli, Carturan, et al. 2011) as reported in Table 6.1.

Comparing the ionic compound concentration measured in this study to those obtained from a 10 m shallow core in 2009 (results showed in Gabrieli, Carturan, et al. 2011) it can be noted that the concentration are slightly different. For NH_4^- the mean concentration in 2015 was $120\,ng\,g^{-1}$, whereas almost the double in the shallow core, $208\,ng\,g^{-1}$; the SO_4^{2-} concentration in this study is $91\,ng\,g^{-1}$ and

more than three times higher between 2005-2009; NO_3^- was 286 ng g^{-1} and before 377 ng g^{-1}; the Cl^- concentrations was half than that of the period 2005-2009 (30 ng g^{-1} to 60 ng g^{-1}). It is very likely that the strong percolation occurred during the summer of 2015 have completely modify the ionic compounds concentrations by diluted them in the underline snow layers or completely removing the percolating water.

A comprehensive comparison between the 2005-2009 data and the results from several other glaciers and locations is shown in Gabrieli, Carturan, et al. 2011.

The *organic* compounds concentration inside the snow pit were characterized by significant concentration level in the first 35 cm of fresh snow, which abruptly decreased to values close to the DL at the summer layer of 2015 (Fig. 6.5). Acetate and Propionate also show an increase of concentration from 110 cm to 140 cm of depth, in correspondence with the winter of 2014 layers (as observed by the water stable isotopes). Instead Formate and Succinate do not recover the initial values in the profile. Oxalate has quite a similar behavior to that observed for NH_4^+ and NO_3^- compared to the other organic compounds; the highest concentration was measured in the fresh snow and a decreased in depth were observed. Contrary to NH_4^+ and NO_3^-, Oxalate doesn't show the summer of 2014 maximum from 180 cm to 220 cm. Oxalate has been used as a proxy for biomass burning but, differently to the very specific marker Levoglucosan (Kehrwald et al. 2012), it may have other sources such as vehicle emissions (Kawamura and I. R. Kaplan 1987). The high oxalate concentration peak in the fresh snow may be the results of an enhanced biomass burning period during the summer of 2015, due to the high temperatures and to the scarcity of precipitations during this period (on-going research). Positive concentrations were measured for Pyruvate in the first 30 cm, but then it's concentration decreased at levels below <DL. Glyoxalat, Glutarate and Tartaric organic acids has concentrations always below the DL.

The snow release of organic compounds was already observed during a field experiment on a sub-tropical glacier and on the Greenland ice sheet (Ginot, Kull, et al. 2001; Legrand and De Angelis 1995). The measured organics behaviour may be explained with few processes: the strong percolation occurred during the summer of 2015 may have diluted and flushed the organic compounds. However, different degrees in water solubility due to the association or not with particulates, may have caused the different behaviours (Wania et al. 1998). Another factor may have be the bacterial activity, especially during the warm periods and for the near zero temperatures recorder in all the snow pit (Amato et al. 2007). As reported in Ginot, Kull, et al. 2001 also the diurnal photochemical reactions may contributed in the organic acids removal.

6.4.2 rBC and Dust, the Radiative Effect

Light absorber compounds (LAC) greatly affect the snow albedo (darkening effect) thus increasing the absorbed percentage of solar radiation, which in turn increases the melting intensity; a further LAC concentration is observed during the melting periods, therefore decreasing the albedo, increasing the absorption and so on. This is an example of positive feedback in the climate system (Dumont et al. 2014).

Dust and rBC are both strong solar light absorbers (Hadley and Kirchstetter 2012) and greatly effect the surface snow energy balance of the glaciers. Many

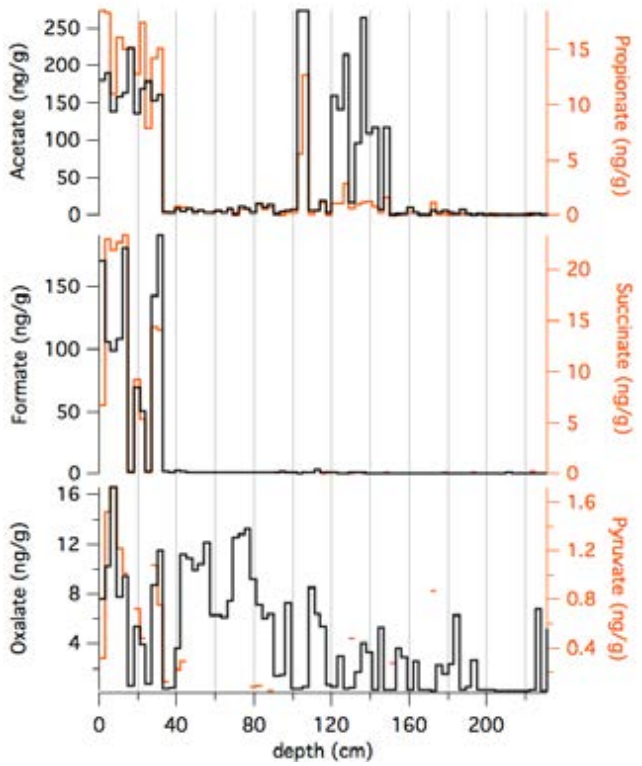

Figure 6.5: The Alto dell'Ortles 2015 snow pit profile for selected organic anions compounds.

studies were focused on measuring, modelling and quantifying the LAC effects on snow surfaces and glaciers, especially on the Tibetan Plateau glaciers where rBC concentrations are usually the highest (Painter, Skiles, et al. 2012, Ginot, Dumont, et al. 2014, S. Kaspari et al. 2014). In the Alpine region the dust and BC role in the glacier retreating was studied and modelled (Oerlemans et al. 2009, Painter, M. G. Flanner, et al. 2013, Gabbi et al. 2015). Large uncertainties still affect the modeling of the BC-induced decreasing of the snow albedo (T. C. Bond, Doherty, et al. 2013).

In the Alto dell'Ortles snow pit the rBC concentrations show a marked seasonality and the maximum concentration was recorded in the summer layer of 2015, 10 ng g^{-1}, and an average value of 0.85 ng g^{-1}. The maximum Ortles value is similar to the average values observed on the Col du Dome (4250 m m.s.l.) and on Mt. Elbrus (5115 m m.s.l.) glaciers (Legrand, Preunkert, Schock, et al. 2007; Lim, Fain, Zanatta, et al. 2014), but the average value is 10 times lower.

In this work, the radiative effect of the measured rBC and dust was modeled by using the Snow Ice Aerosol Radiative (SNICAR) model: it allows the computation of the albedo of snow and ice for combinations of LACs (BC, dust and volcanic ash), snow grain size and direction of the solar radiation (M. G. Flanner, Zender, et al. 2007). Particularly, the conditions of the summer layer of 2015 were used to identify the maximum of the radiative forcing in extreme conditions for the Alto dell'Ortles glacier. The results are expressed in terms of Radiative Forcing (RF), computed by the incoming short wave solar radiation (ISW) and the variation of the albedo ($\Delta\alpha$):

$$RF = R_{ISW} \times \Delta\alpha$$

The variation of the albedo in the solar broad band wavelength (SBB) were

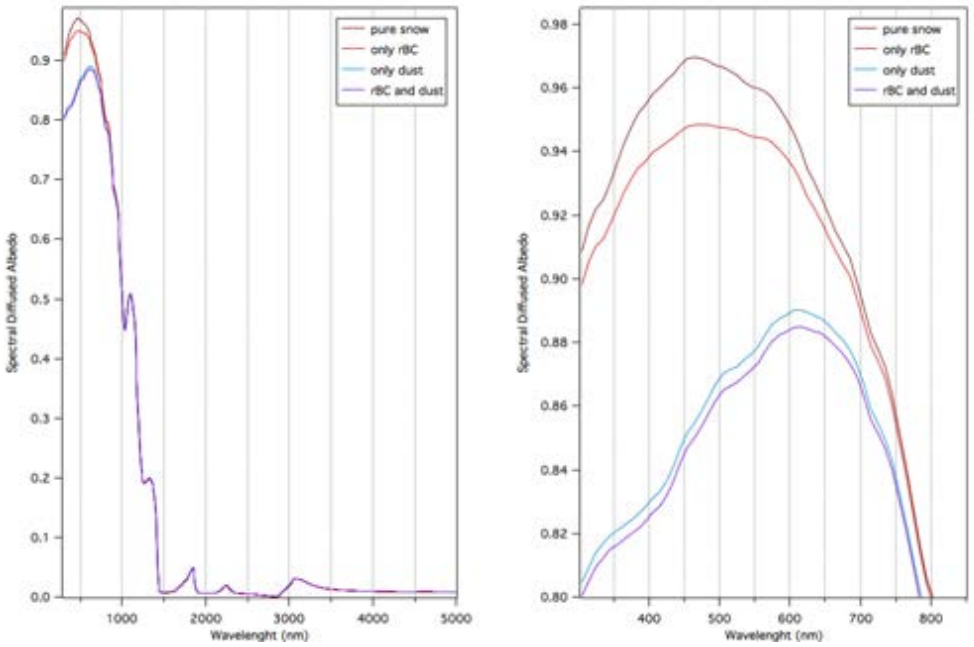

Figure 6.6: Simulated spectral albedo for pure snow and for the measured rBC and dust concentrations in the Ortles sample (relative to the summer surface of 2015) on the whole spectral range (left) and a focus up to 900 nm (right).

calculated with the SNICAR model for pure snow, with an effective *average* grain size of 800 µm, then for snow with rBC, only with dust and finally both the rBC and dust concentration, as measured in the Ortles sample relative to the summer surface of 2015. The results are reported in Fig. 6.6, for the whole wavelength range on the left and a focus up to 2500 nm on the right.

The maximum decrease in the snow albedo caused by rBC and dust is mainly at wavelength from 400 nm to 800 nm. The rBC effect is much lower than that of total dust at the measured concentrations, as it can be seen in Fig. 6.6. rBC alone caused an albedo decrease of about 0.8 %, whereas dust alone of 4.6 %.

The RF was computed by using an average ISW, computed on the AWS measured dataset for the summers 2012-2015, 255 $W\,m^{-2}$. The forcing caused by rBC alone deposition on the glacier was of 1.6 $W\,m^{-2}$, whereas that caused by dust was 9.2 $W\,m^{-2}$; the uncertainties in the measurement were less than 10 %, but the approximations in the parameters in the model cause the RF uncertainties to be in the same order of magnitude of the RF values (Qu et al. 2014). The parameters used in the model are:

1. Incident radiation: direct
2. Solar zenith angle: 60
3. Surface spectral distribution: Mid-latitude winter clear-sky.
4. Snow grain effective radius (µm): 800 (halved the measured diameter; Aoki et al. 2007)
5. Snowpack thickness (m): 2

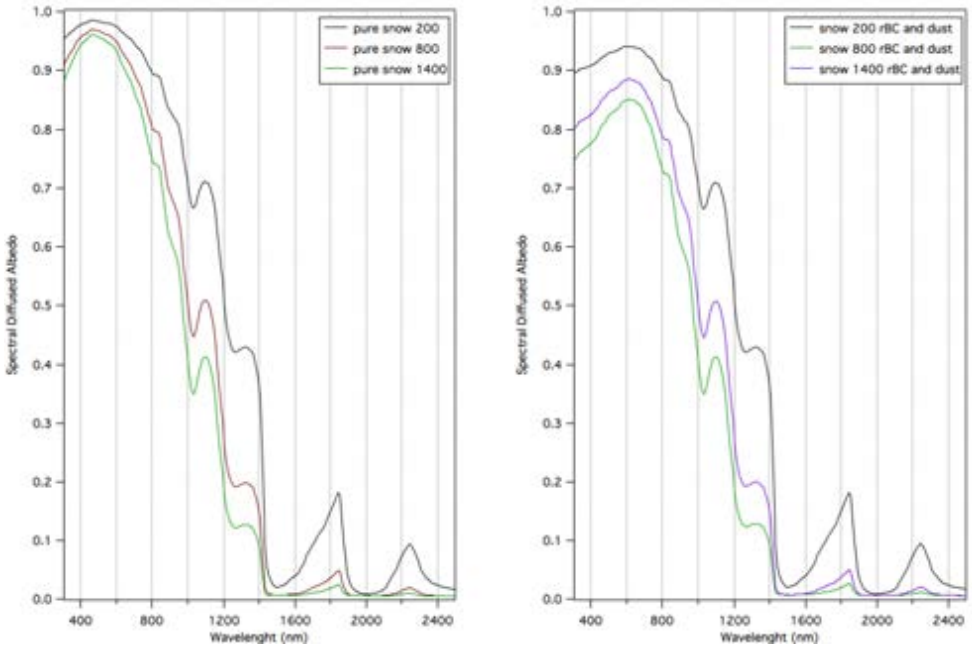

Figure 6.7: Simulated spectral albedo for pure snow (left) and for snow with rBC and dust (right) with varying snow grain effective radius.

6. Snowpack density (kg m^{-3}): 440
7. Albedo of underlying ground (a. Visible, 0.3 µm–0.7 µm. b. Near-infrared, 0.7 µm–5.0 µm): 0.6 and 0.4
8. MAC scaling factor: 1
9. BC concentration (ng g^{-1}, Sulfate-coated): 5
10. BC concentration (ng g^{-1}, Un-coated): 5
11. Dust concentration (mg g^{-1}, 5.0 µm–10 µm diameter): 39
12. Experimental particle 1 concentration (ng g^{-1}): 0
13. Volcanic ash (ng g^{-1}): 0

The results confirme that the rBC has a lower impact on the snow surface when large dust particles are also deposited, as observed in the Tibetan Plateau (S. Kaspari et al. 2014, Ginot, Dumont, et al. 2014).

The snow aging was observed to strongly decrease the snow albedo, mainly by making the snow crystals bigger in diameter (M. G. Flanner, Zender, et al. 2007). In order to check the magnitude of the importance of the snow grains increasing the model were run leaving the parameters unchanged except for the *snow grain effective radius*, whose value was changed in 200 µm, 800 µm and 1400 µm. The model was run with these three values for pure snow and for snow with the rBC and dust values (Fig. 6.7).

In Fig. 6.7 the effect of the snow aging is clearly visible; on the left the albedo decreases as the snow grain effective radius increases (from 200 µm to 1400 µm),

Table 6.3: Comparison between the ratio of some trace species and elements (2000 AD), the Alto dell'Ortles snow pit 2009 (1, (Gabrieli, Carturan, et al. 2011), the Alto dell'Ortles snow pit 2015 (2, this work), the Alto dell'Ortles firn for the period 1990-2011 AD (3, this work) and the Colle Gnifetti firn for the period 1980-1993 AD (4, Gabrieli 2008).

	Emissions		Alto dell'Ortles snow pit 2009 (1)			Alto dell'Ortles snow pit 2015 (2)			Colle Gnifetti firn (3)	Alto dell'Ortles firn (4)
	Po Valley	Local	median	warm	cold	median	warm	cold	1980-1993	1990-2011
NO_3^-/NH_4^+	1.7	1.4	1.7	2	2.5	2.3	3.2	2.2	2.1	
SO_{42}^-/Cd	27	5.9	30	39	21	24.6	26.6	55.6	18	
SO_{42}^-/Cr	5.9	1.4	5.9	11	4.7	1.6	1.8	1.2	12	
Pb/Cd	32	45	15	21	10	41.6	73.6	58.5	44	77
Pb/Cr	5.1	9.8	2.9	5.6	2.3	2.6	3.8	1.1	31	18
Pb/Zn	0.21	0.1	0.13	0.18	0.11	0.2	0.4	0.1	0.49	0.4
Cr/Cd	6.3	2.5	5.1	4.7	4.5	15.2	15.0	15.9	1.4	7.0
Zn/Cu	8.6	35	5.7	4.4	5.7	2.4	2.4	2.0	16	4.9
Zn/SO_{42}^-	5.1	33	4.8	3.6	4.8	7.5	12.9	8.4	5.1	

which is what usually happens for the melt-refreeze grains on the Alto dell'Ortles glacier. The presence of LACs in the snow contributes in decreasing the albedo. The results show that, for the measured concentrations, the rBC contributes in lowering the surface snow albedo in the same order of magnitude of the snow aging.

6.4.3 Sources of Anthropogenic Pollutant

The Po Valley emissions were found to be the main sources for the Alto dell'Ortles glacier for the 2007-2009 period (Gabrieli, Carturan, et al. 2011). In this work the same procedure is used in order to check if the results were still valid six years later and especially if the sources determination can be done also in case of exceptional melting events (this condition is now common for all the glaciers of the eastern Alps).

In order to understand the sources of the anthropogenic pollutants the national emission inventory, created with the CORINAIR methods, was used (European Monitoring and Evaluation Program; the Italian dataset is available at: `http://www.sinanet.isprambiente.it/it/sia-ispra/inventaria`). In Table 6.3 are reported the ratio of some selected anthropogenic pollutants (NH_4^-, NO_3^-, SO_4^{2-}, Cr, Pb, Zn, Cu) computed for the Ortles snow pit of August 2015 (this work) and for the Po Valley and the neighboring Ortles area (at maximum 50 km far) (Gabrieli, Carturan, et al. 2011). The ratio comparison was made between the Ortles 2009 snow pit results (from Gabrieli, Carturan, et al. 2011), the Ortles 2015 snow pit results, the Alto dell'Ortles firn for the period (1990-2010) (this work) and the Colle Gnifetti firn (Gabrieli 2008) for the period 1980-1993.

The correlation coefficient reported in Gabrieli, Carturan, et al. 2011, show that the data from the snow pit of 2009 well correlates with the emission of the Po Valley ($R^2 = 0.83$, $p < 0.001$), whereas the winter values are much less correlated ($R^2 = 0.56$, $p = 0.024$). Moreover, the local sources ratios differ from the snow pit data. The result confirmed the hypothesis that the Po Valley emissions greatly affect the Alto dell'Ortles snow, much more than the local pollution emissions.

The results from the Alto dell'Ortles snow pit of 2015 confirm that the major pollutants source is the Po Valley. The median ratios of the Ortles snow pit 2015 correlates with a Pearson coefficient (PC) of 0.93 ($p<0.001$) with the Po Valley emissions ratios; the warm periods ratios has a PC of 0.88 ($p<0.001$) and the cold periods 0.96 ($p<0.001$). The correlation coefficient with the local pollutions emissions ra-

tios is instead much lower: 0.48 (p=0.18), 0.60 (p=0.1) and 0.46 (p=0.3). Therefore the pollutants source is the same as in the previous study (Gabrieli, Carturan, et al. 2011), however in 2014 and 2015 the contribution of the Po Valley emissions seems to be significant also for the winter period. It is possible that the strong water percolation caused a partial elements and trace species relocation in the snow, therefore bringing the ratios of the cold periods at the level of the warm ones (even if the concentrations remains much lower in absolute values). Or it may have happened that the atmospheric thermal inversion was significantly higher during the 2014 winter/spring (see next paragraph).

The Ortles core #1 firn results covering the period 1990-2011 (this work) shows elemental ratios very well correlated to those of the Po Valley emissions with a PC of 0.96 ($p < 0.001$). However, the results show that during the period 1990-2011 a contribution of the local emissions was not negligible (PC of 0.7, $p = 0.02$).

The Colle Gnifetti and the Alto dell'Ortles are two glaciers located more then 440 km apart. The two datasets are characterized by a PC of 0.85 ($p = 0.002$) therefore showing a significant correlation. This result generally indicates a link between the two glaciers, one in the western and the other in the eastern part of the Alps, in the sources of anthropogenic pollutions. However, some ratios appears slightly different and this is probably due to the different trace element fluxes arriving to the glaciers (Gabrieli, Carturan, et al. 2011). Local dust sources (different geological profiles) or different transport efficiency for different elements due the to aerosol dimensions (A. Allen et al. 2001)) can also explain the differences.

6.4.4 The Atmospheric Structure Influence

The atmospheric structure and the transport synoptic pathways determine the trace species and elements arriving to the Alto dell'Ortles glacier. The ability of the aerosols emitted in the Po Valley to arrive at a high altitude such as that of the Ortles glacier (3905 m) strongly depends on the structure of the troposphere during the year. If a temperature inversion is observed in the vertical thermal profile the atmosphere will be stable below it, enabling the vertical air motions, therefore affecting the aerosol vertical distribution (Kappenberger and Kerkmann 1997). If the inversion layer lies beneath the Ortles altitude the emitted aerosol will be trapped below it, with small possibilities of being transported to high altitudes via convective winds. In (Gabrieli, Carturan, et al. 2011), it was found that the height of the boundary layer was higher during the summer months compared to the winter period for the 2007-2009 years.

An Automatic Weather Station was installed in 2011 on the Ortles glacier, and the wind speeds and directions were measured until the summer of 2015. As reported in the paragraph 2.3.2, the prevailing winds come from South-West and the strongest as well, without any apparent seasonal variation. The back trajectories, obtained with the NOAA HYSPLIT model gave the same results in terms of direction (Gabrieli, Carturan, et al. 2011). Therefore, only the synoptic horizontal pathways cannot explain the seasonal variations of the anthropogenic pollutants.

In order to check if the variability of the depth of the boundary layer (BLD) could explain the high correlation between the measured concentration ratios during cold period with the Po Valley pollutants emission ratio, the daily maximum BLD was computed for the period 2014-2015. The Milano-Linate airport (about

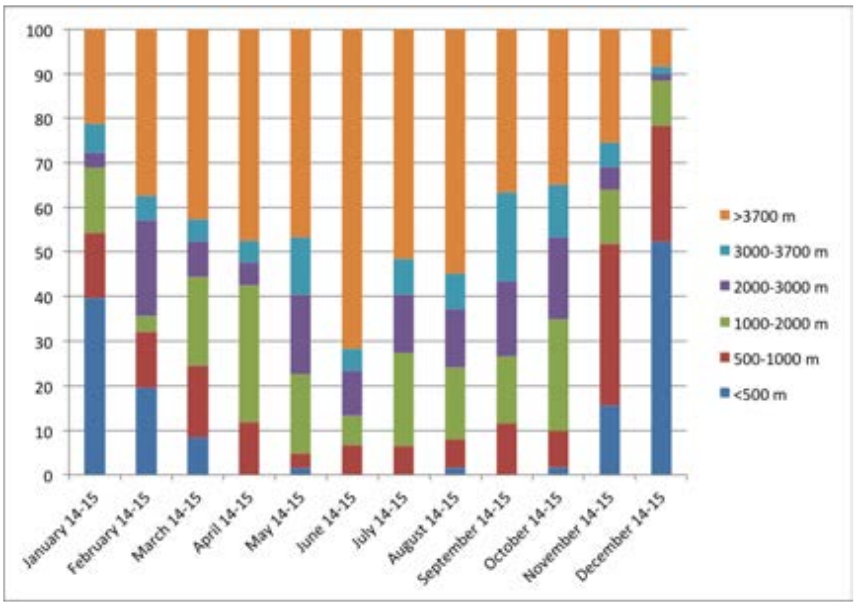

Figure 6.8: Monthly relative frequency of the daily maximum boundary layer depth averaged over the period 2014-2015. The BDLs were computed from the Milano-Linate Airport atmospheric data.

100 km SW from Ortles) atmospheric profiles data obtained from the balloon launches were analysed in this work for the period 2014-2015. The data are available at the University of Wyoming website: `https://www.weather.uwyo.edu/upperair/sounding.html`) with two atmospheric profiles per day (at 00.00 and 12.00 UTC). In order to find the BLD we defined a parameter based on the difference between two altitudinal consecutive temperature data and recording the maximum daily BLD for the two years by defining 6 altitudinal ranges ($<$500 m, 500 m–1000 m, 1500 m–2000 m, 2000 m–3000 m, 3000 m–3700 m and $>$3700 m) as already did by Gabrieli, Carturan, et al. 2011. The monthly average of the relative frequency for two years are reported in Fig. 6.8

The BLD changes over the months according to the solar radiation intensity, higher in summer than in winter. The relative frequency of the occurrence of a BLD higher than the Ortles altitude ($>$3700 m) increases from spring achieving the maximum values during summer, where this condition may occur for more than 20 days over a month. During winter the inversion layer can be lower than 500 m for the 40 % to 50 % of the days (for December and January), therefore causing the pollutants to remain trapped close to the Earth surface (Crosier et al. 2007).

By comparing the atmospheric structure results (this work) with the data for the 2007-2009 period (Gabrieli, Carturan, et al. 2011) an average increase can be observed in the relative frequency of the highest BLD for the 2014-2015 period, especially for the winter months, as reported in Table 6.4.

These significant increases in the relative frequency may explain at least part of the higher correlation observed between the cold period ratios for the snow pit of 2015 compared to those of the snow pit of 2009. Moreover, percolation may have had a role as well in relocating part of the pollutants deposited in the summer layer of 2015.

Another important parameter is the atmosphere's stability, which is usually calculated by means of the Pasquill Classification (Pasquill 1961). The computed

Table 6.4: Relative frequencies of a boundary layer depth (BDL) higher than 3700 m for the period 2007-2009 and 2014-2015. *Gabrieli, Carturan, et al. 2011

	Relative frequency of BLD>3700 m		percentages of increase
	2014-2015 (this work)	2007-2009*	
January	21	10	112
February	38	13	188
March	43	30	42
April	47	45	5
May	47	40	17
June	72	46	56
July	52	42	23
August	55	32	71
September	37	32	15
October	35	20	75
November	25	20	27
December	8	10	-17

values for the Milano-Linate Airport (Gabrieli, Carturan, et al. 2011) again underlay the prevailing of a stable to very stable atmosphere during the winter, when the pollutants cannot be lifted to the free troposphere. On the other side, during summer, the instability is usually more frequent. During the entire year the neutral/slightly unstable atmospheric conditions account for the 60 % of the days per month, the remaining 40 % during the winter months are characterized by a stable atmosphere, whereas in summer by a moderate unstable to extremely unstable conditions.

During the winter period the pollutants emitted in the industrialized Po Valley are trapped below the stable atmosphere thermal inversion layer and cannot be transported by the low speed vertical winds through the boundary layer. The increase of solar radiation during from the spring and culminating in summer causes an average increase of the BLD and of the atmospheric instability. In these conditions the pollutants aerosols can be easily injected in the free troposphere and brought, by the synoptic winds, across Europe and specifically, on the Alto dell'Ortles glacier. However, as demonstrated in this study, the pollutants concentration in the snow may be influenced not only by large scale synoptic transports during the winter periods, but also from the Po Valley emissions, in case of years characterized by high frequency BLD above the Ortles glacier altitude, such as for 2014 and 2015. Despite the increase in the melting/percolating and refreezing cycles, observed in the last three decades caused by the high altitude atmospheric temperature increase, this kind of studies can still be used to evaluate the pollutants sources.

6.5 Conclusions

A detailed case study was performed by analysing a 234 cm snow pit on the Alto dell'Ortles glacier after the extraordinary warm summer of 2015. The AWS data were firstly presented in order to evaluate the potential of the selected summer to

be representative of the very extreme episodes during the history of this glacier. Studying the glacio-chemical response of the Alpine glaciers to these kinds of events is of great importance in order to evaluate both the glaciers potential to store paleo-climatic and paleo-environmental informations despite the recent years temperature increase, and to better understand the results from the ice cores analyses.

The seasonality was found to be preserved for almost all the analytes, but the absolute concentrations was strongly affected by water percolation. The results confirmed that the dust particulates and the elements related to them are less effected by post-depositional processes, and their concentration may even increase due to snow sublimation and enhanced dry deposition (Ginot, Kull, et al. 2001).

rBC was measured for the first time in Eastern Alpine ice. The concentrations appears to be enough for causing a significant albedo reduction, even if at least in the summer of 2015 the high dust concentration in the summer layer was a much stronger radiative forcing.

The pollutants sources and transport mechanisms were also established by comparing the results with those obtained for the analyses of the snow pit for the years 2007-2009 (Gabrieli, Carturan, et al. 2011). The Po Valley was recognized to be the main source of pollutants and the higher pollutants levels measured in the snow pit of summer 2015 was explained with an enhanced transport from the polluted near surface troposphere to the high altitude glacier during the years 2014 and 2015.

Chapter 7

Trace Elements Profiles

7.1 Character of the Data

The Ortles core #1 was completely analysed by means of a *continuous flow analyses system* as described in detail in the Chapter 4 and following the methods explained in the Chapter 5. Not all of the continuously measured profiles are shown in this work because more time has to be spent in cleaning the data. The 14 selected trace elements are: Na, Mg, Al, Ca, Ti, V, Mn, Fe, Cu, Zn, Sr, Ba, Pb, U.

A portion of the decontaminated samples sampled in the direct sampling line (see Paragraph 4.4.4), were melted and treated with 2 % (vol/vol) $HNO_3{}^-$ acidification in a Class 100 clean room under a laminar flow bench (at the University of Venice). A total 1059 samples were eventually obtained: in the first 28 meters, the resolution was reduced by mixing three consecutive samples, below this depth, mixing two samples down to about 55 m where the dating curve indicates a significant thinning; below 54 m of depths all of the 3 cm resolved samples were analysed. The obtained resolutions, from 9 cm at the top to 6 cm to 54 m, and 3 cm below, were enough to catch the seasonal variations reported in the isotopic profiles, except in the lowest part of the core (from about 65 m of depth) where the thinning was too intense.

After less than one day from the acidifications the samples were analyzed with an ICP-QMS and CRC-ICP-MS (Agilent Instrument 7500 series ICP-MS) for 28 elements. The most abundant isotopes were chosen (except for ^{57}Fe): Li, Na, Mg, Al, K, Ca, Ti, V, Cr, Mn, Fe, Co, Cu, Zn, As, Sr, Ag, Cd, Sb, Te, I, Cs, Ba, Hg, Tl, Pb, Bi, U. The decision to analyse the samples a short time after the acidification was taken in order to have results similar to those of the CFA system, therefore checking the measured elemental concentrations and increasing the number of analysed elements.

The statistical analyses and the EFs were computed using the high-resolution discrete data (almost all the CFA data fluctuations are well represented also in the discrete analyses). The summary statistics of the results for the whole dataset are listed in Table 7.1 where the concentrations are in ng g^{-1}. The most abundant elements are Ca, Mg, Al, K and Fe. Those elements are the major constituents of the rocks in the Mt. Ortles area (P. Gabrielli personal communication) and in general of the Earth upper crust (Wedepohl 1995). The minimum concentrations are quite low, ranging from pg g^{-1} to some ng g^{-1} (for the crustal elements); for some elements like Co, As, Ag and Cd the minimum concentrations are below the DL.

Table 7.1: The Ortles ice core#1 data statistics for the 1059 discrete samples analysed with an ICP-QMS and an CRC-ICP-MS.

Elements	Mean	SD	Max	Min	Max/Min	Median	25°percentile	75°percentile
Li	0.024	0.049	0.85	0.001	803	0.013	0.008	0.023
Na	21	29	576	0.52	1117	15	9.0	25
Mg	77	136	2363	3.5	679	50	35	77
Al	23	39	764	0.66	1167	17	10	26
K	13	13	169	0.07	2407	10	5.9	16
Ca	199	359	4749	10	478	119	73	193
Ti	0.26	0.31	5.0	0.003	1861	0.18	0.12	0.29
V	0.064	0.100	1.6	0.002	687	0.030	0.019	0.067
Cr	0.061	0.081	1.2	<DL		0.041	0.023	0.073
Mn	1.8	2.9	57	0.14	412	1.07	0.70	1.8
^{57}Fe	14	22	435	0.065	6692	8.2	5.5	14
Co	0.019	0.052	1.2	<DL		0.011	0.007	0.018
Cu	0.24	0.47	7.4	<DL		0.10	0.032	0.26
Zn	1.7	2.4	34	0.12	273	0.88	0.437	1.92
As	0.060	0.085	1.0	<DL		0.032	0.016	0.073
Sr	0.39	0.43	6.3	0.017	371	0.28	0.17	0.429
Ag	<DL	<DL	0.004	<DL		<DL	<DL	0.001
Cd	0.013	0.018	0.19	<DL		0.006	0.003	0.017
Sb	0.050	0.23	6.1	<DL		0.018	0.008	0.038
Te	0.010	0.011	0.08	<DL		0.007	0.004	0.012
I	0.04	0.045	0.51	<DL		0.029	0.016	0.052
Cs	0.005	0.005	0.050	<DL		0.003	0.002	0.005
Ba	0.42	0.67	14	0.033	438	0.26	0.18	0.47
Hg	0.001	0.002	0.027	<DL		<DL	<DL	<DL
Tl	0.004	0.004	0.028	<DL		0.002	0.001	0.004
Pb	1.4	3.2	87	0.050	1739	0.70	0.31	1.6
Bi	0.007	0.011	0.148	<DL		0.0030	0.0012	0.008
U	0.005	0.008	0.14	<DL		0.003	0.002	0.004

The *max to min ratio* is usually above one hundred. However, the 75° percentile is usually very close to the mean value of the dataset, meaning that the reported maximum values are part of a very small subset. Indeed, the distribution of the data is lognormal rather then normal.

The dataset can be divided in two main parts: the samples for the 2000-1800 AD periods and those from 1800 AD to the end of the core dated about 1000 BC. The former are characterized by a strong anthropogenic influence, covering the industrial revolution period and the European industrial growth of the 1960-70s. The latters, instead, mainly reflect the natural background aerosol deposition except for some periods where intense mining activities released in the atmosphere significant quantities of pollutants, such as Lead and Antimony.

The statistics for the 2000-1800 AD period are reported in Table 7.2, whereas those for the period 1800 AD to about 1000 BC in Table 7.3.

The average, median, maximum and max to min ratio values are significantly greater for the 2000-1800 AD period, mainly as a consequence of the anthropogenic influence on the Alto dell'Ortles glacier, which is located close to high-density populated areas.

The *increase factors* (IF) of the average, median and maximum concentrations

Table 7.2: 2000-1800 AD data statistics of the Ortles ice core#1; 1059 discrete samples.

Elements	Mean	SD	Max	Min	Max/Min	Median	25°percentile	75°percentile
Li	0.025	0.048	0.85	0.001	803	0.015	0.009	0.027
Na	21	19	251	1.7	148	17	9	26
Mg	73	112	1413	3.5	406	47	31	77
Al	24	48	764	0.66	1167	16	7.4	28
K	12	12	169	0.07	2407	8.3	5.1	14
Ca	200	366	4749	9.9	478	107	62	187
Ti	0.30	0.37	5.0	0.003	1861	0.20	0.12	0.39
V	0.08	0.12	1.6	0.002	687	0.0421	0.0212	0.0906
Cr	0.067	0.093	1.2	<DL		0.046	0.026	0.079
Mn	2.0	3.5	57	0.14	412	1.1	0.65	2.1
^{57}Fe	15	26	435	0.065	6692	9.4	5.2	17
Co	0.022	0.062	1.2	<DL		0.012	0.007	0.021
Cu	0.27	0.50	7.4	<DL		0.13	0.048	0.30
Zn	2.2	2.7	34	0.17	198	1.2	0.74	2.6
As	0.076	0.098	1.0	<DL		0.04	0.022	0.095
Sr	0.39	0.49	6.3	0.017	371	0.23	0.14	0.43
Ag								
Cd	0.018	0.019	0.19	<DL		0.011	0.005	0.024
Sb	0.0497	0.2428	6.1115	0.0014	4516	0.0208	0.01	0.04
Te	0.013	0.012	0.075	<DL		0.008	0.005	0.0159
I	0.044	0.049	0.51	<DL		0.031	0.014	0.055
Cs	0.005	0.005	0.050	<DL		0.004	0.002	0.007
Ba	0.49	0.80	14	0.033	438	0.30	0.19	0.54
Hg	0.001	0.002	0.027	<DL		<DL	<DL	0.002
Tl	0.004	0.004	0.028	<DL		0.003	0.002	0.006
Pb	1.8	3.8	87	0.08	1087	1.01	0.49	2.0
Bi	0.0083	0.012	0.15	<DL		0.005	0.002	0.010
U	0.005	0.009	0.14	<DL		0.003	0.001	0.005

were computed for the two selected periods. However, the firn part of the Alto dell'Ortles glacier in the last two/three decades was strongly affected by intense melting during the summer periods, such as that of 2003. The percolating water may have altered the climatic and environmental signals stored in the ice layer. It is likely that during extraordinarily warm summers the percolation events don't only affect the snow and firn of the previous year, but also those of many years before. As will be shown later in this work, some layers were characterized by very high concentrations of chemical species and elements, and the melting water percolation and refreezing probably formed them. The percolation affected the Chernobyl radionuclides deposited on the glacier after 1986 AD and they were found in a firn portion dated 1979 AD, close to a thick ice lens just before the firn ice transition; the melted water transported the radionuclide through the porous temperate firn (Gabrielli, Barbante, Bertagna, et al. 2016). However, the matching between the tritium concentration and the beta peak suggests that the percolation processes didn't affect the firn layers from the time when the radioactive fallout deposited on the surface (1963) to when it was entrapped in the ice matrix.

For this reasons, in Table 7.4 the increase factors were computed for the period 1980-1930 AD (well preserved firn and ice with the highest anthropogenic influence) and before 1800 AD. The IFs for crustal elements, such as Mg, Al and Ca, are close to one meaning that the crustal aerosol deposition remained almost constant.

Table 7.3: 1800 AD - 1000 BC data statistics of the Ortles ice core#1, 1059 discrete samples.

Elements	Mean	SD	Max	Min	Max/Min	Median	25°percentile	75°percentile
Li	0.015	0.046	0.78	0.004	215	0.010	0.007	0.012
Na	13	9.6	76	0.52	147	11	7.0	16
Mg	80	157	2363	21	110	54	41	73
Al	20	7.3	74	5.8	13	19	15	24
K	15	9.7	75	2.8	27	13	8.3	19
Ca	190	313	4260	36	117	137	97	189
Ti	0.18	0.097	0.93	0.053	18	0.16	0.13	0.20
V	0.025	0.02	0.26	0.008	33	0.022	0.017	0.027
Cr	0.043	0.044	0.38	0.004	96	0.030	0.018	0.049
Mn	1.2	0.87	7.3	0.28	26	0.93	0.72	1.3
Fe 57	9.0	9.5	138	2.5	56	7.4	5.8	9.3
Co	0.011	0.006	0.062	0.004	17	0.009	0.007	0.012
Cu	0.096	0.26	3.8	<DL		0.041	0.020	0.091
Zn	0.44	0.37	3.0	0.12	24	0.33	0.25	0.50
As	0.032	0.035	0.280	0.003	92	0.019	0.012	0.038
Sr	0.37	0.28	2.9	0.100	29	0.31	0.22	0.423
Ag	<DL	<DL	0.004	<DL		<DL	<DL	<DL
Cd	0.003	0.003	0.038	<DL		0.002	0.002	0.003
Sb	0.015	0.021	0.12	<DL		0.006	0.002	0.018
Te	0.005	0.003	0.017	<DL		0.004	0.002	0.006
I	0.029	0.022	0.21	<DL		0.025	0.017	0.034
Cs	0.003	0.002	0.021	<DL		0.003	0.002	0.003
Ba	0.26	0.18	1.8	0.075	24	0.22	0.16	0.285
Hg	<DL	<DL	0.004	<DL		<DL	<DL	0.001
Tl	0.002	0.002	0.025	<DL		0.001	0.001	0.002
Pb	0.49	0.61	4.0	0.050	80.268	0.27	0.15	0.55
Bi	0.001	0.001	0.011	<DL		<DL	<DL	0.002
U	0.004	0.006	0.089	<DL		0.003	0.002	0.004

Instead, for anthropogenic elements such as Zn, Cd and Bi (Gabrieli, Carturan, et al. 2011), the IFs are usually greater than 2 (for averages and medians). The IF for the maximum values may differ from the averaged and median IFs because intense aerosol deposition events may have happened, as caused by volcanic events.

7.2 Statistical Description and Explorative Analyses

In order to be able to detect the similarities and differences between the different elemental profiles, a multivariate statistical effort was performed. Particularly, the selected statistical techniques were the *Principal Component Analysis* (PCA) and *Agglomerative Hierarchical Clustering* (AHC).

Matrix algebra, matrices of Eigen vectors, Eigen values and correlation/covariance are involved in PCA analyses. PCA includes all the variance in the variables, including that of each element. This statistical tool allows to reduce the number of variables in the dataset and it is therefore of primarily importance in analyzing big datasets; moreover, a statistical based order of importance (i.e. variance explanation) to the involved variables is given.

Table 7.4: Increase factors for the average, median and maximum concentrations over the period 1980-1930 AD and 1800 AD–1000 BC.

	1930-1980			Increase Factor		
Element	Mean	Median	Max	Mean	Median	Max
Li	0.021	0.014	0.301	1.3	1.4	0.4
Na	23	19	251	1.7	1.7	3.3
Mg	74	56	916	0.9	1.0	0.4
Al	18	11	193	0.9	0.6	3
K	11	8.1	76.3	0.7	0.6	1.0
Ca	217	129	4671	1.1	0.9	1.1
Ti	0.30	0.22	2.06	1.7	1.3	2.2
V	0.088	0.053	0.6106	3.5	2.4	2.3
Cr	0.064	0.049	1.249	1.5	1.7	3.3
Mn	1.9	1.3	15.4	1.6	1.4	2.1
^{57}Fe	14	8.7	156.1	1.6	1.2	1.1
Co	0.016	0.011	0.247	1.5	1.1	4.0
Cu	0.24	0.13	7.43	2.5	3.3	1.9
Zn	2.4	1.5	18.6	5.4	4.7	6.3
As	0.098	0.067	1.05	3.1	3.5	3.7
Sr	0.45	0.29	6.30	1.2	0.9	2.2
Ag						
Cd	0.022	0.017	0.131	8.3	7.8	3.4
Sb	0.031	0.022	0.5109	2.0	3.4	4.2
Te	0.014	0.010	0.075	3.1	2.4	4.5
I	0.051	0.036	0.512	1.8	1.4	2.4
Cs	0.006	0.004	0.035	1.8	1.6	1.7
Ba	0.50	0.35	3.90	1.9	1.6	2.2
Hg	0.001	0.001	0.027			6.5
Tl	0.005	0.004	0.028	2.8	2.9	1.1
Pb	2.0	1.3	15.96	4.0	5.0	4.0
Bi	0.011	0.006	0.148	8.6	5.1	13.7
U	0.004	0.002	0.139	1.1	0.8	1.6

The co-variance matrix of the standardized elements is firstly computed and then the eigenvectors and the relative eigenvalues are extracted from it. The *factors* used to explain the variance of the dataset are the eigenvectors of the co-variance matrix. The variance explanation percentage of each factor (*principal components*) is given by the ratio of its eigenvalue with the sum of all the computed eigenvalues.

The principal components are ordered in terms of explanation percentages, and they are used as orthogonal axis in simple visualization plots. The variables, dots on the graph, are placed in the position corresponding to the percentage of explanation of each of the two principal component vectors selected as axis.

In geo-chemical analyses this technique is usually adopted in order to separate the elements in terms of their behavior in the dataset, in this case formed by many time series, and therefore their sources: natural (crustal) or anthropogenic (pollutants).

The AHC statistical tool allows building of a hierarchy of cluster of elements. The clusters are found by considering the *similarity index*, which is based on the *Euclidean distance* between each element. A dendrogram is then produced in order to visualize the various clusters and the nodes between them.

In this work both PCA and AHC were performed by using the free-software *Past3* (Ø. Hammer et al. 2001).

7.2.1 PCA and AHC Applied on the Ortles Ice Core TE dataset

The Alto dell'Ortles ice core#1 dataset of trace element (discrete samples) was statistically analysed by using both PCA and AHC statistical tools.

Particularly, the PCA analyses require the data to be normally distributed, which is not the case for the Ortles trace element data: the distributions are indeed *log-normal* rather than *normal*. Before applying the PCA and AHC tools the elements concentration matrix was logarithmically transformed in order to improve the *normality* of the data. Moreover, a ranking of the data was performed in order to give the same weight to all the profile, independently from the concentrations and therefore only focusing on the variances.

In order to distinguish the intense anthropogenic-influenced period from the less influenced period the dataset was divided in two: from 2000 AD to 1800 AD, and from 1800 AD to the end of the core, about 1000 BC.

The PCA results for the period 2000-1800 AD are shown in Fig. 7.1. The first principal component (PC1) explained the 93.49 % of the total variance, while the second (PC2) only 1.1 % and the third (PC3) 0.9 %. The values are reported in the eigenvalues scale. The first plot (PC1-PC2) seems to separate the crustal elements with the Component 1. Crustal elements, red dots, are those more concentrated and have positive loadings on the PC1. PC2, explains about 1 % of the variance and it was interpreted as separating the anthropogenic influenced elements and the marine ones (Na) from the crustals. Interestingly As and Cu are well divided by the Component 2. PC3, in the central and rightmost graphs separate even more the crustal elements, characterized by a negative loading, from those anthropogenic and marine; I is divided with the Component 3 and has a positive loading as well as Na, suggesting a marine origin; however, the Ortles *potential sources analysis* (P. Gabrielli personal communication) shows that Na may have also a strong crustal influence. Two groups are also divided by Components 3, Tl, Cd and Sb with a positive loading and U, Bi, Li, Cs and Co. However, by considering all the profiles from 2000 AD it is possible that the percolation effect in relocating the elements (especially the soluble ones) may have influenced the PCA results.

The AHC mainly describes the same information given by the PCA, dividing the most abundant crustal elements from those with mainly anthropogenic origin (Fig. 7.2).

The correlation matrix (Table 7.5) was performed by using the free software R (R Development Core Team 2008) and the *cor* function applied to the discrete raw dataset. The missing values were treated by using the command *pairwise.complete.obs* and the selected method was *spearman*, which calculate the *non-parametric Spearman Correlation* between the TEs time vectors. All the correlation coefficients are reported in Table 7.5 and the coefficients higher than 0.6 were highlighted in green. A clear correlation results for Mg, Ca, Ba, Sr and Mn which have usually crustal

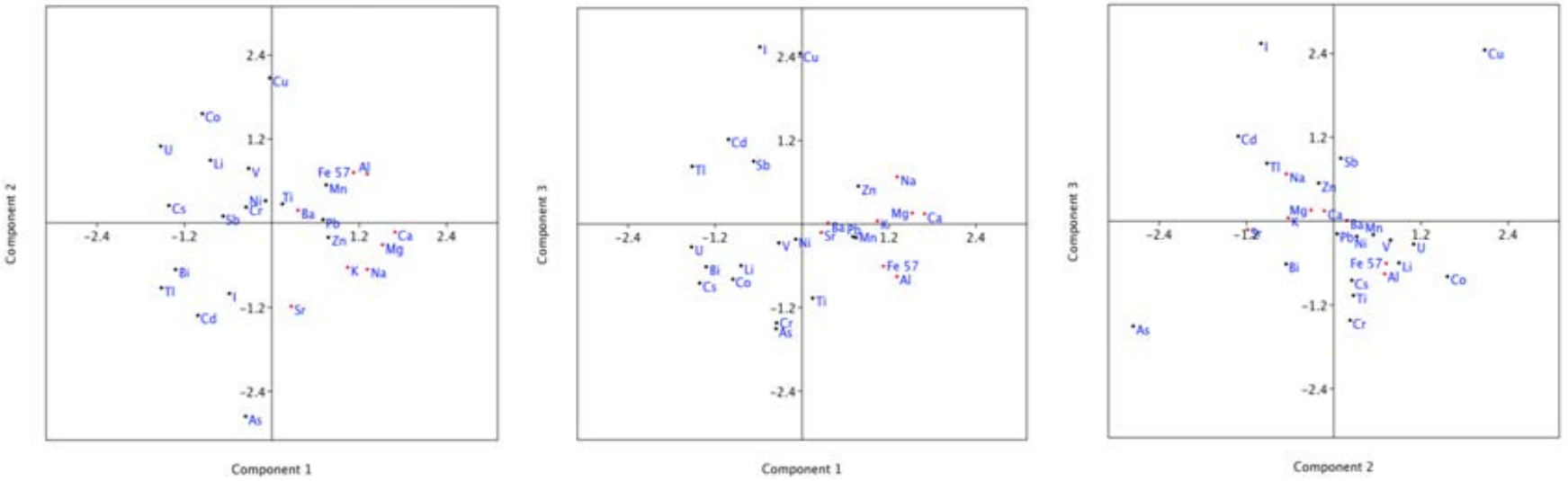

Figure 7.1: PCA results for the period 1800-2000 AD for the Ortles core#1 dataset. The three graphs correspond to the various PCs combinations. The PSA crustal elements are showed with red dots.

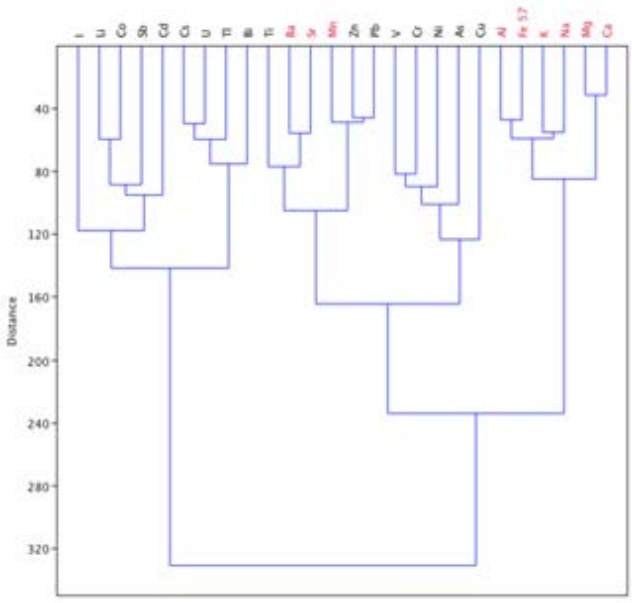

Figure 7.2: AHC results for the period 1800-2000 AD for the Ortles core#1 dataset. The PSA crustal elements are written in red.

origin; however, Al, Fe and Ti (correlating with eahc other) don't correlate with most element of this group; Co and U correlate with elements from both the two groups. I, Cr, Ni don't show almost any significant correlation. V, Pb, Bi, Sb, Zn, Cd, Tl and As form a clear correlation group and their origin appears to be anthropogenic (industrial activities and coal combustion). The strong correlations of U with all the other crustal (and crustal/anthropogenic) elements seems to prove that at the Alto dell'Orltes glacier the U has mainly crustal origin in contrast with the results for the Colle Gnifetti ice core for this period (Gabrieli 2008).

The period from 1800 AD to 1000 BC was less influenced by the anthropogenic activities and pollutants in the European region, as observed in the only other Alpine ice core covering this period, Colle Gnifetti ice core (Gabrieli 2008). However, the anthropogenic pollutants source was significant during the Roman Empire and the Medieval periods and after 1300 AD with the increase of mining activities.

In Fig. 7.3 the PCA results for the 1800AD-1000BC period are shown. The first principal component (PC1) explained the 95.8 % of the total variance, while the second (PC2) 1.4 % and the third (PC3) 0.7 %. The first component seems to divide the crustal elements from the anthropogenic and low concentrated ones, as observed also for the period 2000-1800 AD. Some elements, such as Cu, Ti and Ba appear not to be as explained as in other crustal elements as Ca or Mg. The second component creates an interesting group of elements with positive loading: Pb, Sb, As and Bi. As it will be point out later in this work in the concentration profiles and EF descriptions, during three distinct periods (Roman period and about 1300 and 1600 AD) these four elements increased together, and this was probably caused by intense smelting activities, especially for Ag mines (Uglietti, Gabrielli, Cooke, et al. 2015).

The third component clearly separates Cu from all the other elements. A distinct behavior of Cu was also observed in Gabrieli 2008. The biplot for the 2nd and 3rd components clearly indicates which were the most anthropogenically-

Table 7.5: The correlation matrix for the period 1800-2000 AD of the Ortles ice core#1 dataset.

	Na	Mg	Al	K	Ca	Ti	^{57}Fe	I	Ba	Li	V	Cr	Mn	Co	Ni	Cu	Zn	As	Sr	Cd	Cs	Tl	Pb	U	Sb	Bi
Na		0.43	0.07	0.66	0.56	0.18	0.14	0.25	0.46	0.41	0.17	0.21	0.33	0.28	0.36	0.28	0.44	0.42	0.65	0.44	0.12	0.40	0.17	0.07	0.46	0.18
Mg			0.47	0.47	0.86	0.45	0.55	0.22	0.62	0.53	0.46	0.45	0.65	0.57	0.41	0.34	0.47	0.55	0.73	0.54	0.60	0.67	0.47	0.56	0.44	0.47
Al				0.31	0.29	0.49	0.81	0.01	0.57	0.68	0.51	0.46	0.54	0.76	0.32	0.34	0.32	0.20	0.30	0.18	0.78	0.35	0.49	0.82	0.27	0.47
K					0.49	0.29	0.36	0.07	0.48	0.57	0.20	0.28	0.39	0.49	0.39	0.34	0.39	0.38	0.56	0.34	0.29	0.34	0.16	0.29	0.41	0.22
Ca						0.43	0.43	0.31	0.67	0.46	0.43	0.40	0.59	0.44	0.41	0.33	0.55	0.64	0.91	0.64	0.49	0.72	0.43	0.38	0.47	0.41
Ti							0.68	0.28	0.59	0.52	0.46	0.38	0.53	0.51	0.36	0.35	0.46	0.32	0.38	0.39	0.62	0.50	0.44	0.53	0.40	0.42
^{57}Fe								0.20	0.68	0.68	0.65	0.51	0.63	0.74	0.52	0.46	0.53	0.32	0.38	0.38	0.80	0.52	0.59	0.80	0.39	0.55
I									0.39	0.24	0.45	0.13	0.34	0.25	0.23	0.33	0.40	0.14	0.25	0.41	0.14	0.36	0.35	0.16	0.34	0.15
Ba										0.70	0.72	0.51	0.73	0.67	0.51	0.53	0.76	0.50	0.68	0.68	0.70	0.73	0.64	0.56	0.59	0.55
Li											0.55	0.53	0.66	0.82	0.58	0.70	0.60	0.28	0.45	0.44	0.63	0.45	0.45	0.64	0.65	0.39
V												0.53	0.64	0.64	0.62	0.56	0.71	0.26	0.31	0.58	0.61	0.59	0.75	0.62	0.51	0.60
Cr													0.45	0.45	0.50	0.48	0.52	0.35	0.33	0.42	0.51	0.43	0.48	0.45	0.47	0.49
Mn														0.80	0.50	0.60	0.66	0.33	0.48	0.63	0.70	0.61	0.55	0.66	0.55	0.43
Co															0.57	0.61	0.51	0.19	0.37	0.41	0.69	0.44	0.48	0.81	0.51	0.38
Ni																0.65	0.65	0.27	0.29	0.51	0.39	0.44	0.43	0.44	0.62	0.35
Cu																	0.68	0.17	0.20	0.52	0.42	0.40	0.45	0.48	0.72	0.32
Zn																		0.45	0.47	0.78	0.55	0.71	0.70	0.41	0.67	0.52
As																			0.65	0.62	0.47	0.69	0.45	0.22	0.37	0.55
Sr																				0.55	0.42	0.64	0.33	0.27	0.40	0.35
Cd																					0.51	0.77	0.63	0.30	0.60	0.48
Cs																						0.68	0.70	0.79	0.41	0.66
Tl																							0.72	0.47	0.51	0.64
Pb																								0.58	0.48	0.73
U																									0.40	0.53
Sb																										0.48

influenced elements.

The AHC dendogram (Fig. 7.4) still divides the crustal and the anthropogenic elements, whereas the strong relations of the anthropogenically influenced elements is not clearly visible.

The correlation matrix, instead, partly confirm what found for the first three PCA factors: Pb, Sb, As and Bi are strongly correlated (which was not the case for the last two centuries) (Table 7.6). Most of the crustal elements (both groups identified in the correlation matrix for the period 1800-2000 AD) appears to be more correlated in this time interval, even if Ca and Al still show some differences. Ni, Zn, Ag, Cr and Cd don't significantly correlates with the other elements, nor between each other.

7.3 Seasonality of Trace Elements Deposition in the Firn/Ice

Generally, the aerosol and dust deposition doesn't take place at a constant rate during the year but it is characterized instead by a more or less marked seasonality, with the highest deposition during summer. Indeed, both the pollutant sources and the atmospheric circulation patterns and vertical structure can significantly vary year by year or on decades-long time scales. In the Paragraph 6.4.4 the author computed the daily maximum depth of the boundary layer, defined as the height of the temperature inversion layer, and the monthly averaged values for the years 2014-2015. The results clearly show that during summer the frequency of days with a DBL higher than the Alto dell'Ortles glacier altitude are much more frequent than during winter, when very low altitude (below 500 m msl) temperature inversions usually doesn't allow the emitted pollutants to be transported at high altitude by uplift winds.

In order to check the preservation of the seasonal cycles in the firn, despite the recent intense melting events, selected trace elements profiles were plotted with the water stable isotopes, which are amongst the most resistant during percolation events. The comparison was done using the high resolution $\delta^{18}O$ profile measured by G. Dreossi (Dreossi 2016) and three selected trace elements discretely analised (this work): Ba, Mg and Pb. Ba and Mg have mainly crustal origin, been component of the rocks forming Mt. Ortles and the surrounding areas, whereas Pb has mainly anthropogenic origin on the Alto dell'Ortles glaciers (Gabrieli, Carturan, et al. 2011), even if almost the same amount of Ba and Pb was found in the soil and dust sampled close to the Mt. Ortles area (*principal sources areas*, PSA; P. Gabrielli and G. Bertagna personal communication).

The Ortles ice core#1 profiles were divided in 6 subsections in order to better analyse and observe the seasonal fluctuations: 0 m–20 m, 20 m–40 m, 40 m–60 m, 60 m–64 m, 64 m–68 m, 68 m–73.5 m. The trace elements profiles are represented in a logarithmic scale in order to decrease in amplitude the highest concentration peaks and to easily visualize the small oscillations; in this way, the comparison with the generally smoothed isotopic signal is facilitated. In figures 7.6, 7.7 and 7.8 the 6 intervals are showed and the grey lines represents the simultaneous isotopic and trace elements increase. Especially in the deepest part of the core, characterized by very thin ice layers, grey lines were drawn even if two of the three selected trace

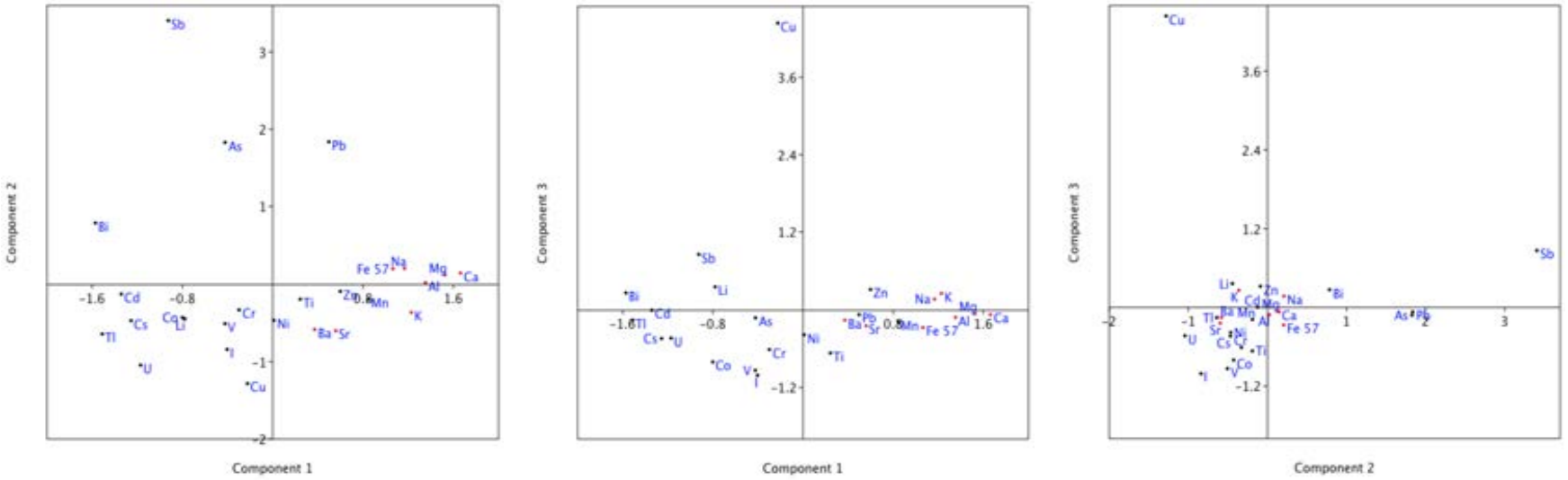

Figure 7.3: PCA results for the period 1800 AD - 1000 BC for the Ortles core#1 dataset. The three graphs correspond to the various PCs combinations. The PSA crustal elements are showed with red dots.

Table 7.6: The correlation matrix for the period 1800 AD - 1000 BC of the Ortles ice core#1 dataset.

	Na	Mg	Al	K	Ca	Ti	^{57}Fe	I	Ba	Li	V	Cr	Mn	Co	Ni	Cu	Zn	As	Sr	Ag	Cd	Cs	Tl	Pb	U	Sb	Bi
Na		0.41	0.16	0.77	0.52	0.21	0.22	0.41	0.61	0.44	0.30	0.12	0.23	0.27	0.39	0.36	0.43	0.23	0.68	0.21	0.40	0.05	0.27	0.01	0.16	0.09	−0.09
Mg			0.38	0.68	0.91	0.41	0.61	0.57	0.66	0.57	0.61	0.16	0.54	0.47	0.44	0.35	0.37	−0.04	0.72	0.12	0.47	0.46	0.58	−0.08	0.75	−0.23	−0.33
Al				0.29	0.33	0.73	0.76	0.26	0.57	0.71	0.72	0.27	0.63	0.74	0.29	0.19	0.33	0.16	0.33	0.24	0.40	0.76	0.58	0.25	0.57	0.09	0.17
K					0.75	0.32	0.43	0.57	0.78	0.61	0.42	0.13	0.43	0.40	0.52	0.56	0.53	0.08	0.78	0.21	0.51	0.25	0.47	−0.08	0.51	−0.17	−0.28
Ca						0.40	0.57	0.59	0.75	0.55	0.58	0.13	0.56	0.46	0.44	0.33	0.40	0.04	0.89	0.12	0.51	0.37	0.56	−0.05	0.68	−0.19	−0.34
Ti							0.75	0.25	0.60	0.62	0.71	0.17	0.56	0.68	0.32	0.13	0.31	0.20	0.38	0.25	0.35	0.75	0.58	0.24	0.58	0.08	0.15
^{57}Fe								0.32	0.67	0.72	0.79	0.29	0.69	0.78	0.48	0.26	0.40	0.08	0.50	0.21	0.46	0.81	0.65	0.10	0.76	−0.06	0.00
I									0.48	0.35	0.39	0.13	0.53	0.43	0.29	0.25	0.35	0.09	0.53	0.15	0.40	0.27	0.45	0.03	0.54	−0.17	−0.16
Ba										0.76	0.69	0.17	0.65	0.62	0.43	0.38	0.48	0.15	0.84	0.20	0.54	0.50	0.59	0.05	0.60	−0.07	−0.15
Li											0.66	0.28	0.56	0.66	0.43	0.47	0.52	0.12	0.57	0.18	0.49	0.62	0.60	0.17	0.55	0.10	0.02
V												0.51	0.66	0.72	0.40	0.25	0.34	0.14	0.55	0.23	0.46	0.70	0.61	0.15	0.68	0.00	0.03
Cr													0.16	0.26	0.33	0.31	0.24	0.05	0.10	0.09	0.23	0.24	0.20	0.05	0.16	0.07	0.12
Mn														0.80	0.34	0.21	0.41	0.11	0.54	0.19	0.56	0.66	0.65	0.19	0.73	−0.08	−0.02
Co															0.46	0.28	0.40	0.15	0.48	0.19	0.49	0.74	0.66	0.20	0.68	0.01	0.11
Ni																0.45	0.47	−0.03	0.39	0.14	0.33	0.37	0.42	−0.16	0.42	−0.12	−0.09
Cu																	0.45	0.05	0.33	0.06	0.32	0.17	0.32	−0.06	0.34	−0.03	−0.08
Zn																		0.26	0.38	0.43	0.56	0.26	0.41	0.34	0.36	0.29	0.15
As																			0.15	0.32	0.28	0.10	0.16	0.66	−0.04	0.69	0.62
Sr																				0.10	0.52	0.29	0.49	−0.03	0.53	−0.10	−0.28
Ag																					0.31	0.30	0.32	0.45	0.17	0.34	0.38
Cd																						0.35	0.50	0.29	0.50	0.17	0.09
Cs																							0.75	0.16	0.71	−0.02	0.18
Tl																								0.22	0.74	0.00	0.10
Pb																									0.02	0.77	0.64
U																										−0.27	−0.16
Sb																											0.70

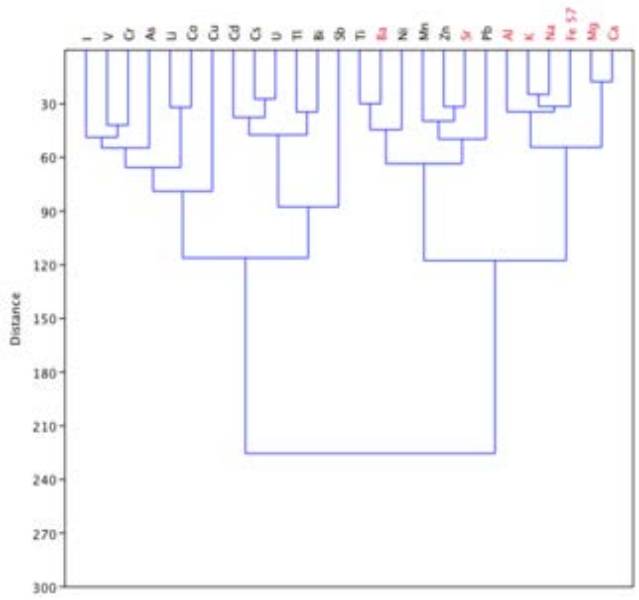

Figure 7.4: AHC results for the period 1800 AD -1000 BC for the Ortles core#1 dataset. The PSA crustal elements are written in red.

elements grown and the other remain almost constant.

From 0 m to 20 m (Fig. 7.6a) the isotopic oscillations are clearly followed by the trace elements concentrations. A decrease in the isotopic oscillation amplitude is observed throughout the first 20 m, and it is likely caused by the melting water percolation. The upper isotopic values are quite high for an alpine site (Dreossi 2016), but going deeper the maximum values decrease according to the post-depositional smoothing processes. In Dreossi 2016 a tentative seasonality was given in the first 0 m–20 m by following the seasonal cycles but the actual dating doesn't agree (Gabrielli, Barbante, Bertagna, et al. 2016); this may be explained by the post-depositional smoothing effect in the firn part. Comparing the proposed annual layer counting with the actual Ortles dating at the end of the first 20 m the Dreossi 2016 is about ten years less. Therefore, the isotopic oscillations don't follow the real dating and consequently also the highlighted common oscillations of the trace elements. However, oscillations characterized by a higher frequency can be observed in the TEs profiles, meaning that a more preserved seasonality characterized their profiles. The isotopic peak at about 15 m dating is dated to 17 years B2011 and, for all the selected TEs there are enough oscillations to infer the correct dating (even if this is not straightforward without a clear isotopic profile).

In the second graph of Fig. 7.6 the comparison is made from 20 m to 40 m of depth. The oscillations of the isotopic profile become less clear, but the relation with the trace elements oscillations remains high. A decreasing of the average isotopic value is observed as a consequence of the recent increase in atmospheric temperature but it was probably amplified by the percolation events. On the contrary, the trace elements profiles remain constant on average, or slightly increasing. Around 30 m of depth the isotopic profiles was clearly affected by the percolation events but the trace elements, especially Ba and Pb, instead preserved the seasonal oscillations. It's interesting to observe that trace elements have seasonal oscillations that modulate other kinds of bigger amplitude oscillations, clearly visible

Figure 7.5: Dolomites, Eastern Alps (28/09/2015). The termal inversion layer is below the mountain summit (Cima Tosa, 3173 m). Photograph taken from Cima Presanella (3558 m) by G. Comai.

with the logarithmic scale. The firn ice transition is between 24 m and 30 m and, as already described in the Paragraph 2.4.2 and 2.4.3, it is smoothed thus confirming the continuity of the record. A thick ice lens was observed at a depth of 24 m (Paragraph 2.4.5) and both $\delta^{18}O$ and trace elements show particular features at this depth: the profile of the former appears almost completely smoothed, whereas the latter present high concentration levels. Particularly, the Lead concentration measured at this level is the highest of the whole dataset, about 80 ng g^{-1} (the same happens for Sb). It is likely that this is a layer where the percolating water refreezes causing the concentration of many elements.

From 40 m to 60 m, the isotopic oscillations become thinner but almost all of them are still observable in the trace elements profiles. In the lower part of the graph the isotopic resolution changed as well as that of the trace elements (3 cm). At a depth of 47 m the lowest minimum is observed in the isotopic profile and very interestingly this minimum is observed also in the trace elements profiles, with very low values especially for Ba and Pb. It is likely that these minimum was caused by an extraordinarily snowy winter season (ongoing research).

After 60 m of depth, the profile was divided again in three lower intervals in order to clearly observe the oscillations. Four cold periods (isotopic minima) are observed at 60.7 m, 61.6 m, 62.5 m and 63.4 m, and a simultaneous decrease of the Pb and Mg concentrations are also detected, whereas the Ba profile seems not to be strongly affected during each minimum. Probably the cold periods caused a decrease of the incoming anthropogenic derived Pb, while the increased high altitude winds may have caused an increased in crustal dust deposition.

Considering the final Ortles core#1 dating a time range of about 300 years is between 64 m and 68 m. 300 years in 4 meters means that a complete seasonal cycle is preserved in about 0.75 cm of ice, therefore the 2 cm samples for the isotopic analyses and the 3 cm samples from the CFA were not sufficiently small to resolve the cycles. The consequence is an inevitable *aliasing* in the climatic and environmental

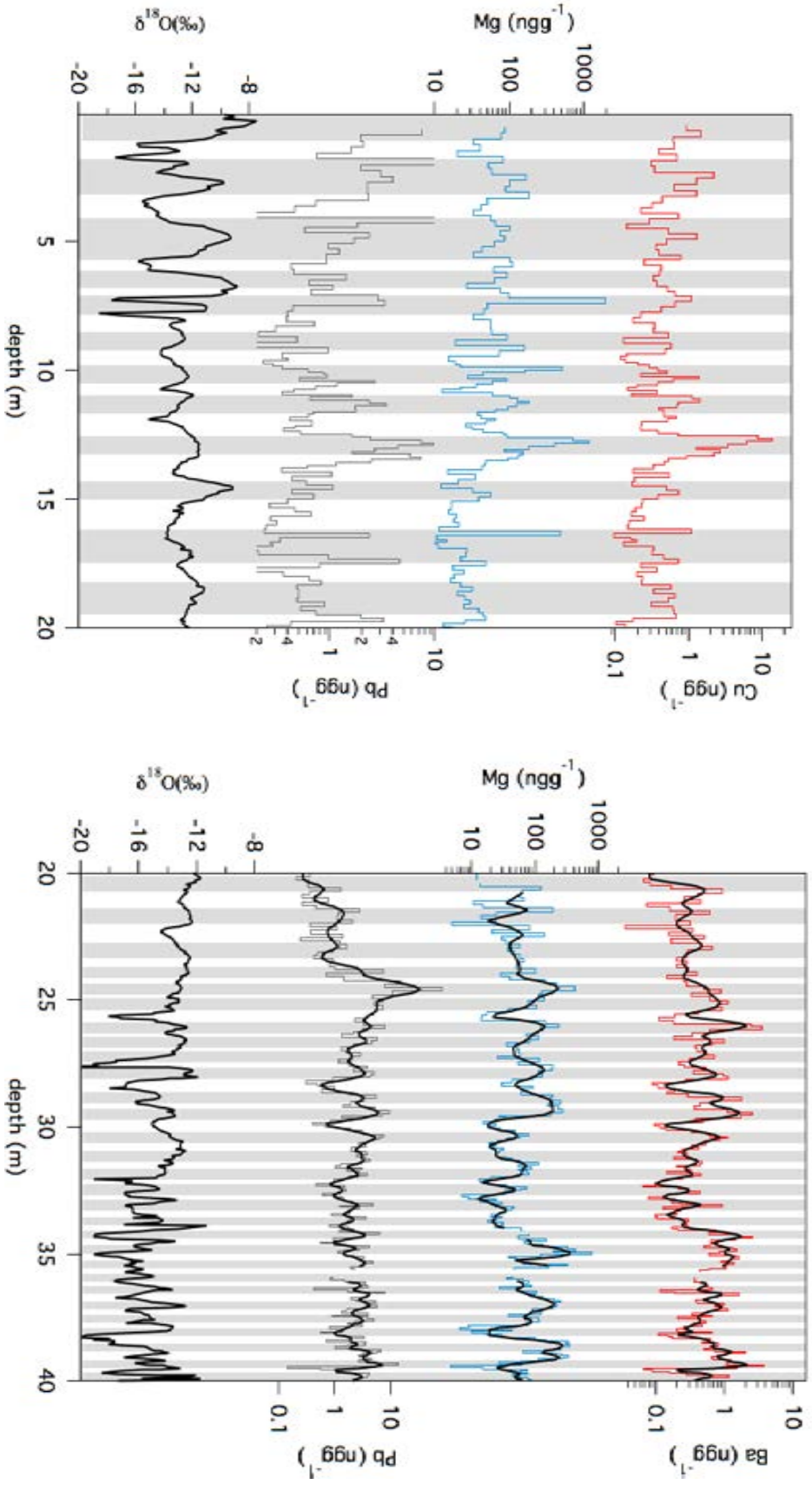

Figure 7.6: Ortles ice core#1 profiles of $\delta^{18}O$ (Dreossi 2016), Ba, Mg and Pb (this work) divided in 6 sections (here 0 m–20 m, 20 m–40 m). grey lines represent the simultaneous increasing periods, i.e. warm periods.

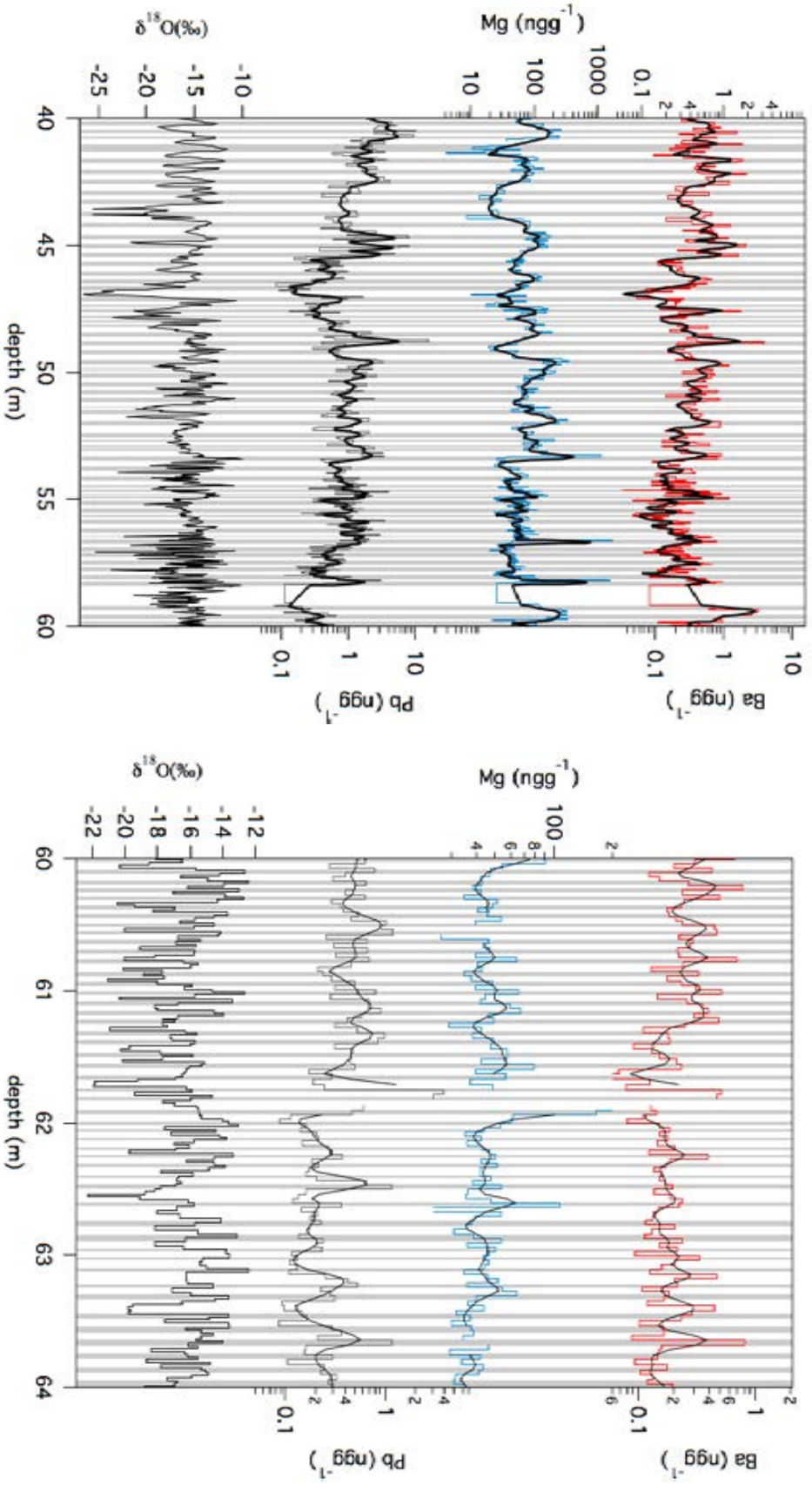

Figure 7.7: Ortles ice core#1 profiles of $\delta^{18}O$ (Dreossi 2016), Ba, Mg and Pb (this work) divided in 6 sections (40 m–60 m, 60 m–64 m). grey lines represent the simultaneous increasing periods, i.e. warm periods.

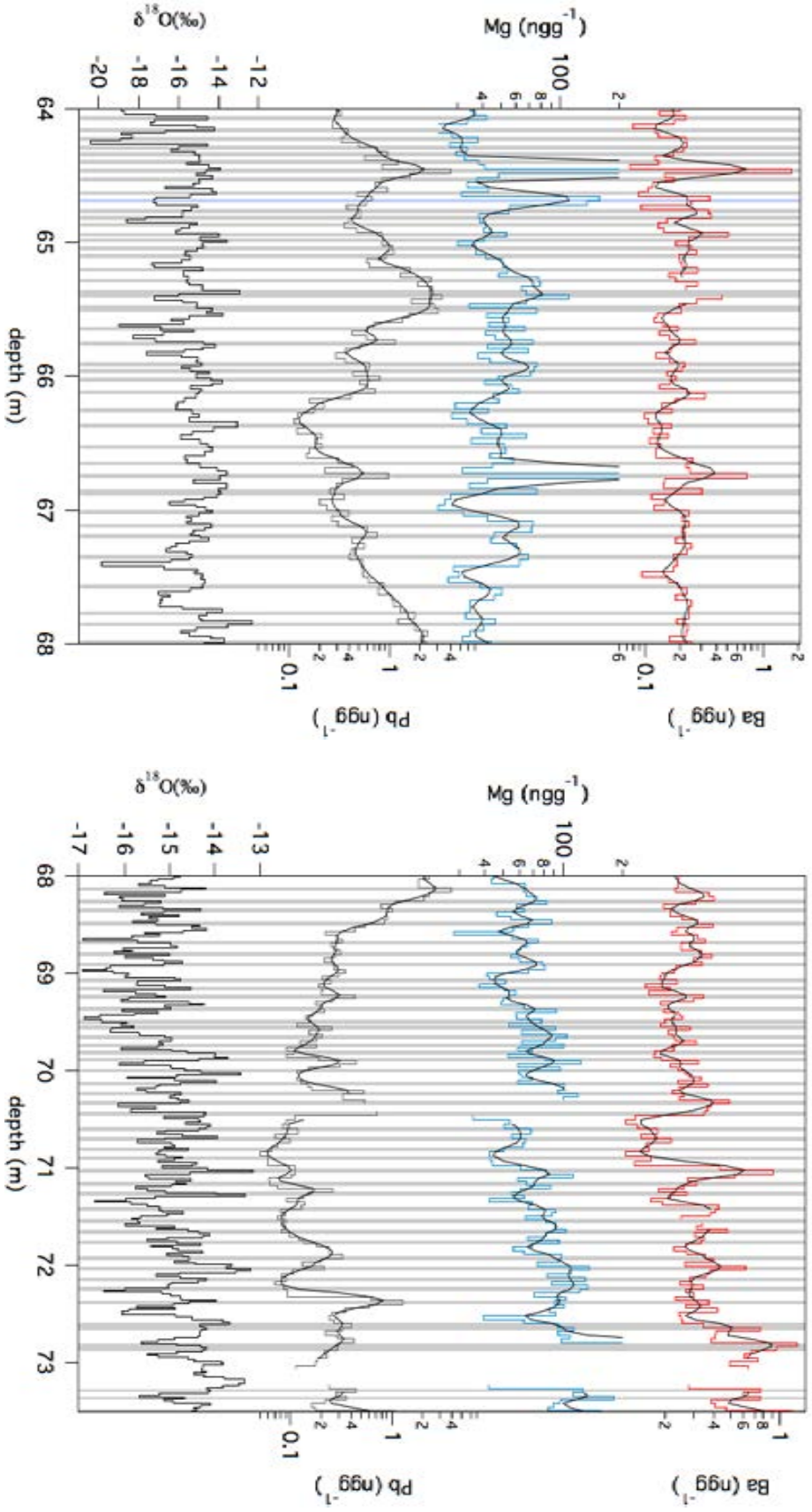

Figure 7.8: Ortles ice core#1 profiles of $\delta^{18}O$ (Dreossi 2016), Ba, Mg and Pb (this work) divided in 6 sections (64 m–68 m, 68 m–73.5 m). grey lines represent the simultaneous increasing periods, i.e. warm periods.

signal; but, the variation trends can still be observed.

From 68 to 73.5 meters simultaneous variations can still be observed in the signals, despite high amplitude oscillations characterized the trace elements profiles.

7.4 Trace Elements Deposition Over the Last 3000 Years

7.4.1 Results

The Ortles ice core#1 was melted and analysed for trace elements concentration by mean of a melting system coupled with a CFA system connected to an ICP-QMS. Moreover, more than 1000 water discrete samples were analysed discretly with an ICP-QMS and a CRC-ICP-MS. All the elements measured continuously were also measured discreetly. The method used is described in Chapter 5.

The EFs were computed for the discrete dataset by using Ba as a reference crustal element but in a slightly different way compared to Gabrieli 2008. The common way was to use as a reference the elemental concentrations in the upper crust as reported by Wedepohl 1995. However, the results may be greatly influenced by the changing in the rocks composition in different areas and that's why usually only EFs greater than 10 were considered. The Ortles PSA could also be used but the results were obtained after a 30 days acidifications of the airborne dust particles following the methods described in Uglietti, Gabrielli, Cooke, et al. 2015. For this work the samples were acidified and analysed after less than one day, therefore the concentrations may be underestimate but, on the other side, the analyses of I, Ag and Hg were performed (I and Hg are not stable in Nitric acid solutions and, as reported in Uglietti, Gabrielli, Olesik, et al. 2014, the Ag concentrations halves in a two weeks acidification period, making its concentration not detectable by the ICP-QMS used for this work).

In this work the reference concentration of Ba and of all the other elements was taken at a depth corresponding to a very low anthropogenic influenced period (8th century) were the measured concentration where low (without any apparent influence neither natural, as volcanoes, nor anthropogenic). For Na and I the EF compared to a crustal elements could be misleading but considering the marine and crustal sources of Na and the not well understood sources of I in this region, it may give interesting hints.

The trace elements profiles over the last 3000 years are reported in the graphs from Fig. 7.9 to Fig. 7.20 (the uncertainty in the dating is reported in the Section 2.5.2). In the graphs of the results the discrete analyses profiles are shown with black lines (filled to zero and not) and, when available, they are together with the continuous flow results, the background grey line filled to zero. The EFs are always shown with a grey line filled to zero.

7.4.2 Discussion

Crustal Elements

The concentration of the crustal elements (Li, Na, Mg, Al, K, Ca, Ti, Fe, Sr, Ba) remained almost constant in the last three millennia. The highest median increase

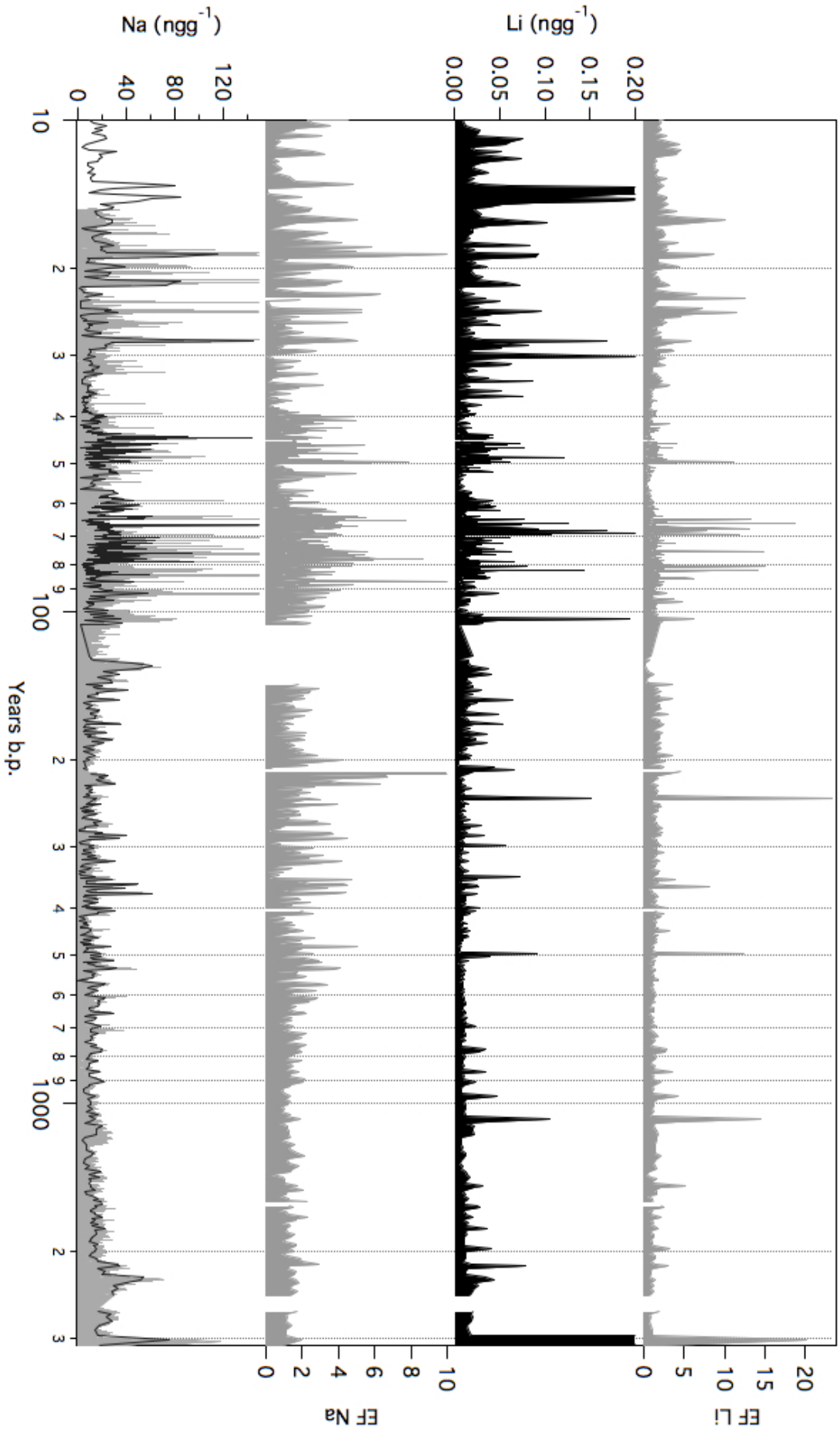

Figure 7.9: Li and Na profiles and EFs in the Ortles ice core#1. Black line: discrete dataset; grey line: continuous dataset and EFs.

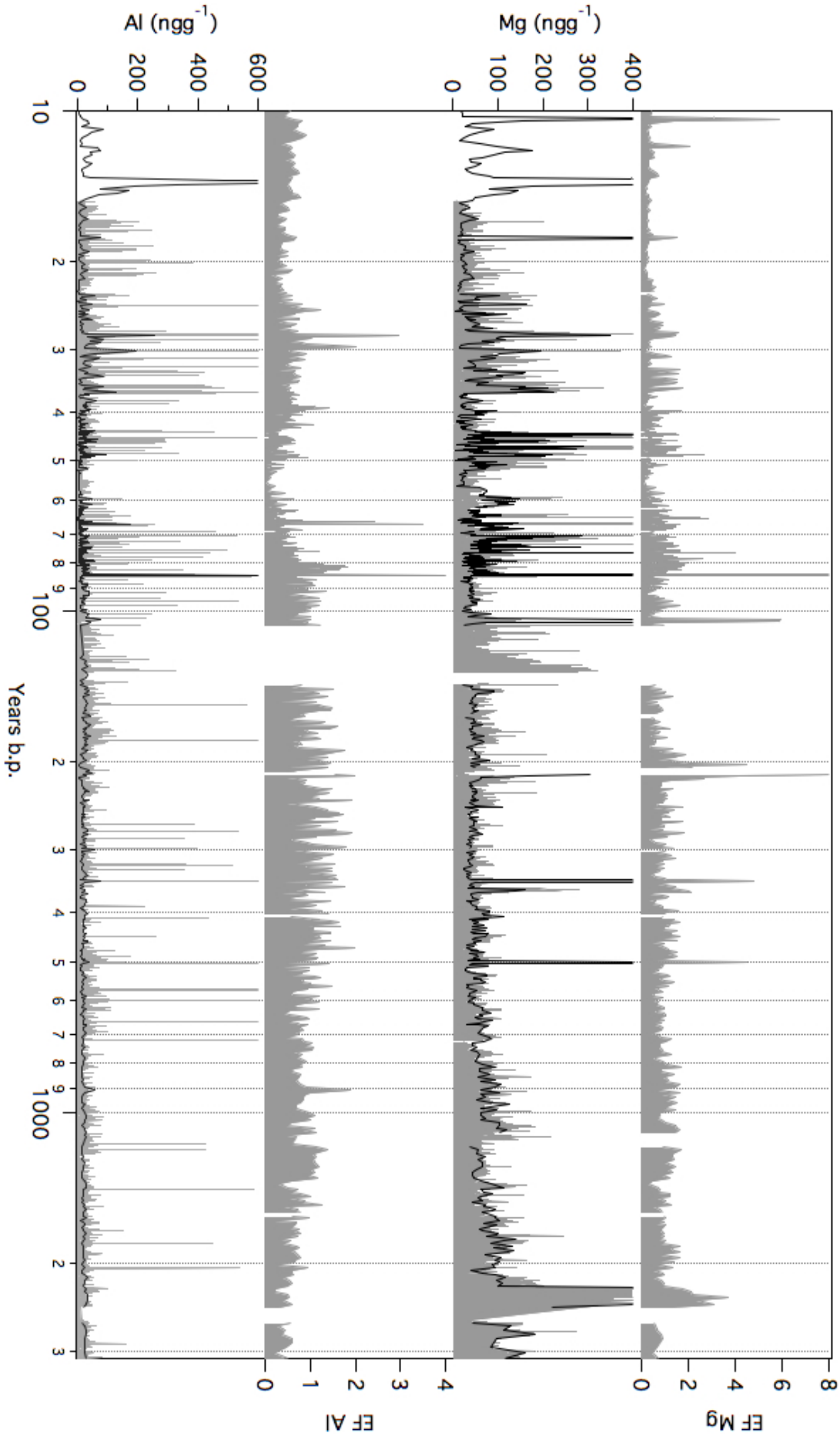

Figure 7.10: Mg and Al profiles and EFs in the Ortles ice core#1. Black line: discrete dataset; grey line: continuous dataset and EFs.

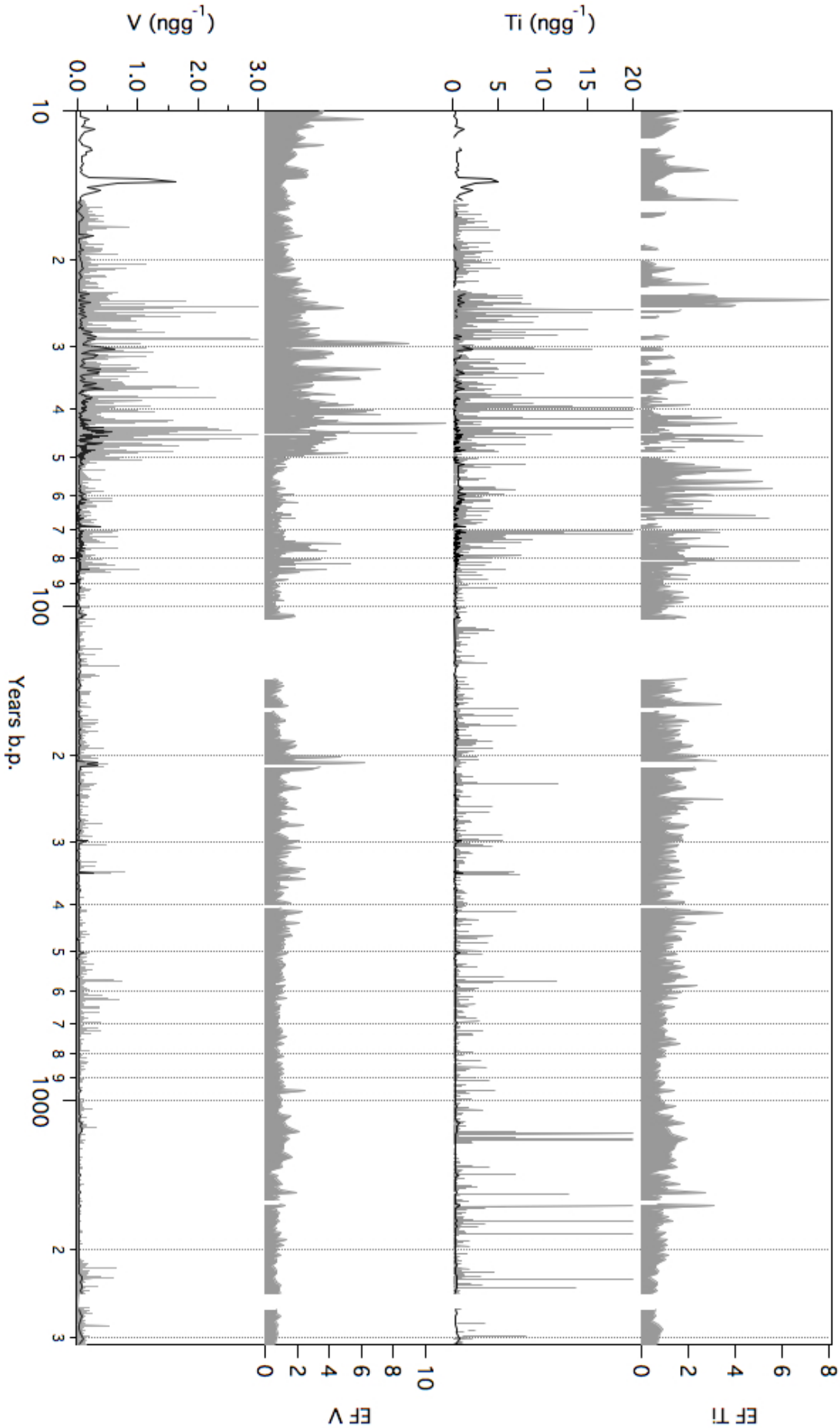

Figure 7.11: Ti and V profiles and EFs in the Ortles ice core#1. Black line: discrete dataset; grey line: continuous dataset and EFs.

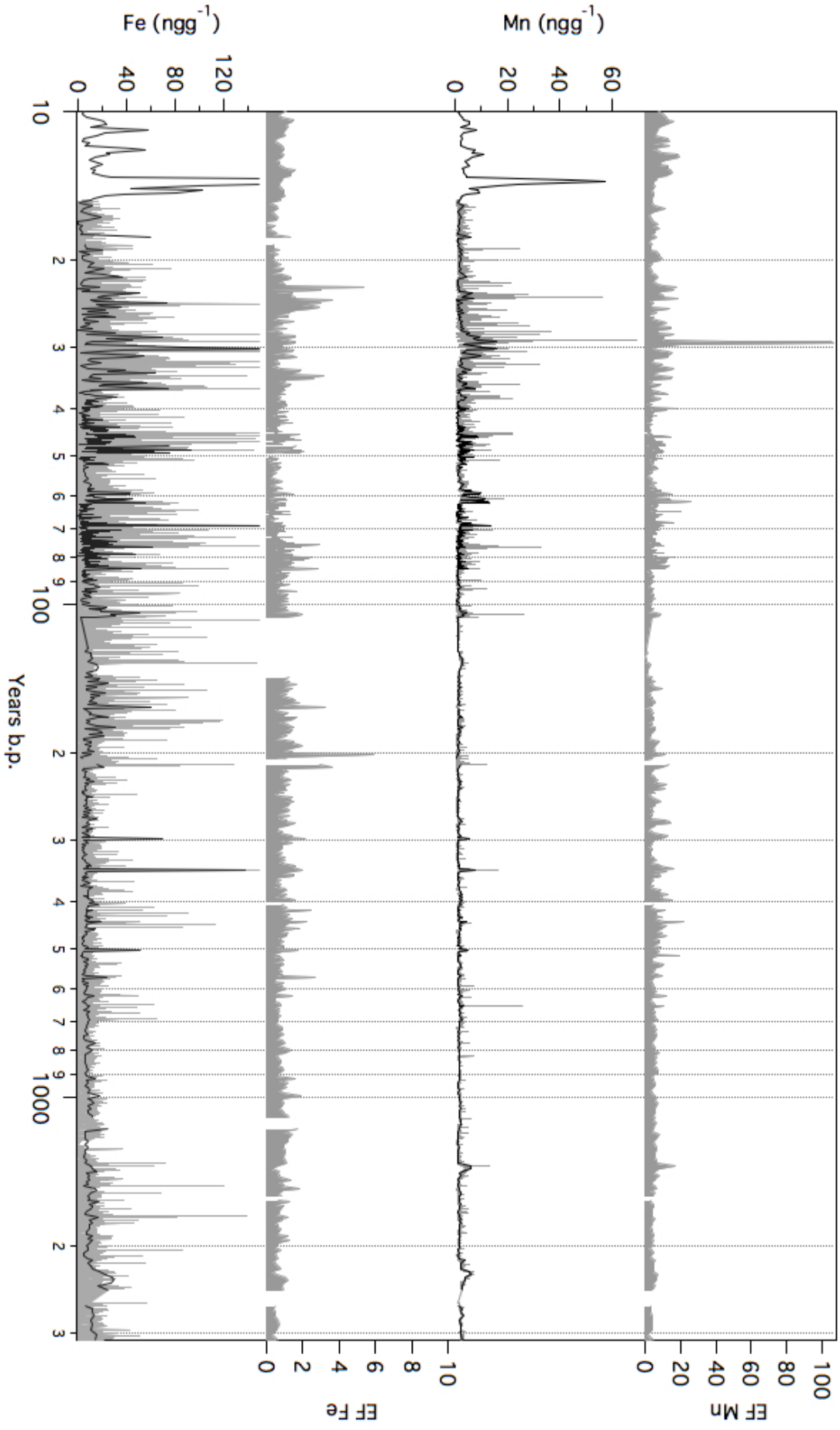

Figure 7.12: Mn and Fe profiles and EFs in the Ortles ice core#1. Black line: discrete dataset; grey line: continuous dataset and EFs.

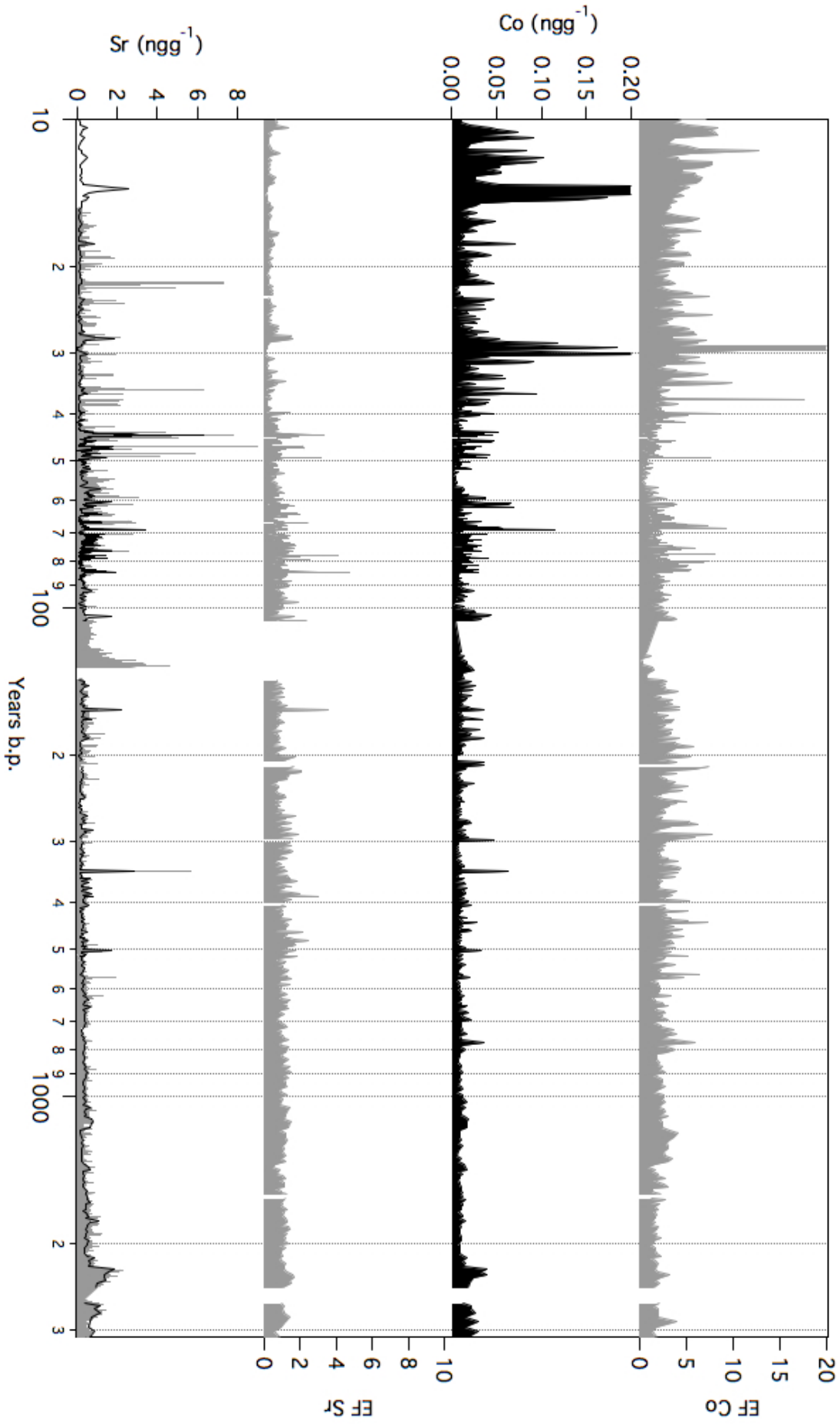

Figure 7.13: Co and Sr profiles and EFs in the Ortles ice core#1. Black line: discrete dataset; grey line: continuous dataset and EFs.

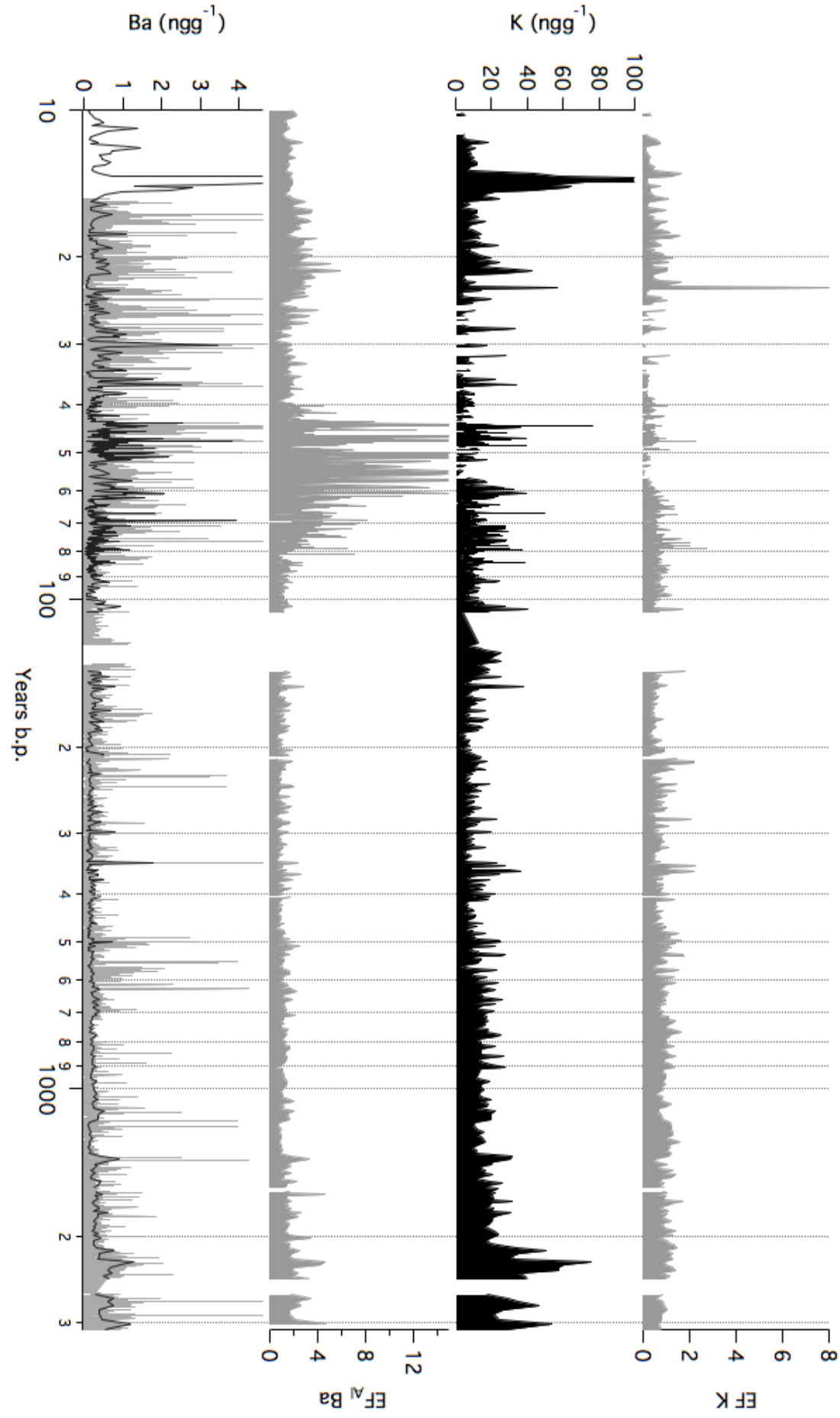

Figure 7.14: K and Ba profiles and EFs in the Ortles ice core#1. Black line: discrete dataset; grey line: continuous dataset and EFs.

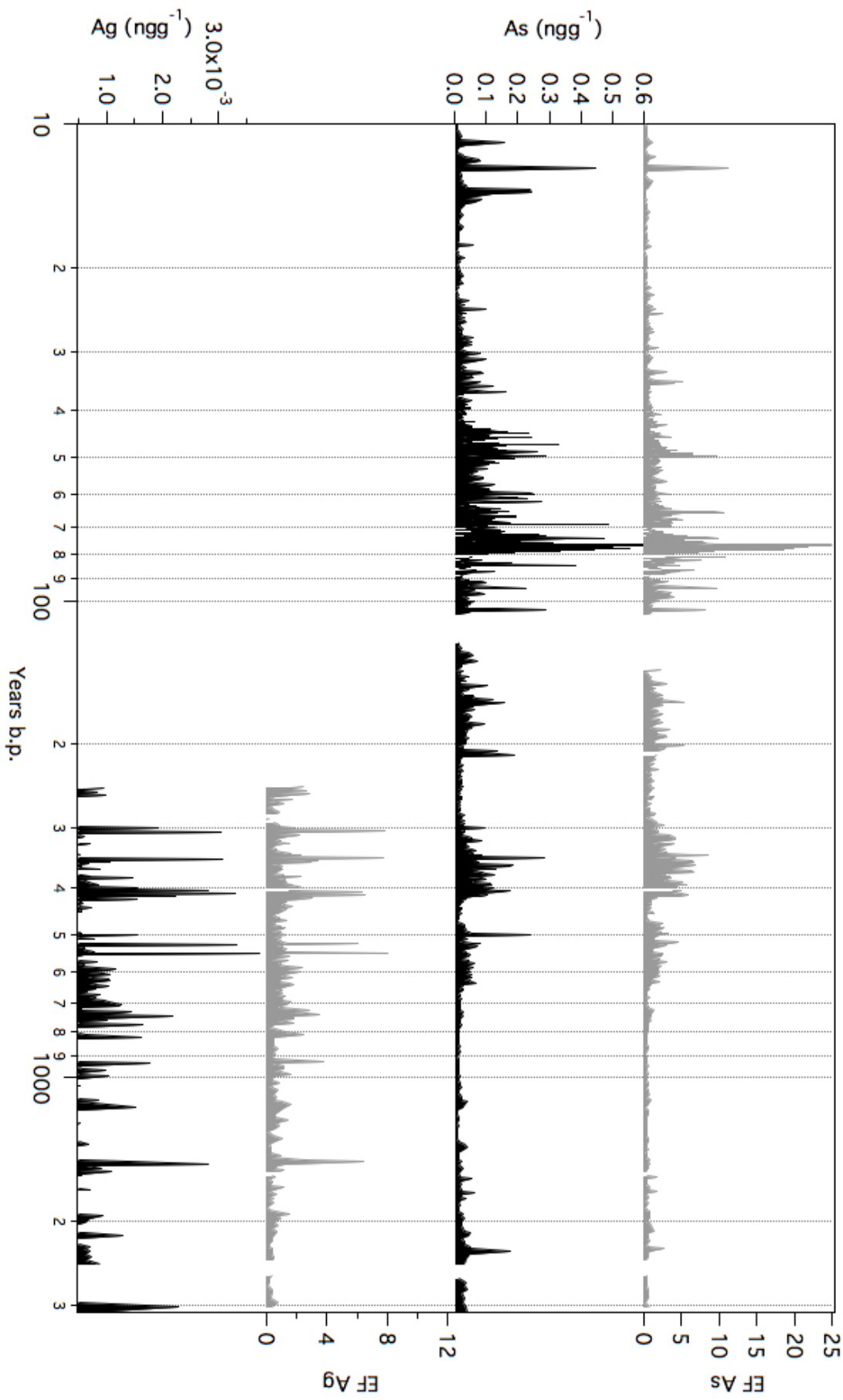

Figure 7.15: As and Ag profiles and EFs in the Ortles ice core#1. Black line: discrete dataset; grey line: continuous dataset and EFs.

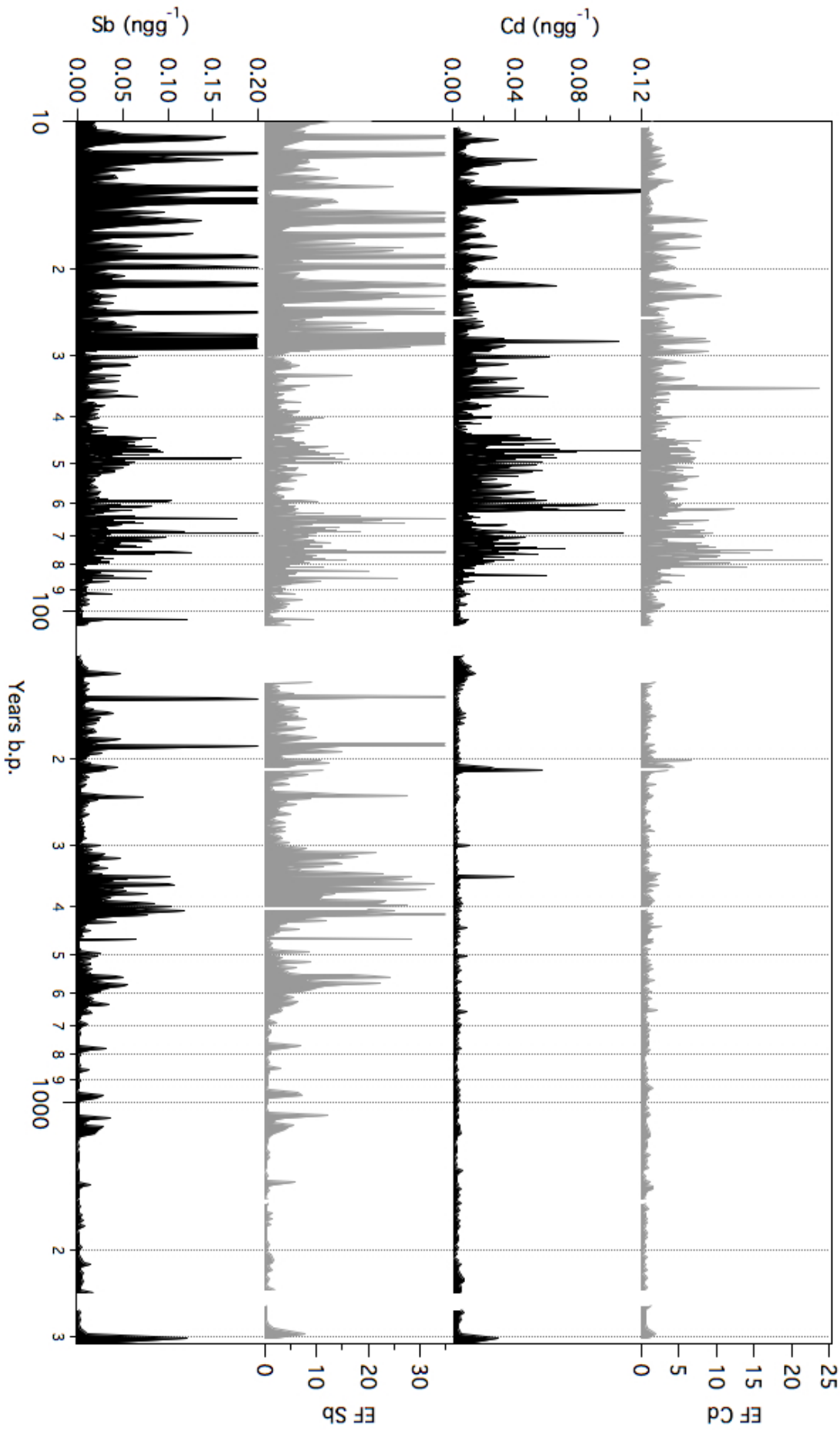

Figure 7.16: Cd and Sb profiles and EFs in the Ortles ice core#1. Black line: discrete dataset; grey line: continuous dataset and EFs.

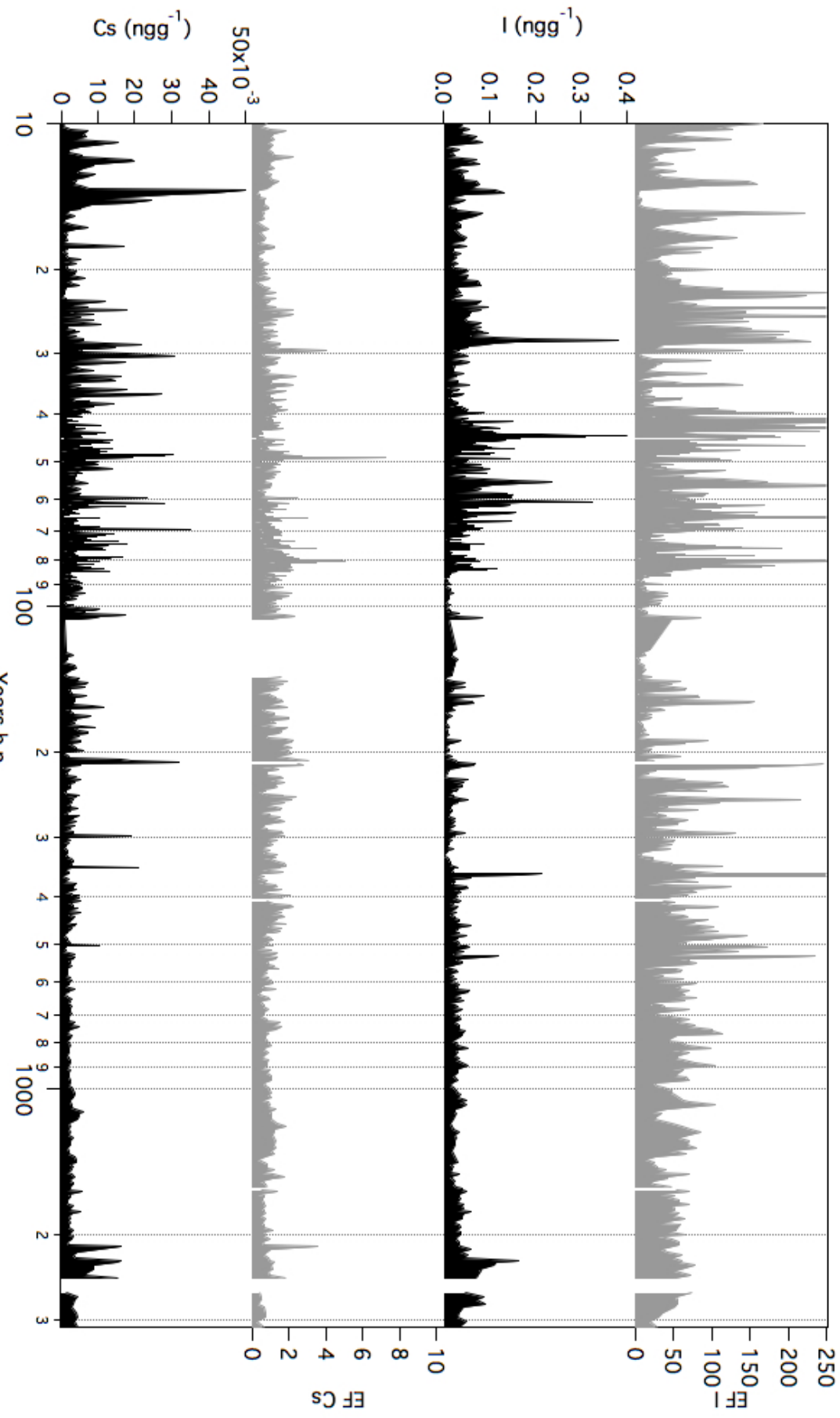

Figure 7.17: I and Cs profiles and EFs in the Ortles ice core#1. Black line: discrete dataset; grey line: continuous dataset and EFs.

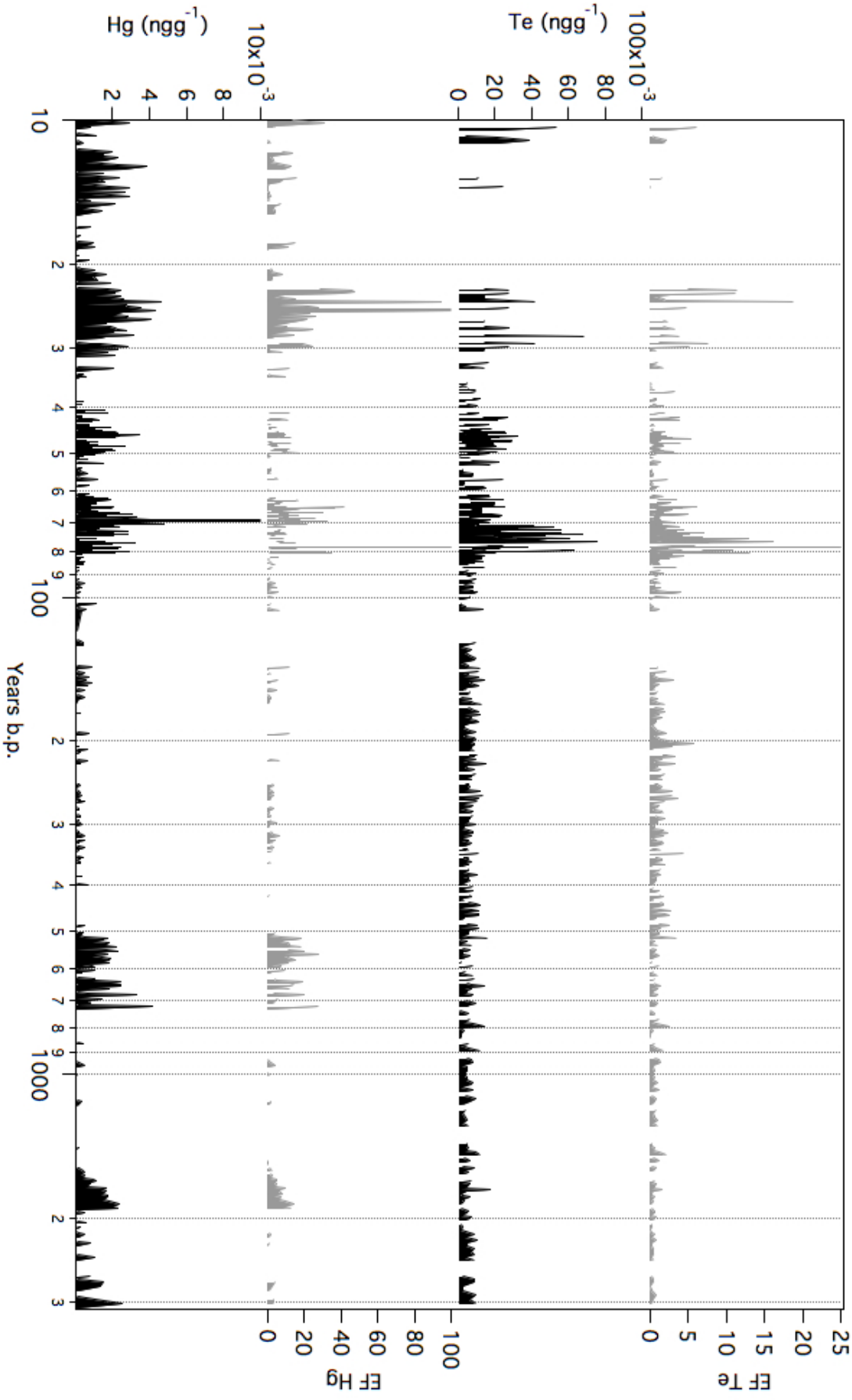

Figure 7.18: Te and Hg profiles and EFs in the Ortles ice core#1. Black line: discrete dataset; grey line: continuous dataset and EFs.

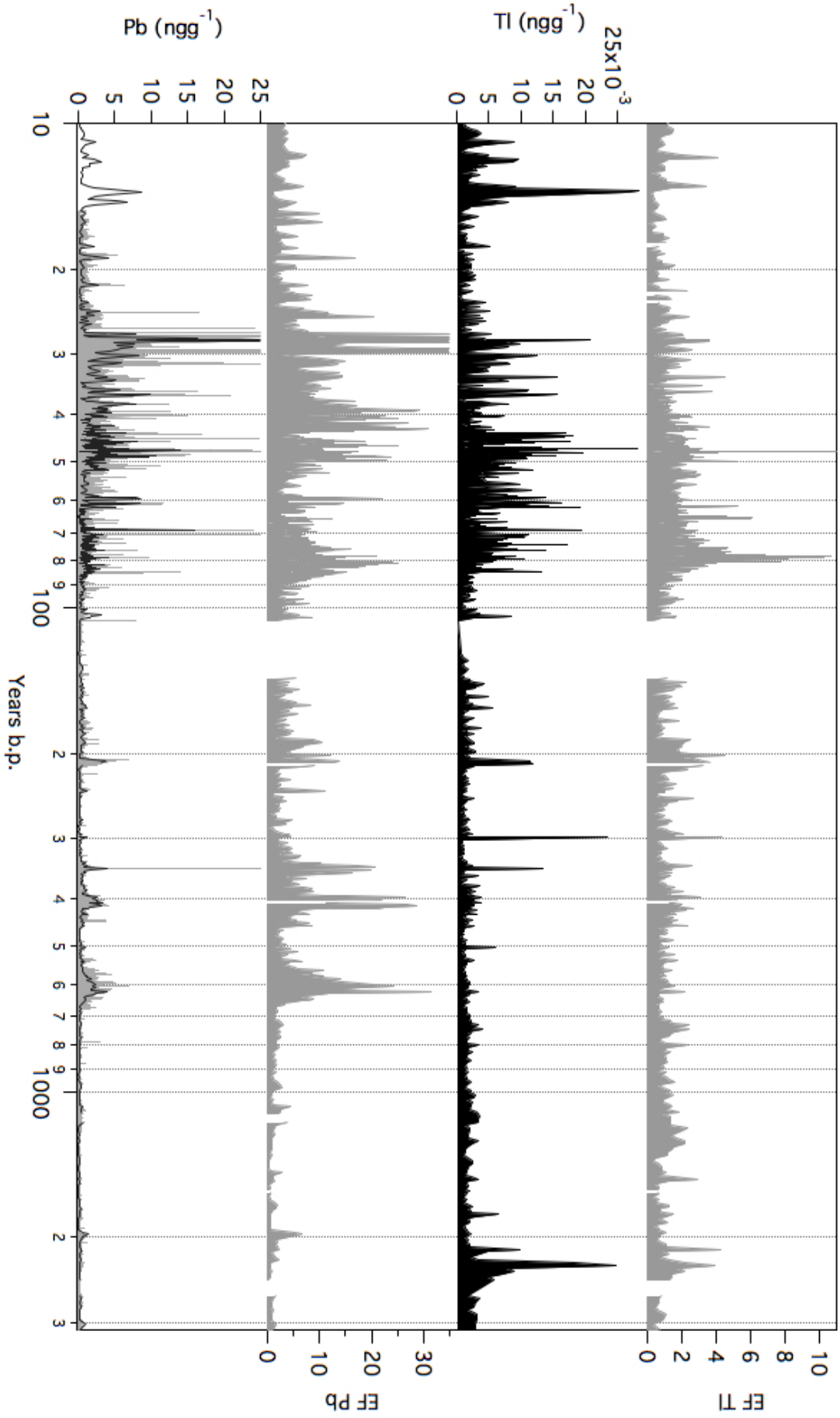

Figure 7.19: Tl and Pb profiles and EFs in the Ortles ice core#1. Black line: discrete dataset; grey line: continuous dataset and EFs.

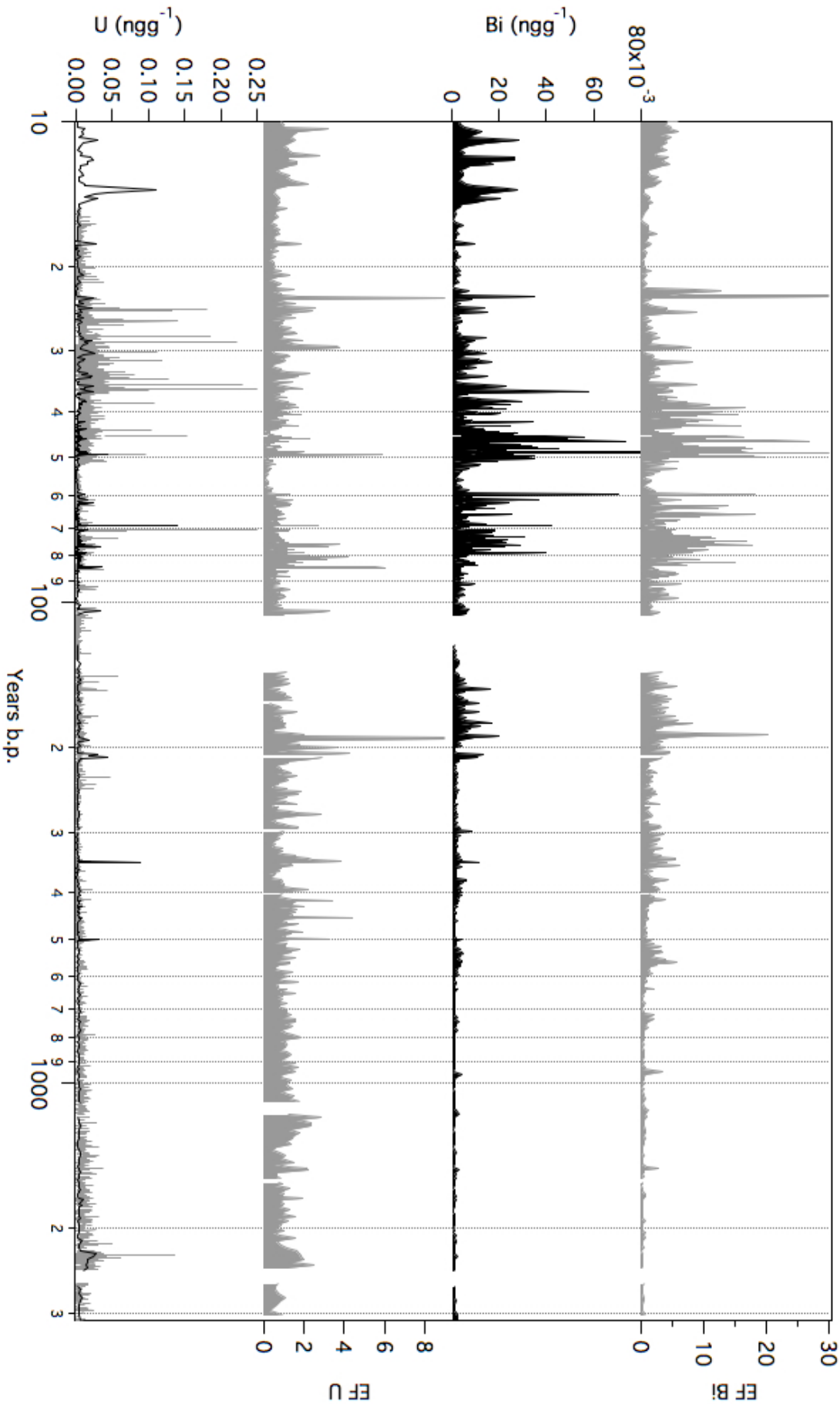

Figure 7.20: Bi and U profiles and EFs in the Ortles ice core#1. Black line: discrete dataset; grey line: continuous dataset and EFs.

factor between the periods 1989-1930 AD and 1800 AD - 1000 BC was observed for Mn and Ba): 1.4 and 1.6 respectively. The EF for Ba was computed by considering the concentration of Al and a significant increase is observed around 1955 AD. This increase is not observed in the EF of the other crustal elements.

An increase in the concentrations of almost all of the crustal elements is observed around 1950 AD, except for the Al and Fe and Mn, and this explains the increase of the EF Ba in this period. The different behaviours of this elements was detected by the PCA of the period 2000-1800 AD (7.1), while Ba was somehow in the middle between the two groups of crustal elements divided by the second component.

The overall behaviour of the crustal elements appears to follow the isotopic variations and therefore the climate of the Mt. Ortles region. The isotopic values decrease from the 1000 BC to about 1800 AD, with a small increase during the period 1400-1600 AD. From 1800 AD to 1880 AD the isotopic values became less negative (higher temperatures) and remained constant until 1940 when an intense increase took place. After 10 years of colder climate another temperature increase is observed for 5-6 years. After a small decrease the isotopic values start to increase again in the last 4 decades. Particularly, an increase in concentration is observed around the 1940 and 1960. After the 70s the Fe concentration increases, whereas Ba, Sr and K decreased. Probably the different behaviours are due to the different response to the percolation events.

The crustal elements profiles seem to have a similar behaviour (Fig. 7.21). This important observation appears to be simply explainable by considering two climatic and atmospheric aspects: firstly, periods characterized by higher temperatures cause a decrease in the snow cover areas around the glacier therefore increasing the dust emissions from local sources and secondly, higher temperatures are usually connected with enhanced convective activities, bringing to the glacier more aerosols from the polluted boundary layer.

A 1 cm rock pebble was found in the section number 104 (from 72.47 m to 73.19 m) at a depth of 72.85 m. The piece of ice was cut from the section in order to preserve the rocks for a complete geochemical analysis. The pebble was at a distance of 1.4 m from the bedrock. This pebble was probably wind-blown from the rock outcrops of the Mt. Ortles summit (about 250 m from the drilling site) to the glacier surface or maybe it was entrained from the bedrock. However, during the melting of this section the CFA system stopped because of the presence of dust (not visible at naked-eye). The remaining 20 cm of the section were not melted in order not to lose the sample. The last 50 cm ice section was clean ice and it was melted easily.

Deep Ice Core Sections Results

Many elements concentrations increased significantly in the last part of the core. Particularly, in Table 7.7 are shown the averaged concentrations and EFs for the depth interval between 70.3 m–72.4 m and 73.185 m–73.53 m (the last ice core section) and the corresponding *increase factors*. The highest concentration IFs were found for Cu (8.9), Li (7.9), Sb (5.2), Cd (2.9) and Cr (2.6), while the highest for the EFs for Cu (2.7), Li (2.3), Sb (1.7). The statistical results seems to suggest a non-crustal source for the elements of the last section (on-going research).

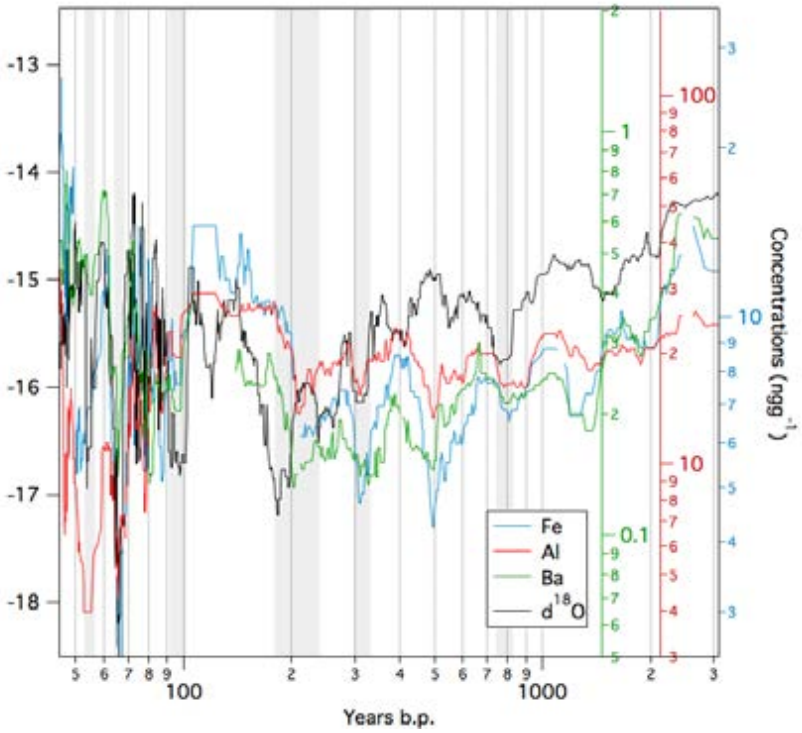

Figure 7.21: $\delta^{18}O$ and selected crustal elements profiles for the Ortles ice core#1 over the last 3000 yrs. The sharph steps in the TE profiles are a results of the *box* smoothing algorithm in the presence of intense concentration peaks.

Table 7.7: Increase factors (IF) for the elemental concentrations in the last core section, from 73.19 m to 73.53 m, and in the previous undisturbed interval from 70.3 m to 72.4 m. The average concentrations are in ng g^{-1}.

Element	Concentrations			Enrichment Factors		
	Average (70.3 m–72.4 m)	Average (73.19 m–73.5 m)	IF	Average (70.3 m–72.4 m)	Average (73.19 m–73.5 m)	IF
Na	12	27	2.1	1.3	1.3	1.0
Mg	77	112	1.4	0.82	1.2	1.5
Al	20	24	1.2	0.45	0.76	1.7
K	18	31	1.7	1.3	1.6	1.2
Ca	190	288	1.5	1.1	1.5	1.4
Ti	0.20	0.26	1.3	0.66	1.1	1.7
^{57}Fe	9.5	12	1.2	0.53	0.88	1.7
I	0.027	0.052	1.9	0.94	0.99	1.1
Ba	0.30	0.60	2.0	2.52	1.5	0.59
Li	0.013	0.10	7.9	1.64	0.71	0.43
V	0.026	0.045	1.7	0.75	0.95	1.3
Cr	0.035	0.091	2.6	0.86	0.87	1.0
Mn	1.3	1.7	1.3	0.90	1.3	1.4
Co	0.010	0.020	2.0	0.77	0.78	1.0
Cu	0.072	0.64	8.9	0.24	0.088	0.37
Zn	0.42	0.73	1.7	0.66	0.93	1.4
As	0.016	0.027	1.7	0.48	0.54	1.1
Sr	0.42	0.76	1.8	1.0	1.1	1.1
Ag	0.0005	0.0006	1.2	0.36	0.74	2.1
Cd	0.002	0.007	2.9	0.81	0.66	0.81
Cs	0.003	0.004	1.2	0.51	0.85	1.7
Tl	0.002	0.003	1.4	0.71	1.0	1.5
Pb	0.18	0.360	2.0	0.57	0.64	1.1
U	0.004	0.005	1.3	0.71	1.2	1.6
Sb	0.003	0.018	5.2	1.5	0.88	0.58
Te	0.004	0.005	1.3	0.32	0.51	1.6
Bi	0.0006	0.001	1.7	0.34	0.44	1.3
Hg	0.0009	0.0012	1.4	0.49	0.73	1.5

Iodine profile

At the best of our knowledge the Iodine concentration profile measurement performed in this work was the first ever in an Alpine ice core.

The I atmospheric chemistry is quite complex and the main Iodine containing aerosols source seems to be the sea-spray and the biogenic production (O'Dowd et al. 2002). The wet-deposition should be the most important in the Alpine regions and the iodine content depends both from the humidity source and the season. Moreover, the modulation caused by synoptic scale atmospheric patters seems to have a significant role; even if the role of NAO and AMO in the Alpine region are still largely debated (see Paragraph 1.5). At the moment the Ortles I time series (Fig. 7.17) is under analyses.

Trace Elements Natural Emissions

The estimation of natural emissions of trace elements is of great importance in order to understand the geo-chemical elemental cycles and to distinguish and know the anthropogenic influence. The natural sources are generally the airborne rock dust component, the sea spray, volcanic eruptions and the particulates emitted during biomass natural fires.

A complete worldwide estimation of natural emissions for the 20th century was drafted in Nriagu, J. M. Pacyna, et al. 1988. The comparison between the averaged measured trace elements concentration in the 20th century in the Alto dell'Ortles and Colle Gnifetti (Gabrieli 2008) ice core and the natural emissions (Nriagu, J. M. Pacyna, et al. 1988) was performed in order to evaluate the trace elements deposition in the Alpine region in a worldwide emission scenario (Table 7.8). Particularly, a normalization of the concentrations was computed by using Manganese (Mn) as a reference element because it had the highest natural yearly emissions during the 20th century and because 90% of the emissions are from natural sources (Nriagu 1989). The normalization was done by dividing the elemental concentration by the measured Mn average value, and multiplying the result by 100 (as suggested in Gabrieli 2008).

The Ortles ice core normalized values are generally comparable with the natural emission, except for Cr whose values is about 4 times smaller then the natural emission and Hg, 8 times smaller. The values for the two Alpine ice cores are well in agreement even if the Colle Gnifetti values are the double of the Ortles ones for V and Cr.

Heavy metals

In the Alto dell'Ortles ice core#1 almost all of the non-crustal elements (as reported by the PCA results) are characterized by EFs that are significantly higher than one, especially during the 20th century; an exception is for Li, Cs, and U (Na and I are not considered here) that only sporadically have an EF higher than one: this means that, even if they are not in the same group of the crustal elements in PCA results, their behavior cannot be easily explained; another possible explanation could be that those elements may just be more soluble and prone to post-depositional effects.

In the Ortles ice core both variations in the concentrations and in the EFs of heavy metals can be observed at different historical periods. The most evident

Table 7.8: Natural trace elements emissions during the 20th century (Nriagu 1989) and averaged concentrations measured in the Colle Gnifetti (Gabrieli 2008) and in the Ortles ice cores (this work).

Element	Ratio: (Conc. element/Conc. Mn)∗100		
	Natural emissions (a)	Ortles core	C. Gnifetti core (b)
As	3.8	3.3	
Cd	0.4	0.8	
Cr	13.9	3.0	5.7
Cu	8.8	12	11
Co	1.9	1.0	1.8
Hg	0.8	0.1	
Ni	9.5	6.1	
Sb	0.8	2.4	
V	8.8	4.1	9.1

increase was detected from the beginning of the 20th century and especially from the 1920s (see for instance Fig. 7.19). However, mainly two other periods of elevated environmental contamination can be noted, around 1400 AD and 1600 AD. The EFs of Pb, Sb, As and Bi during these two periods reached values similar to those observed during the 20th century.

Trace Elements profiles in the Roman-Greek period (500 BC - 400 AD) Before the 20th century and the Industrial Revolution the major source of atmospheric heavy metals emissions were mining and smelting activities. The concentration increase of Lead detected 2000 yr BP can be attributed to the mining activities carried on during the Roman Empire (the uncertainty on the dating at these ages is quite high, see Paragraph 2.5.2). Particularly, the Pb EF peak is of about 6.5 with concentrations ranging from 0.4 ng g^{-1} to 1.2 ng g^{-1} (Fig. 7.22). The ice sections corresponding to the Roman period in the Colle Gnifetti ice core were of poor quality and were not analysed (Gabrieli 2008). Therefore, the Alto dell'Ortles ice core #1 may be the first Alpine ice core in preserving the heavy metals heritage of the Roman Empire.

The Roman period Pb sign was found in an ice core from Greenland in the period from 500 BC to 300 AD (Hong, Candelone, et al. 1994). The sources of Pb contaminations were the ancient mining and smelting activities during the Roman and Greek period. By mean of Pb isotopic measurements the two most important sources were found to be two smelters in the southern Spain. From 150 BC to 100 AD more than half of the Pb arrived from the Rio Tinto smelter (K. J. Rosman et al. 1997). After the 40 AD new Pb mines were exploited in Great Britain but the emissions were about ten times lower than those from the smelters in Spain (Nriagu 1989). Records of the Pb emissions during the Roman period were also found in a peat bog core from the Jura Mountains, Switzerland (Shotyk et al. 1996).

In Fig. 7.22 the Ortles ice core #1 Pb dataset is compared with two Pb datasets obtained from Greenland's ice cores (Hong, Candelone, et al. 1994 and K. Rosman et al. 1993). The direct comparison appears to corroborate the presence of the Roman Pb emissions stored in the Ortles ice core, even if the timing of the highest peaks

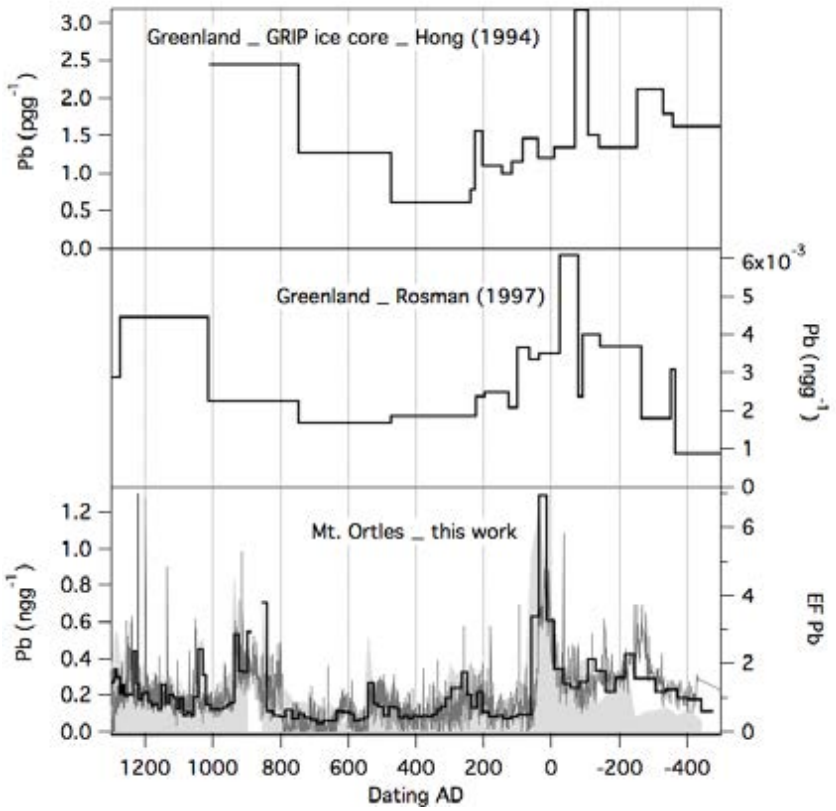

Figure 7.22: Pb concentrations and EF during the period 400 BC to 1400 AD measured in the Ortles ice core (this work) and in two Greenland ice cores (Hong, Candelone, et al. 1994 and K. Rosman et al. 1993). In the Ortles results the CFA (dark grey line), the discrete (black) and the EF (light grey) datasets are shown.

of all the three datasets are slightly shifted (the actual dating uncertainties at this depth are in the order of 300/400 years). The EF values are slightly above one but the increase, compared to the following period, is clearly visible, particularly at the concentration peak where the EF is about 7.

Also the Cu profiles show an increase during the Roman Empire, from 400 BC to about 200 BC, with EFs of about 2.5 (Fig. 7.23). Cd instead has quite high concentrations before the 100 BC (0.006 ng g^{-1}) but the EF is 1 on average, meaning that an increase in the overall dust deposition was also recorded (Fig. 7.24).

A strong decrease in the European anthropogenic trace elements emissions resulted after the fall of the Roman Empire. The abrupt decrease in these smelting activities appears to be recorded in the Alto dell'Ortles ice core (Fig. 7.22 and 7.23).

Trace Elements profiles from the Early to the Late Middle Ages (400 AD-1400 AD) At the beginning oh the 9th century the concentration of Pb increased again from an average value of 0.1 to more than 0.5 ng g^{-1}, and the EF from 0.8 to more than 2. The Cu profile reported as well this increase from the 800 AD. Despite considerable oscillations, the average value remained higher than that of the previous centuries, as well as the EF (Fig. 7.23).

During the 10th century a significant economic growth characterized the European region and, indeed, was the beginning of the *Renaissance*. In this period, new ores were found and abandoned ores were opened again. Particularly, other

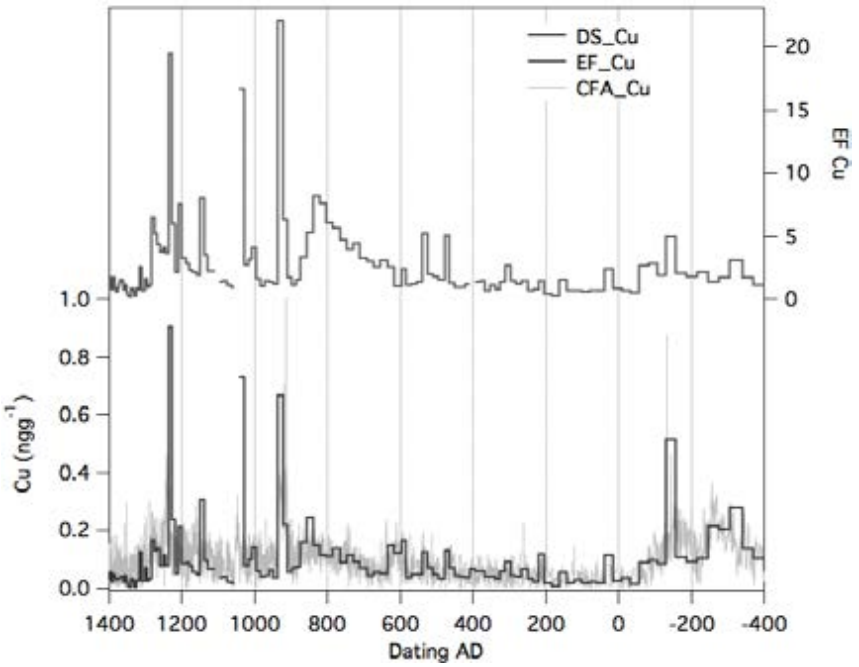

Figure 7.23: Cu concentration and EFs during the period 400 BC to 1400 AD.

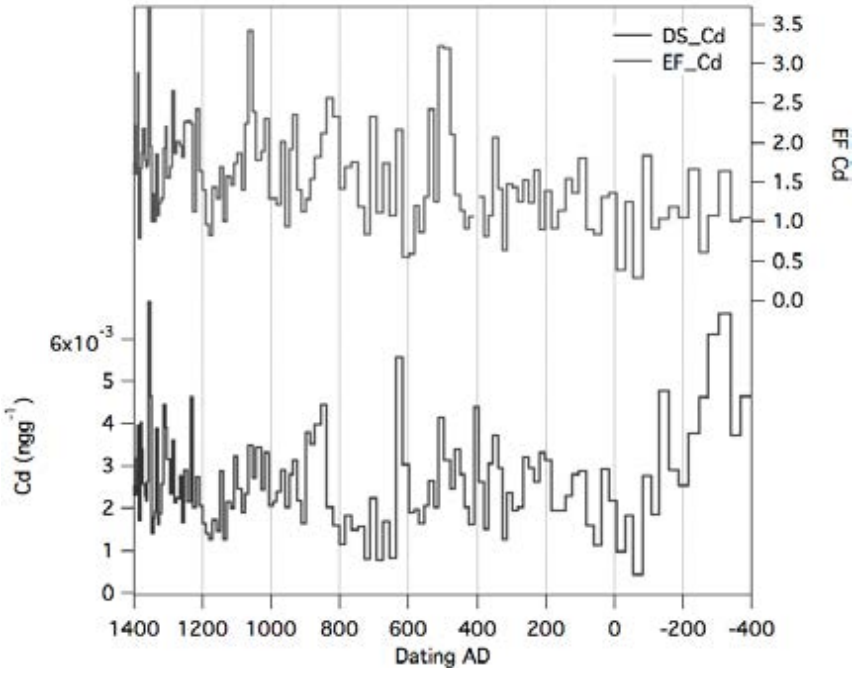

Figure 7.24: Cd concentration and EFs during the period 400 BC to 1400 AD.

European states started new mining activities, as reported by Bränvall et al. 2001, especially Germany. The most important European Silver mines were in Germany, in the German Harz mountains (Rammelsberg). In this region Ag, Cu, Pb and Fe were extracted. The Silver mines were one of the most Pb emitting activities before the Industrial Revolution. Particularly, Ag was extracted from Lead ores and moreover, Lead was used during the Silver refining (Nriagu 1989). After 1300 AD the *Black Death* plague caused the death of 25% of the Europe's population (Bränvall et al. 2001 and Ziegler 2013). A general decrease of concentration is observed after this period, especially for the Pb and Cu profiles (Fig. 7.22 and in Fig. 7.23); the CFA data (grey dots) appear to catch better this emission and deposition decrease.

Trace Elements profiles before the Industrial Revolution (1400 AD - 1700AD)
From the end of 13th century a Pb concentration increase is observed in the Ortles core#1, with an average EF value of 15, and peaking in 1400 AD (Fig. 7.25). This increase appears to be connected to the increase of other heavy metals: As, Sb, Bi and Ag; however, the Pb increase was relatively much higher. Moreover, As, Sb, Bi concentrations peak around the 1450 AD. All these metals were clearly separate from the others in the PCA results for the period 1800 AD- 1000 BC (Fig. 7.25). Interestingly, the concentration of Ag increased with the same timing of Pb during the 17th century, meaning that Silver ores may have been the pollutants sources (during the Pb concentration increase at the end of the 14th century the Ag increase is only moderate). In many ores Ag was extracted from mineral rocks that are rich in Sb and As (Tanaka 1988), possibly explaining the simultaneous increase of these metals.

Historical Pb emission reconstructions were performed in other archives, such as in peat bogs and lake sediments. The Pb increase was detected in the sediments archives of four Swedish lake, and they all suggest an early increase from the 900 AD, achieving the maximum around 1200 AD (Bränvall et al. 2001).

The 1400 AD Lead increase is not observed in other archives, but only in the Colle Gnifetti ice core (Gabrieli 2008): a significant increase just before the 1400 AD (almost simultaneous to the Ortles ice core) ending at the end of the century. This polluted ice layers may be an heritage of Ag mines in the Southern Alps affecting more the lower altitude Ortles glacier (on-going research).

From the end of 1500 AD, the Ag mining related elements (Pb, As and Sb) pollutants increased again in the Alto dell'Ortles ice core#1, simultaneously to the highest EF level of Ag, about 8 on average (Fig. 7.25). The peaks in concentrations and in EFs were observed just before the end of 1500 AD in accordance with the results from the Swedish lake sediments cores (Bränvall et al. 2001) and, slightly later, with the Colle Gnifetti ice core Gabrieli 2008 (the Pb second peak is almost simultaneous).

Interestingly, also the Bi concentrations increased in this period and its sources can be related to the Ag and Cu and Pb mines rocks by-products. Bi, As and ceSb were released during the mineralization of Cu and Pb and, indeed, contaminations of those elements were found in soils close to historic mining and smelting areas (e.g. Li and Thornton 1993). It is noteworthy that the Pb increase is decoupled to the other TEs in the earliest peak (Pb concentration peaks in the 1400 AD and the others TEs in 1450 AD), whereas it is perfectly synchronized in the second one (the highest concentrations are observed in the 1600 and 1660 AD).

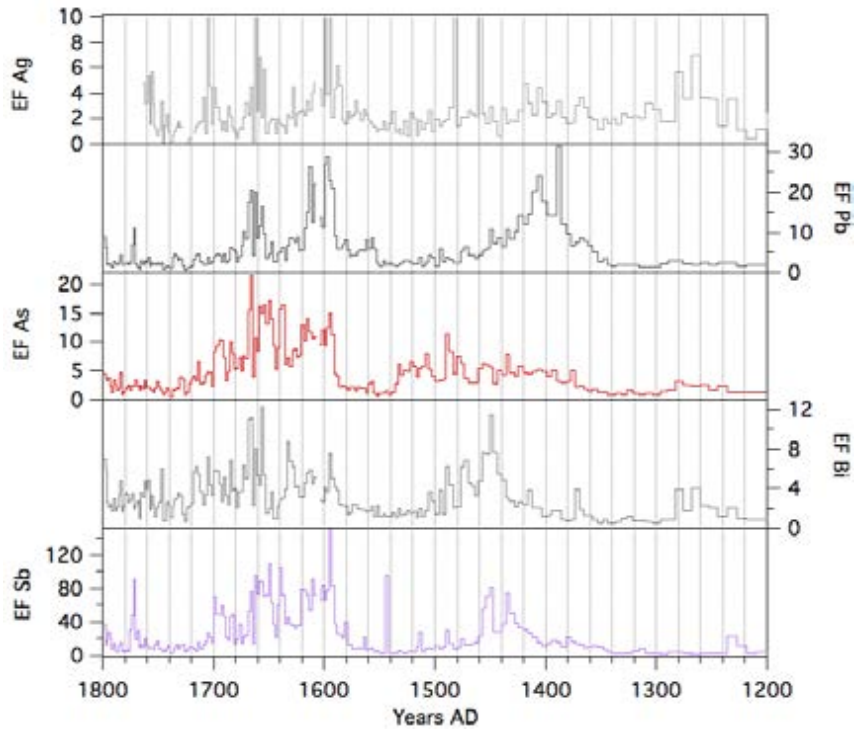

Figure 7.25: Concentration profiles of Ag, Pb, As, Sb and Bi form 1200 BC to 1800 AD.

In the Colle Gnifetti ice core two Bi peaks were detected around 1250 and 1600 AD (Gabrieli 2008).

At the beginning of the period 1400-1700 AD mining activities increased considerably thanks to the discovery of new ores and of new technologies: Ag was extracted from Cu ores by exploiting huge quantitative of Pb.

After the 1600 peak, another concentration increase was measure around the year 1650 AD for Pb, As, Sb, Bi, Ag. There are significant uncertainties in the dating (about 150 years, see the Section 2.5.2) for this period but all these observations, however, may led to a confirmation of the dating in the last 2000 years.

After the 1600 peak a decrease in heavy metals concentrations was recorded. The concentration levels between the 1700 and the 1800 remained very low, for Pb, As and Sb the EFs decreased to values equal to the 1550 level. The decreased was mainly due to the beginning of the exploitation of new American ores (Bränvall et al. 2001), that strongly increased in these periods (Uglietti, Gabrielli, Cooke, et al. 2015).

Comparing the European and the South American mining activities histories In Fig. 7.26 the Ortles core #1 concentration profiles of Pb, As, Sb, Bi, Ag are compared with those retrieved from an ice core from the Quelccaya (Peru) glacier (Uglietti, Gabrielli, Cooke, et al. 2015); in this way the different timings of the two mining activities histories in Europe and in South America may be evaluated. As reported in Uglietti, Gabrielli, Cooke, et al. 2015, a significant anthropogenic pollution signal is observed in the Quelccaya ice core after around the 1540 AD, as a consequence of the colonial mining activities. By comparing the Ortles and the Quelccaya results it can be observed that the concentrations of Pb, As, Sb, Bi (not so evident) and Ag started to increase in the Andean atmosphere almost simultane-

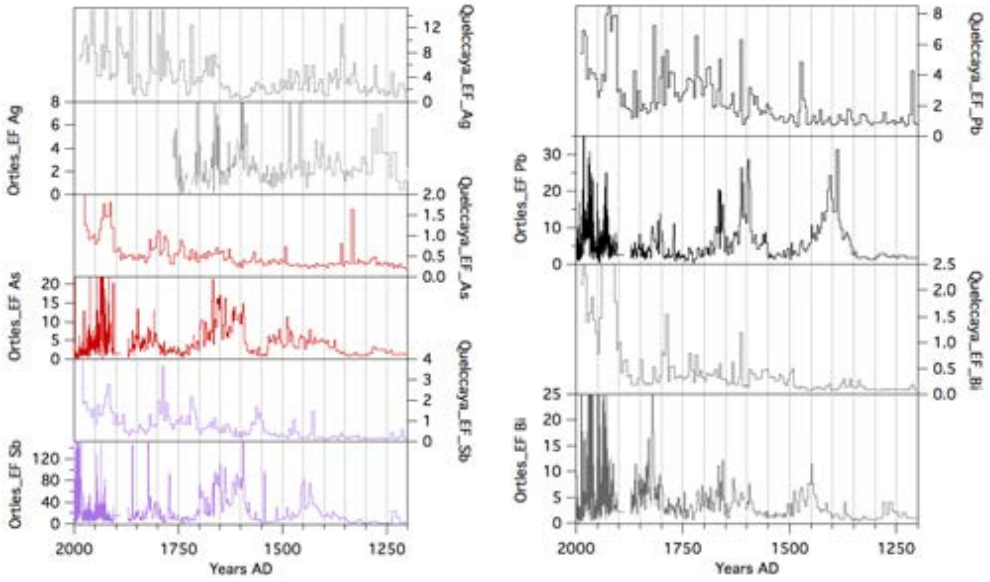

Figure 7.26: Comparison between the Ortles core #1 Pb, As, Sb, Bi, Ag concentrations (this work) with the same elemental profiles from the Quelccaya (Peru) ice cores, takes from Uglietti, Gabrielli, Cooke, et al. 2015.

ous to the decline of the European mining activities' emissions after the 1600-1650 AD. Despite more historical investigations are needed, these preliminary results seems to confirm the European mining activities decline after around the 1600 AD, and the significant increase in exploitation of the South American mines.

The analyses of Pb in the Illimani (Bolivia) ice core led to very similar interpretations (Eichler, Gramlich, et al. 2015). The first Pb anthropogenic impact was observed during the Tiwanaku/Wari culture period, about 450-950 AD, the Inca empires, about 1450-1532 AD, due to silver refining related emissions. Significant anthropogenic emissions, before the leaded gasoline introduction during the 1960s, were related to the colonial Ag mining activities in the period 1532-1900 AD, followed by the boom in Sn production at the beginning of the last century (Eichler, Gramlich, et al. 2015).

Trace Elements profiles from the onset of the Industrial revolution (1700 AD – 2000 AD) Almost all the trace elements profiles show the highest concentrations values during the 20th century in the Ortles ice core#1. The EFs are very close to one for the crustal elements, whereas for many heavy metals the EFs are much greater. The concentrations profiles and the EFs for the all trace elements datasets are reported from Fig. 7.9 to Fig. 7.20.

Particularly, the list of heavy metals average, median and maximum concentrations during the period 1700 AD- 1800 AD is compared to those measured during the most polluted period, 1930 AD- 1980 AD in the Table 7.9. The IFs for the three statistics were computed and the highest average increases were found for Cd (12.1), Pb (8), Bi (7.8) and Zn (6.1). The other heavy metals in the list increased from three to six times on average (Table 7.9). Pb, Cd and Tl increases were also measured in the ACT2 ice core (central-south Greenland) starting from the end of the 18th century and the source was found to be the coal burning in North America

Table 7.9: Heavy metals increase from 1700 AD- 1800 AD to 1930 AD- 1980 AD. Average, median, maximums and relative increase factors. The average, median and maximum concentrations are in ng g^{-1}.

	1700 AD - 1800 AD			1980 AD - 1930 AD			Increase factors		
Element	Average	Median	Max	Average	Median	Max	Average	Median	Max
V	0.023	0.019	0.023	0.0879	0.0528	0.6106	3.8	2.7	26
Cu	0.063	0.016	0.063	0.2392	0.1349	7.4251	3.8	8.4	117
Zn	0.33	0.24	0.33	2.4	1.5	18.6	7.1	6.4	56
As	0.017	0.016	0.017	0.098	0.067	1.046	5.7	4.3	61
Cd	0.0018	0.0015	0.0018	0.022	0.017	0.131	12.1	11.4	72
Pb	0.25	0.18	0.25	2.0	1.3	16.0	8.0	7.3	64
Sb	0.0092	0.0066	0.0092	0.031	0.022	0.51	3.4	3.4	56
Bi	0.0014	0.0012	0.0014	0.011	0.0065	0.15	7.8	5.3	107
Hg	0.0002	0.0002	0.0002	0.0012	0.0010	0.027	6.3	5.3	139

and Europe (McConnell and Edwards 2008).

The high-resolution trace elements profiles exhibit large variations both at seasonal and decadal time scales. The anthropogenic emission intensity was not stable during the last centuries and was not the same for the all elements. In the graphs reported from Fig. 7.9 to Fig. 7.20 a significant increase can be observed for many elements, such as As, Bi, Cr, Sb, Cd, Pb, Hg and Te, started at the beginning of the 20^{th} century, and showing the "firsts" concentration peaks during the 1930s, the WWII period.

Particularly, a Hg increase was also observed in this period in an ice core from the Upper Fremont (Wind River Range, Wyoming, USA) and the increase was attribute to the WWII manufacturing activities (Schuster et al. 2002). It is very likely that also in Europe this kind of activities released significant amount Hg in the atmosphere. An increase of deposition during the last century was also observed in an ice core from the Mt. Blanc (Col du Dome, Chamonix, France) (Jitaru et al. 2003); particularly, a six-fold increase was observed in 1965 AD compared to 1885 AD, and a three-fold increase in the middle of the 1980s.

In order to focus more on the general deposition trend the 5 year averages were computed for the last three centuries for some non-natural elements. The concentration profiles for the Ortles ice core #1 are reported (black line) in Fig. 7.27, Fig. 7.28 and Fig. 7.29, as well as the EFs (grey line) and the Colle Gnifetti concentrations profiles (red thin line) taken from Gabrieli 2008. It's important to underline that the uncertainties on the dating are very between 1200 and 1900 AD, because no evident time markers was found (Table 2.2). However, by using the average dating values as computed with the COPRA model (see the Section 2.5), it appears that the results are quite in agreement with the Colle Gnifetti ice core dataset, characterized by an accurate dating (Gabrieli 2008).

As reported in Fig. 7.27, Fig. 7.28 and Fig. 7.29 the concentration of the selected TEs are measured in the Ortles ice core #1 (black lines) show an increasing trend starting from the beginning of the 20^{th} century similarly to what observed in the Colle Gnifetti ice core (Gabrieli 2008). Particularly, the Bi highest concentrations are observed during the period 1945-1970 AD, as well as for Cd, Zn (in both the ice cores the concentration decrease rapidly after the 1960s) and Pb (except for the very high peak observed at the very end of the 1970s in the Ortles ice core, possibly

due to post-depositional effects). The V profiles almost show the same increasing trend but in the Ortles core the concentration abruptly decreased after the 1960s, whereas in the Colle Gnifetti it continuously increased; interestingly in the last part of the Ortles V profile the concentration increased again reaching values similar to those observed in the Colle Gnifetti core. The highest differences are observed in the As profile: in the Colle Gnifetti core a maximum of concentration was observed in 1920 AD, whereas in the Ortles core in the 1930s. In both the profiles another increase was observed at the end of the 1950s. In a peat bog from Jura Mountains, Switzerland, the As concentration profile showed the highest concentration in the period from 1905 to 1930 AD, and than it continuously decreased (Shotyk et al. 1996), similarly to the Ortles core results. The As increase observed from the beginning of the 20th century in the peat bog, in the Colle Gnifetti ice core and, less distinctly in the Ortles core may be due to the significant increase in coal combustion (usually enriched in As); the shifting from coal to oil for domestic heating possibly was the reason of the subsequent decrease Shotyk et al. 1996.

The author doesn't have a realistic interpretation for the concentration peak measured for many TEs in the layers corresponding to the 1800 AD.

Worldwide Pb emissions over the last three centuries

Pb emissions and deposition have been measured since the 1960s with the pioneering reaserach made by Patterson Flegal 1998 and the first paper about analyses in Antarctic and Greenland's snow samples by Murozumi et al. 1969 (for more information referred to Gabrielli and Vallelonga 2015). The historical atmospheric Pb emissions were extensively reconstructed by analyzing environmental archives such as ice cores or peat bogs (e.g. Shotyk et al. 1996). Many of the ice core based Pb concentration profiles are reported in Fig. 7.30, adapted from Gabrielli and Vallelonga 2015 (all the references are reported in the caption of the figure). The graph was updated by adding the Ortles (this work) and the Quelccaya datasets (Uglietti, Gabrielli, Cooke, et al. 2015).

A significant atmospheric Pb deposition increase, over the last three centuries, was observed at the end of the 19th century and the beginning of the 20th century, particularly over Greenland, South America, Antarctica and in the European Alps (even if relatively less strong). The principal sources at this time were the burning of coal for industrial activities and for domestic heating and the smelting activities (Gabrielli and Vallelonga 2015). However, during the 1960s and the 1970s the emissions from the vehicle engines burning loaded gasoline (Pb was used as an antiknock agent) caused the highest worldwide Pb atmospheric emissions. As observed in the Section 7.4.2, the Ortles core #1 Pb concentration dataset is well in agreement with Colle Gnifetti core results, both from Gabrieli 2008 and from Schwikowski, Barbante, et al. 2004.

Worldwide and European emission inventories In the Paragraph 7.4.2 the Ortles ice core trace elements concentrations were compared to the natural worldwide emission inventory (Nriagu 1989). The major natural sources of trace elements were already been categorized, such as in J. Pacyna 1986 and in Nriagu 1979.

The first complete comparison between natural and anthropogenic trace elements emissions was published in 2001 (J. M. Pacyna and E. G. Pacyna 2001, using

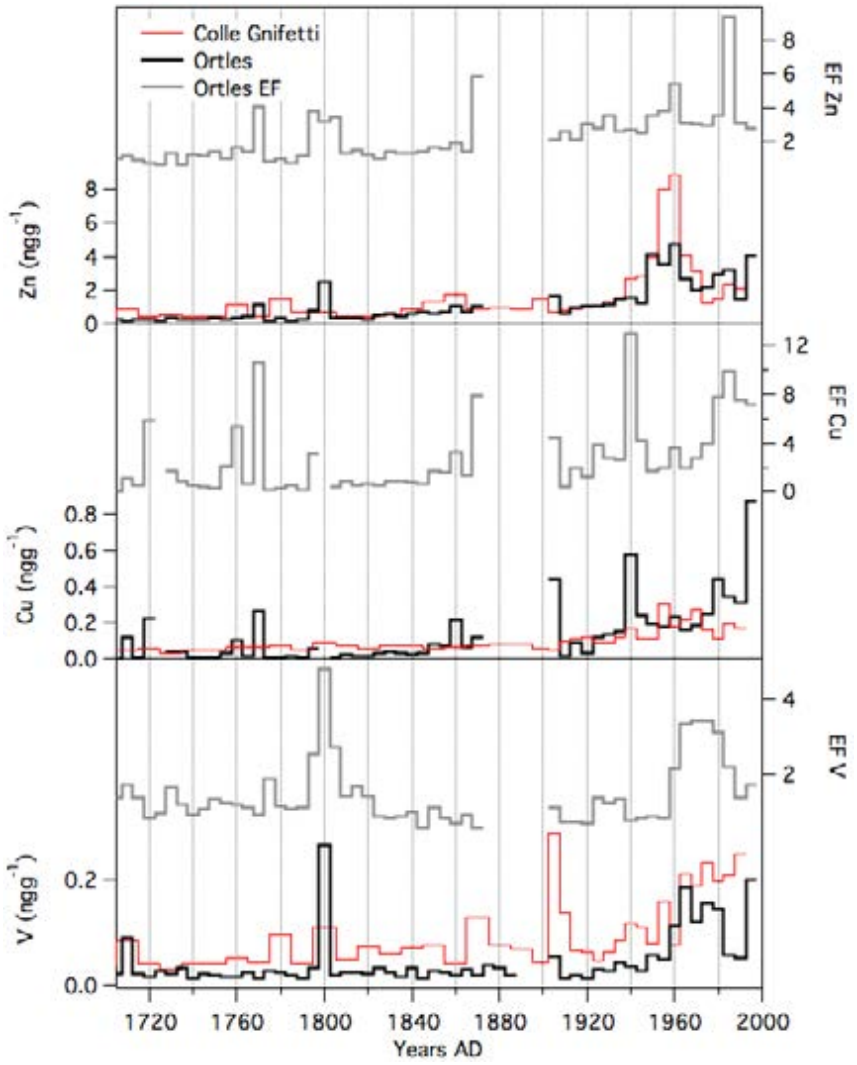

Figure 7.27: 5 and 10 years averaged V, Cu and Zn concentrations profile and EFs for the period 1700 AD - 2000 AD.

the anthropogenic emissions values of Nriagu 1979). The reported data suggest that for some elements, such as Cu and Hg the anthropogenic emissions were very close to the natural emissions, whereas for other elements the anthropogenic emissions in the mid 1990s were much higher than the natural (V and Cd). In the same work a detailed description of the emissions from many different anthropogenic activities is reported. The two main sources responsible for the majority of the emissions are the *stationary fossil fuel combustion* and the *non-ferrous metal productions* (J. M. Pacyna and E. G. Pacyna 2001). The greatest source of Pb during the 1990s was attributable to *vehicular traffic*; the final policy forbidding the use of Pb as an additive in gasoline in the European region was redacted in 1998, called the *Arhus Treaty*, giving 2005 as the final date.

The first European project dedicated to establish an emissions inventory for the European region started during the 90s; it was called the UNECE EMEP project (European Monitoring and Evaluation Program). The emissions of anthropogenic trace elements were monitored state by state in order to assess the contaminations risks and to evaluate the pollutants trans-boundary atmospheric transports.

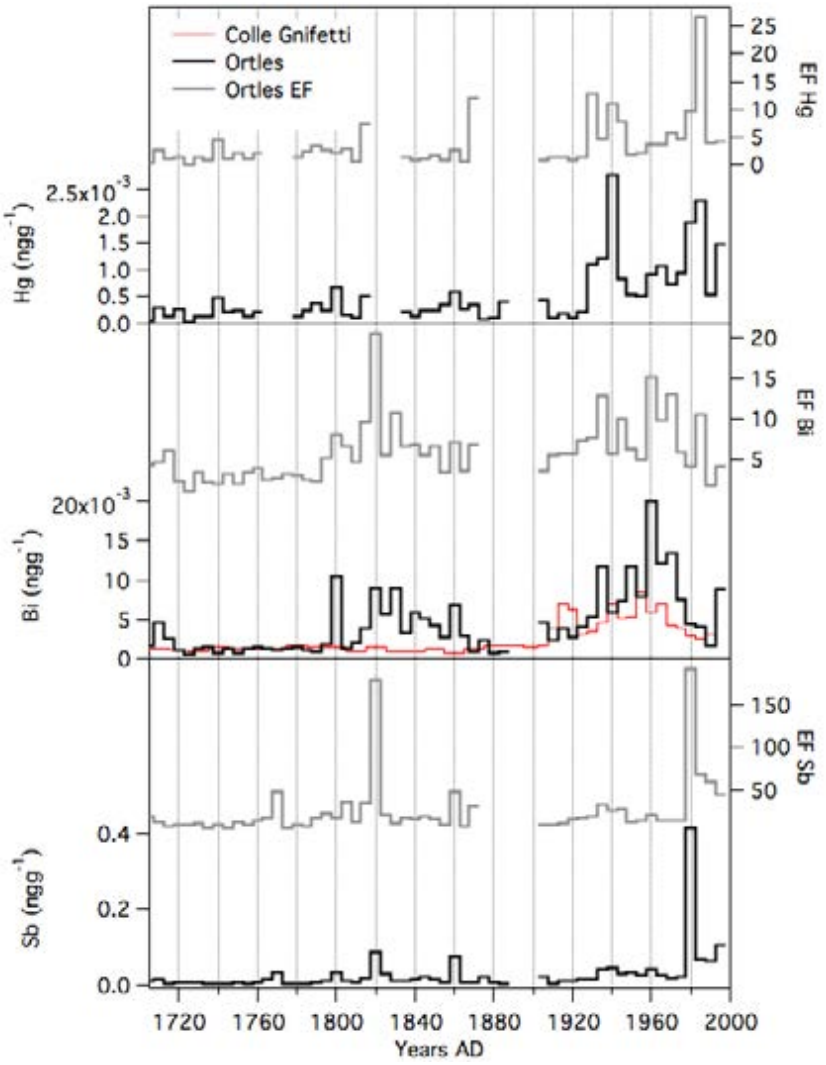

Figure 7.28: 5 and 10 years averaged Sb, Bi and Hg concentrations profile and EFs for the period 1700 AD - 2000 AD.

However, the EMEP data appeared to be underestimated by a factor of two when compared with many other independent datasets (E. G. Pacyna et al. 2007).

In 2008 two independent studies focused on the aerosol trace elemental composition in the atmosphere and in precipitations in the Norwegian area (Berg et al. 2008) and in soil in Scandinavian forests (Hovmand et al. 2008). However, both studies referred to the northernmost European regions and therefore they may not be suitable for the Ortles ice core comparison; the EMEP dataset and those reported in E. G. Pacyna et al. 2007 should be addressed.

In order to evaluate if the trace elements deposition on the Alto dell'Ortles glacier reflect the European emissions for the periods covered by emission inventories, a comparison was performed with the normalized measured concentrations and the emission data for the two inventories: J. M. Pacyna and E. G. Pacyna 2001 for the 1990s and J. M. Pacyna, Semb, et al. 1984 for the end of the 70s.

The normalization of the elemental concentrations was performed using the Zinc concentration and multiplying the ratios by 1000, as already done in Gabrieli 2008. The Ortles results were also compared with the concentration data of the

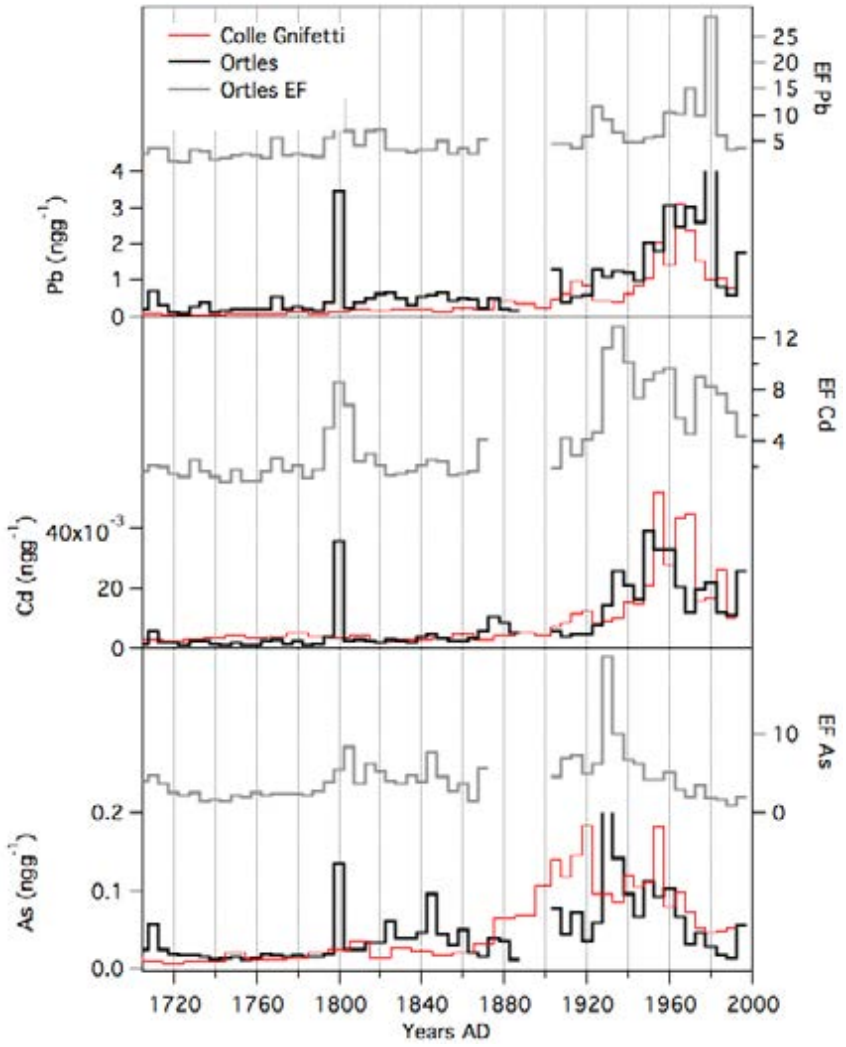

Figure 7.29: 5 and 10 years averaged As, Cd and Pb concentrations profile and EFs for the period 1700 AD - 2000 AD.

Colle Gnifetti ice core for the periods 1960-1970 AD, 1970-1980 AD and 1980-1990 AD. The results are reported in Table 7.10.

The results underline the similarity of the emission sources of the two Alpine ice cores; at the same time the estimated European emissions don't match precisely with the elemental ratios measured in the two ice cores, despite being always in the same order of magnitude. For the period 1960-1970 AD the ratios for the two cores differs on average 15 % for the selected elements. In the period 1970-1980 the results are still comparable but the Ortles values are always smaller, except for Pb and Mn. V, Cr, As and Cd in the Ortles core are smaller than the values for the Colle Gnifetti core in the period 1980-1990 (they are never less than half the value), whereas Mn, Co, Cu and Pb are higher (less than the double) compared to those of the Colle Gnifetti core (Table 7.10). However, it is possible that during the last period the Ortles ice core was affected by the strong percolation of the last two decades and this could eventually explain the differences.

The ratios for the Ortles ice core are much smaller than those reported from Pycna for the three temporal ranges. The Ortles ratios, as well as the Colle Gnifetti's,

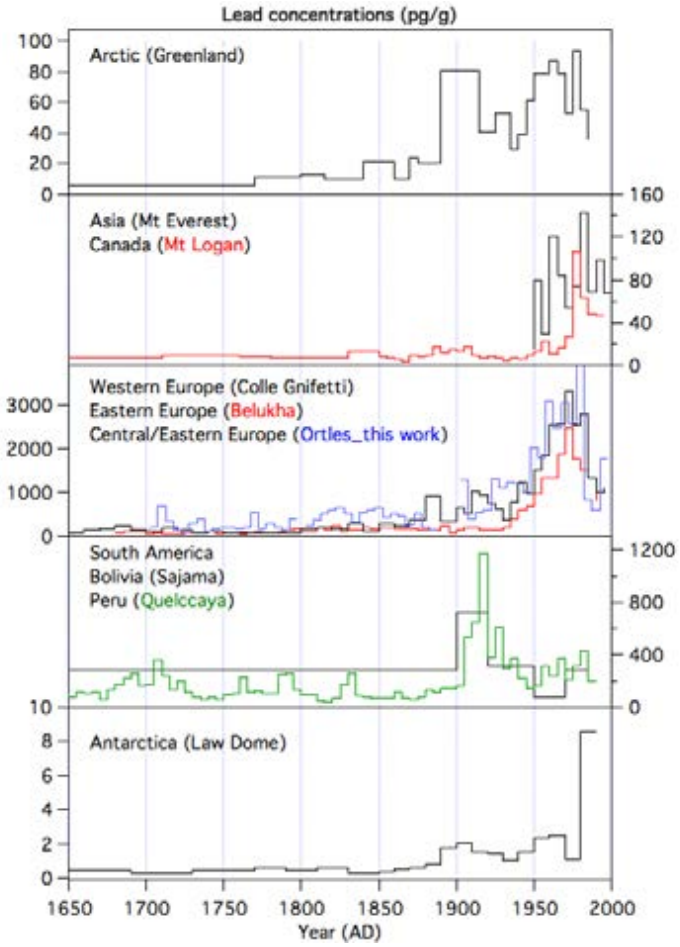

Figure 7.30: Lead concentrations measured in ice cores from: Greenland (Eurocore, Rosman, from Gabrielli and Vallelonga 2015, and Summit, K. Rosman et al. 1993) and Devon Island (Krachler et al. 2005); Asia: Mt. Everest (K. Lee et al. 2011); North America: Mt. Logan (E. Osterberg et al. 2008); Europe: Colle Gnifetti (Schwikowski, Barbante, et al. 2004), Alto dell'Ortles (this work) and Belukha (Eichler, Tobler, et al. 2012); South America: Sajama (Roman et al. 2003) and Quelccaya (Uglietti, Gabrielli, Cooke, et al. 2015); Antarctica: Law Dome (Vallelonga, Van de Velde, et al. 2002) and Coats Land (Planchon et al. 2003). Adapted from Gabrielli and Vallelonga 2015.

are in a reasonable accordance with emission data computed for Italy, France, Germany, Belgium, the Netherlands, Austria and Switzerland, using the dataset reported in J. M. Pacyna, Semb, et al. 1984. As already noted for the Colle Gnifetti core the Eastern European states doesn't appear to hold considerable importance in explaining the Southern Alpine high altitude aerosol depositions.

Volcanic Eruptions Recorded in the Alto dell'Ortles Glacier The TE enrichment factors profiles, computed from the discrete dataset, can be used to search for volcanic eruptions signs in the ice cores. The results should be corroborated by the presence of conductivity peaks (Clausen et al. 1997; Palais et al. 1992). In the following a tentative list of the possible volcanic horizons preserved in the Ortles ice core#1 is discussed, however this is a result of an on-going research and the specific volcanic geochemical trace element were still not compared with the literature

Table 7.10: Comparison of the Ortles ice core trace elements concentrations, the European emissions data (J. M. Pacyna and E. G. Pacyna 2001 and J. M. Pacyna, Semb, et al. 1984), and the Colle Gnifetti data for the periods 1960-1970 AD, 1970-1980 AD and 1980-1990 AD.

	V	Cr	Mn	Co	Cu	As	Cd	Pb
European emission for 1995 (Pacyna, 2001)	7432	436	304		292	79	47	3653
European emission for 1979 (Pacyna, 1984)	431	236	220	25	194	81	34	1538
European (9 countries)* for 1979	342	170	161	18	100	50	30	689
Colle Gnifetti (1960-1970)	36	20	368	5	43	24	9	616
Colle Gnifetti (1970-1980)	117	49	644	13	103	42	14	1060
Colle Gnifetti (1980-1990)	110	53	725	14	79	24	10	500
Alto dell'Ortles (1960-1970)	36	19	432	3	59	25	7	751
Alto dell'Orltes (1970-1980)	70	29	697	9	89	20	7	1392
Alto dell'Ortles (1980-1990)	46	38	1334	15	180	12	8	783

Table 7.11: Preliminary list of some selected volcanic horizons detected in the Ortles core #1. Depth, name of the volcano and year of eruption, TEs with an increased EF and the corresponding conductivity value.

Depth	Volcanoes	Year (AD)	TE with EF>1	Conductivity (μS)
46 m	Stromboli and Vesuvio	1944	Bi (30), Cr (6), Sb (80), Tl (6)	4.1
56.7 m	Raikoke	1924	Pb (15), Sb (50), Cr (9), Cu (25), Cd (12) , Al (26), V (4), U (6), Sr (5)	5.8
58 m	Katmai	1912	Hg (6), Pb (8), Cr (3.2), Cd7, Bi (11), Zn (5), Te (4)	2.5
59 m	Krakatoa	1881	NO TEs data	5.8
61.5 m	Tambora	1815	Sb (461), Bi (40), Pb (10), (4.2) and I (2)	2.2
62 m	Laki	1783	V (6), U (4), Te (5), Pb (10), Cu (7), Cr (>7), Cd (10	2.2
65.7 m	Hekla	1693	Hg (17), Cu (22), As (22) and Ag (27)	2.6

datasets. Many of the selected volcanoes were found through sulfates concentration analyses in the GISP2-H Greenland ice cores (Dreschhoff and Zeller 1990).

In Table 7.11 a preliminary list of some possible volcanic horizons is given, as well as the list of the TEs whose EFs increased and the conductivity value. Many other possible eruptions are suggested in the following lines even if this investigation was only preliminary and not complete. In Fig. 7.31 the conductivity profile (described in details in the Chapter 8) is shown together with the detected volcanic eruptions.

At a depth of 46 m the EF of some trace elements show value much higher than one: Bi (30), Cr (6), Sb (80), Tl (6). This heavy metal enriched layer could be due to the *Stromboli* (Italy) eruption in 1944 and the *Vesuvio* violent Strombolian Eruption in the same year (Scandone et al. 2008).

A significant peak is observed at a depth of 56.7 m. According to the actual dating of the core this peak can be the effect of the stratovolcano of the island *Raikoke*, in the North Pacific Ocean. An increase of the typically volcanic emitted trace elements concentrations is also observed (Pb, Sb, Li).

Two conductivity peaks (even if not so large in magnitude) can be observed at a depth of 58 m and this part of the core is dated from 98 to 99 years BP. The Katmai is an Alaskan stratovolcano and in 1912 strongly erupted and its signal was measured in Greenland ice cores. An increase of dust is also observed at this depth.

A conductivity peak can be observed at about 59 m (130 year BP in dating) (Fig. 8.2). Despite the great dating uncertainties at this depth, the peak could be the heritage of the *Krakatoa* volcanic eruption, happened in the 1881 AD. Unfortu-

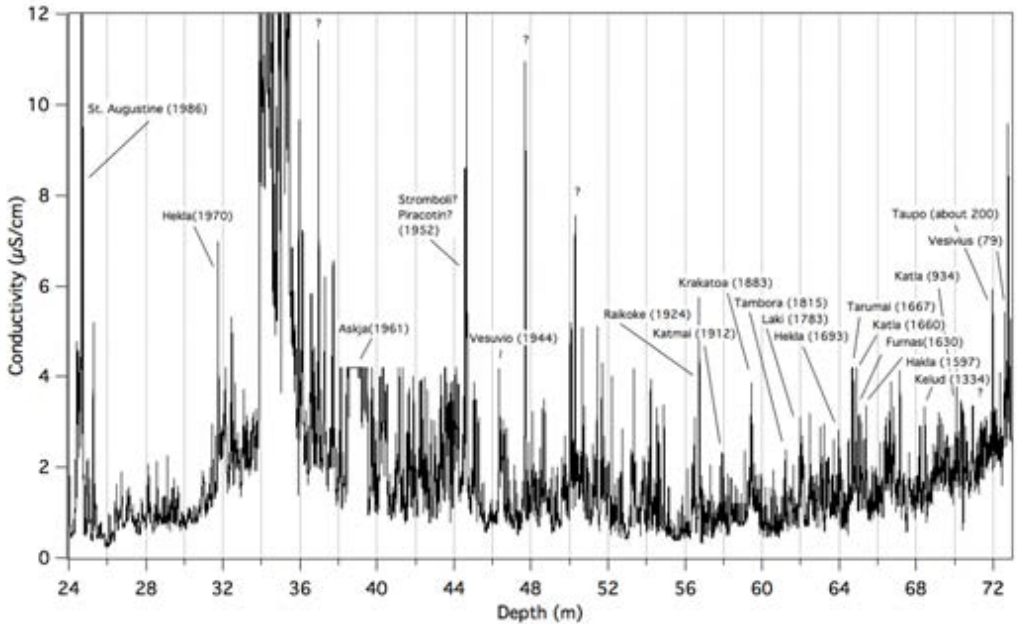

Figure 7.31: Conductivity profiles and tentative list of volcanoes recorded on the Alto dell'Ortles glacier.

nately, during the continuous flow analyses of the section 85, corresponding to this age, the ICP-MS line was blocked by an overpressure probably caused by a small stone (not observed in the ice). Therefore, the trace elements CFA results still require some analyses and therefore the volcanic eruption cannot be confirmed.

The trace elements EFs for Sb, Bi, Pb, Cd and I suggest the presence of a possible volcanic eruption dust layer at a depth of 61.5 m. The conductivity values are not very high but the peak is rather *large*, about 10 cm, suggesting a multi-annual dust deposition, maybe emitted from the *Tambora* eruption of 1815 in Indonesia. This was the world's greatest dust eruption after the last glacial period (Stothers 1984) The conductivity peak is quite large and with actual dating it covers about 7 years and it could therefore contains the large stratospheric eruption occurred in 1809 from a still unknown volcano (Cole-Dai et al. 2009).

At a depth of 62 m, a clearly visible conductivity peak is present (Fig. 8.1). The EFs of many trace elements suggest the presence of a volcanic layer. The observed EFs are: V (6), U (4), Te (5), Pb (>10), Cu (7), Cr (>7), Cd (10). The volcanic eruption that likely was observed at this depth is that of the Icelandic volcano called *Laki*, erupted in 1783. The eruption column was extended for more than 10 km in the atmosphere and it released a tephra volume of about 0.91 km^3 (Thordarson and Self 2003).

Hg (17), Cu (22), As (22) and Ag (27) EFs peaks are found at about 64 m, coupled with a conductivity peak. The author suggest that this could be the effect of the *Hekla* eruption of 1693, the strongest in the history of this Icelandic volcano (Dugmore et al. 2007).

High conductivity peaks were observed at a depth of 64.7 m, at about 70 cm and at 65.4 m. At this depth it's not easy to interpret the heavy metals EF because they show quite different results. However, by following the Cu and Cd EFs and the conductivity profile it appear that the first two peaks may be related to the *Tarumai* eruption (1667) in Japan and the *Katla* (1660) in Iceland (two eruptions

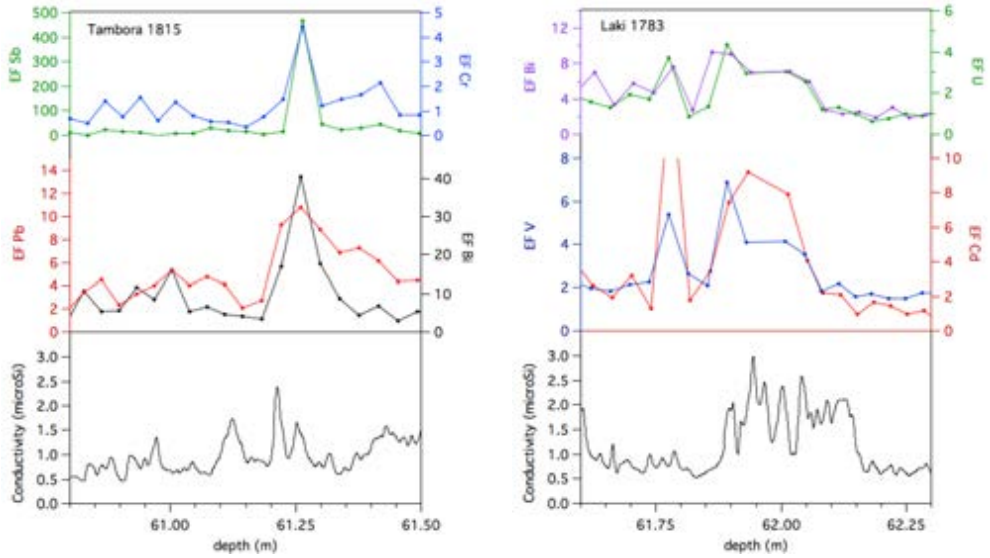

Figure 7.32: The Tambora (1815) and Laki (1783) volcanic eruptions signes in the Ortles ice core #1. The heavy metals EFs (the colors of the lines are related to the colors of the axes labels) and the corresponding conductivity peaks.

were detected in the GISP2 Greenland ice core in this period). The last peak could be the *Furnas* eruption of 1630 AD (one of the largest Holocene explosive eruptions in the Azores).

At 65.7 m the *Helka* eruption of 1597 may be indicated by a peak in the Bi, Cr, Cd, Ti and Tl EFs and a modest conductivity peak (about 3.2 µS).

High EFs values for Cr, Li and Cu were observed at a depth of 70.1 m with a conductivity peak of about 4 µS. Moreover, a significant dust content increase was detected in the years after the event. However, this layer may be the result of the *Katla* volcanic eruption of 934 AD (the actual Ortles dating states that this layer dates back to about 960 AD). This was an eruption comparable with the Pinatubo one (1991) with an emitted tephra volume of 5 km^3 and had a *Volcanic Explosivity Index* of 5/6 (over 7).

A strong Pb, Sb and smaller Bi EFs increase were detected at a depth of 72.3 m, coupled with a conductivity peak and a smaller one in dust. This increase may be associated to the *Vesuvius* (Italy) eruption in 79 BC (on-going research).

Two big conductivity and dust peaks are found at 72.5 m and 72.8 m, dated back to the last centuries BC. Tl EFs seems to confirm the presence of two volcanic layers (on-going research).

Chapter 8

Number of Particles and Conductivity Profiles

8.1 Introduction

During the continuous flow analyses of the Ortles ice core#1, the *particles number* and the total conductivity were measured, for the whole length of the core. A brief description of the instruments and of their position in the CFA system are given in the Chapters 4 and 5.

Particularly, the space resolution in the dust and conductivity measurements is the highest of all the measured profiles; it is due to their intrinsic fast response and short cleaning time and because of their position very close to the de-bubbler and the peristaltic pump. The ABAKUS particle counter results in a measurement data every 3 seconds, whereas the conductivity micro-cell gives a data every second.

A calibration of the ABAKUS system could be performed by mean of a comparison with Coulter Counter measurement on various samples. This would results in a more accurate and precise particles number results. However, the total mass of insoluble dust couldn't still be found from the ABAKUS results (P. Ginot personal communication). The ABAKUS/Coulter Counter calibration for the Ortles ice cores is currently under analyses at the Byrd Polar and Climate Research Center of Columbus (BPCRC, Ohio, USA).

The 32 dimensional channels were selected in order to cover the range where most of the particles dimensions are but also the biggest particles frequency was also analysed by selecting a dimension of 80 µm for the last channel.

The dust particles' content in the ice layers are usually characterized by a strong seasonality due both the varying depth of the atmospheric boundary layer and to the different atmospheric circulation patterns. Usually, the highest concentrations are found in summer but, especially in the Alpine region, dusty layers can be found also in late winter/spring do to the arrivals of Saharan dust (Schwikowski, Seibert, et al. 1995). In the dust particles' content profiles, this frequent events may significantly alter the annual layer counting.

The total water conductivity is the measure of the *ability* to conduct electricity, and it clearly depends from the dissolved impurities concentration. The conductivity is usually measured in $S\,cm^{-1}$ and the ultrapure water used in this work for cleaning the CFA lines was characterized by an electrical conductivity of about $0.05\,\mu S\,cm^{-1}$ (all the conductivity measurements in this work are per cm).

Water conductivity is often measured during ice cores continuous flow analyses because it is a very simple measurement that require simple instruments and it allows to check the cleaning of the system. From a scientific point of view the conductivity profiles represent the convolution of the ionic compounds envelops, therefore giving an important view of the total impurities in the ice.

The number of particles is mainly related to the insoluble dust component that is considered to be the kind of impurity most resistant to percolation (Wong et al. 2013). Water conductivity, instead, measures the soluble ionic components, which are usually the most affected from the water percolation events. The two profiles can result in different information, especially in the presence of melting and refreezing cycles, as in the Alto dell'Ortles ice cores. During the analyses it was not possible to detect a unique simple relation between the conductivity and the particle content in the presence of ice lenses (on-going research).

8.2 Results and Discussion

The Ortles ice core#1 conductivity and particles content profiles are shown in Fig. 8.1 as a function of the core depth, and a more focused profile as a function of the dating curve in Fig. 8.2. The depth profiles are very useful to grasp the presence of glaciological strange features and to determine the chemical response to them.

It is immediately clear that the conductivity presents some interesting features. Starting from the top a very ionic compounds concentrated layer is visible at a depth of 24 m. The conductivity reaches the 15 μS but curiously in the ice lenses profile (Fig. 2.14) no lenses were observed at this depth. This could be an impurities enriched layer due to post-depositional effect, thus bringing ionic soluble compounds from the upper firn and, indeed, the density profiles appears to achieve the ice values from this depth to about 33.5 m. Very high peaks are observed for the soluble trace elements concentration profiles: Na, Mg and I concentrations show a peak at this depth. In contrast, the crustal elements, such as Ba or V do not show any increase, but increases at about 26 m, where the dust particles contents increase and the conductivity show the lowest value in the core.

The most interesting feature is the conductivity increase detected at the depth of 33 m to 36 m: from 1 μS to 32 μS. The beginning of the peak is quite abrupt but then high values are observed for about 2.5 m (with high and less high peaks).

By considering the Ortles core dating, the overall signal may be divided into three parts, where the conductivity behaves quite differently. A linear decreasing trend can be observed from the very end of the core, dated 1000 BC, to the 19^{th} century, where the signal appears to stabilize. A large variability and increase in absolute values characterize the period between 1910 and 1970 AD and, especially in the most recent part this may be due to the firsts melting episodes at the beginning of the atmospheric warming in the 1980s. After this period the conductivity started to increase again since 2000 AD, possibly showing a progressive post-accumulation washing.

The ice layers related to the highest conductivity peak (around 35 m of depth, Fig. 8.1) are referred to the years at the end of the 1960s (Fig. 8.2). This is considered to be most polluted period in the European history and it was caused by the economic expansion and the grown of industrial activities. However, these con-

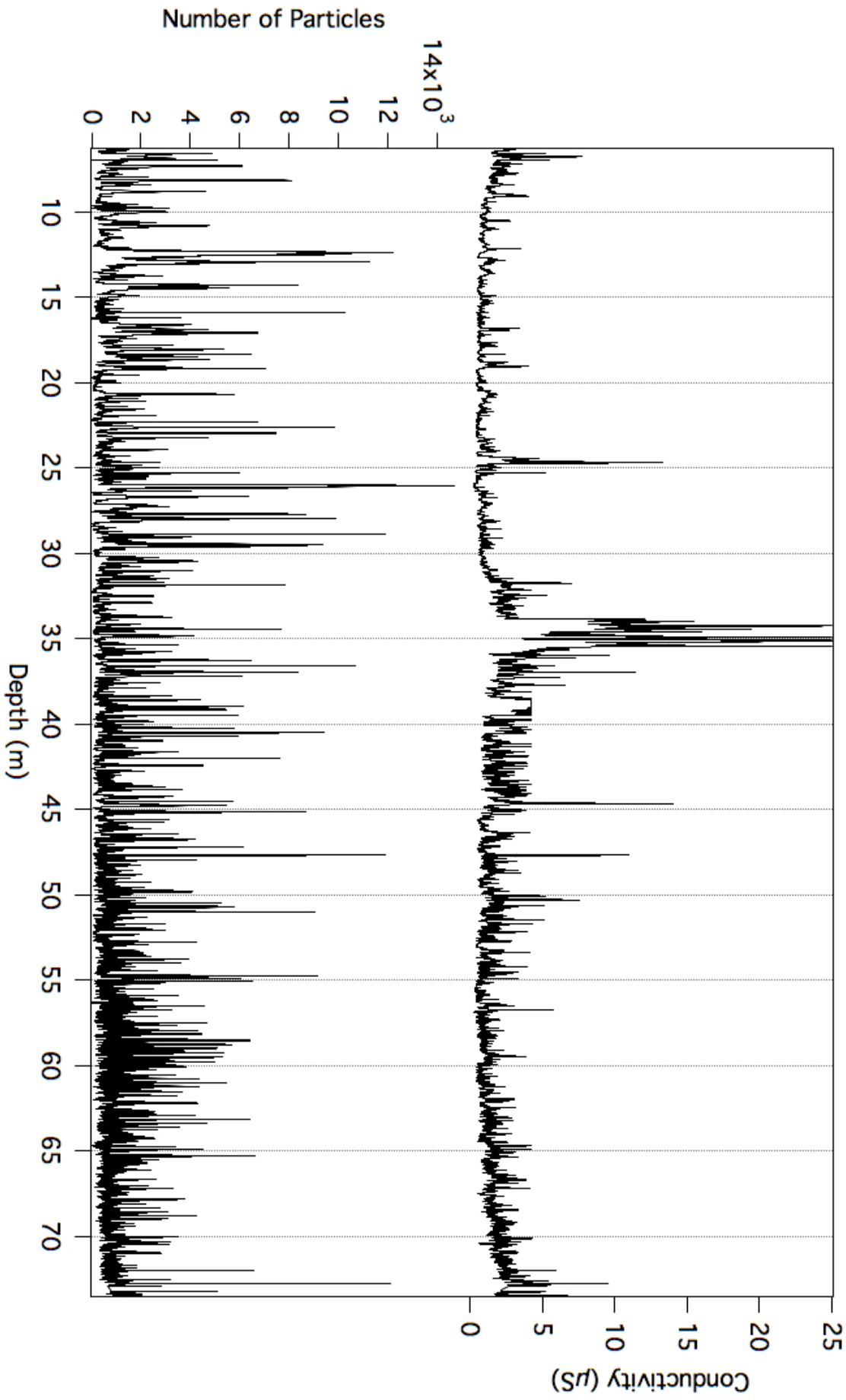

Figure 8.1: Conductivity and particles content profiles as a function of depth for the Alto dell'Ortles ice core#1.

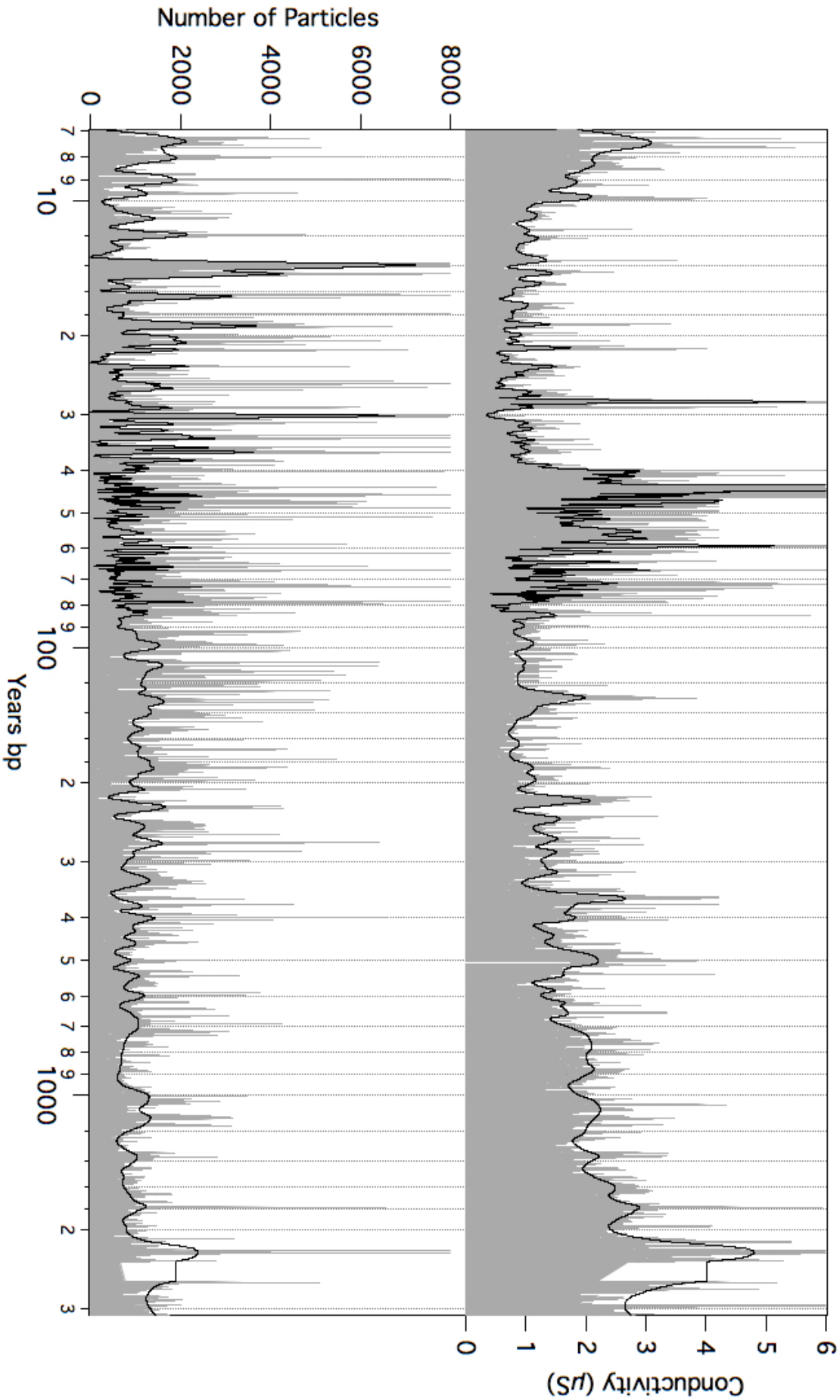

Figure 8.2: Conductivity and particles content profiles over the last 3000 years for the Alto dell'Ortles ice core#1.

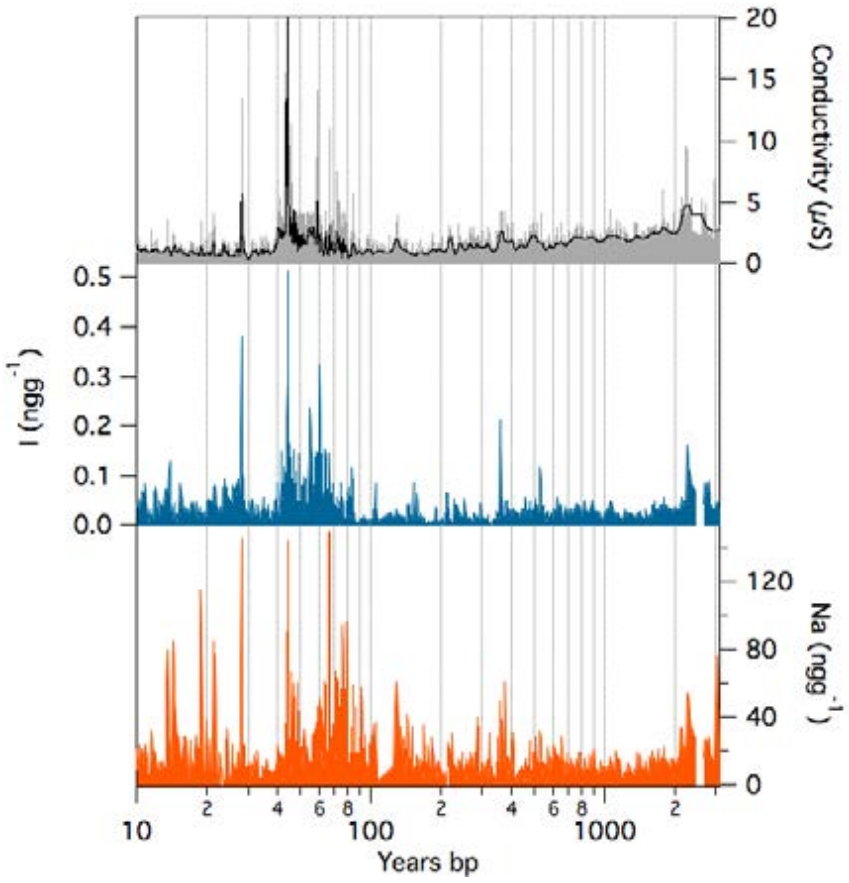

Figure 8.3: Conductivity, Iodine (I) and Sodium (Na) profiles over the last 3000 years for the Alto dell'Ortles ice core#1.

ductivity values may suggest a percolation and reallocation of ionic compounds at this level, possibly representing the past firn-ice transition during the 80s. At this level many elements show high concentration, as for Na, Mg, Ca, and I; the latter has the highest concentration of the whole record (about 0.4 ng g^{-1}). On the contrary, the more insoluble crustal elements as Fe and Ba do not show any particular increase.

In Fig. 8.3 the similarities between the Conductivity, I and Na profiles can be observed for the whole core time period. Particularly, this information is very useful in order to double check the conductivity measurements when showing this huge thirty-fold increase 45 yrs BP.

At a depth of 38.7 m the conductivity profile show a plateau at a value of 4.2 μS: this signal envelope is not the realistic one because the conductimeter saturated at this level. After this section analysis the system was changed in order to change scale automatically. Giving the linear correlation between the conductivity profile and the I concentration profile, it could be possible to reconstruct the saturated conductivity peak values from the I concentration, with a small uncertainty level (on-going research).

The complete *number of particles* profile was continuously obtained for the Ortles ice core #1, exploiting the 32 dimensional channels of the ABAKUS. In Fig. 8.4 is reported a 3D graph showing the number of particles as a function of the dimensional channels and of the depth of four Ortles ice core sections (from 10 to 13).

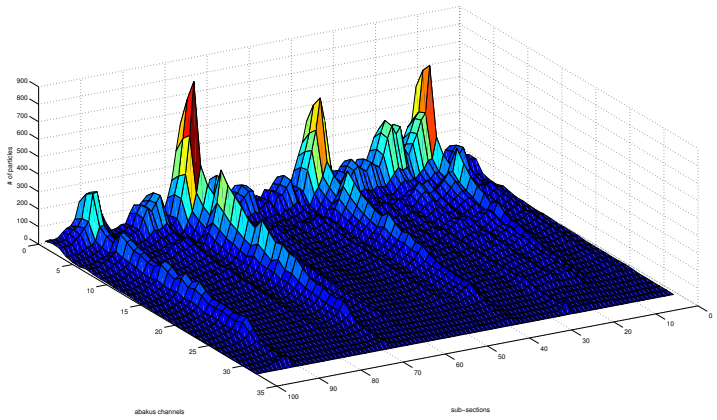

Figure 8.4: Particles contents per dimensional channel as a function of depth for the Ortles ice core#1 sections 10, 11, 12 and 13.

The graph was obtained by mean of an *ad hoc* MATLAB code (the code divides the section length in an adaptable number of sub-sections and computes for each of them the average concentrations per channel). It is clearly visible that the highest particles dimension concentration lies in the first three dimensional channels, at 0.8 µS, 0.9 µS and 1 µS respectively. Moreover, four seasonal cycles can be observed. A statistical study of the dimensional properties and distribution of the particles measured in the Alto dell'Ortles ice core should still be performed.

Chapter 9

Black Carbon Profile

9.1 Introduction

Black carbon (BC) is a primary emission aerosol that is emitted by biomass burning and fossil fuel consumption. The strong visible light absorbing properties of BC makes it the second most important anthropogenic forcing in the Earth climate system after carbon dioxide (T. C. Bond, Doherty, et al. 2013). Particularly, BC is one of the main responsible factors for global warming strongly influencing the atmosphere and cryosphere radiative properties towards a higher solar radiation absorption and a consequent heating (T. C. Bond, Doherty, et al. 2013). The small BC particles dimensions caused them to be easily transported by atmospheric motions over long distances (Ramanathan and Carmichael 2008). The BC deposition on snow and glaciers contributes to the darkening of the surface therefore decreasing the *albedo*. A significant contribution to the snow melting was observed in many studies (Hadley and Kirchstetter 2012, B. Xu et al. 2009, Y. Xu et al. 2016).

Despite the important role in the climate system BC emissions and variability reconstructions over the past centuries are still limited both in number and in the considered time range (Novakov et al. 2003, Collaud Coen, Weingartner, et al. 2007 and Collaud Coen, Andrews, et al. 2013). The only possible way to quantitatively reconstruct the BC variability over centuries or millennia time scale is to exploit environmental archives, such us ice cores. Yearly BC depositions on glaciers or ice sheet can be studied and the BC past variability can be assessed. BC deposition reconstructions were performed for ice and firn cores from many locations such as Antarctica, Greenland (Bisiaux et al. 2012, S. D. Kaspari et al. 2011, McConnell, Edwards, et al. 2007). Only few reconstruction were performed in the European region, and the time interval covered never exceed the last millennium: Colle Gnifetti ice core (1000-1980 AD with centennial resolution before 1500; Thevenon et al. 2009), Fiescherhorn glacier (1650-1940 AD, with decadal and multi-decadal resolution; Jenk 2006), Col du Dôme (1920-1990 AD, annual resolution; Legrand, Preunkert, May, et al. 2013) and Mt.Elbrus (1825-2013 AD, sub-annual resolution; Lim, Fain, Ginot, et al. 2016).

The BC and chemical compounds reconstruction from glaciers in the European Alpine region are of extraordinary importance in order to asses the anthropogenic environmental impacts in this highly densely populated region. Particularly, all of the reported reconstructions revealed a significant BC increase from the middle of the 20th century, as a result of the increased industrial sector and anthropogenic

activities in general (for the Western European Alpine area: Lamarque et al. 2010).

The only rBC record from the Eastern Europe, in the Caucasus region, was derived from an ice core from Mt. Elbrus covering the period 1825-2013 with sub-annual resolution (Lim 2014 and Lim, Fain, Ginot, et al. 2016). Particularly, the measured BC concentration significantly increased from the 1950s decreasing then from 1990s; the BC deposition in the last decade is still comparable to that of the most polluted period, especially during the summer period.

In this work the results from a continuous flow analyses on a 73.5 m deep ice core are presented in terms of rBC concentration and dimensional characteristics. This is the first BC deposition reconstruction time series covering the last 3 millennia in the European Alps. Particularly, a refractory BC (rBC) high-resolution record is presented for the Alto dell'Ortles glacier ice core (3905 m a.s.l., South Tyrol, Italy).

For information about the ice core site, meteorology, glaciological characteristics, the dating, the continuous flow system, the SP2 functioning principles and calibration and the method used refer to Chapters 2, 4, 3 and the 5, respectively.

9.2 Inventories of past BC emissions

The two main sources of BC are the energy production sector and biomass burning (T. C. Bond, Doherty, et al. 2013), and 90 % of the total BC worldwide emissions in 2000 it was of about 7500 Gg $year^{-1}$ are due to diesel engines, to industrial coal burning, residential solid fuels (such as wood), and open burning (natural sources are savannas or forest burning) (T. C. Bond, Doherty, et al. 2013).

The BC residence time in the atmosphere is much lower compared to those of greenhouse gases, about 10 days after which it is removed both by *wet* and *dry* depositions; wet deposition is considered to be 3 times more efficient than the dry (S. E. Bauer et al. 2013). However, the small dimensions of the BC particles makes that it can be transported over very long distances and it can therefore be found even in the most far from sources places, as in Greenland, Antarctica and in the Tibetan Plateau (McConnell, Edwards, et al. 2007, Bisiaux et al. 2012 and Ginot, Dumont, et al. 2014).

The drafting of BC emission inventories requires both the knowledge of the various emission sources, and of the emission factor per each single source (how much of the total emission of the burned fossil fuel quantity, for instance, is released as BC) (Lamarque et al. 2010). Large uncertainties derived by the emission factor estimates: the technological level of each emitting country has to be taken into account for each time interval of an emission inventory. Particularly, high quality data characterized the emissions of the occidental states, such as Europe or North America, whereas very poor data are available especially for the developing countries. The result is the presence of a significant discrepancy between the various inventories, which is however decreasing in the last decade (Granier et al. 2011).

Three different historical BC emission inventories are considered in the following sections in order to evaluate and compare the BC concentration trend detected in the Ortles ice core. The reconstructions cover the period 1850-2000, thus covering both the concentration increase at the beginning of the 19^{th} century and the

consequent decrease during the second half. The three datasets will be called *ACCMIP* (Emissions for Atmospheric Chemistry and Climate Model Intercomparison Project), *Junker and Liousse*, and *Bond*; the respectively sources are Lamarque et al. 2010; Junker and Liousse 2008 and T. C. Bond, Bhardwaj, et al. 2007. *ACCMIP* and *Junker and Liousse* includs some states of non-OECD Europe. Only anthropogenic emissions are considered in these databases. *Bond* and *Junker and Liousse* slightly differs in the followed methodology in creating the datasets (see the references). *ACCMIP*, instead, is the results of an harmonization between many BC emission reconstruction dataset, comprehending the other two datasets as well. This dataset was created in order to be used during the *Coupled Model Intercomparison Project Phase 5* (CMIP5) of the *World Climate Research Programme* (WCRP) (Granier et al. 2011).

9.3 Results and Discussion

9.3.1 The rBC High-Resultion Profile

The first high-resolution rBC profile obtained from an ice core from one of the highest summit of the Eastern European Alps, Alto dell'Ortles (3905 m), is presented in Fig. 9.1. In order to visualize better the profile the y-scale was fixed at 20 ng g^{-1} and the values of the three outliers peaks were written on the graph. It is clear that the rBC concentration profile can be mainly divided in two parts, from 6 m to 58 m and from 58 m to the end of the core. The former is characterized by a large rBC variability with some intense concentration peaks, whereas in the latter the rBC variations are much smaller in amplitude. This difference is due both to the decreasing of rBC concentration from the end of the 18th century and to the considerable thinning of the ice layers in the second part; the system is no more able to separate the seasonal signals as before and the diffusion as well may have smoothed the signal. In the last 13.5 meters of the core about 2800 years are compressed and preserved. The maximum values are observed between 40 m and 58 m of depth and the highest peak is at (42 ± 16) ng g^{-1} at 51.7 m.

rBC profile as a function of depth show very detailed seasonal oscillations. By applying the dating curve, the precise dating of almost each yearly oscillation can be observed (Fig. 9.2). For the first 80 years BP the rBC profiles exhibits a large variability and the seasonal oscillations appears to be enough to cover all the annual oscillations. However, in some part of the core the oscillations have a higher frequency compared to the seasonality of the dating (e.g between 30 and 40 m), whereas in some other parts the oscillations are less than what suggests by the dating curve. A possible explanation could be the inter-calibration of depth between the core #1 and the core #2 (which the samples for the dating were obtained from), or this may be the results of post-depositional effects. Given the criticalities in establishing the annual layers, the author decided to perform the characterization of the profile by considering the whole dataset without dividing into sub-annual signals.

The rBC profiles ranges from a minimum value of 0.024 ng g^{-1} to a maximum of 40.6 ng g^{-1}. The mean value over the whole core is 2.07 ng g^{-1} (with a standard deviation of 1.94 ng g^{-1}) and the median is 1.55 ng g^{-1}. The instrumental resolution was sufficient to have sub-annual resolution, especially in the first 58 m, whereas

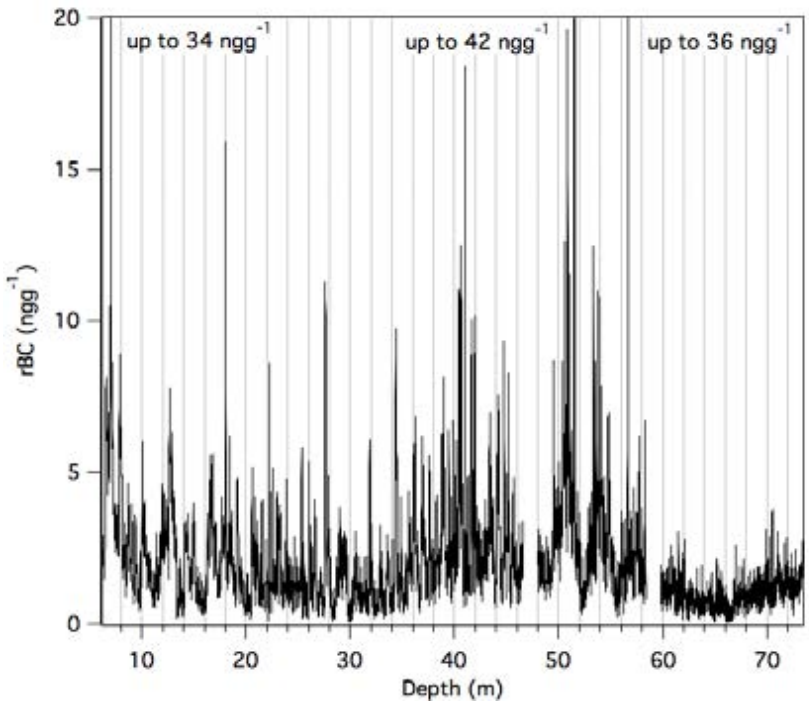

Figure 9.1: High resolution profile of rBC continuously measured in the Alto dell'Ortles ice core#1 for the period 2004 AD-1000 BC.

after that the resolution decreased due to the intense thinning of the ice layers; in the last meters of the core a multi-annual to decadal resolution was obtained.

For the moment, it was not possible to separate between the summer and winter layers. The main reason is that the Alto dell'Ortles, at least in the last three decades, was characterized by more or less intense surface melting during the summer periods (Gabrielli, Barbante, Bertagna, et al. 2016). Extremely warm summers like that of 2003, may have caused a water percolation down to about the firn ice transition, at about 25 m, therefore affecting the firn layers dated back to the 80s. The rBC profiles is shown from the year 2004 but down to 1980s the concentrations results may be affected by percolation. The first seasonal oscillations in the profile, are indeed very smoothed and this may be due to the percolation and/or to a smoothing *created* by the CFA firn melting. In order to have the continuous profiles for all the analytes of the CFA system the decision was to melt all the firn part with the melting system. However, the discrete samples of the first snow/firn sections where also analyzed discreetly, showing that the smoothing was at least partly a real feature in the core (data currently under analyses), part of the smoothing in the discrete samples may also derive from the melt water flowing in the CFA system.

Unfortunately, two holes are shown in the profile and the signal of 2.8 m of ice is not present: an instrumental problem and an erroneous decision (not of the author) are the causes, respectively. Hopefully, the profiles will be completed by using discrete samples in the near future.

The significant short-term variability of the rBC profile can be attributed, however, to the seasonality. Particularly, the warm summer of 2003 appears to be preserved despite the strong surface melting (it may also be that the rBC deposited in the summer of 2003 accumulated on a summer surface cumulating several years; on-going research). The rBC peaks at about 34 ng g^{-1} and also the two to three

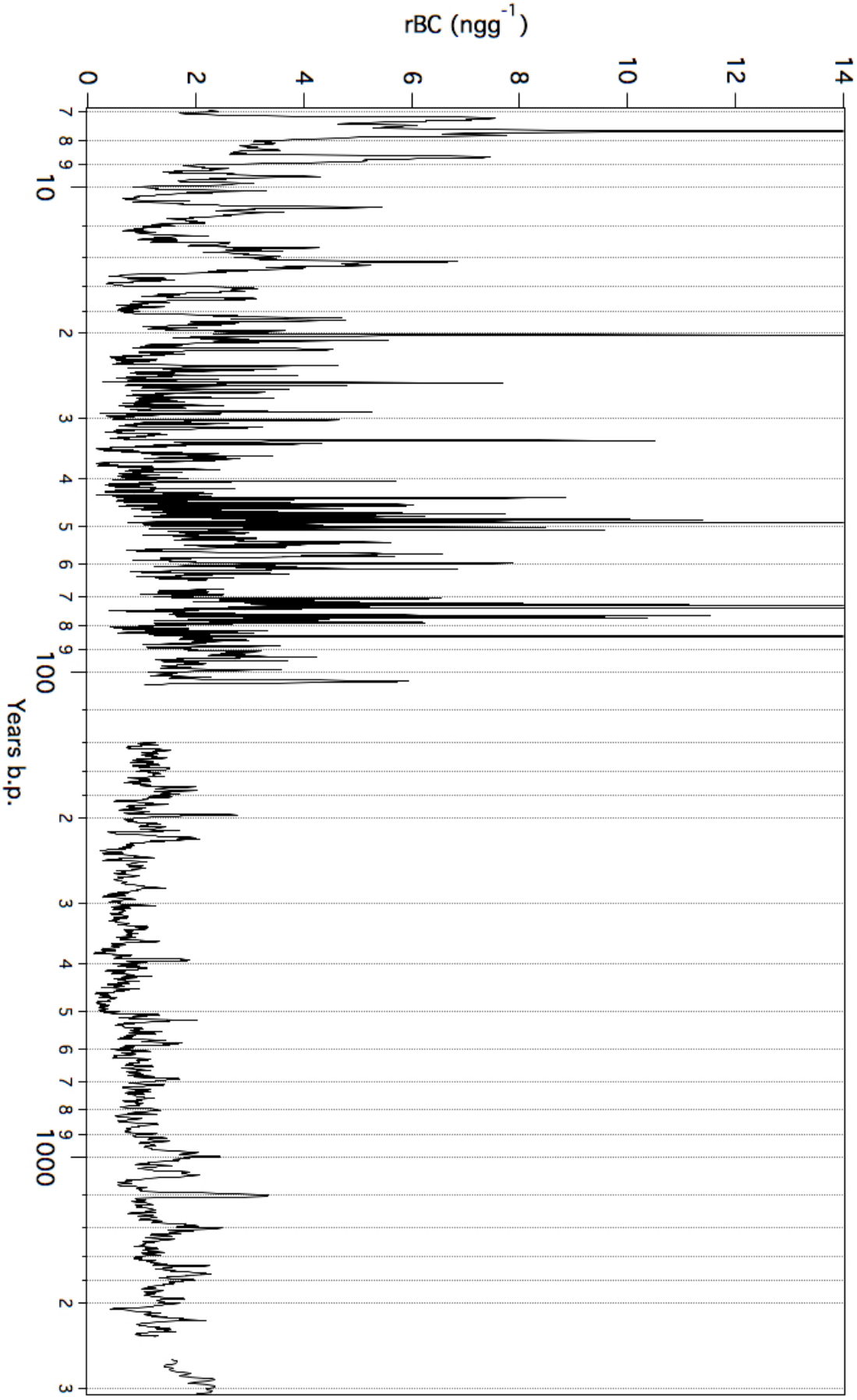

Figure 9.2: High resolution rBC profile as a function of the dating curve. The highest peaks were cut in order to better observed the smaller oscillations.

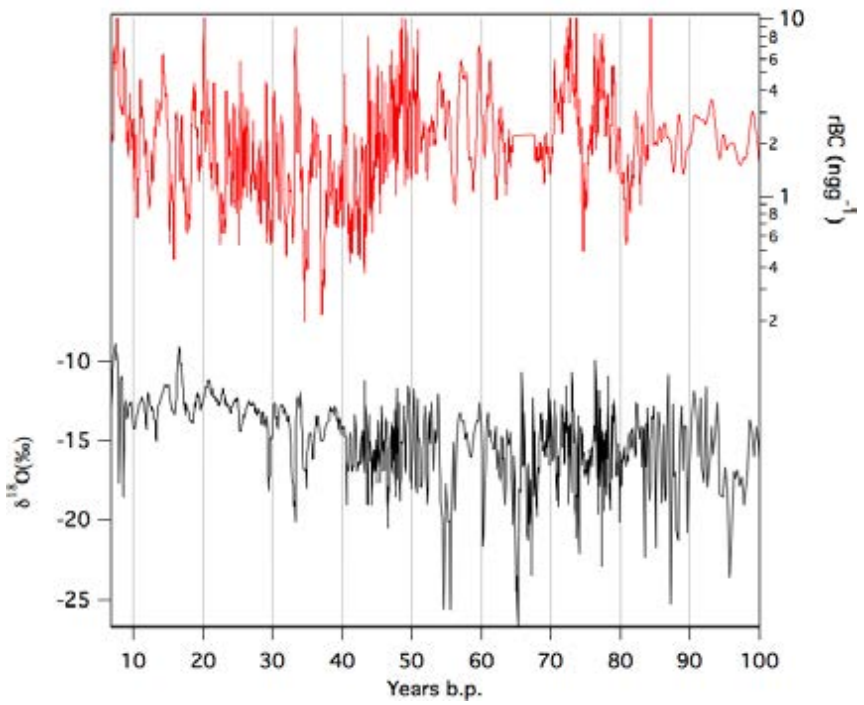

Figure 9.3: High resolution rBC profile on a logarithmic scale (red line) and water stable isotopes (black line) in the Alto dell'Ortles ice core#1, as a function of the dating curve.

years before 2003 seems to be affected by it, likely as a consequence of melting.

The peaks of rBC concentration are usually observed during summer and it can be clearly observed by comparing the rBC profile with that of the water stable isotopes. (Fig. 9.3). It is clear, from the most recent oscillations, that the highest rBC concentration are simultaneous to the less negative isotopic values, meaning warm periods. Another interesting observation, which is of fundamental importance for the Alto dell'Ortles ice cores, is that the rBC profile seems to catch every yearly oscillation, even when the layers are quite thin, like at about 25 m, even when the isotopic profiles don't; the pollen profiles, currently under analyses on the Ortles ice core #1, will clarify about the seasonal signals preservation or not, particularly in the firn part of the core.

The summer maximum peaks are due to the atmospheric layers characteristics during the year. As reported in the Section 6.4.4 the boundary layer depth (BDL), defined as the altitude where the thermal inversion is, is more frequently higher than the Ortles glacier during the summer period than in winter. The atmospheric BD *blocking* doesn't allow the pollutants to be injected in the free troposphere and being consequently transported by the atmospheric motions. Particularly, ground aerosol measurement performed in the Western and Central Europe revealed the highest elemental carbon (EC) concentration in winter, caused by domestic heating systems and road traffic; almost the double compared to the summer concentrations (Pio et al. 2007). On the contrary, EC aerosol measurements at high altitude sites (e.g. Sonnblick, 3106 m) revealed that during summer the atmospheric concentrations are from 2 to 3 times higher compared to the winter ones (Venzac et al. 2009; Pio et al. 2007). During summer the convective motions are stronger than in winter and the boundary layer is thicker, allowing a increased BC transport

from the polluted near surface zones to high altitude sites (Matthias and Bösenberg 2002).

The intense melting and water percolation of the last decades may have affected the concentrations in the firn, by partially re-locating the soluble impurities and the small particles. Only few studies were directed toward the post-depositional effects of black carbon. The preservation of the EC was the results of a four years study of shallow core at Summit, Greenland, whereas OC was found to be strongly influenced by post-depositional processes. The first preliminary results of a 80 days experiment with daily resolution and another of 3 days with hourly resolution for the surface snow at Ny-Alesund (Svalbard), reflected a short time scale variability in the rBC concentration, mainly following the solar radiation behavior causing snow sublimation and rBC removing from the surface (Bertò et al., in preparation); more analyses have to be done in order to quantify and to give a detailed physico-chemical explanation of this effect. A variation of the rBC mean diameter (enhanced co-agglomeration) as a consequence of the surface snow sublimation and/or melting and percolation was also suggested (Lim 2014), even if this was not observed on average in the firn part of the Ortles core, strongly influenced by frequent melting and percolation events (on-going research).

9.3.2 The rBC Profile Over the Last 3000 years

The rBC profile over the entire time range cover by the Alto dell'Ortles ice core#1 is characterized by a significant concentration variability. The statistics for the various periods are reported in the Table 9.1.

From 1000 BC to about 1800 AD the rBC concentration seems to be almost stable at low values, with an average and a σ of $(1.0 \pm 0.5)\,\mathrm{ng\,g^{-1}}$ and a median of $0.89\,\mathrm{ng\,g^{-1}}$. For all the 19^{th} century the rBC concentration remained almost constant on average at about $1.1\,\mathrm{ng\,g^{-1}}$. An increased was detected from the onset of the 20th century, from 1900 to 1930. The average concentration grows to $2.3\,\mathrm{ng\,g^{-1}}$ and the variability also increased (Max/Min of about 97). The highest increase was observed one decade after, during 1930-1940, and the average was $3.5\,\mathrm{ng\,g^{-1}}$ with a Max to Min ration of 186. A decrease is observed in the next decade, from 1940-1950, with an average decrease of 40%. Another increase was then observed from the beginning of the 1950s to the end of the 1960s and the first years of the 1970s, the average concentration was of $2.6\,\mathrm{ng\,g^{-1}}$. A sudden decrease was detected during the 70s and the concentration dropped to values similar of those of the period before 1900, about $1.4\,\mathrm{ng\,g^{-1}}$. In the next two decades, the rBC concentration slightly increased again. However, the frequent melting episodes may have concentrated or re-located the rBC particles in the firn.

The rBC concentrations of the Ortles ice core may be compared with other rBC and EC long range records. Particularly, as described in the introduction only one long record is published for the rBC concentration over the last two centuries (Lim, Fain, Ginot, et al. 2016) (measured with an SP2, Droplet Measurement Technologies, Boulder, Colorado). The other datasets, from the Western Alps, focused on the EC and OC concentration. Despite the different instruments and methods these two kinds of datasets can be compared.

The Colle Gnifetti (CG) ice core dataset (Thevenon et al. 2009), the Col du Dôme (CD, Legrand, Preunkert, May, et al. 2013) and the Mt. Elbrus (ME, Lim, Fain,

Table 9.1: Descriptive statistics for the rBC concentration measured in the Alto dell'Ortles ice core#1. The time interval were chosen in order to underlain the cariability.

	Average	Increase from pre-industrial period	Median	Max	Min	Max/Min	25% perc.	75% perc
1000 BC-1800 AD	0.99	1.0	0.89	3.8	0.04	90	0.61	1.3
1800-1825	1.1	1.1	1.0	3	0.25	12	0.78	1.2
1825-1850	1.2	1.2	1.2	2.6	0.3	8.7	0.94	1.4
1850-1870	1.1	1.1	1.1	2.0	0.45	4.3	0.93	1.3
1900-1930	2.3	2.3	1.9	26	0.27	97	1.5	2.6
1930-1940	3.5	3.6	2.9	41	0.22	186	1.8	4.3
1940-1950	2.2	2.2	1.9	8.7	0.52	17	1.5	2.5
1950-1960	2.7	2.8	2.4	9.3	0.52	18	1.8	3.4
1960-1970	2.4	2.5	1.9	18.4	0.024	759	1.1	3.1
1970-1980	1.4	1.4	1.1	11.3	0.076	149	0.66	1.8
1980-2000	2.2	2.2	1.7	23.7	0.11	220	1.0	2.8

Ginot, et al. 2016) datasets report values also for the last two decades, whereas the Fiescherhorn dataset (F, Jenk 2006) is available up to the 1940. The longest dataset is that from the CG (from 1000 AD), followed by the F (from 1650 AD), by ME (from 1825) and by CD (from 1920 AD). In the CG dataset the reported temporal resolutions are almost centennial or multi-centennial before the 1600.

The Ortles record appears to have the lowest rBC concentration value for almost all the dataset. Particular, for the pre-industrial period (mid-1800) the measured concentration was of 2 ng g^{-1} at CD, 7 ng g^{-1} at CG and 4.3 ng g^{-1} on ME, whereas 1.2 ng g^{-1} for the Ortles ice core. From 1924 to 2009 the average concentration for ME increased at about 13.3 ng g^{-1} and comparable values for the other datasets. The increase factor was computed between the concentration of the pre-industrial period (mid 1800) and for the period 1900-1990 (or 1940 for F). However, for Mt. Ortles, a maximum average increase of 3.5 was observed between the 1930 and 1940; the increase between the 1920 and 1980 is only 2.4. The most similar results are: CDD with an increase of about 1.54, F with 1.55 and ME with an increase of about 3. The CG instead, show an increase higher than 10, probably caused by the winter snow wind removal.

All the datasets agree in the significant increase during the mid of the 20^{th} century, however strong differences can be observed for the various profiles. Particularly, the ME show a rBC increase from the 1940s, without any sign of strong increase during the period 1930-1940, as observed in the Ortles ice core. The EC in CG increase during the 50s, then decrease and a strong increase is observed in the beginning of the 60s-70s, quite similar to the Ortles dataset. Differences in the profiles may be due to different sources areas, and also the altitudinal differences may have a role, the Alto dell'Ortles is at 3905 m, whereas ME is at 5115 m. The Ortles and ME profiles, differ for many aspects: the absolute rBC concentration value is 5 times lower in the former ice core. Moreover, the strong increase during the period 1930-1940 on the Alto dell'Ortles, probably due to an industrial mobilization for WWII (as measured also for many heavy metals, like Hg; see the Chapter 7), was not at all observed in the ME ice core; probably the proximity of Mt. Ortles to the center of the Europe made it more influenced by these episodes; also the other oscillations of rBC concentrations can be explained in this way.

9.3.3 The rBC Size Distribution Variability

The *mass equivalent diameter* can be obtained by the SP2 data analyses (contrary to all the other EC/OC measurement techniques). The rBC particles diameter is a very interesting physical parameter that may give insights both into the different rBC sources (such as road traffic or biomass burning), into the atmospheric processes happened before the deposition and into the post-depositional effects (J. Schwarz, Gao, Spackman, et al. 2008 and reference therein). Only a part of the complete dimensional spectrum of particle in the atmosphere or deposited in the snow can be covered by the SP2 measurement; particularly, only the particles with a diameter in between 60 nm and 620 nm were considered in this work.

The rBC particles diameter is expressed as a *mass equivalent diameter* and it is computed with the following formula, by considering an rBC effective density of 1.8 g^{-3}cm (Moteki and Kondo 2010):

$$D_{MEV} = (6M/\rho\pi)^{\frac{1}{3}}$$

M is the particle refractory mass (computed from the incandescence signal) and ρ is the effective rBC particles density.

The first long-term rBC particles diameter study was performed for the ME ice core (Lim, Fain, Ginot, et al. 2016). The summer and winter layers were analysed separately for the mass equivalent diameter and the mode of the diameters distribution were computed by fitting with a log-normal distribution. A significant difference was found between the two results, with the summer layers mean *Mass Mode Diameter* equal to 290.8 nm, and the winter one to 268.7 nm. The explanation is that the summer rBC deposition on the ME glacier mainly derived from the thermal-convection processes uplifting the pollutants from the boundary layer. Whereas, during winter the wet-deposition is mainly composed by particles that were in the free troposphere and therefore characterized by smaller diameters due to the long-range transport and long atmospheric residence. A similar result for atmospheric measurement at high altitude was obtained at different European mountain stations (from 1000 m to 3000 m a.s.l.) (Asmi et al. 2011).

The *mass equivalent mean diameter* was analyzed in this work and particular attention was given to long-range temporal variations. This is the first time that the rBC mass equivalent diameter (DrBC) is analyzed for a 2000 years time range.

The Alto dell'Ortles DrBC size distribution was log-normal. For each ice section analized both the rBC time series and the mass equivalent diameter time series were obtained. Therefore the mass equivalent diameter time series was created for the whole length of the core. The procedure followed in this work was slightly different from the previously reported one (Lim, Fain, Ginot, et al. 2016): in this work all the available diameter data from the SP2 signal were considered, whereas only the mode was used in creating the time series Lim, Fain, Ginot, et al. 2016. In this way the variability range was evident in the box plot time series, reported in Fig. 9.4. The DrBC profile was clearly noisy because of the various particles dimensions in the summer and winter layers. A box-plot approach was chosen by dividing the dataset in five time intervals in such a way as to highlight the observed mass equivalent diameter changes along the time cover by the ice core. In the various ranges the DrBC didn't vary significantly. The selected time intervals were from 0 to 600 AD, from 600 to 1200, from 1200 to 1800, from 1800 to 1950 and from 1950

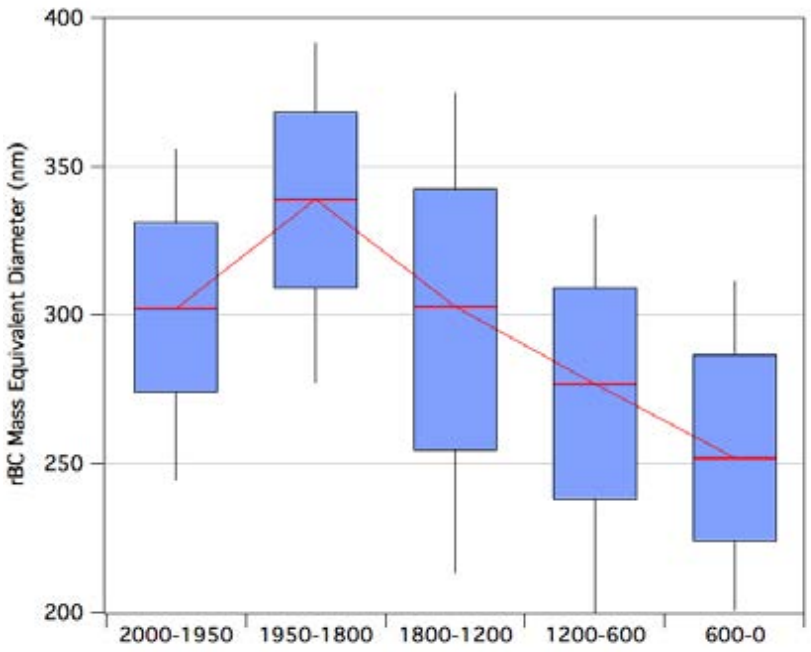

Figure 9.4: Box-plots for the rBC *mass equivalent diameter* (DrBC) time series measured in the Alto dell'Orltes ice core#1. Median (red line), 25% (blu boxes) and 75% (black lines).

to 2000. The resulting box-plots are characterized by the median (red line), the 25% and the 75% percentiles of the dataset (Fig. 9.4).

Despite the high intra-interval variability in the DrBC two clear trends can be observed. The DrBC values from the very ancient ice of the core (from 0 to 600 AD) were characterized by a median of about 250 nm. A significant increasing trend of about 25 nm every 600 years was then observed until the 1200-1800 interval, where the median of the DrBC was about 300 nm. The median of the DrBC distributions reached the value of 330 nm in the interval that mainly covers the European *industrial revolution* period. After the 1950/1960 and to 2000, the DrBC distribution returned to a median value of 300 nm, equal to that observed in the pre-industrial period.

The measured values are comparable to those recorded for the ME ice core in the period 1940-2010: the median annual DrBC was about 280 nm. However, larger DrBC median values were found in the Ortles ice core from about 1200 AD to the most recent years: in the period 1200-1800 AD the DrBC median was about 300 nm, in the period 1800-1950 AD was about 340 nm and from 1950 to 2000 AD it decreased to about 300 nm (Fig. 9.4). This may be due to the lower altitude of the Ortles glacier, which is more than 1000 m lower compared to ME. Therefore, especially during summer, the rBC particles from the polluted boundary layers can more easily achieve the glacier and less wet deposition particles size filtering occurs before the eventual deposition. On the other side, the rBC concentration are usually 7 times lower in the Ortles ice core, and this probably reflects its geographical position (on-going research). Interestingly, a smaller DrBC median value was computed for the last 50 years, despite the frequent melting episodes meaning that post-depositional effect may not strongly affect the DrBC. This result appears to

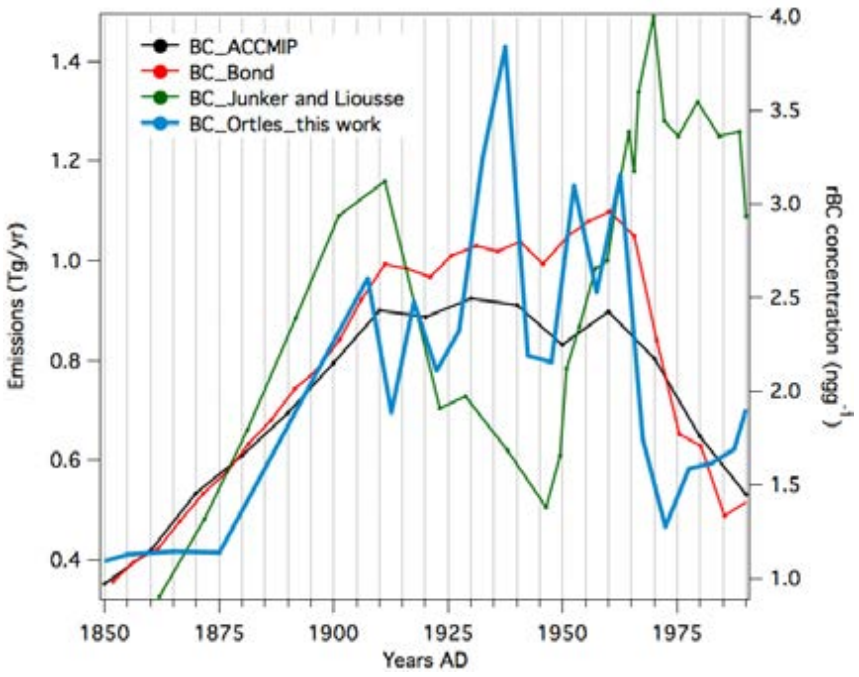

Figure 9.5: Historical BC emissions reconstructions for the period 1850-1985. *ACCMIP* (black line), *Bond* (red line), *Junker and Liousse* (green line) and the 5 years average Ortles ice core#1 rBC profile.

suggest that the dimensional increase during the industrial revolution period was the result of the dry deposition changes. A preliminary interpretation may be that the intense use of *dirty* fuels like coal or wood, may have caused a dimensional increase in the rBC particles, followed by a decreasing caused by a shift in the energy sector in the 70s (on-going research).

9.3.4 rBC Estimated Historical Emissions

The measured rBC profile was compared with three available historical European BC emission reconstruction datasets. As described in the *Introduction* the datasets are the following: *ACCMIP* ((Emissions for Atmospheric Chemistry and Climate Model Intercomparison Project), *Junker and Liousse*, and *Bond*; taken from Lamarque et al. 2010; Junker and Liousse 2008 and T. C. Bond, Bhardwaj, et al. 2007, respectively.

The Ortles rBC concentration profile was averaged in 5 years intervals for all the 20th century and in 10 year averages from 1850 to 2000. The averaged time series was compared to the available datasets for the anthropogenic emissions and the result in shown in Fig. 9.5.

The rBC profiles appear to be in very good agreement with both the *ACCMIP* and the *Bond* datasets. The decadal variations, however, may reflect local emission variations, which may not reflect the average European emission. Particularly, the periods characterized by the highest values are very well described by the two dataset, whereas the very beginning and the abrupt decrease in the rBC Ortles concentration are later and earlier respectively, compared to the datset.

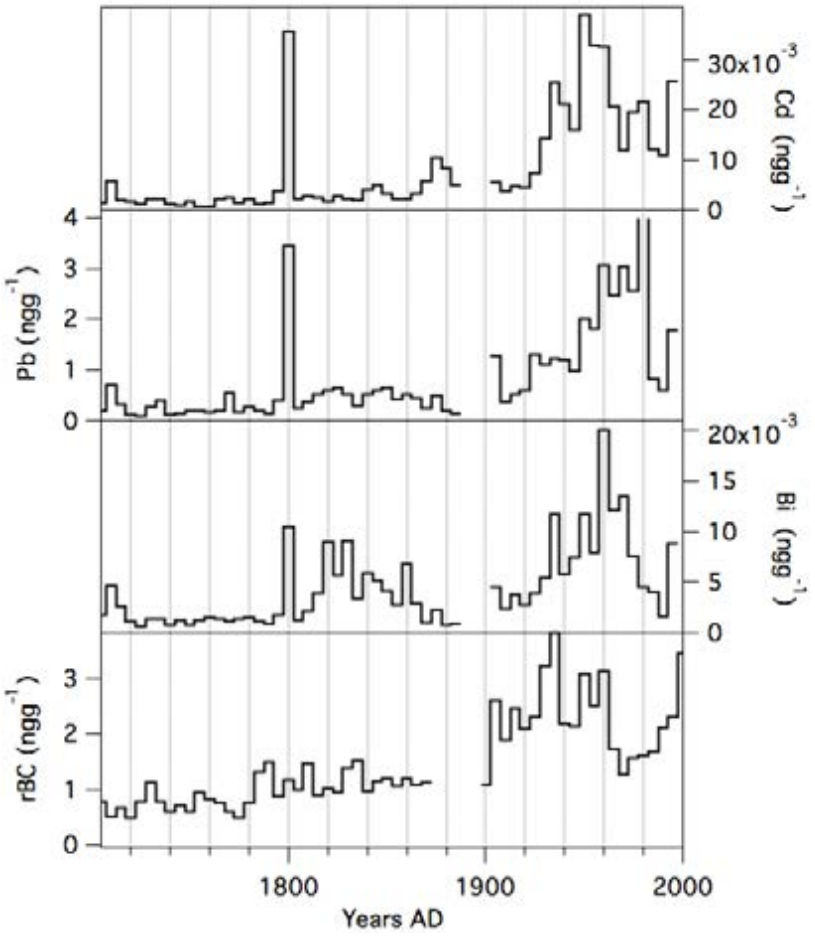

Figure 9.6: Long term variations of rBC (50-points binomial average, black line), Bi (2 points average, red line) and Pb (2 points average, green line) in the Alto dell'Ortles ice core#1 profile.

9.3.5 rBC and Trace Elements

The concentration profiles for 30 *trace elements* were obtained from the Ortles ice core#1 (see the Section 7). Particularly, anthropogenic emitted heavy metals has many common sources with rBC: the principal emission sectors are road traffic, fossil fuel related energy production, coal and biomass burning. Therefore, the behavior of the rBC and trace elements concentrations in the Ortles ice core was compared.

Three anthropogenic emitted trace elements were chosen for the comparison: Cd, Pb and Bi. From the beginning of the 20th century the emissions of these metals strongly increased, as reported in Alpine ice core records (Gabrielli, Cozzi, et al. 2008; Barbante, Gabrieli, et al. 2011 and reference therein). A first comparison was performed by using the 5 and 10 years averages for the period 1700-2000 (the dating is quite uncertain before the 1900s but the comparison should not be affected). The heavy metals show almost the same behaviour the last century, and the rBC also shows a very similar trend (Fig. 9.6). Particularly, the lowest correlation appeared to be with Pb, whereas both Cd and Bi increase almost simultaneously with rBC (especially during the 30s and the 50s). However, rBC shows the fastest decrease after the 60s.

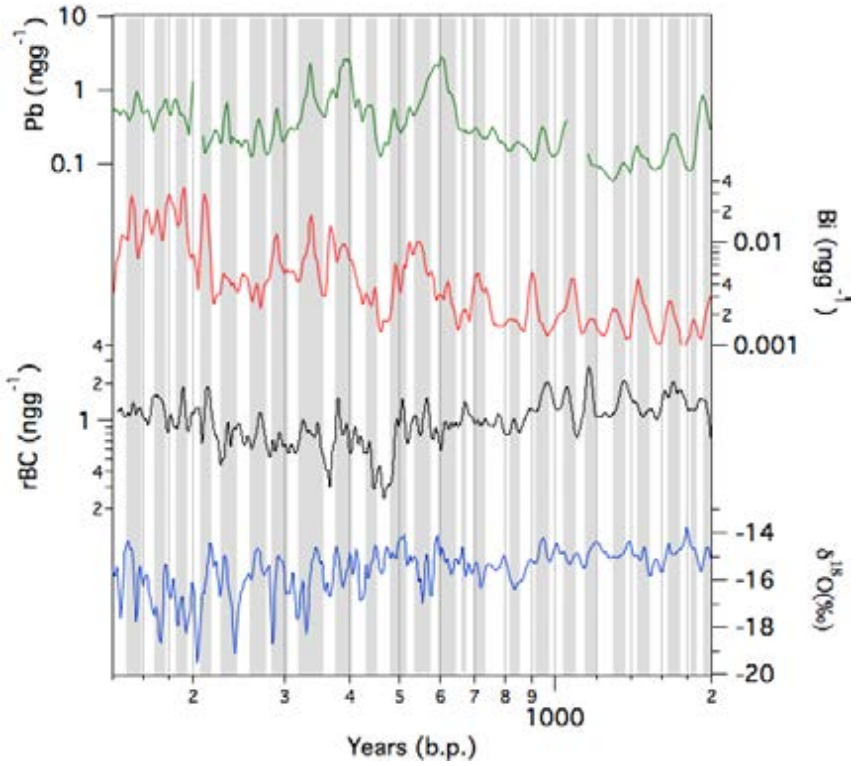

Figure 9.7: Alto dell'Ortles ice core#1 long term variations of rBC (50-points binomial average, black line), Bi (2 points average, red line) and Pb (2 points average, green line) and the water stable isotope enrichment (blue line). The gray shaded areas highlighted the simultaneous variations of rBC and the selected TEs, which are not always followed by the isotopic profile.

The long-term evolution of trace elements and rBC has never been studied in a mid-latitude Alpine ice core. Particularly, the profiles of Pb, Bi and rBC from the mid 19th century to 2000 years BP are compared in Fig. 9.7. These three profiles appear to be in agreement, and almost all of the climatic and environmental variations (the seasonality was lost before 200 year BP) can be observed. Therefore, the emission sources were likely the same, or they were at the very least simultaneous, as in the case of the smelting activities: heavy metals and emissions from mining activities and rBC from coal and biomass burning. However, before 500 years pb an inverse trend is observed for rBC and Bi. Variations in the natural and anthropogenic biomass burning may be the cause of this separation (on-going research). The isotopic profile (blue line) doesn't follow all the TE's oscillations, probably because of the anthropogenic impacts on the emissions during the 15^{th} and the 17^{th} centuries. However, the increasing trend of rBC toward the bottom end of the core is similar to what observed in the isotopic profile: a preliminary interpretation of this results may be the climatic control on the rBC atmospheric emissions, mainly through natural fires (on-going research) and the enhanced atmospheric convective activity during warmer periods.

Chapter 10

Conclusions and Future Perspectives

Glaciers and ice sheets are valuable sources of informations about the past atmospheric composition and are therefore used to reconstruct the past climatic and environmental conditions. A new melting system was set-up and used for the first time in this project. The melted water derived from the melting of the ice core over an aluminum heated melting head was continuously analyzed for refractory black carbon, trace elements concentrations, water total conductivity and dust particles content. Moreover, two water samples were stored every minute. The Venetian continuous flow system has been revealed to be a very efficient and clean way to analyse ice cores. The MATLAB codes done by the author greatly decreased the data analysis time, avoids errors and results in very precise concentrations datasets.

The continuous flow technique was used to analyze an ice core from one of the highest summits of the Eastern European Alps. Particularly, in 2011, four ice core were drilled at the Alto dell'Ortles glaciers (3905 m a.s.l.). The brand new dating gave the ice near the bedrock an age of about 7000 years, making the Ortles ice core the second longest time spanning ice core of the entire Alpine region. However, the Alto dell'Ortles ice core#1, was 73.5 m long, and therefore covering 3000 years.

In order to evaluate the glacio-chemical response in case of the extraordinary warm summer of 2015, and to evaluate the present day aerosol fluxes, a 3 m snow pit was dug on the 28th of August 2015, after the warmest summer (after that of 2003) since at least 1864. The 3 cm resolution samples were analyzed for trace elements, rare Earth elements, total dust content (with a Coulter Counter), refractory black carbon (with the SP2) and a complete list of ionic compounds. Despite the intense water percolation and surface sublimation the seasonality was preserved, even if the analytes' concentrations were probably modified by post-depositional processes. The layer corresponding to the summer of 2015 was strongly enriched in natural and anthropogenic aerosols. The glaciological description of the snow pit was compared to the physico-chemical profiles and the main features were explained. The dust and the rBC snow radiative influences were computed with the SNICAR model resulting in a *radiative forcing* of 1.6 W m^{-2} for rBC and of 9.2 W m^{-2} for the dust content of the summer layer of 2015. The atmospheric structure was analyzed during the two years covered by the snow pit finding that the height of the boundary layer was more frequently higher than the Ortles summit compared to previous results, partly explaining the higher aerosol deposition on the glacier.

and the climatological data from the Automated Weather Station placed on the Alto dell'Ortles glacier in 2011 that were used to determine principal wind directions. By using the European and Italian emission datasets the Po Valley was established to be the main source of anthropogenic pollutants.

The chemical elements concentrations in the Ortles ice core #1 were continuously analyzed by mean of an ICP-QMS and 1063 samples were analyzed discreetly with a CRC-ICP-MS and a ICP-QMS. Continuous profiles were obtained for the following elements: Na, Mg, Al, Ca, Ti, V, Mn, Fe, Cu, Zn, Sr, Ba, Pb and U. The discrete profiles were obtained for 29 elements, all those measured with CFA system and Li, K, ^{52}Cr, ^{53}Cr, Co, As, Se, Ag, Sb, As, Te, Cs, Hg and Bi. The most abundant isotopes were chosen except for ^{57}Fe.

The rBC concentration was continuously measured with a Single Particle Soot Photometer (SP2), and the mass equivalent particles diameter were also analyzed.

Dust particle content and conductivity profiles were obtained with a resolution of less than 1 cm.

The trace elements dataset was statistically analyzed in order to evaluate the natural and/or the anthropogenic sources for the various elements (*Principal Components* and *Clustering* analyses). The overall dataset was divided in two by considering a pre-industrial period, from 1000 BC to 1800 AD, and an anthropogenically influenced period from 1800 to 2000. The results for the period 1800-2000 AD separated the crustal elements (Mg, Al, Ca, Ti, Fe, Ba, Sr) from the anthropogenically emitted heavy metals which strongly increased in concentration from the end of the 18th century, such as V, Zn, Cd, Pb, Sb, As, Tl, Hg and Bi. For the period 1800 AD to 1000 BC, the PCA underlined an interesting relation between some particular elements: Pb, Sb, Bi, As and Ag. The Enrichment Factor was computed for all the elements by taking the concentrations of the 8th century as a reference, when the anthropogenic influence was the lowest.

Mining activities and especially the Silver and Copper extraction and refining, were the most important sources of heavy metals contaminations during the pre-industrialized period. In the Ortles ice core the Roman and Greek periods resulted in a Pb enhanced deposition from 400 BC to 100 AD and a less evident Cu deposition from 400 to 50 BC. The concentration remained very low after the falling of the Roman Empire. Another increase was observed for Pb and Cu starting from the 10th century. Between the 1346 and the1353 AD the "Black Death" caused a rapid decline of the mining activities and, indeed, a decrease was measured both for Pb and for Cu. The Pb concentrations increased again at the end of the 14th century reaching a maximum at the beginning of the 15th century. Interestingly, this increase appeared to be decoupled from the increase in concentration of Sb, As and Bi, peaking about 50 years later. The highest contaminations in the pre-industrial period were measured from the very end of the 16th century, where the EFs of Pb, Sb, As, Bi and, very interestingly, of Ag significantly increased, possibly due to the intense Silver mines related activities in the European continent. The concentrations of those toxic metals slightly decreased reaching the previous concentrations values from the onset of the 18th century. A comparison between the Ortles results and the Pb concentrations and EFs measured in two South American ice cores (from Quelccaya and Illimani glaciers) highlighted the quasi-simultaneous beginning of the decrease of the European contamination level and the increase of that of the South America, caused by the colonial mining activities.

Very low trace elements concentrations were found in the 18th followed by a small increase from the middle of the 18th century, the onset of the *Industrial Revolution*. The heavy metal deposition over the Ortles glacier was enhanced from the 1920s. The most notable heavy metals in the period between the 20s and the 40s were V, Cd, Pb, Sb, As, Hg and Bi. It is possible that these increases were mainly due to the industrial coal burning emissions and the WWII manufacturing activities. Another significant increase was detected during the 60s, particularly for Zn, V, Bi, Pb, Cd and As; this was the most industrialized period especially in the Northern Italy. In 1980 the EFs of Zn, Cu, Bi, Sb, Pb and Cd was significantly above one, particularly for Sb and Pb. Afterwards, a general decrease was observed, except for Cu, V, Hg, Sb and Cd; however, in this part of the core the post-depositional processes may have alter the seasonal aerosol deposition.

The heavy metals profiles for the period 1700-2000 AD were compared with those obtained from the very well preserved Colle Gnifetti ice core. A substantial agreement is observed for the two environmental archives both during the 20th century and during the last two millennia.

The Ortles Pb concentration profile was compared with most of the ice core measurement from all around the world. As expected, the highest similarities were found with the European ice cores: Colle Gnifetti (Western European Alps) and Belukha (Eastern Europe) ice cores.

The TEs enrichment factors were also used to search for volcanoes eruptions signatures, whose detection would be of great importance for confirming the dating; particularly between the 1200 and the 1900 AD. A preliminary research led to the finding of some volcanic horizons presenting an increase of selected TEs' enrichment factors. Between the others, Katmai (1912), Tambora (1815) and Laki (1783) horizons were observed, at least preliminarily.

A strong increase of many trace elements was observed during the analyses of the last ice section of the Ortles core#1, from 73 m to 73.5 m. The increase factors were computed and the highest values were obtained for Cu, Li and Sb, respectively. A possible external source may be the cause of this strange behaviour.

The water conductivity and the particles contents were used to give a bulk chemical and physical description of a core. The particles' content, measured on 32 different dimensional channels, clearly described the seasonal oscillations and the summer peak in dust deposition. However, long-range dust sources in the Alps may influence the snow particle contents, such us the Saharan dust events. No particular trend was observed in the dust profile. Total water conductivity linearly decreased from 3000 years BP until the 19th century, where it got stable; afterwards, the conductivity increased from the beginning of the 20th century showing a huge peak around the 1960s. Lower values (about 1 µS) were reached again during the 1980s and an increasing trend was observed toward the 2000 AD. The water conductivity was also used for corroborate the presence of volcanic eruptions signatures, together with the TEs enrichment factors.

The black carbon profile covering the last 3000 years was firstly described in this work. An interval of time as long as this one has never been analyzed in the Alpine area before this study. The concentration of rBC remained almost constant and low (about 1 ng g^{-1}) until the beginning of the 20th century, when it started to increase especially from the 20s, reaching concentrations of about 8 ng g^{-1}, and peaking in the 1960s with about 6 ng g^{-1}. After the 1960s the rBC concentration

abruptly decreased to about 1 ng g^{-1}, followed by a positive increase trend toward the year 2000. Marked oscillations characterized the rBC profile and the author suggests that they could be explained by the low altitude of the Alto dell'Ortles glacier, making it more influenced by short term intense variations, as during the WWII. The mass equivalent diameter was also analyzed and an interesting increasing trend from smaller median diameters of 250 nm to 330 nm was observed from the beginning of the last two millennia to the industrial period, peaking during the end of the 50s. A shift in the energy production sector may explain the subsequent diameter decrease observed toward the 2000s.

In future years an effort has to be made in order to preserve the ice archives, especially the Alpine ones, before they are compromised or disappear forever. Studying the Alpine glaciers is certainly not easy and the influence of global warming in recent years will increase the challenging of these studies. The history of natural and anthropogenic aerosols atmospheric concentrations is preserved in these archives, which represent a priceless heritage.

The Ortles ice cores, particularly, still require a great deal in order to completely described all of the obtained results. Most importantly, it appears to be an incredible source of past atmospheric information, despite the fact that in recent years percolation events have started to degrade the glacier from the top.

The preservation of the seasonality in the climatic and environmental signals in the ice core #1 will be further investigated and the pollen analyses results will hopefully reduce the dating uncertainties and corroborate the seasonal oscillations observed in the rBC and in the high resolution TEs profiles.

The total number of particles profile, made up of 32 specific dimensional channels profiles, deserves to be more deeply investigated in order to search for correlations with the TEs, to check the dependence from the climatic history in the Mt. Ortles region and to compare the past Saharan dust events.

The discrete samples obtained from the CFA system, were stored in pre-clean vials and could be therefore analyzed for specific biomass burning proxies, such us Levoglucosan, entirely emitted during woody vegetation combustions. The results, together with the rBC dataset, would lead to a better understanding of the natural or anthropogenic rBC sources in the European Alpine region over the last millennia.

Whiting the framework of the *Protecting Ice Memory* project, the CFA analyses would certainly be a unique opportunity to study the past and recent heavy metals and black carbon deposition with a very high temporal resolution in many glaciers of the world and especially for the Alpine region, establishing a high-resolution past aerosols emissions network over the last centuries and millennia.

Acknowledgements

I want to thank my supervisor Carlo Barbante for having given me the opportunity to do my PhD in ice core science and to take part in many field missions on the European glaciers.

My gratitude goes to Paolo Gabrielli, leader of the Ortles Project, for all the scientific support and discussions.

My heartfelt thanks to all the colleagues of the University of Venice, whose help was fundamental. I really want to thank Jacopo Gabrieli and Andrea Spolaor for teaching me how to work with ice cores and for all their concrete support. Thanks to all the colleagues that helped me during the Ortles core analyses and to all the members of the venetian team.

I really want to thank all the LGGE group for the priceless collaboration and help. First of all thank to Paolo Laj for his support and for having given me the chance to spend my research period abroad in Grenoble. Thanks to Patrick Ginot for the fruitful collaboration and for organizing the Col du Dome ice core drilling campaign. Thanks to Xavier Fain and Saehee Lim for their help and availability. Special thanks to Marco Zanatta for teaching me how to use the SP2.

I want to thanks all my PhD collegues of the *Scince and Management of Climate Change* and all the CMCC members; thanks to the professors of the *Dynamic Climatology* master, between the others Silvio Gualdi and Simona Masina, for their passion in the climate science.

Thanks to all the Ortles Project members and particularly to Luca Carturan, Roberto Seppi and Giuliano Bertagna. The *Ortles project* is a programme supported by two NSF awards no. 1060115 and no. 1461422 to The Ohio State University and by the Ripartizione Protezione antincendi e civile of the autonomous province of Bolzano in collaboration with the Ripartizione Opere idrauliche e Ripartizione Foreste of the autonomous province of Bolzano, the Stelvio National Park and the Institute of Mountain Emergency Medicine of EURAC.

My heartfelt thanks to my family, Giulia and all my friends for their endless support.

Bibliography

Abram, N. J. et al. (2016). "Early onset of industrial-era warming across the oceans and continents". In: *Nature* 536.7617, pp. 411–418.

Allen, A. et al. (2001). "Size distributions of trace metals in atmospheric aerosols in the United Kingdom". In: *Atmospheric Environment* 35.27, pp. 4581–4591.

Alley, R. (1987). "Firn densification by grain-boundary sliding: a first model". In: *Le Journal de Physique Colloques* 48.C1, pp. C1–249.

Amato, P. et al. (2007). "Bacterial characterization of the snow cover at Spitzberg, Svalbard". In: *FEMS Microbiology Ecology* 59.2, pp. 255–264.

Angelisi, d. M. and A. Gaudichet (1991). "Saharan dust deposition over Mont Blanc (French Alps) during the last 30 years". In: *Tellus B* 43.1, pp. 61–75.

Aoki, T. et al. (2007). "ADEOS-II/GLI snow/ice products—Part II: Validation results using GLI and MODIS data". In: *Remote Sensing of Environment* 111.2, pp. 274–290.

Arendt, A. et al. (2012). "Randolph Glacier Inventory [v2. 0]: A Dataset of Global Glacier Outlines, Global Land Ice Measurements from Space, Boulder Colorado, USA". In: *Digital Media*.

Asmi, A. et al. (2011). "Number size distributions and seasonality of submicron particles in Europe 2008–2009". In: *Atmospheric Chemistry and Physics* 11.11, pp. 5505–5538.

Auer, I. et al. (2007). "HISTALP—historical instrumental climatological surface time series of the Greater Alpine Region". In: *International Journal of Climatology* 27.1, pp. 17–46.

Augustin, L. et al. (2004). "Eight glacial cycles from an Antarctic ice core". In: *Nature* 429.6992, pp. 623–628.

Barbante, C., J. Gabrieli, et al. (2011). "A historical record of heavy metal pollution in Alpine snow and ice". In: *Persistent Pollution–Past, Present and Future*. Springer, pp. 71–94.

Barbante, C., M. Schwikowski, et al. (2004). "Historical record of European emissions of heavy metals to the atmosphere since the 1650s from Alpine snow/ice cores drilled near Monte Rosa". In: *Environmental science & technology* 38.15, pp. 4085–4090.

Barbante, C., K. Van De Velde, et al. (2001). "Post-World War II uranium changes in dated Mont Blanc ice and snow". In: *Environmental science & technology* 35.20, pp. 4026–4030.

Bartolini, E., P. Claps, and P. D'odorico (2009). "Interannual variability of winter precipitation in the European Alps: relations with the North Atlantic Oscillation." In: *Hydrology and Earth System Sciences* 13.1, pp. 17–25.

Bauer, S. E. et al. (2013). "Historical and future black carbon deposition on the three ice caps: Ice core measurements and model simulations from 1850 to 2100". In: *Journal of Geophysical Research: Atmospheres* 118.14, pp. 7948–7961.

Baumgardner, D. et al. (2012). "Soot reference materials for instrument calibration and intercomparisons: a workshop summary with recommendations". In: *Atmospheric Measurement Techniques* 5, pp. 1869–1887.

Berg, T. et al. (2008). "Atmospheric trace metal concentrations at Norwegian background sites during 25 years and its relation to European emissions". In: *Atmospheric Environment* 42.32, pp. 7494–7501.

Bisiaux, M. et al. (2012). "Changes in black carbon deposition to Antarctica from two high-resolution ice core records, 1850–2000 AD". In: *Atmospheric Chemistry and Physics* 12.9, pp. 4107–4115.

Bolius, D. (2006). "Paleo climate reconstruction based on ice cores from the Andes and the Alps". PhD thesis.

Bond, T. C., E. Bhardwaj, et al. (2007). "Historical emissions of black and organic carbon aerosol from energy-related combustion, 1850–2000". In: *Global Biogeochemical Cycles* 21.2.

Bond, T. C., S. J. Doherty, et al. (2013). "Bounding the role of black carbon in the climate system: A scientific assessment". In: *Journal of Geophysical Research: Atmospheres* 118.11, pp. 5380–5552.

Boucher, O. et al. (2013). "Clouds and aerosols". In: *Climate change 2013: The physical science basis. Contribution of working group I to the fifth assessment report of the intergovernmental panel on climate change*. Cambridge University Press, pp. 571–657.

Boutron, C. F. (1990). "A clean laboratory for ultralow concentration heavy metal analysis". In: *Fresenius' Journal of Analytical Chemistry* 337.5, pp. 482–491.

Bovchaliuk, A. et al. (2013). "Variability of aerosol properties over Eastern Europe observed from ground and satellites in the period from 2003 to 2011". In: *Atmospheric Chemistry and Physics* 13.13, pp. 6587–6602.

Bramall, N. et al. (2005). "A deep high-resolution optical log of dust, ash, and stratigraphy in South Pole glacial ice". In: *Geophysical research letters* 32.21.

Bränvall, M.-L. et al. (2001). "Four thousand years of atmospheric lead pollution in northern Europe: a summary from Swedish lake sediments". In: *Journal of Paleolimnology* 25.4, pp. 421–435.

Breitenbach, S. et al. (2012). "Constructing proxy records from age models (COPRA)". In: *Climate of the Past* 8.5, pp. 1765–1779.

Brook, R. D. (2008). "Cardiovascular effects of air pollution". In: *Clinical science* 115.6, pp. 175–187.

Brown, R. and D. Robinson (2011). "Northern Hemisphere spring snow cover variability and change over 1922–2010 including an assessment of uncertainty". In: *The Cryosphere* 5.1, pp. 219–229.

Brunetti, M. et al. (2006). "Precipitation variability and changes in the greater Alpine region over the 1800–2003 period". In: *Journal of Geophysical Research: Atmospheres* 111.D11.

Buntgen, U. et al. (2011). "'2500' years of European climate variability and human susceptibility". In: *Science* 331.6017, pp. 578–582.

Butt, E. et al. (2016). "The impact of residential combustion emissions on atmospheric aerosol, human health, and climate". In: *Atmospheric Chemistry and Physics* 16.2, pp. 873–905.

Carturan, L., C. Baroni, et al. (2013). "Decay of a long-term monitored glacier: Careser glacier (Ortles-Cevedale, European Alps)". In: *The Cryosphere* 7.6, pp. 1819–1838.

Carturan, L., R. Filippi, et al. (2013). "Area and volume loss of the glaciers in the Ortles-Cevedale group (Eastern Italian Alps): controls and imbalance of the remaining glaciers". In: *The Cryosphere* 7.5, pp. 1339–1359.

Casty, C. et al. (2005). "Temperature and precipitation variability in the European Alps since 1500". In: *International Journal of Climatology* 25.14, pp. 1855–1880.

Chuang, K.-J. et al. (2010). "Long-term air pollution exposure and risk factors for cardiovascular diseases among the elderly in Taiwan". In: *Occupational and environmental medicine*, oem–2009.

Clarke, A. D. and K. J. Noone (1985). "Soot in the Arctic snowpack: A cause for perturbations in radiative transfer". In: *Atmospheric Environment (1967)* 19.12, pp. 2045–2053.

Clausen, H. B. et al. (1997). "A comparison of the volcanic records over the past 4000 years from the Greenland Ice Core Project and Dye 3 Greenland ice cores". In: *Journal of Geophysical Research: Oceans* 102.C12, pp. 26707–26723.

Cole-Dai, J. et al. (2009). "Cold decade (AD 1810–1819) caused by Tambora (1815) and another (1809) stratospheric volcanic eruption". In: *Geophysical Research Letters* 36.22.

Collaud Coen, M., E. Weingartner, et al. (2007). "Long-term trend analysis of aerosol variables at the high-alpine site Jungfraujoch". In: *Journal of Geophysical Research: Atmospheres* 112.D13.

Collaud Coen, M., E. Andrews, et al. (2013). "Aerosol decadal trends–Part 1: In-situ optical measurements at GAW and IMPROVE stations". In: *Atmospheric Chemistry and Physics* 13.2, pp. 869–894.

COM, E. (2009). "White paper-Adapting to climate change: Towards a European framework for action". In: *European Commission. Available at: http://eur-lex. europa. eu/LexUriServ/LexUriServ. do.*

Conway, H., A. Gades, and C. Raymond (1996). "Albedo of dirty snow during conditions of melt". In: *Water resources research* 32.6, pp. 1713–1718.

Coppola, A. et al. (2013). "Tree-ring–based summer mean temperature variations in the Adamello–Presanella Group (Italian Central Alps), 1610–2008 AD". In: *Climate of the Past* 9.1, pp. 211–221.

Crosier, J. et al. (2007). "Chemical composition of summertime aerosol in the Po Valley (Italy), northern Adriatic and Black Sea". In: *Quarterly Journal of the Royal Meteorological Society* 133.S1, pp. 61–75.

Cross, E. S. et al. (2010). "Soot particle studies—instrument inter-comparison—project overview". In: *Aerosol Science and Technology* 44.8, pp. 592–611.

Crowley, T. J. (2000). "Causes of climate change over the past 1000 years". In: *Science* 289.5477, pp. 270–277.

Davidson, C. I., R. F. Phalen, and P. A. Solomon (2005). "Airborne particulate matter and human health: a review". In: *Aerosol Science and Technology* 39.8, pp. 737–749.

Davis, B. A. et al. (2003). "The temperature of Europe during the Holocene reconstructed from pollen data". In: *Quaternary Science Reviews* 22.15, pp. 1701–1716.

Delchiaro, S. (2014). "Tuning of continuous flow analysis and analysis of Mount Ortles ice cores".

Delmonte, B., J. Petit, and V. Maggi (2002). "Glacial to Holocene implications of the new 27000-year dust record from the EPICA Dome C (East Antarctica) ice core". In: *Climate Dynamics* 18.8, pp. 647–660.

Delworth, T. L. and M. E. Mann (2000). "Observed and simulated multidecadal variability in the Northern Hemisphere". In: *Climate Dynamics* 16.9, pp. 661–676.

Desio, A., S. Belloni, and A. Giorcelli (1967). *I ghiacciai del gruppo Ortles-Cevedale:(Alpi centrali)*.

Döscher, A. et al. (1995). "A130 years deposition record of sulfate, nitrate and chloride from a high-alpine glacier". In: *Water, Air, & Soil Pollution* 85.2, pp. 603–609.

Dreossi, G. (2016). "A recent past temperature reconstruction based on oxygen and hydrogen stable isotopes in Alpine ice cores". In:

Dreschhoff, G. A. and E. J. Zeller (1990). "Evidence of individual solar proton events in Antarctic snow". In: *Solar Physics* 127.2, pp. 333–346.

Dugmore, A. J. et al. (2007). "Abandoned farms, volcanic impacts, and woodland management: revisiting jórsárdalur, the "Pompeii of Iceland"". In: *Arctic Anthropology* 44.1, pp. 1–11.

Dumont, M. et al. (2014). "Contribution of light-absorbing impurities in snow to Greenland/'s darkening since 2009". In: *Nature Geoscience* 7.7, pp. 509–512.

Dunkeloh, A. and J. Jacobeit (2003). "Circulation dynamics of Mediterranean precipitation variability 1948–98". In: *International Journal of Climatology* 23.15, pp. 1843–1866.

Eichler, A., M. Schwikowski, M. Furger, et al. (2004). "Sources and distribution of trace species in Alpine precipitation inferred from two 60-year ice core paleorecords". In: *Atmospheric Chemistry and Physics Discussions* 4.1, pp. 71–108.

Eichler, A., G. Gramlich, et al. (2015). "Pb pollution from leaded gasoline in South America in the context of a 2000-year metallurgical history". In: *Science advances* 1.2, e1400196.

Eichler, A., M. Schwikowski, and H. W. Gäggeler (2001). "Meltwater-induced relocation of chemical species in Alpine firn". In: *Tellus B* 53.2, pp. 192–203.

Eichler, A., M. Schwikowski, H. W. Gäggeler, et al. (2000). "Glaciochemical dating of an ice core from upper Grenzgletscher (4200 m asl)". In: *Journal of Glaciology* 46.154, pp. 507–515.

Eichler, A., L. Tobler, et al. (2012). "Three centuries of Eastern European and Altai lead emissions recorded in a Belukha ice core". In: *Environmental science & technology* 46.8, pp. 4323–4330.

Elsasser, H. and P. Messerli (2001). "The vulnerability of the snow industry in the Swiss Alps". In: *Mountain research and development* 21.4, pp. 335–339.

Enfield, D. B., A. M. Mestas-Nuñez, and P. J. Trimble (2001). "The Atlantic multidecadal oscillation and its relation to rainfall and river flows in the continental US". In: *Geophysical Research Letters* 28.10, pp. 2077–2080.

Etemad, B. and J. Luciani (1991). *Production Mondiale D'energie, 1800-1985*. Vol. 7. Librairie Droz.

Evaluation of Carcinogenic Risks to Humans, G. on the (2010). "IARC monographs on the evaluation of carcinogenic risks to humans. Ingested nitrate and nitrite, and cyanobacterial peptide toxins." In: *IARC monographs on the evaluation of carcinogenic risks to humans/World Health Organization, International Agency for Research on Cancer* 94, p. v.

Federer, U. et al. (2008). "Continuous flow analysis of total organic carbon in polar ice cores". In: *Environmental science & technology* 42.21, pp. 8039–8043.

Festi, D. et al. (2015). "A novel pollen-based method to detect seasonality in ice cores: a case study from the Ortles glacier, South Tyrol, Italy". In: *Journal of Glaciology* 61.229, pp. 815–824.

Fierz, C. et al. (2009). *The international classification for seasonal snow on the ground*. Vol. 25. UNESCO/IHP Paris.

Flanner, M. G. and C. S. Zender (2006). "Linking snowpack microphysics and albedo evolution". In: *Journal of Geophysical Research: Atmospheres* 111.D12.

Flanner, M. G., C. S. Zender, et al. (2007). "Present-day climate forcing and response from black carbon in snow". In: *Journal of Geophysical Research: Atmospheres* 112.D11.

Flegal, A. R. (1998). "Clair Patterson's influence on environmental research". In: *Environmental research* 78.2, pp. 65–70.

Frei, C. and C. Schär (1998). "A precipitation climatology of the Alps from high-resolution rain-gauge observations". In: *International Journal of climatology* 18.8, pp. 873–900.

Gabbi, J. et al. (2015). "The impact of Saharan dust and black carbon on albedo and long-term mass balance of an Alpine glacier". In: *The Cryosphere* 9.4, pp. 1385–1400.

Gabrieli, J., L. Carturan, et al. (2011). "Impact of Po Valley emissions on the highest glacier of the Eastern European Alps". In: *Atmospheric Chemistry and Physics* 11.15, pp. 8087–8102.

Gabrieli, J. (2008). "Trace elements and Polycyclic Aromatic Hydrocarbons (PAHs) in snow and ice sampled at Colle Gnifetti, Monte Rosa (4450 m), during the last 10,000 years: environmental and climatic implications". PhD thesis. Université Joseph-Fourier-Grenoble I.

Gabrieli, J. and C. Barbante (2014). "The Alps in the age of the Anthropocene: the impact of human activities on the cryosphere recorded in the Colle Gnifetti glacier". In: *Rendiconti Lincei* 25.1, pp. 71–83.

Gabrielli, P., C. Barbante, G. Bertagna, et al. (2016). "Age of the Mt. Ortles ice cores, the Tyrolean Iceman and glaciation of the highest summit of South Tyrol since the Northern Hemisphere Climatic Optimum". In: *The Cryosphere Discussions* 2016, pp. 1–30. DOI: 10.5194/tc-2016-159. URL: http://www.the-cryosphere-discuss.net/tc-2016-159/.

Gabrielli, P., L. Carturan, et al. (2010). "Atmospheric warming threatens the untapped glacial archive of Ortles mountain, South Tyrol". In: *Journal of Glaciology* 56.199, pp. 843–853.

Gabrielli, P., G. Cozzi, et al. (2008). "Trace elements in winter snow of the Dolomites (Italy): a statistical study of natural and anthropogenic contributions". In: *Chemosphere* 72.10, pp. 1504–1509.

Gabrielli, P., C. Barbante, L. Carturan, et al. (2012). "Discovery of cold ice in a new drilling site in the Eastern European Alps". In: *GEOGRAFIA FISICA E DINAMICA QUATERNARIA* 35.1, pp. 101–105.

Gabrielli, P. and P. Vallelonga (2015). "Contaminant records in ice cores". In: *Environmental Contaminants*. Springer, pp. 393–430.

Gabrielli, P., A. Wegner, et al. (2010). "A major glacial-interglacial change in aeolian dust composition inferred from Rare Earth Elements in Antarctic ice". In: *Quaternary Science Reviews* 29.1, pp. 265–273.

Gilfedder, B. et al. (2008). "Iodine speciation in rain, snow and aerosols". In: *Atmospheric Chemistry and Physics* 8.20, pp. 6069–6084.

Ginot, P., M. Dumont, et al. (2014). "A 10 year record of black carbon and dust from a Mera Peak ice core (Nepal): variability and potential impact on melting of Himalayan glaciers". In: *The Cryosphere* 8.4, pp. 1479–1496.

Ginot, P., C. Kull, et al. (2001). "Effects of postdepositional processes on snow composition of a subtropical glacier (Cerro Tapado, Chilean Andes)". In: *Journal of Geophysical Research* 106.D23, pp. 32575–32386.

Gobiet, A. et al. (2014). "21st century climate change in the European Alps—a review". In: *Science of the Total Environment* 493, pp. 1138–1151.

Granier, C. et al. (2011). "Evolution of anthropogenic and biomass burning emissions of air pollutants at global and regional scales during the 1980–2010 period". In: *Climatic Change* 109.1-2, pp. 163–190.

Gysel, M. et al. (2011). "Effective density of Aquadag and fullerene soot black carbon reference materials used for SP2 calibration". In: *Atmospheric Measurement Techniques* 4.12, pp. 2851–2858.

Hadley, O. L. and T. W. Kirchstetter (2012). "Black-carbon reduction of snow albedo". In: *Nature Climate Change* 2.6, pp. 437–440.

Hammer, Ø., D. Harper, and P. Ryan (2001). "Paleontological Statistics Software: Package for Education and Data Analysis". In: *Palaeontologia Electronica*.

Hartmann, D. L. et al. (2013). "Observations". In: *Cambridge University Press*.

Hawley, R. L., O. Brandt, et al. (2008). "Instruments and Methods Techniques for measuring high-resolution firn density profiles: case study from Kongsvegen, Svalbard". In: *Journal of Glaciology* 54.186, pp. 463–468.

Hawley, R. L. and E. M. Morris (2006). "Borehole optical stratigraphy and neutron-scattering density measurements at Summit, Greenland". In: *Journal of Glaciology* 52.179, pp. 491–496.

Hinds, W. C. (2012). *Aerosol technology: properties, behavior, and measurement of airborne particles*. John Wiley & Sons.

Holzhauser, H., M. Magny, and H. J. Zumbuühl (2005). "Glacier and lake-level variations in west-central Europe over the last 3500 years". In: *The Holocene* 15.6, pp. 789–801.

Hong, S., J.-P. Candelone, et al. (1994). "Greenland ice evidence of hemispheric lead pollution two millennia ago by Greek and Roman civilizations". In: *Science* 265.5180, pp. 1841–1843.

Hong, S., K. Lee, et al. (2009). "An 800-year record of atmospheric As, Mo, Sn, and Sb in central Asia in high-altitude ice cores from Mt. Qomolangma (Everest), Himalayas". In: *Environmental science & technology* 43.21, pp. 8060–8065.

Hovmand, M. F. et al. (2008). "Atmospheric heavy metal deposition accumulated in rural forest soils of southern Scandinavia". In: *Environmental Pollution* 155.3, pp. 537–541.

Huber, C. and M. Leuenberger (2003). "Fast high-precision on-line determination of hydrogen isotope ratios of water or ice by continuous-flow isotope ratio mass spectrometry". In: *Rapid communications in mass spectrometry* 17.12, pp. 1319–1325.

Huber, C. and M. Leuenberger (2005). "On-line systems for continuous water and gas isotope ratio measurements†". In: *Isotopes in environmental and health studies* 41.3, pp. 189–205.

Huber, T. M., M. Schwikowski, and H. W. Gäggeler (2001). "Continuous melting and ion chromatographic analyses of ice cores". In: *Journal of Chromatography A* 920.1, pp. 193–200.

Hurrell, J. (1995). "Decadal trends in the North Atlantic Oscillation: Regional temperatures and precipitation". In: *Nature* 269, pp. 676–679.

Huss, M. et al. (2010). "100-year mass changes in the Swiss Alps linked to the Atlantic Multidecadal Oscillation". In: *Geophysical Research Letters* 37.10.

Janssen, N. A. et al. (2011). "Black Carbon as an Additional Indicator of the Adverse Health Effects of Airborne Particles Compared with PMˆ sub 10ˆ and PMˆ sub 2.5ˆ". In: *Environmental Health Perspectives* 119.12, p. 1691.

Jenk, T. M. (2006). "Ice core based reconstruction of past climate conditions and air pollution in the Alps using radiocarbon". In: *Universtiy of Bern*.

Jenk, T. M. et al. (2009). "A novel radiocarbon dating technique applied to an ice core from the Alps indicating late Pleistocene ages". In: *Journal of Geophysical Research: Atmospheres* 114.D14.

Jitaru, P. et al. (2003). "Present century record of mercury species pollution in high altitude alpine snow and ice". In: *Journal de Physique IV (Proceedings)*. Vol. 107. EDP sciences, pp. 683–686.

Jones, P., K. Briffa, et al. (1998). "High-resolution palaeoclimatic records for the last millennium: interpretation, integration and comparison with General Circulation Model control-run temperatures". In: *The Holocene* 8.4, pp. 455–471.

Jones, P., T. Jonsson, and D. Wheeler (1997). "Extension to the North Atlantic Oscillation using early instrumental pressure observations from Gibraltar and South-West Iceland". In: *International Journal of climatology* 17.13, pp. 1433–1450.

Jones, P. D. and M. E. Mann (2004). "Climate over past millennia". In: *Reviews of Geophysics* 42.2.

Jouzel, J., M. Legrand, et al. (1984). "Chronologie d'un carottage de 20 m au col du Dôme (Massif du Mont Blanc)". In: *La Houille Blanche* 6-7, pp. 491–498.

Jouzel, J., L. Merlivat, and M. Pourchet (1977). "Deuterium, Tritium, and β activity in a snow core taken on the summit of mont blanc (french alps). Determination of the accumulation rate". In: *Journal of Glaciology* 18.80, pp. 465–470.

Junge, C. E. (1963). "Air chemistry and radioactivity". In: *1963*, p. 382.

Junker, C. and C. Liousse (2008). "A global emission inventory of carbonaceous aerosol from historic records of fossil fuel and biofuel consumption for the period 1860–1997". In: *Atmospheric Chemistry and Physics* 8.5, pp. 1195–1207.

Kanakidou, M. et al. (2005). "Organic aerosol and global climate modelling: a review". In: *Atmospheric Chemistry and Physics* 5.4, pp. 1053–1123.

Kappenberger, G. and J. Kerkmann (1997). *Il tempo in montagna: manuale di meteorologia alpina*. Zanichelli.

Kaspari, S. D. et al. (2011). "Recent increase in black carbon concentrations from a Mt. Everest ice core spanning 1860–2000 AD". In: *Geophysical Research Letters* 38.4.

Kaspari, S. et al. (2014). "Seasonal and elevational variations of black carbon and dust in snow and ice in the Solu-Khumbu, Nepal and estimated radiative forcings". In: *Atmospheric Chemistry and Physics* 14.15, pp. 8089–8103.

Kaufmann, P. R. et al. (2008). "An improved continuous flow analysis system for high-resolution field measurements on ice cores". In: *Environmental science & technology* 42.21, pp. 8044–8050.

Kawamura, K. and I. R. Kaplan (1987). "Motor exhaust emissions as a primary source for dicarboxylic acids in Los Angeles ambient air". In: *Environmental Science & Technology* 21.1, pp. 105–110.

Kehrwald, N. et al. (2012). "Levoglucosan as a specific marker of fire events in Greenland snow". In: *Tellus B* 64.

Kim, K.-H., E. Kabir, and S. Kabir (2015). "A review on the human health impact of airborne particulate matter". In: *Environment International* 74, pp. 136–143.

Knight, J. R. et al. (2005). "A signature of persistent natural thermohaline circulation cycles in observed climate". In: *Geophysical Research Letters* 32.20.

Knüsel, S. et al. (2003). "Accuracy of continuous ice-core trace-element analysis by inductively coupled plasma sector field mass spectrometry". In: *Environmental science & technology* 37.10, pp. 2267–2273.

Krachler, M. et al. (2005). "Increasing atmospheric antimony contamination in the northern hemisphere: snow and ice evidence from Devon Island, Arctic Canada". In: *Journal of Environmental Monitoring* 7.12, pp. 1169–1176.

Kuhn, M. et al. (1998). "Seasonal development of ion concentration in a high alpine snow pack". In: *Atmospheric Environment* 32.23, pp. 4041–4051.

Laborde, M. et al. (2012). "Single Particle Soot Photometer intercomparison at the AIDA chamber". In: *Atmospheric Measurement Techniques* 5, pp. 3077–3097.

Lamarque, J.-F. et al. (2010). "Historical (1850–2000) gridded anthropogenic and biomass burning emissions of reactive gases and aerosols: methodology and application". In: *Atmospheric Chemistry and Physics* 10.15, pp. 7017–7039.

Lambert, F. et al. (2008). "Dust-climate couplings over the past 800,000 years from the EPICA Dome C ice core". In: *Nature* 452.7187, pp. 616–619.

Leclercq, P., J. Oerlemans, and J. Cogley (2011). "Estimating the glacier contribution to sea-level rise for the period 1800–2005". In: *Surveys in Geophysics* 32.4-5, pp. 519–535.

Lee, K. et al. (2011). "Isotopic signatures for natural versus anthropogenic Pb in high-altitude Mt. Everest ice cores during the past 800years". In: *Science of the Total Environment* 412, pp. 194–202.

Legrand, M., S. Preunkert, B. May, et al. (2013). "Major 20th century changes of the content and chemical speciation of organic carbon archived in Alpine ice cores: Implications for the long-term change of organic aerosol over Europe". In: *Journal of Geophysical Research: Atmospheres* 118.9, pp. 3879–3890.

Legrand, M. and M. De Angelis (1995). "Origins and variations of light carboxylic acids in polar precipitation". In: *Journal of Geophysical Research: Atmospheres* 100.D1, pp. 1445–1462.

Legrand, M., S. Preunkert, M. Schock, et al. (2007). "Major 20th century changes of carbonaceous aerosol components (EC, WinOC, DOC, HULIS, carboxylic acids, and cellulose) derived from Alpine ice cores". In: *Journal of Geophysical Research: Atmospheres* 112.D23.

Leuenberger, M. and C. Huber (2002). "On-line determination of oxygen isotope ratios of water or ice by mass spectrometry". In: *Analytical chemistry* 74.18, pp. 4611–4617.

Li, X. and I. Thornton (1993). "Arsenic, antimony and bismuth in soil and pasture herbage in some old metalliferous mining areas in England". In: *Environmental geochemistry and health* 15.2-3, pp. 135–144.

Lim, S., X. Fain, P. Ginot, et al. (2016). "Black carbon variability since preindustrial times in Eastern part of Europe reconstructed from Mt Elbrus, Caucasus ice cores". In: *Atmospheric Chemistry and Physics Discussions* 2016, pp. 1–30. DOI: 10.5194/acp-2016-804. URL: http://www.atmos-chem-phys-discuss.net/acp-2016-804/.

Lim, S., X. Fain, M. Zanatta, et al. (2014). "Refractory black carbon mass concentrations in snow and ice: method evaluation and inter-comparison with elemental carbon measurement". In: *Atmospheric Measurement Techniques* 7.10, pp. 3307–3324.

Lim, S. (2014). "Variability and trends of black carbon in Europe over the last 140 years retrieved from a Caucasian ice core". PhD thesis. Grenoble.

López-Moreno, J. et al. (2011). "Effects of the North Atlantic Oscillation (NAO) on combined temperature and precipitation winter modes in the Mediterranean mountains: observed relationships and projections for the 21st century". In: *Global and Planetary Change* 77.1, pp. 62–76.

Lukacs, H. et al. (2007). "Seasonal trends and possible sources of brown carbon based on 2-year aerosol measurements at six sites in Europe". In: *Journal of Geophysical Research: Atmospheres* 112.D23.

Luterbacher, J. et al. (2004). "European seasonal and annual temperature variability, trends, and extremes since 1500". In: *Science* 303.5663, pp. 1499–1503.

Lüthi, M. P. and M. Funk (2001). "Modelling heat flow in a cold, high-altitude glacier: interpretation of measurements from Colle Gnifetti, Swiss Alps". In: *Journal of Glaciology* 47.157, pp. 314–324.

Maggi, V. et al. (2000). "Ice core drilling on Colle del Lys (Monte Rosa, Italian Alps): climate and environmental signals". In: *Bollettino geofisico* 23, pp. 57–66.

Magny, M. and J. N. Haas (2004). "A major widespread climatic change around 5300 cal. yr BP at the time of the Alpine Iceman". In: *Journal of Quaternary Science* 19.5, pp. 423–430.

Mann, M. E. and P. D. Jones (2003). "Global surface temperatures over the past two millenia". In: *Geophysical Research Letters* 30.15, pp. 5–1.

Marzeion, B., A. Jarosch, and M. Hofer (2012). "Past and future sea-level change from the surface mass balance of glaciers". In: *The Cryosphere* 6.6, pp. 1295–1322.

Masiello, C. A. (2004). "New directions in black carbon organic geochemistry". In: *Marine Chemistry* 92.1, pp. 201–213.

Matthias, V. and J. Bösenberg (2002). "Aerosol climatology for the planetary boundary layer derived from regular lidar measurements". In: *Atmospheric Research* 63.3, pp. 221–245.

Maupetit, F. et al. (1995). "Seasonal fluxes of major ions to a high altitude cold alpine glacier". In: *Atmospheric Environment* 29.1, pp. 1–9.

Maynard, D. et al. (2007). "Mortality risk associated with short-term exposure to traffic particles and sulfates". In: *Environmental health perspectives*, pp. 751–755.

McConnell, J. R. and R. Edwards (2008). "Coal burning leaves toxic heavy metal legacy in the Arctic". In: *Proceedings of the National Academy of Sciences* 105.34, pp. 12140–12144.

McConnell, J. R., R. Edwards, et al. (2007). "20th-century industrial black carbon emissions altered arctic climate forcing". In: *Science* 317.5843, pp. 1381–1384.

McConnell, J. R., G. W. Lamorey, et al. (2002). "Continuous ice-core chemical analyses using inductively coupled plasma mass spectrometry". In: *Environmental science & technology* 36.1, pp. 7–11.

McCreanor, J. et al. (2007). "Respiratory effects of exposure to diesel traffic in persons with asthma". In: *New England Journal of Medicine* 357.23, pp. 2348–2358.

Meehl, G. A., J. M. Arblaster, and W. D. Collins (2008). "Effects of black carbon aerosols on the Indian monsoon". In: *Journal of Climate* 21.12, pp. 2869–2882.

Mie, G. (1908). "Beiträge zur Optik trüber Medien, speziell kolloidaler Metallösungen". In: *Annalen der physik* 330.3, pp. 377–445.

Mitchell, T. D. et al. (2004). "A comprehensive set of high-resolution grids of monthly climate for Europe and the globe: the observed record (1901–2000) and 16 scenarios (2001–2100)". In: *Tyndall centre for climate change research working paper* 55, p. 25.

Moberg, A. et al. (2005). "Highly variable Northern Hemisphere temperatures reconstructed from low-and high-resolution proxy data". In: *Nature* 433.7026, pp. 613–617.

Mölg, T., N. J. Cullen, and G. Kaser (2009). "Solar radiation, cloudiness and longwave radiation over low-latitude glaciers: implications for mass-balance modelling". In: *Journal of Glaciology* 55.190, pp. 292–302.

Moosmüller, H., R. Chakrabarty, and W. Arnott (2009). "Aerosol light absorption and its measurement: A review". In: *Journal of Quantitative Spectroscopy and Radiative Transfer* 110.11, pp. 844–878.

Moteki, N., Y. Kondo, et al. (2012). "Size dependence of wet removal of black carbon aerosols during transport from the boundary layer to the free troposphere". In: *Geophysical Research Letters* 39.13.

Moteki, N. and Y. Kondo (2007). "Effects of mixing state on black carbon measurements by laser-induced incandescence". In: *Aerosol Science and Technology* 41.4, pp. 398–417.

— (2010). "Dependence of laser-induced incandescence on physical properties of black carbon aerosols: Measurements and theoretical interpretation". In: *Aerosol Science and Technology* 44.8, pp. 663–675.

Murozumi, M., T. J. Chow, and C. Patterson (1969). "Chemical concentrations of pollutant lead aerosols, terrestrial dusts and sea salts in Greenland and Antarctic snow strata". In: *Geochimica et Cosmochimica Acta* 33.10, pp. 1247–1294.

Myhre, G. et al. (2013). "Anthropogenic and natural radiative forcing". In: *Climate change* 423.

Novakov, T. et al. (2003). "Large historical changes of fossil-fuel black carbon aerosols". In: *Geophysical Research Letters* 30.6.

Novo, A. and G. Rossi (1998). "A four-year record (1990–94) of snow chemistry at two glacier fields in the Italian Alps (Careser, 3090m; Colle Vincent, 4086m)". In: *Atmospheric Environment* 32.23, pp. 4061–4073.

Nriagu, J. O. (1979). "Global inventory of natural and anthropogenic emissions of trace metals to the atmosphere". In:

— (1989). "A global assessment of natural sources of atmospheric trace metals". In: *Nature* 338.6210, pp. 47–49.

Nriagu, J. O., J. M. Pacyna, et al. (1988). "Quantitative assessment of worldwide contamination of air, water and soils by trace metals". In: *nature* 333.6169, pp. 134–139.

O'Dowd, C. D. et al. (2002). "Marine aerosol formation from biogenic iodine emissions". In: *Nature* 417.6889, pp. 632–636.

Oerlemans, J., R. Giesen, and M. Van den Broeke (2009). "Retreating alpine glaciers: increased melt rates due to accumulation of dust (Vadret da Morteratsch, Switzerland)". In: *Journal of Glaciology* 55.192, pp. 729–736.

Oerter, H., D. Baker, et al. (1985). "Isotope studies of ice cores from a temperate Alpine glacier (Vernagtferner, Austria) with respect to the meltwater flow". In: *Annals of Glaciology* 7, pp. 90–93.

Oerter, H. and W. Rauert (1982). "Core drilling on Vernagtferner (Oetztal Alps, Austria) in 1979: tritium contents". In: *Zeitschrift für Gletscherkunde und Glazialgeologie* 1, pp. 13–22.

Oeschger, H. et al. (1977). "First results from Alpine core drilling projects". In: *Zeitschrift für Gletscherkunde und Glazialgeologie* 13.1/2, pp. 193–208.

Orombelli, G. and C. Barbante (2004). *Il ghiaccio nelle Alpi: una risorsa strategica per l'ambiente dell'alta montagna*. Istituto Nazionale della Montagna; Bonomia University Press.

Osterberg, E. C. et al. (2006). "Continuous ice core melter system with discrete sampling for major ion, trace element, and stable isotope analyses". In: *Environmental science & technology* 40.10, pp. 3355–3361.

Osterberg, E. et al. (2008). "Ice core record of rising lead pollution in the North Pacific atmosphere". In: *Geophysical Research Letters* 35.5.

Pacyna, E. G. et al. (2007). "Current and future emissions of selected heavy metals to the atmosphere from anthropogenic sources in Europe". In: *Atmospheric Environment* 41.38, pp. 8557–8566.

Pacyna, J. M., A. Semb, and J. E. Hanssen (1984). "Emission and long-range transport of trace elements in Europe". In: *Tellus B* 36.3.

Pacyna, J. M. (1998). "Source inventories for atmospheric trace metals". In: *Atmospheric particles, IUPAC series on analytical and physical chemistry of environmental systems* 5, pp. 385–423.

Pacyna, J. M. and E. G. Pacyna (2001). "An assessment of global and regional emissions of trace metals to the atmosphere from anthropogenic sources worldwide". In: *Environmental Reviews* 9.4, pp. 269–298.

Pacyna, J. (1986). "Atmospheric trace elements from natural and anthropogenic sources". In: *Toxic Metals in the Atmosphere. New York: Wiley*.

Painter, T. H., J. S. Deems, et al. (2010). "Response of Colorado River runoff to dust radiative forcing in snow". In: *Proceedings of the National Academy of Sciences* 107.40, pp. 17125–17130.

Painter, T. H., M. G. Flanner, et al. (2013). "End of the Little Ice Age in the Alps forced by industrial black carbon". In: *Proceedings of the national academy of sciences* 110.38, pp. 15216–15221.

Painter, T. H., S. M. Skiles, et al. (2012). "Dust radiative forcing in snow of the Upper Colorado River Basin: 1. A 6 year record of energy balance, radiation, and dust concentrations". In: *Water Resources Research* 48.7.

Palais, J. M., M. S. Germani, and G. A. Zielinski (1992). "Inter-hemispheric transport of volcanic ash from a 1259 AD volcanic eruption to the Greenland and Antarctic Ice Sheets". In: *Geophysical Research Letters* 19.8, pp. 801–804.

Palmer, A., M. Schwikowski, and H. Gaeggeler (2003). "A Sub-Seasonal Trace Chemical Ice Core Record from Piz Zupo, Swiss Alps". In: *EGS-AGU-EUG Joint Assembly*. Vol. 1, p. 1331.

Pasquill, F. (1961). "The estimation of the dispersion of windborne material". In: *Meteorol. Mag* 90.1063, pp. 33–49.

Pio, C. et al. (2007). "Climatology of aerosol composition (organic versus inorganic) at nonurban sites on a west-east transect across Europe". In: *Journal of Geophysical Research: Atmospheres* 112.D23.

Planchon, F. et al. (2003). "One hundred fifty–year record of lead isotopes in Antarctic snow from Coats Land". In: *Geochimica et Cosmochimica Acta* 67.4, pp. 693–708.

Pohjola, V. et al. (2002). "Effect of periodic melting on geochemical and isotopic signals in an ice core from Lomonosovfonna, Svalbard". In: *Journal of Geophysical Research: Atmospheres* 107.D4.

Pope III, C. A. and D. W. Dockery (2006). "Health effects of fine particulate air pollution: lines that connect". In: *Journal of the air & waste management association* 56.6, pp. 709–742.

Preunkert, S. et al. (2000). "Col du Dôme (Mt Blanc Massif, French Alps) suitability for ice-core studies in relation with past atmospheric chemistry over Europe". In: *Tellus B* 52.3, pp. 993–1012.

Price, P. B., K. Woschnagg, and D. Chirkin (2000). "Age vs depth of glacial ice at South Pole". In: *Geophysical Research Letters* 27.14, pp. 2129–2132.

Puxbaum, H. and A. Limbeck (2008). "Chemical Compounds in the Atmosphere". In: *Elements and Their Compounds in the Environment: Occurrence, Analysis and Biological Relevance, Second Edition*, pp. 17–46.

Puxbaum, H. and W. Tscherwenka (1998). "Relationships of major ions in snow fall and rime at Sonnblick observatory (SBO, 3106m) and implications for scavenging processes in mixed clouds". In: *Atmospheric Environment* 32.23, pp. 4011–4020.

Qu, B. et al. (2014). "The decreasing albedo of the Zhadang glacier on western Nyainqentanglha and the role of light-absorbing impurities". In: *Atmospheric Chemistry and Physics* 14.20, pp. 11117–11128.

Quadrelli, R. et al. (2001). "Observed winter Alpine precipitation variability and links with large-scale circulation patterns". In: *Climate Research* 17.3, pp. 275–284.

R Development Core Team (2008). *R: A Language and Environment for Statistical Computing*. ISBN 3-900051-07-0. R Foundation for Statistical Computing. Vienna, Austria. URL: `http://www.R-project.org`.

Raible, C. C. et al. (2016). "Tambora 1815 as a test case for high impact volcanic eruptions: Earth system effects". In: *Wiley Interdisciplinary Reviews: Climate Change*.

Ramanathan, V. and G. Carmichael (2008). "Global and regional climate changes due to black carbon". In: *Nature geoscience* 1.4, pp. 221–227.

Raynaud, D. et al. (2003). "The Late Quaternary history of atmospheric trace gases and aerosols: interactions between climate and biogeochemical cycles". In: *Paleoclimate, Global Change and the Future*. Springer, pp. 13–31.

Rich, D. Q. et al. (2005). "Association of short-term ambient air pollution concentrations and ventricular arrhythmias". In: *American Journal of Epidemiology* 161.12, pp. 1123–1132.

Ripoll, A. et al. (2014). "Three years of aerosol mass, black carbon and particle number concentrations at Montsec (southern Pyrenees, 1570 m asl)". In: *Atmospheric Chemistry and Physics* 14.8, pp. 4279–4295.

Roman, K. et al. (2003). "Pb and Sr isotopes from an ice-core provides evidence for changing atmospheric conditions at the Sajama icecap, South America". In: *Journal de Physique IV (Proceedings)*. Vol. 107. EDP sciences, pp. 1157–1160.

Ronseaux, F. and R. Delmas (1988). "Chemical composition of bulk atmospheric deposition to snow at Col de La Brenva (Mt Blanc area)". In: *Acid Deposition at High Elevation Sites*. Springer, pp. 491–510.

Rosman, K. J. et al. (1997). "Lead from Carthaginian and Roman Spanish mines isotopically identified in Greenland ice dated from 600 BC to 300 AD". In: *Environmental science & technology* 31.12, pp. 3413–3416.

Rosman, K. et al. (1993). "Isotopic evidence for the source of lead in Greenland snows since the late 1960s". In: *Nature* 362.6418, pp. 333–335.

Röthlisberger, R. et al. (2000). "Technique for continuous high-resolution analysis of trace substances in firn and ice cores". In: *Environmental Science & Technology* 34.2, pp. 338–342.

Rufli, H., B. Stauffer, and H. Oeschger (1976). "Lightweight 50-meter core drill for firn and ice". In: *Ice-core drilling. University of Nebraska Press, Lincoln, NB*, pp. 139–153.

Samset, B. et al. (2013). "Black carbon vertical profiles strongly affect its radiative forcing uncertainty". In: *Atmospheric Chemistry and Physics* 13.5, p. 2423.

Scandone, R., L. Giacomelli, and F. F. Speranza (2008). "Persistent activity and violent strombolian eruptions at Vesuvius between 1631 and 1944". In: *Journal of Volcanology and Geothermal Research* 170.3, pp. 167–180.

Schmidli, J. et al. (2002). "Mesoscale precipitation variability in the region of the European Alps during the 20th century". In: *International Journal of Climatology* 22.9, pp. 1049–1074.

Schöner, W., I. Auer, and R. Böhm (2009). "Long term trend of snow depth at Sonnblick (Austrian Alps) and its relation to climate change". In: *Hydrological Processes* 23.7, pp. 1052–1063.

Schotterer, U., K. Fröhlich, et al. (1997). "Isotope records from Mongolian and Alpine ice cores as climate indicators". In: *Climatic Change at High Elevation Sites*. Springer, pp. 287–298.

Schotterer, U., H. Oeschger, et al. (1985). "Information on paleo-precipitation on a high-altitude glacier, Monte Rosa, Switzerland". In: *Zeitschrift für Gletscherkunde und Glazialgeologie* 21.1-2, pp. 379–388.

Schotterer, U., W. Stichler, et al. (2001). "Stable isotopes in alpine ice cores: do they record climate variability?" In: *Study of environmental change using isotope techniques. IAEA, Vienna*, pp. 292–300.

Schotterer, U. and W. Good (1978). *Datierung von kaltem Firn und Eis in einem Bohrkern vom Colle Gnifetti, Monte Rosa.* Birkhäuser.

Schuster, P. F. et al. (2002). "Atmospheric mercury deposition during the last 270 years: a glacial ice core record of natural and anthropogenic sources". In: *Environmental Science & Technology* 36.11, pp. 2303–2310.

Schwarz, J., R. Gao, D. Fahey, et al. (2006). "Single-particle measurements of midlatitude black carbon and light-scattering aerosols from the boundary layer to the lower stratosphere". In: *Journal of Geophysical Research: Atmospheres* 111.D16.

Schwarz, J., R. Gao, J. Spackman, et al. (2008). "Measurement of the mixing state, mass, and optical size of individual black carbon particles in urban and biomass burning emissions". In: *Geophysical Research Letters* 35.13.

Schwarz, J., J. Spackman, et al. (2010). "The detection efficiency of the single particle soot photometer". In: *Aerosol Science and Technology* 44.8, pp. 612–628.

Schwikowski, M., S. Brütsch, et al. (1999). "A high-resolution air chemistry record from an Alpine ice core: Fiescherhorn glacier, Swiss Alps". In: *Journal of Geophysical Research: Atmospheres* 104.D11, pp. 13709–13719.

Schwikowski, M., P. Seibert, et al. (1995). "A study of an outstanding Saharan dust event at the high-alpine site Jungfraujoch, Switzerland". In: *Atmospheric Environment* 29.15, pp. 1829–1842.

Schwikowski, M., C. Barbante, et al. (2004). "Post-17th-century changes of European lead emissions recorded in high-altitude alpine snow and ice". In: *Environmental science & technology* 38.4, pp. 957–964.

Severi, M. et al. (2015). "Recovering Paleo-Records from Antarctic Ice-Cores by Coupling a Continuous Melting Device and Fast Ion Chromatography". In: *Analytical chemistry* 87.22, pp. 11441–11447.

Shah, A. S. et al. (2013). "Global association of air pollution and heart failure: a systematic review and meta-analysis". In: *The Lancet* 382.9897, pp. 1039–1048.

Shotyk, W. et al. (1996). "Two thousand years of atmospheric arsenic, antimony, and lead deposition recorded in an ombrotrophic peat bog profile, Jura Mountains, Switzerland". In: *Earth and Planetary Science Letters* 145.1, E1–E7.

Shumskii, P. A. and D. Kraus (1958). *Principles of structural glaciology.* Geophysics research directorate, AFCRL.

Sigg, A. et al. (1994). "A continuous analysis technique for trace species in ice cores". In: *Environmental science & technology* 28.2, pp. 204–209.

Sigl, M. (2009). "Ice core based reconstruction of past climate conditions from Colle Gnifetti, Swiss Alps". PhD thesis.

Sigl, M. et al. (2016). "End of the" Little Ice Age" in the Alps not forced by industrial black carbon". In: *EGU General Assembly Conference Abstracts.* Vol. 18, p. 14585.

Skiles, S. M. et al. (2012). "Dust radiative forcing in snow of the Upper Colorado River Basin: 2. Interannual variability in radiative forcing and snowmelt rates". In: *Water Resources Research* 48.7.

Smith, S. J. and T. C. Bond (2014). "Two hundred fifty years of aerosols and climate: the end of the age of aerosols". In: *Atmospheric Chemistry and Physics* 14.2, pp. 537–549.

Solomon, S. (2007). *Climate change 2007-the physical science basis: Working group I contribution to the fourth assessment report of the IPCC*. Vol. 4. Cambridge University Press.

Stephens, M., N. Turner, and J. Sandberg (2003). "Particle identification by laser-induced incandescence in a solid-state laser cavity". In: *Applied optics* 42.19, pp. 3726–3736.

Sterle, K. et al. (2013). "Retention and radiative forcing of black carbon in eastern Sierra Nevada snow". In: *The Cryosphere* 7.1, pp. 365–374.

Stocker, T. et al. (2013). "Technical summary". In: *Climate Change 2013: The Physical Science Basis. Contribution of Working Group I to the Fifth Assessment Report of the Intergovernmental Panel on Climate Change*. Cambridge University Press, pp. 33–115.

Stocker, T. F. et al. (2013). "Climate change 2013: the physical science basis. Intergovernmental panel on climate change, working group I Contribution to the IPCC fifth assessment report (AR5)". In: *New York*.

Stothers, R. B. (1984). "The great Tambora eruption in 1815 and its aftermath". In: *Science* 224.4654, pp. 1191–1198.

Sutton, R. T. and B. Dong (2012). "Atlantic Ocean influence on a shift in European climate in the 1990s". In: *Nature Geoscience* 5.11, pp. 788–792.

Tanaka, T. (1988). "Distribution of arsenic in the natural environment with emphasis on rocks and soils". In: *Applied Organometallic Chemistry* 2.4, pp. 283–295.

Taylor, H. E. (2001). *Inductively coupled plasma-mass spectrometry: practices and techniques*. Academic Press.

Tegen, I. and I. Fung (1994). "Modeling of mineral dust in the atmosphere: Sources, transport, and optical thickness". In: *Journal of Geophysical Research: Atmospheres* 99.D11, pp. 22897–22914.

Terada, H. et al. (2012). "Atmospheric discharge and dispersion of radionuclides during the Fukushima Dai-ichi Nuclear Power Plant accident. Part II: verification of the source term and analysis of regional-scale atmospheric dispersion". In: *Journal of Environmental Radioactivity* 112, pp. 141–154.

Thevenon, F. et al. (2009). "Mineral dust and elemental black carbon records from an Alpine ice core (Colle Gnifetti glacier) over the last millennium". In: *Journal of Geophysical Research: Atmospheres* 114.D17.

Thordarson, T. and S. Self (2003). "Atmospheric and environmental effects of the 1783–1784 Laki eruption: A review and reassessment". In: *Journal of Geophysical Research: Atmospheres* 108.D1.

Uglietti, C., A. Zapf, et al. (2016). "Radiocarbon dating of glacier ice". In: *The Cryosphere Discussions* 2016, pp. 1–19. DOI: 10.5194/tc-2016-160. URL: http://www.the-cryosphere-discuss.net/tc-2016-160/.

Uglietti, C., P. Gabrielli, C. Cooke, et al. (2015). "Widespread pollution of the South American atmosphere predates the industrial revolution by 240 years". In: *EGU General Assembly Conference Abstracts*. Vol. 17, p. 5456.

Uglietti, C., P. Gabrielli, J. W. Olesik, et al. (2014). "Large variability of trace element mass fractions determined by ICP-SFMS in ice core samples from worldwide high altitude glaciers". In: *Applied Geochemistry* 47, pp. 109–121.

Vallelonga, P., K. Van de Velde, et al. (2002). "The lead pollution history of Law Dome, Antarctica, from isotopic measurements on ice cores: 1500 AD to 1989 AD". In: *Earth and Planetary Science Letters* 204.1, pp. 291–306.

Vallelonga, P., P. Gabrielli, et al. (2005). "A 220 kyr record of Pb isotopes at Dome C Antarctica from analyses of the EPICA ice core". In: *Geophysical Research Letters* 32.1.

Van de Velde, K., C. Barbante, et al. (2000). "Changes in the occurrence of silver, gold, platinum, palladium and rhodium in Mont Blanc ice and snow since the 18th century". In: *Atmospheric Environment* 34.19, pp. 3117–3127.

Van de Velde, K., C. Boutron, et al. (1998). "Seasonal variations of heavy metals in the 1960s Alpine ice: sources versus meteorological factors". In: *Earth and planetary science letters* 164.3, pp. 521–533.

Van de Velde, K., C. Ferrari, et al. (1999). "A 200 year record of atmospheric cobalt, chromium, molybdenum, and antimony in high altitude alpine firn and ice". In: *Environmental science & technology* 33.20, pp. 3495–3501.

Vaughan, D. G. et al. (2013). "Observations: cryosphere". In: *Climate change*, pp. 317–382.

Vega, C. P. et al. (2016). "A synthetic ice core approach to estimate ion relocation in an ice field site experiencing periodical melt: a case study on Lomonosovfonna, Svalbard". In: *The Cryosphere* 10.3, p. 961.

Venzac, H. et al. (2009). "Seasonal variation of aerosol size distributions in the free troposphere and residual layer at the puy de Dôme station, France". In: *Atmospheric Chemistry and Physics* 9.4, pp. 1465–1478.

Veysseyre, A. et al. (2001). "Heavy metals in fresh snow collected at different altitudes in the Chamonix and Maurienne valleys, French Alps: initial results". In: *Atmospheric Environment* 35.2, pp. 415–425.

Vincent, C. et al. (2007). "Climate warming revealed by englacial temperatures at Col du Dôme (4250 m, Mont Blanc area)". In: *Geophysical Research Letters* 34.16.

Vollweiler, N. et al. (2006). "A precisely dated climate record for the last 9 kyr from three high alpine stalagmites, Spannagel Cave, Austria". In: *Geophysical Research Letters* 33.20.

Wagner, S. and E. Zorita (2005). "The influence of volcanic, solar and CO2 forcing on the temperatures in the Dalton Minimum (1790–1830): a model study". In: *Climate dynamics* 25.2-3, pp. 205–218.

Wania, F. et al. (1998). "The effects of snow and ice on the environmental behaviour of hydrophobic organic chemicals". In: *Environmental Pollution* 102.1, pp. 25–41.

Warren, S. (1984). "Impurities in snow: effect on albedo andsnowmelt". In: *Annals of Glaciology* 5, pp. 177–179.

Warren, S. G. (1982). "Optical properties of snow". In: *Reviews of Geophysics* 20.1, pp. 67–89.

Warren, S. G. and W. J. Wiscombe (1980). "A model for the spectral albedo of snow. II: Snow containing atmospheric aerosols". In: *Journal of the Atmospheric Sciences* 37.12, pp. 2734–2745.

Wedepohl, K. H. (1995). "The composition of the continental crust". In: *Geochimica et cosmochimica Acta* 59.7, pp. 1217–1232.

Weingartner, E., H. Burtscher, and U. Baltensperger (1997). "Hygroscopic properties of carbon and diesel soot particles". In: *Atmospheric Environment* 31.15, pp. 2311–2327.

Wiscombe, W. J. and S. G. Warren (1980). "A model for the spectral albedo of snow. I: Pure snow". In: *Journal of the Atmospheric Sciences* 37.12, pp. 2712–2733.

Wong, G. J. et al. (2013). "Trace-element and physical response to melt percolation in Summit (Greenland) snow". In: *Annals of Glaciology* 54.63, pp. 52–62.

Xu, B. et al. (2009). "Black soot and the survival of Tibetan glaciers". In: *Proceedings of the National Academy of Sciences* 106.52, pp. 22114–22118.

Xu, Y., V. Ramanathan, and W. Washington (2016). "Observed high-altitude warming and snow cover retreat over Tibet and the Himalayas enhanced by black carbon aerosols". In: *Atmospheric Chemistry and Physics* 16.3, pp. 1303–1315.

Yttri, K. et al. (2007). "Elemental and organic carbon in PM 10: a one year measurement campaign within the European Monitoring and Evaluation Programme EMEP". In: *Atmospheric Chemistry and Physics* 7.22, pp. 5711–5725.

Zagorodnov, V., L. Thompson, and E. Mosley-Thompson (2000). "Portable system for intermediate-depth ice-core drilling". In: *Journal of Glaciology* 46.152, pp. 167–172.

Zampieri, M., E. Scoccimarro, and S. Gualdi (2013). "Atlantic influence on spring snowfall over the Alps in the past 150 years". In: *Environmental Research Letters* 8.3, p. 034026.

Zanatta, M. et al. (2016). "A European aerosol phenomenology-5: Climatology of black carbon optical properties at 9 regional background sites across Europe". In: *Atmospheric Environment* 145, pp. 346–364.

Zemp, M. et al. (2006). "Alpine glaciers to disappear within decades?" In: *Geophysical Research Letters* 33.13.

Zennaro, P. et al. (2014). "Fire in ice: two millennia of boreal forest fire history from the Greenland NEEM ice core". In: *Climate of the Past* 10.5, pp. 1905–1924.

Zhang, R., T. L. Delworth, and I. M. Held (2007). "Can the Atlantic Ocean drive the observed multidecadal variability in Northern Hemisphere mean temperature?" In: *Geophysical Research Letters* 34.2.

Ziegler, P. (2013). *The black death*. Faber & Faber.

Zwiers, F. W. and X. Zhang (2003). "Toward regional-scale climate change detection". In: *Journal of Climate* 16.5, pp. 793–797.